Doctoral School of Geosciences

OPEN-SYSTEM IGNEOUS PROCESSES IN THE FELSIC ROCKS OF THE DITRĂU ALKALINE MASSIF (EASTERN CARPATHIANS, ROMANIA)

A Ditrói Alkáli Masszívum (Keleti-Kárpátok, Románia) felzikus kőzeteinek nyílt rendszerű magmás folyamatai

PhD Dissertation

Author

LUCA KIRI

Supervisor

Elemér Pál-Molnár, DSc

Head of institute, Institute of Geography and Geology, University of Szeged

Department of Mineralogy, Geochemistry and Petrology

'Vulcano' Petrology and Geochemistry Research Group

Faculty of Science and Informatics

University of Szeged

Szeged

2023

For Dad, with all my love

Early predictions would seem to suggest

I ain't quite where I think I am

– Alex Turner, Arctic Monkeys

TABLE OF CONTENTS

LIST OF FIGURES

LIST OF TABLES

LIST OF SUPPLEMENTARY FIGURES

LIST OF SUPPLEMENTARY TABLES

<center>**CHAPTER I**</center>

<center>**INTRODUCTION**</center>

Volcanic and igneous plumbing systems (VIPSs) or magma plumbing systems are a combination of environments where magma is produced, transported, and stored. The holistic approach in the research of VIPSs combines the results of disciplines such as field observations, petrology, geochemistry, and geophysics to unravel the mechanisms occurring before, during, and after magma ascent (Burchardt, 2018).

The high-level plutonic complexes exposed on the current surface are the "fossilized" and solidified versions of the once-active igneous plumbing systems, providing a unique opportunity to trace and understand the mechanisms operating deep beneath the volcanoes (Ubide et al., 2021). The research of ancient plumbing systems is of both scientific and economic importance.

I.1. Trans-crustal magma reservoirs

The scientific relevance is founded in our understanding of igneous processes and their effects on volcanic activity. The classic conceptual models of magmatic processes and volcanism hypothesized that the large, stable, long-lived, and shallow upper crustal magma reservoirs (magma chambers) supplying volcanic eruptions are melt-dominated (e.g., Hildreth, 1979; Bachmann and Bergantz, 2004). Nevertheless, the features unraveled by modern analytical techniques (e.g., geophysical, geochronological, geochemical, petrological, and volcanological investigations as well as numerical modeling) in the past decades disproved this theory and led to a paradigm shift. According to the new approach, the unstable, multi-level, and vertically extensive, so-called trans-crustal magmatic systems (TCMSs) are generally crystalline (dominated by non-eruptible crystal mush) and contain heterogeneously dispersed minerals, melt, and exsolved volatiles. In a mushy system, the melt is distributed in the continuous framework of crystals. TCMSs usually exhibit a transition from deep crustal (ultra)mafic cumulates to upper crustal granites (e.g., Marsh, 2004; Solano et al., 2014; Annen et al., 2015; Cashman et al., 2017; Jackson et al., 2018; Holness et al., 2019; Sparks et al., 2019).

The new concept emphasizes the influence of open-system processes (such as repeated invasion of replenishing magma batches, magma mixing and mingling as well as crustal assimilation) on the evolution of magma chambers (Cashman et al., 2017).

The hot lower crust is the site of voluminous, compaction-driven melt segregation, fractional crystallization, and cumulate formation. In contrast, the upper crust is characterized

by a permanent, non-eruptible crystal mush. Unstable, melt-dominated segregations can advance through mushy regions and get concentrated into shallow chambers; however, substantial volumes of upper crustal melts are short-lived (Solano et al., 2014; Cashman et al., 2017; Jackson et al., 2018). Magmas may stall in shallow reservoirs during their ascent and interact with the surrounding country rock (e.g., crustal and mantle rocks or rocks of the same igneous system). Vast blocks of the enveloping rock may fall into the magma (stoping) and get completely or partially consumed (assimilation). Xenoliths are the vestiges of the country rock (Jerram et al., 2018).

The upper crustal magma chambers get episodically replenished by recharge magmas. The replenishing magmas are prone to interact with the previously emplaced magma pulses (Cashman et al., 2017). Magma mingling involves the physical interplay of magmas, typical when a voluminous felsic magma gets replenished by a comparably smaller amount of mafic magma. A heterogeneous mixture is produced, with remnants of the mafic end-member forming distinct units (Frost and Mahood, 1987), referred to as mafic magmatic/microgranular enclaves (MMEs; Didier and Barbarin, 1991). Interaction between a volumetrically large mafic and a minor felsic magma results in magma mixing (Frost and Mahood, 1987); however, this process is more effective when the interacting end-members are of comparable composition and rheological properties (e.g., Ubide et al., 2014b). Quasi-homogeneous, hybrid magmas of intermediate geochemical composition are formed by blending of the end-members (Frost and Mahood, 1987). Composition of the hybrids can be modified after the mixing event(s), for instance by fractional crystallization (Campos et al., 2002).

The intrusion of replenishing magma batches is necessary for the development of extensive magma bodies and it also triggers volcanic eruptions. The crystal mush can be remobilized prior to an eruption by the recharge of mantle-derived, hot and mafic magmas that provide additional heat. The frequency of recharge, the volume of the replenishing magma batches, and the structure of the reservoir determine the efficacy of remobilization. Buoyant, unstable, and ephemeral eruptible magmas are characterized by a voluminous melt fraction with suspended crystals (Solano et al., 2014; Cashman et al., 2017).

Crystals of distinct origins (e.g., phenocrysts, antecrysts, and xenocrysts), carried by the ascending magmas, are also known as crystal cargo. Phenocrysts are crystallized from their host magma under equilibrium conditions. Antecrysts are formed in the same igneous system but represent an earlier magmatic episode or a different magma batch. Xenocrysts are exotic to the igneous system (e.g., originated from the country rock) and were incorporated during magma ascent. The final igneous structures and textures, therefore, bear important information on

complex processes such as assimilation, crystal transfer/recycling, fractional crystallization as well as magma mixing and mingling events (Jerram et al., 2018).

Detailed investigation of the crystal cargo ejected by volcanoes (e.g., cumulate nodules, crystal aggregates, and phenocrysts) or fossilized in plutonic rocks is the first stage in understanding magmatic processes since they provide a window into the subvolcanic mechanisms of igneous systems. Textural and compositional variations (e.g., complex zoning) within and between individual minerals provide indirect insights into the physically yet-impassable regions of magma plumbing systems and their mechanisms such as assimilation, crystal transfer, fractionation, mixing and mingling as well as recharge (Cashman et al., 2017; Jerram et al., 2018; Ubide et al., 2021). Crystal-scale data could thus help us to trace the evolution of magmas from their source to emplacement and to unravel the main stages of their evolution (Jerram et al., 2018).

Certain minerals (e.g., titanite and zircon) can be regarded as chronometers, bearing important information on the time scales of igneous differentiation and magma transport (Cashman et al., 2017; Ubide et al., 2021). Field and geochronological evidence confirm that plutons are assembled by the incremental emplacement of multiple magma pulses over a period of thousands to millions of years (Coleman et al., 2004; Glazner et al., 2004; Schoene et al., 2012). This is in agreement with the theory of periodic magma extraction and transport and reactivation of VIPSs. The emplacement time of a single magma batch is relatively rapid; nevertheless, if there are long time gaps between pulses, the net emplacement time may be significantly greater. Individual batches are preserved in rapidly emplaced and solidified intrusions. However, the internal contacts of discrete pulses could be erased by crystallization, melt segregation, and/or if the temperature of the pluton remains high for an extended period of time (e.g., due to the intrusion of subsequent magma batches) (Cruden and Weinberg, 2018; Morgan, 2018). The internal contacts may be difficult to identify if pulses of similar composition are emplaced (Morgan, 2018).

Unraveling the inner dynamics of volcanoes is essential to appropriately interpret volcanism and mitigate volcanic hazards. Volcanology plays an important part in this field of research, focusing on surface and near-surface igneous processes. Nevertheless, the key factors lie underground, in the deep crust, well beneath the volcanic edifices. The study of igneous processes gives an improved comprehension of the architecture, behavior, and temporal constraints of magma plumbing systems. Since the internal mechanisms (such as magma recharge, mixing, and mingling) have a fundamental impact on volcanic activity, it is essential to understand them from a hazard perspective (Cashman et al., 2017). The detection and monitoring of magma pockets are crucial for prognosing volcanic eruptions (Ubide et al., 2021).

I.2. The Ditrău Alkaline Massif

The exhumed magma storage system of the Ditrău Alkaline Massif (DAM) presents an exceptional natural setting for investigating the open- and closed-system igneous processes occurring in trans-crustal magmatic systems. Due to the associated rare earth element (REE) mineralization, the massif has the potential to become an economically feasible deposit in the near future (Honour et al., 2018).

The DAM crops out in an area of approximately 225 km^2 and makes up the southern and southwestern parts of the Giurgeu Mountains in the Eastern Carpathians (Romania). A broad spectrum of rock types, varying from ultramafic cumulates to granitoid rocks, is exposed in the area, exhibiting an intricate structural framework (Pál-Molnár, 2000; Batki et al., 2014; Pál-Molnár et al., 2015a, b). The igneous event occurred at the southwestern periphery of the East European Craton in the Middle–Late Triassic (Pál-Molnár et al., 2021). The magmatism took place in an intra-plate, rift-related, extensional tectonic setting (e.g., Morogan et al., 2000; Pál-Molnár, 2000, 2010b; Batki et al., 2014; Pál-Molnár et al., 2015b). The Tethyan rifting resulted in a restricted igneous activity (Stampfli, 2000); therefore, the DAM does not belong to any particular alkaline magmatic province (Honour et al., 2018). The Variscan metamorphic rocks of the Eastern Carpathians had been intruded by the alkaline magmas of the DAM, followed by nappe-forming Alpine tectonic events (Săndulescu, 1984; Balintoni, 1997).

Since the first scientific description of the massif (Lilienbach, 1833), the DAM has been in the focus of research, with a significant emphasis on its mineralogy, petrology, structure, evolution, and timing as well as on the economic potential of the rocks and mineralized zones. At the beginning of the 20th century, the DAM was one of the most renowned igneous massifs in Europe. Thanks to the research of Streckeisen (e.g., 1938, 1952, 1954, 1960), the DAM earned its European and worldwide reputation. Scientific and economic interest grew after World War II and geophysical research began in the 1950s, focusing, among others, on the REE and polymetallic sulfide mineralization (Pál-Molnár, 1994a).

Over the 190-years-long research of the DAM, several concepts and genetic models have been proposed, including (a) assimilation and fractional crystallization of a basic intrusion (Streckeisen, 1938; Morogan et al., 2000; Pál-Molnár, 2000); (b) fractional crystallization of a syenitic parental magma (Streckeisen, 1960); (c) emplacement of a mantle-derived basic magma and a crust-derived felsic magma (Anastasiu and Constantinescu, 1979); (d) intrusion of dioritic, gabbroic, nepheline syenitic and syenitic magmas, the latter having undergone crustal assimilation leading to the formation of granite (Streckeisen and Hunziker, 1974); (e) emplacement of mantle-derived gabbroic-dioritic, crust-derived syenitic, and mantle-derived nepheline syenitic magmas (Kräutner and Bindea, 1998).

The timing of magmatism and the emplacement sequence of the different rock types were also in the focus of research. Incipient field and structural inspections (e.g., Reinhardt, 1911; Streckeisen, 1952, 1954; Codarcea et al., 1957) were supplemented by numerous investigations utilizing different dating techniques (such as $^{40}Ar/^{39}Ar$, K/Ar, and U–Pb age determinations) on distinct rock types and mineral phases of the DAM. Conflicting evolution theories have been proposed based on the interpretation of the age data varying between 237.4 ± 9.1 and 81.3 ± 3.1 Ma. Pál-Molnár and Árva-Sós (1995) hypothesized that the DAM is the product of prolonged magmatism and that the massif was formed in two stages: (1) ultramafic rocks (hornblendite), nepheline syenite, and granite (Middle Triassic–Lower Jurassic) and (2) syenite and diorite (Middle Jurassic–Lower Cretaceous). Kräutner and Bindea (1998) summarized the available age data and proposed a three-stage emplacement model covering an extensive time span of ~70 Ma in the Triassic and Jurassic. Nevertheless, based on zircon U–Pb ages from syenite, Pană et al. (2000) suggested that the igneous event was significantly shorter than formerly assumed and that the intrusion of syenite was almost coeval with that of gabbro and diorite.

The archive age data had to be revised and supplemented for multiple reasons: (a) some of the analyzes were performed on whole-rock samples (e.g., by Bagdasarian, 1972; Streckeisen and Hunziker, 1974; Mînzatu and Ardeleanu, 1980; Mînzatu et al., 1981) containing variably altered minerals with distinct closure temperatures; therefore, the results can be considered as mixed ages; (b) the low closure temperature of biotite (300 ± 50°C; Purdy and Jäger, 1976; Harrison and McDougall, 1980) and feldspars (150 ± 40°C; Dodson and McClelland Brown, 1985) make them less appropriate for K/Ar dating since their isotopic system can be easily overprinted by post-magmatic processes. Amphibole has a higher closure temperature (510 ± 25°C; Harrison, 1981), making it a preferred candidate for K/Ar age determination (Hart, 1961). More consistent information can be obtained by U–Pb dating of chemically resistant accessory phases with high closure temperatures [e.g., titanite: 635–780°C (Cherniak, 1993); zircon: 900°C< (Cherniak and Watson, 2001)] (Xie, 2018); (c) the conflicting age data and the resulting evolution theories made it difficult to fit the DAM into the inherently complex palinspastic framework of the Tethyan realm.

Evidence of open-system igneous processes was recognized early on in the research of the massif: Streckeisen (1954) noted that syenite hosts abundant basic enclaves along the peripheral areas of basic rocks. According to Kräutner and Bindea (1998), hybrid rocks were formed by magma mingling and mixing of gabbroic-dioritic and syenitic magmas. "Pillowy forms" infer the simultaneous emplacement, mingling, mixing, and hybridization of felsic and

mafic magmas (Morogan et al., 2000). Nevertheless, details of the open-system mechanisms remained unresolved.

Recently, structural investigations, whole-rock and mineral chemical analyzes shed light on some of the features of the open-system processes (e.g., magma mixing and mingling, country rock assimilation, crystal transfer and recycling) that have a significant impact on the evolution of the DAM (e.g., Batki et al., 2018; Heincz et al., 2018; Ódri et al., 2020).

Apart from some studies (e.g., Streckeisen, 1954; Kräutner and Bindea, 1998; Morogan et al., 2000), the felsic unit in the northern part of the massif has been considered as a uniform, homogeneous suite of the DAM. Nevertheless, Batki et al. (2018) identified clinopyroxene antecrysts, among others, in syenite and diorite, necessitating the reinvestigation of the felsic rocks. Initial petrographic study of the archive syenite samples revealed that the studied rocks bear important traces (e.g., mafic clots, two generations of apatites, inclusion-free rims of feldspars) of magma mixing and mingling; however, the peculiarities of these processes remained enigmatic (Kiri, 2018).

The previously collected samples could no longer be used since GPS technology was not available at the time of the former fieldwork. Therefore, sampling sites are either unknown or obscure and limited to the names of valleys, making it almost impossible to accurately retrace the previous sampling locations. Archive but unpublished mineral geochemical data of syenite are available. Nevertheless, these rocks were regarded homogeneous at the time of the analyzes and the textural position of the minerals (e.g., isolated and clot-forming) was not taken into consideration during the sample selection process, making these data less reliable.

I.3. Objectives, methods, and the structure of the dissertation

The main goal of the PhD research was the integrated study of the felsic rocks cropping out in the northern part of the Ditrău Alkaline Massif, including field observations, petrographic investigations, whole-rock and mineral-scale geochemical analyzes, and radiometric age dating.

The following chapters are an anthology of accepted and published papers on the felsic rocks in the northern part of the Ditrău Alkaline Massif.

In Chapter II, the archive age data of the DAM were revised and supplemented by new K/Ar (amphibole from amphibole- and pyroxene-rich cumulate, nepheline syenite and granite, along with biotite from granite) and U–Pb (titanite and zircon from syenite and nepheline syenite) geochronological data that refine the formerly recorded ages, challenge the age and extent of the multi-stage evolution hypotheses (e.g., by Pál-Molnár and Árva-Sós, 1995; Kräutner and Bindea, 1998; Morogan et al., 2000), and imply a short-lived igneous event. The

age data were correlated with corresponding palinspastic reconstructions to locate the paleogeographic setting in which the DAM was formed. The results were published in *Central European Geology*.

The detailed petrographic study of the recently and systematically collected samples is presented in Chapter III. The new samples were gathered from *in situ* outcrops during two sampling campaigns in 2019 and 2021. Documentation included the recording of GPS coordinates and field relations with other rock types (e.g., crosscutting relations). Not only felsic but also some mafic (e.g., cumulates and lamprophyres) and metamorphic country rocks were sampled and the most representative specimens were studied. Investigations were performed on both hand specimens and thin sections. The latter were examined with Olympus BX41 and Brunel SP300P optical microscopes. Mineral phases were determined by a THERMO Scientific DXR Raman microscope. Compositional zoning as well as microtextural and reaction relations were unraveled by an AMRAY 1830 SEM equipped with an EDAX PV 9800 EDS detector. The studied rocks are characterized by exceptionally complex macroscopic and microscopic textural features. Most of the significant characteristics could only be unveiled by classical polarized-light microscopy. Outcrop-to-micro-scale traces of felsic crystal accumulation, flow fabrics, mafic clots, and metamorphic wall rock xenoliths imply that the studied rocks crystallized in a dynamic, open-system magmatic environment. The paper was published in *Central European Geology*.

Petrographic observations were supplemented by bulk-rock and mineral-scale major and trace element data (determined by ICP-ES and ICP-MS along with EMPA and LA-ICP-MS, respectively) in Chapter IV. Mineral chemical data (amphibole, clinopyroxene, and plagioclase) were obtained from crystals of distinct textural situations (isolated and aggregated). Whole-rock as well as amphibole, clinopyroxene, and plagioclase compositions imply the hybrid nature of most of the investigated felsic rocks. The geochemical data are in accordance with previous hypotheses, based mainly on petrography, and support the theory that the studied felsic suite was formed in an open-system igneous setting, where country rock assimilation, mafic and felsic crystal accumulation as well as magma mixing and mingling prevailed. The article was published in *Geologica Carpathica*.

New results on the felsic rocks in the northern part of the Ditrău Alkaline Massif are summed up in Chapter V (Conclusions). The summarized reference list is provided at the end of the dissertation.

Since the two journals (*Central European Geology* and *Geologica Carpathica*) use different formats (e.g., grammar, citations, references), in order to keep the style of the PhD Dissertation consistent, the format of *Central European Geology* was preferred and followed.

TIMING OF MAGMATISM OF THE DITRĂU ALKALINE MASSIF, ROMANIA – A REVIEW BASED ON NEW U–PB AND K/AR DATA

Elemér Pál-Molnár[*]
'Vulcano' Petrology and Geochemistry Research Group, Department of Mineralogy, Geochemistry and Petrology, University of Szeged, Szeged, Hungary;
MTA-ELTE Volcanology Research Group, Budapest, Hungary
e-mail: palm@geo.u-szeged.hu

Luca Kiri[*]
'Vulcano' Petrology and Geochemistry Research Group, Department of Mineralogy, Geochemistry and Petrology, University of Szeged, Szeged, Hungary
e-mail: kiri.luca@gmail.com

Réka Lukács
'Vulcano' Petrology and Geochemistry Research Group, Department of Mineralogy, Geochemistry and Petrology, University of Szeged, Szeged, Hungary;
MTA-ELTE Volcanology Research Group, Budapest, Hungary
e-mail: reka.harangi@gmail.com

István Dunkl
Geoscience Center, Department of Sedimentology and Environmental Geology, University of Göttingen, Göttingen, Germany
e-mail: istvan.dunkl@geo.uni-goettingen.de

Anikó Batki
'Vulcano' Petrology and Geochemistry Research Group, Department of Mineralogy, Geochemistry and Petrology, University of Szeged, Szeged, Hungary;
MTA-ELTE Volcanology Research Group, Budapest, Hungary
e-mail: batki@geo.u-szeged.hu

Máté Szemerédi
'Vulcano' Petrology and Geochemistry Research Group, Department of Mineralogy, Geochemistry and Petrology, University of Szeged, Szeged, Hungary;
MTA-ELTE Volcanology Research Group, Budapest, Hungary
e-mail: szemeredi.mate@gmail.com

Enikő Eszter Almási
'Vulcano' Petrology and Geochemistry Research Group, Department of Mineralogy, Geochemistry and Petrology, University of Szeged, Szeged, Hungary
e-mail: almasieniko@geo.u-szeged.hu

Edina Sogrik
'Vulcano' Petrology and Geochemistry Research Group, Department of Mineralogy, Geochemistry and Petrology, University of Szeged, Szeged, Hungary
e-mail: sogrik.edina@geo.u-szeged.hu

Szabolcs Harangi
MTA-ELTE Volcanology Research Group, Budapest, Hungary
e-mail: szabolcsharangi@gmail.com

[*]The first two authors have contributed equally to this work.

Timing of magmatism of the Ditrău Alkaline Massif, Romania – A review based on new U–Pb and K/Ar data

by: Elemér Pál-Molnár, Luca Kiri, Réka Lukács, István Dunkl, Anikó Batki, Máté Szemerédi, Enikő Eszter Almási, Edina Sogrik, Szabolcs Harangi

Abstract

The timing of Triassic magmatism of the Ditrău Alkaline Massif (Eastern Carpathians, Romania) is important for constraining the tectonic framework and emplacement context of this igneous suite during the closure of Paleotethys and coeval continental rifting as well as formation of back-arc basins.

Our latest geochronological data refine the previously reported ages, ranging between 237.4 ± 9.1 and 81.3 ± 3.1 Ma. New K/Ar and U–Pb age data combined with all recently (post-1990) published ages indicate a relatively short magmatic span (between 238.6 ± 8.9 Ma and 225.3 ± 2.7 Ma; adding that the most relevant U–Pb ages scatter around ~230 Ma) of the Ditrău Alkaline Massif. The age data, complemented by corresponding palinspastic reconstructions, shed light on the paleogeographic environment wherein the investigated igneous suite was formed.

The magmatism of the Ditrău Alkaline Massif could be associated with an intra-plate, rift-related extensional tectonic setting at the southwestern margin of the East European Craton during the Middle–Late Triassic (Ladinian–Norian) period.

II.1. Introduction

The Ditrău Alkaline Massif (DAM), located in the Eastern Carpathians (Romania) is an igneous suite characterized by a complex structure and lithology. Since its first mention by Lilienbach (1833), the DAM has been studied, including its petrotectonic environment, petrogenetic relations, and the timing of magmatism (e.g., Koch, 1876, 1879; Streckeisen, 1938, 1960; Codarcea et al., 1957, 1958; Bagdasarian, 1972; Streckeisen and Hunziker, 1974; Pál-Molnár and Árva-Sós, 1995; Dallmeyer et al., 1997; Kräutner and Bindea, 1998; Morogan et al., 2000; Pál-Molnár, 2000, 2010a; Pană et al., 2000; Batki et al., 2004, 2014, 2018; Fall et al., 2007; Pál-Molnár et al., 2015a, b).

Several analyzes have been conducted with various dating methods (e.g., K/Ar, $^{40}Ar/^{39}Ar$, and U–Pb age determinations) on different rock types and mineral phases of the

Ditrău Alkaline Massif. Interpretation of the results led to contradictory hypotheses on the genesis of the igneous complex and its rock associations. In order to better understand the evolution and magmatic processes of the massif, these data needed to be reconsidered and supplemented by additional, up-to-date age determination.

The aim of our study – based on the revision of previous age data and interpretation of new amphibole and biotite K/Ar as well as titanite and zircon U–Pb ages of amphibole- and pyroxene-rich cumulate, syenite, nepheline syenite, and granite samples – is to review and specify the age, time span, and sequence of the open-system magmatic processes (e.g., Batki et al., 2018), that played an important role in the formation of the Ditrău Alkaline Massif.

II.2. Geologic setting

The Ditrău Alkaline Massif is located in the southern and southwestern part of the Giurgeu Mountains (Eastern Carpathians, Romania) and crops out in an area of ca. 225 km^2 (Fig. II.1A). The DAM consists of diverse rock types in an elaborate structural relationship. The most common rock types of the massif are as follows: mafic-ultramafic cumulates (e.g., hornblendite, olivine-rich cumulate, amphibole- and pyroxene-rich cumulate, amphibole-rich cumulate), alkali gabbro, alkali diorite, monzodiorite, monzonite, monzosyenite, syenite, nepheline syenite, quartz syenite, and alkali granite (Fig. II.1B). These rocks are crosscut by lamprophyre, tinguaite, and syenite dykes (Pál-Molnár, 2000; Batki et al., 2014; Pál-Molnár et al., 2015a, b).

The DAM had intruded into the Mesozoic crystalline rocks of the Eastern Carpathians and was subjected to nappe-forming Alpine tectonic events (Pál-Molnár, 1994a, b; Pál-Molnár and Árva-Sós, 1995). The Central Eastern Carpathian Zone or Crystalline Mesozoic Zone is an east-verging nappe system that was formed during the Austrian tectogenesis. It derives from the marginal part of the Getic microcontinent that forms the basement of the Transylvanian Basin. The nappe system is referred to as Median Dacides (Săndulescu, 1984) or Eastern Getides (Balintoni, 1997). According to Săndulescu (1984), the Median Dacides can be divided into three Alpine nappes (Infrabucovinian, Subbucovinian, and Bucovinian), composed of pre-Alpine metamorphic rocks and Permo-Mesozoic cover sequences. Pre-Alpine, west-verging, petrographically uniform tectonic units of the Subbucovinian and Bucovinian Nappes and their respective metamorphic terranes (or alternatively: lithogroups) are as follows: Rodna (Rebra Terrane), Pietrosu Bistriţei (Negrişoara Terrane), Putna (Tulgheş Terrane), and Rarău Nappe (Bretila Terrane and Hăghimaş Granitoids) (Balintoni et al., 1983; Vodă and Balintoni, 1994; Balintoni, 1997).
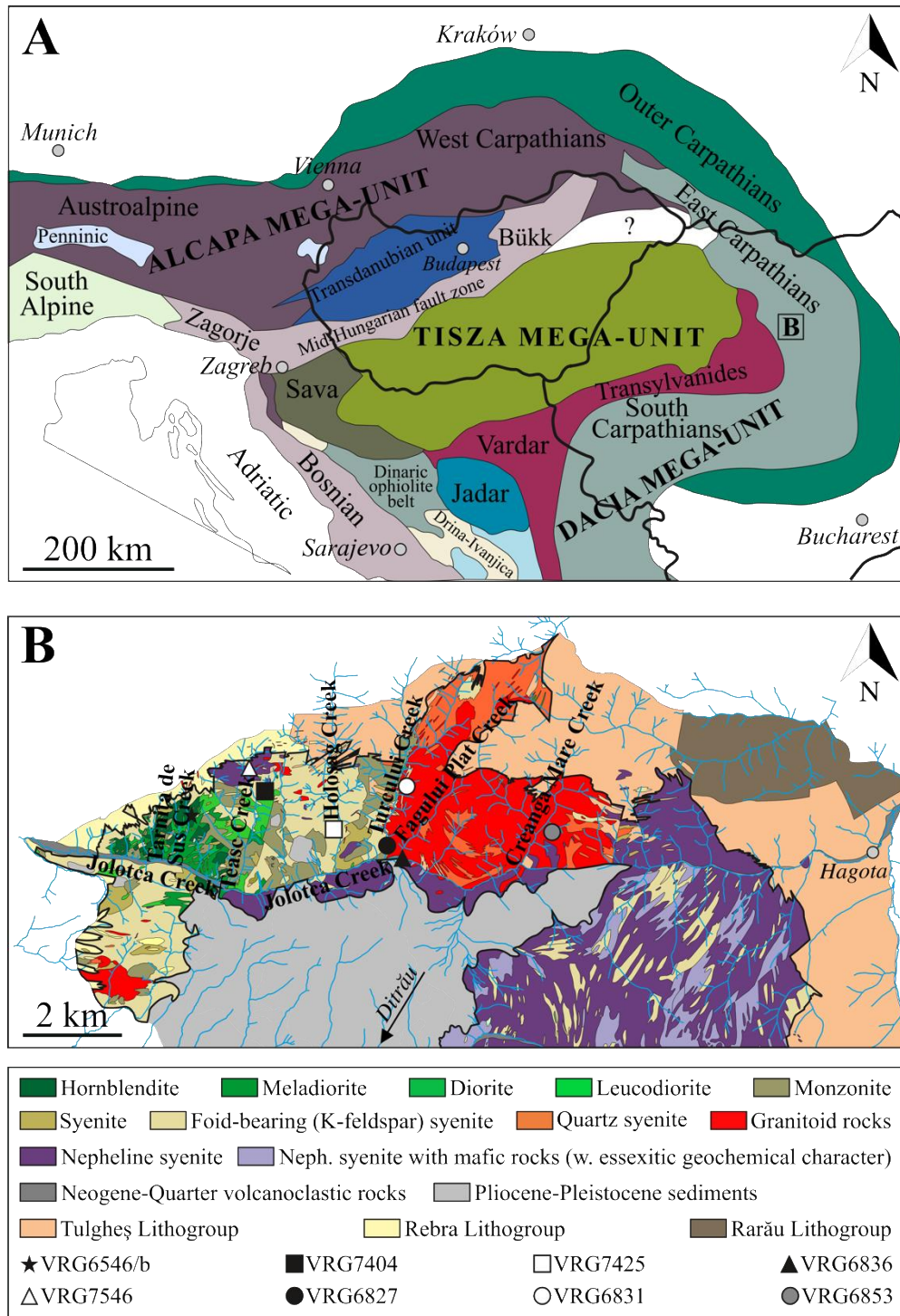
Fig. II.1. (A) Location of the Ditrău Alkaline Massif (marked by the black rectangle) in the structural system of the Alpine–Carpathian–Dinaric region (after Haas et al., 2010). (B) Geologic map of the northern part of the Ditrău Alkaline Massif, displaying sample locations (Pál-Molnár et al., 2015a)

The Ditrău Alkaline Massif structurally belongs to the Bucovinian Nappe and is in direct contact with four of its pre-Alpine metamorphic units (Bretila, Tulgheş, Negrişoara, and Rebra Terrane; Pál-Molnár, 2000; Pál-Molnár, 2010b; Fig. II.2). The massif was uprooted during the Alpine tectonic events and cut by the Bucovinian shear zone at a depth of ca. 1800–2000 m. Hence, the Subbucovinian Nappe and the DAM are bounded by a tectonic unconformity (Kräutner and Bindea, 1995).

21
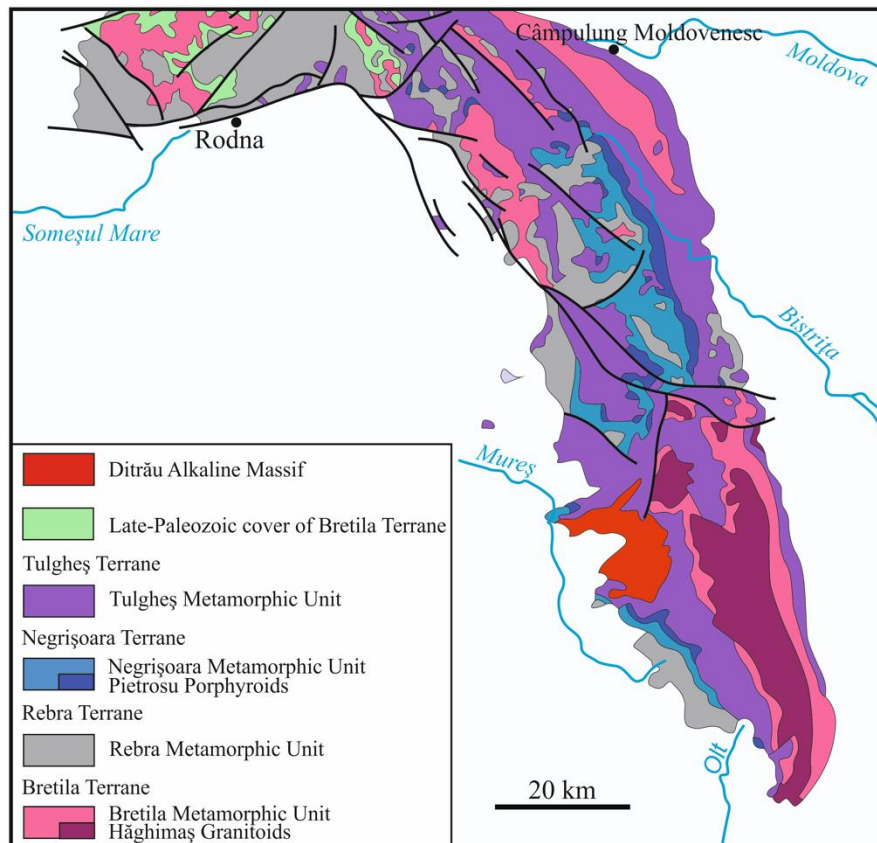
Fig. II.2. Lithologic map of the pre-Alpine tectonic units of the Eastern Carpathians (after Kräutner, 1996–1997; Balintoni, 1997; Balintoni and Balica, 2013; Balintoni et al., 2014)

II.3. Timing of the Ditrău Alkaline Massif – previous work

Early investigations – based on field and structural observations (e.g., Reinhardt, 1911; Streckeisen, 1952, 1954; Codarcea et al., 1957) – were complemented and specified by modern instrumental analytical techniques providing more precise data (Table II.1). The sample locations of former studies are either unknown or the descriptions are constrained to the name of valleys alone. Since the previous sampling points are not accurately retraceable, these data are not marked on the geologic map.

The first K/Ar dating of whole-rock samples (hornblendite, syenite, granite, nepheline syenite) was carried out by Bagdasarian (1972): hornblendite yielded K/Ar mean ages of $196 \pm 6 - 161 \pm 2$ Ma. The age of syenite ranges between 142 ± 7 and 121.5 ± 0.5 Ma. Granite was suggested to be formed 125 ± 10 Ma ago. Nepheline syenite gave a K/Ar age of 152 ± 1 Ma.

According to the results of Streckeisen and Hunziker (1974), the K/Ar ages of biotite crystals from nepheline syenite are 153 ± 3 and 151 ± 9 Ma. An age of 150 ± 6 Ma was determined for biotite of the contact metamorphic rock (hornfels). Whole-rock samples of tinguaite yielded K/Ar ages of 161 ± 7 and 156 ± 6 Ma. In their hypothesis, Streckeisen and Hunziker (1974) assumed the following formation sequence for the different rock types of the

22

massif: (1) intrusion of dioritic and gabbroic magmas into the crystalline country rocks; (2) intrusion of syenitic magma and formation of granitoid rocks by assimilation in the marginal zones of the massif; (3) intrusion of nepheline syenite magma, accompanied by metasomatism and hybridization; (4) formation of lamprophyre, pegmatite and aplite dykes.

Considering the results of formerly conducted K/Ar age determinations, Kräutner et al. (1976) assumed that the emplacement age of the DAM is 135 Ma.

Mînzatu and Ardeleanu (1980) as well as Mînzatu et al. (1981) performed K/Ar analyzes on minerals and whole-rock samples as well. Muscovite separated from syenite yielded a K/Ar age of 161.8 ± 6.1 Ma, whereas the ages of biotite range between 139.3 ± 5.1 and 113.6 ± 4.6 Ma. Whole-rock samples of syenite gave K/Ar ages of 136 – 112 Ma. The ages of biotite of metasomatically altered syenite are 126.0 ± 5 and 120.0 ± 4.5 Ma. An age of 141.9 ± 5.5 Ma was obtained for whole-rock samples of granite aplite. Biotite of hornblendite yielded K/Ar ages of 161.0 ± 6.3 and 134.5 ± 5.2 Ma. Measured ages of nephelines from nepheline syenite are 150.9 ± 5.8 and 116.1 ± 4.4 Ma. Biotite of metasomatically altered nepheline syenite gave a K/Ar age of 136.9 ± 5.1 Ma, while the ages of nephelines are 147.4 ± 6 and 81.3 ± 3.1 Ma. Whole-rock ages of tinguaite range from 172.0 ± 6.6 to 141.9 ± 5.5 Ma. Whole-rock samples of the contact rock (hornfels) yielded a K/Ar age of 138 Ma, whereas the age of biotite is 156.8 ± 5.9 Ma.

Based on Popescu (1985), the Rb–Sr whole-rock age of ultrabasic rocks and syenite is 200 and 160 Ma, respectively.

Zincenco (1991) reinterpreted the available K/Ar and Rb–Sr data. According to his hypothesis, the DAM entered the subsolidus stage 171 ± 3 Ma ago. Pneumatolytic and hydrothermal phases ended 165 ± 5 and 154 Ma ago, respectively. Based on supplementary Rb–Sr whole-rock data, Zincenco et al. (1994) proposed an emplacement age of 201 ± 1 Ma.

Pál-Molnár and Árva-Sós (1995) determined the K/Ar age of minerals of different rock types (cumulate rocks, diorite, granite, nepheline syenite, syenite, and alkaline feldspar syenite). Amphiboles of cumulate rocks gave K/Ar ages of 237.4 ± 9.1 – 216.0 ± 8.8 Ma. Amphiboles of diorite display various ages between 218.7 ± 8.3 and 176.6 ± 6.7 Ma. The obtained K/Ar age of biotite and feldspar of syenite is 107.6 ± 4.1 and 182.7 ± 6.9 Ma, respectively. Biotite and alkaline feldspar of alkaline feldspar syenite yielded a K/Ar age of 102.6 ± 4 and 113.5 ± 4.3 Ma, respectively. Biotite and nepheline + sodalite of sodalite nepheline syenite reached their closure temperatures at 182.4 ± 6.9 and 232.7 ± 8.8 Ma, respectively. K/Ar ages of biotite of granite range from 217.6 ± 8.3 to 206.3 ± 7.8 Ma, whereas the age of alkaline feldspar is 142.7 ± 5.7 – 139.1 ± 5.4 Ma. Based on the above results, Pál-Molnár and Árva-Sós (1995) developed a two-stage evolution history for the massif: (1) Middle Triassic–Lower Jurassic (hornblendite,

nepheline syenite, granite); (2) Middle Jurassic–Lower Cretaceous (syenite, alkaline feldspar syenite, diorite).

Dallmeyer et al. (1997) estimated the age of hornblendes with $^{40}Ar/^{39}Ar$ method. The $^{40}Ar/^{39}Ar$ plateau age of amphibole from hornblendite and gabbro is 231.5 ± 0.1 and 227.1 ± 0.1 Ma, respectively.

Copious age data by Bagdasarian (1972), Streckeisen and Hunziker (1974), Kräutner et al. (1976), Mînzatu and Ardeleanu (1980), Mînzatu et al. (1981), Popescu (1985), Zincenco (1991), Zincenco et al. (1994), Pál-Molnár and Árva-Sós (1995), and Dallmeyer et al. (1997) were summarized and interpreted by Kräutner and Bindea (1998). According to their hypothesis, the DAM was formed by a five-stage magmatic process: (1) generation of a mantle-derived gabbroic-dioritic magma in an extensional tectonic environment (at 230 Ma); (2) 215 Ma ago, the subsolidus gabbroic-dioritic magma intruded into the crust and interacted with the crustal syenitic melt. Hybrid rocks were formed as a consequence of magma mixing and mingling; (3) the parental melt of nepheline syenite was formed by the opening of the Civcin-Severin Rift Zone (160 Ma ago). Mafic, feldspathoid-bearing rocks [ditro-essexite (alkali gabbro or monzodiorite with essexitic-theralitic chemistry)] were generated by hybridization and partial metasomatic substitution; (4) the magmatic system cooled to below 300°C at 135 Ma. Hydrothermal activity ceased 115 Ma ago; (5) closure of the Ar-system (115 Ma) can be attributed to tectonic uplift caused by nappe transport (Kräutner and Bindea, 1998).

Pană et al. (2000) conducted U–Pb analyzes on zircons of syenite; 116 separated grains were examined by Thermal Ionization Mass Spectrometry (TIMS). An age of 229.6 +1.7/–1.2 Ma (Mean Square of Weighted Deviations, MSWD = 1.7) was reported for syenite. They concluded that syenite intruded almost at the same time as gabbro and diorite; hence, the magmatic evolution of the massif was considerably shorter than previously presumed (e.g., by Pál-Molnár and Árva-Sós, 1995; Kräutner and Bindea, 1998).

Table II.1. Results of the previously conducted age determinations on different rock types and mineral phases of the Ditrău Alkaline Massif (Romania)

Source	Rock type	Locality	Method	Studied sample	Age (Ma)
Bagdasarian (1972)	Hornblendite	West of the conjunction of Teasc and Jolotca Creeks	K/Ar	Whole-rock	196 ± 6
	Hornblendite	West of the conjunction of Jolotca and Simo Creeks	K/Ar	Whole-rock	161 ± 2
	Hornblendite	West of the conjunction of Jolotca and Holoşag Creeks	K/Ar	Whole-rock	161 ± 10
	Hornblendite	Ditrău-valley and the spring area of Putna Creek	K/Ar	Whole-rock	177 ± 1
	Syenite	East of the conjunction of Jolotca and Simo Creeks	K/Ar	Whole-rock	128 ± 3
	Syenite	Central part of the Jolotca-valley	K/Ar	Whole-rock	121 ± 2
	Syenite	Road between Ditrău-valley and Putna Creek	K/Ar	Whole-rock	121.5 ± 0.5
	Syenite pegmatite	East of the conjunction of Teasc and Jolotca Creeks	K/Ar	Whole-rock	142 ± 7
	Nepheline syenite	Road between Ditrău-valley and Putna Creek	K/Ar	Whole-rock	152 ± 1
	Leucogranite	Conjuction of Jolotca and Hompot Creeks	K/Ar	Whole-rock	125 ± 10
	Mica schist	Basin of Putna Creek, Ditrău-Tulgheş road, km 20	K/Ar	Whole-rock	284 ± 14
Streckeisen and Hunziker (1974)	Nepheline syenite	Comarnic plateau	K/Ar	Biotite	151 ± 9
	Nepheline syenite	Ditrău Creek, gallery I.	K/Ar	Biotite	153 ± 3
	Tinguaite	Cianodul, 500 m E	K/Ar	Whole-rock	161 ± 7
	Tinguaite	Prişca, 500 m NE	K/Ar	Whole-rock	156 ± 6
	Hornfels	Teasc Creek, 750 m SE	K/Ar	Biotite	150 ± 6
Mînzatu and Ardeleanu (1980); Mînzatu et al. (1981)	Biotitized hornblendite	Jolotca-valley	K/Ar	Biotite	161.0 ± 6.3
	Biotite hornblendite	Jolotca-valley	K/Ar	Biotite	134.5 ± 5.2
	Biotite syenite	Ditrău-valley	K/Ar	Whole-rock	112
				Biotite	117
	Biotite syenite	Ditrău-valley, gallery VII.	K/Ar	Whole-rock	131
				Biotite	134.3 ± 4.8
	Biotite syenite	Ditrău-Tulgheş road, km 11	K/Ar	Whole-rock	136
				Biotite	139.3 ± 5.1
	Biotite syenite	Ditrău-valley, quarry	K/Ar	Biotite	113.6 ± 4.6
	Syenite pegmatite	Hereb-valley, gallery VI.	K/Ar	Muscovite	161.8 ± 6.1
	Biotite syenite with cancrinite	Cianodul-valley	K/Ar	Biotite	126.0 ± 5.0
	Syenite with sodalite (vein)	Ditrău-Tulgheş road, km 7	K/Ar	Biotite	120.0 ± 4.5
	Nepheline syenite	Ditrău-valley	K/Ar	Nepheline	150.9 ± 5.8
	Pegmatoidic nepheline syenite	Ditrău-valley, quarry	K/Ar	Nepheline	116.1 ± 4.4
	Nepheline syenite with cancrinite	Ditrău-valley	K/Ar	Nepheline	147.4 ± 6.0
	Nepheline syenite with cancrinite	Ditrău-valley	K/Ar	Biotite	136.9 ± 5.1
	Liebneritized nepheline syenite	Ditrău-valley	K/Ar	Nepheline	81.3 ± 3.1
	Aplite granite	Borehole 120, m 2	K/Ar	Whole-rock	141.9 ± 5.5
	Tinguaite	Conjunction of Aurora and Belcina Creeks	K/Ar	Whole-rock	172.0 ± 6.6
	Tinguaite	Aurora-valley	K/Ar	Whole-rock	159.3 ± 6.1
	Tinguaite	Cianodul-valley	K/Ar	Whole-rock	141.9 ± 5.5
	Biotite hornfels	Aurora, borehole F 144.	K/Ar	Whole-rock	138
	Biotite hornfels	Aurora-valley, gallery VII.	K/Ar	Whole-rock	172
	Phlogopite marble	Lazarea, borehole, 141, m 137	K/Ar	Biotite	150.0 ± 6.0

Table II.1. Continued

	Hornblendite with textural ordering	Jolotca, Tarnița de Sus Creek	K/Ar	Amphibole	237.4 ± 9.1
	Hornblendite with textural ordering	Jolotca, Pietrarilor Creek	K/Ar	Amphibole	216.0 ± 8.8
	Hornblendite without textural ordering	Jolotca, gallery VI.	K/Ar	Amphibole	226.0 ± 9.6
	Pegmatoidic hornblendite	Jolotca, Tarnița de Sus Creek, gallery XXV.	K/Ar	Amphibole	234.7 ± 10.8
				Plagioclase	161.3 ± 9.8
				Biotite	162.4 ± 6.1
				Biotite	168.3 ± 7.2
	Meladiorite with textural ordering	Jolotca, Teasc Creek	K/Ar	Amphibole	208.3 ± 8.3
				Feldspar	138.2 ± 5.8
	Diorite with textural ordering	Jolotca, Teasc Creek	K/Ar	Amphibole	176.6 ± 6.7
				Feldspar	137.4 ± 5.5
Pál-Molnár and Árva-Sós (1995)	Diorite with feldspar aggregates	Jolotca, Tarnița de Jos Creek	K/Ar	Amphibole	218.7 ± 8.3
				Feldspar	155.4 ± 5.8
	Syenite	Jolotca, Teasc Creek, gallery XIX.	K/Ar	Biotite	107.6 ± 4.1
				K-feldspar	182.7 ± 6.9
	Alkaline feldspar syenite	Jolotca, Simo Creek	K/Ar	Biotite	102.6 ± 4.0
				K-feldspar	113.5 ± 4.3
	Sodalite nepheline syenite	Jolotca, Teasc Creek	K/Ar	Biotite	182.4 ± 6.9
				Nepheline + sodalite	232.7 ± 8.8
	Granite	Jolotca, Turcului Creek	K/Ar	Biotite	217.6 ± 8.3
				Feldspar	146.0 ± 5.6
	Granite	Jolotca, Teasc Creek	K/Ar	Biotite	213.5 ± 8.2
				K-feldspar	139.1 ± 5.4
	Granite	Jolotca, Creanga Mare Creek	K/Ar	Biotite	206.3 ± 7.8
				K-feldspar	142.7 ± 5.7
Dallmeyer et al. (1997)	Gabbro	Jolotca-valley	[40]Ar/[39]Ar	Amphibole	227.1 ± 0.1
	Hornblende diorite	Ditrău-Tulgheș road, km 7	[40]Ar/[39]Ar	Amphibole	231.5 ± 0.1
Panǎ et al. (2000)	Syenite	Jolotca, Jolotca Creek	U-Pb	Zircon	229.6 + 1.7/- 1.2

II.4. Sampling and analytical techniques

II.4.1. Sampling and petrography

Eight rock samples (1 cumulate, 2 syenites, 2 nepheline syenites, and 3 granites) were collected from surface outcrops of the DAM. The cumulate rock (VRG6546/b), syenite (VRG7404, VRG7425), and nepheline syenite (VRG6836, VRG7546) were sampled in the valleys of the Tarniţa, Teasc, Holoşag, and Fagului Plat Creeks. Granite samples (VRG6827, VRG6831, VRG6853) were collected in the valleys of the Turcului and Creanga Mare Creeks (Fig. II.1B). Petrographic observations were carried out at the Department of Mineralogy, Geochemistry and Petrology, University of Szeged, Szeged, Hungary with optical microscopes. Mineral phases were identified with a THERMO Scientific DXR Raman microscope. Modal compositions (vol%) in the petrographic descriptions were estimated from thin sections. Radiometric age data were classified by the Geologic Time Scale of the ICS (2018/08) (Cohen et al., 2013, updated).

II.4.2. K/Ar geochronology

For the purpose of K/Ar age determination, the least-altered rocks were selected from more than 100 samples. The investigations were performed on separated mineral phases (amphibole and biotite) at the Institute for Nuclear Research, Hungarian Academy of Sciences, Debrecen, Hungary, using a digital flame photometer and a magnetic mass spectrometer. The Asia-1/65 Russian, GL-O French, LP-6 American, and HD-B1 German reference materials were used as external standards. The given errors only represent analytical errors (standard deviation); consequently, geologic factors (e.g., Argon-loss, excess Argon) cannot be identified. Description of the equipment, methodology of the analysis, and calibration of the device can be found in studies by Odin et al. (1982) and Balogh (1985).

II.4.3. U–Pb geochronology

Titanite (VRG7404) and zircon (VRG7425) crystals were separated from two syenite samples and from one nepheline syenite sample (VRG7546) from the northern part of the DAM (Fig. II.1B). Sample preparation for U–Pb geochronology included standard gravity and magnetic separation from the 63–500 μm size fractions. Zircon and titanite crystals were mounted in epoxy resin mounts and were polished to a 1 μm finish. All mineral species were investigated and mapped by optical microscopy, cathodoluminescence (CL), and back-scattered (BSE) imaging. CL and BSE images of mineral separates from nepheline syenite were obtained at the Department of Petrology and Geochemistry, Eötvös Loránd University, Budapest, Hungary, using an AMRAY 1830 SEM equipped with a GATAN MiniCL (3 nA, 10 kV setup). Imaging of crystals separated from syenite was carried out at the Department of Geosciences, Johann

Wolfgang Goethe University, Frankfurt, Germany. *In situ* U–Pb geochronology was performed at the GÖochron Laboratories, Georg-August University of Göttingen, Göttingen, Germany, using an excimer laser and a Thermo Finnigan Element2 sector field mass spectrometer.

Spot diameters were 23 and 33 μm with an ablation system of ASI Resolution 155. The method employed for the analysis is described in detail by Frei and Gerdes (2009). GJ-1 reference zircon (Jackson et al., 2004) was used as the "primary standard" and Plešovice zircon (Sláma et al., 2008) and 91500 zircon (Wiedenbeck et al., 1995) were measured as secondary reference materials along with unknown zircon crystals. The MKED1 reference material (Spandler et al., 2016) was used as the primary titanite standard, whereas the OLT1 (Kennedy et al., 2010) and BLS (Aleinikoff et al., 2007) were applied as secondary reference materials.

The concordia plots were constructed by IsoplotR (Vermeesch, 2018).

II.5. Petrography of the dated samples

II.5.1. Amphibole- and pyroxene-rich cumulate

Amphibole- and pyroxene-rich cumulate (VRG6546/b) consists of idiomorphic–hypidiomorphic cumulus amphibole (Fig. II.3A) with variable grain size (macrocrysts ≤11 mm; microcrysts: 100–500 μm). Amphibole oikocrysts (larger than 10 mm) are rich in clinopyroxene, titanite, magnetite, and apatite inclusions. Some of the amphiboles alter to epidote and chlorite. Clinopyroxene (≤16 vol%) occurs as macrocrysts or as inclusions in amphibole oikocrysts and often shows alteration to secondary amphibole, chlorite, or epidote. Hypidiomorphic biotite occurs in small amount (1–20 vol%). Hypidiomorphic–xenomorphic intercumulus plagioclase (≤12 vol%) fills up the residual space between mafic minerals. Magnetite (≤5 vol%), primary titanite (≤3 vol%), and apatite (≤5 vol%) occur as inclusions in cumulus minerals and as intergranular crystals.

II.5.2. Syenite

Syenite (VRG7404, VRG7425) is phaneritic with a medium-to-coarse-grained, inequigranular, serial, and hypidiomorphic texture. It consists of alkaline feldspar (67–81 vol%) and plagioclase (18–26 vol%), accompanied by muscovite (0–1 vol%), cancrinite (0–7 vol%), and primary accessory minerals (apatite, zircon, and titanite; 0–4 vol%) (Fig. II.3B). Mafic minerals of the "groundmass" (the phaneritic, holocrystalline, felsic mineral-rich domain of the rocks) occur in negligible amounts (biotite: 0–1 vol%). Mafic components form aggregates enclosed in syenite, comprising amphibole (4–83 vol%), biotite (3–59 vol%), clinopyroxene (0–7 vol%), minor amounts of alkaline and plagioclase feldspars (1–13 and 1–10 vol%, respectively), accessory (apatite, zircon, and titanite; 0–22 vol%) and opaque minerals (1–14 vol%).

II.5.3. Nepheline syenite

Nepheline syenite (VRG6836, VRG7546) is holocrystalline and displays an equigranular, medium-to-coarse-grained texture. The most common rock-forming minerals are idiomorphic nepheline (7–35 vol%) and hypidiomorphic–xenomorphic alkaline feldspar (59–90 vol%) (Fig. II.3C). Nepheline is 5–15 mm in size, albeit it often occurs as microcrystals (∼0.5 mm). Along cracks and fissures, nepheline is replaced by cancrinite, sodalite, or analcime. The amount of plagioclase is negligible (≤10 vol%). The dominant mafic components are biotite (2–10 vol%), clinopyroxene (2–7 vol%), and amphibole (2–5 vol%). Titanites occur in two generations: 0.1–0.3 and 2.1–2.5 mm in size. Additional magmatic accessory phases are apatite, zircon, magnetite, and ilmenite (3–5 vol%).
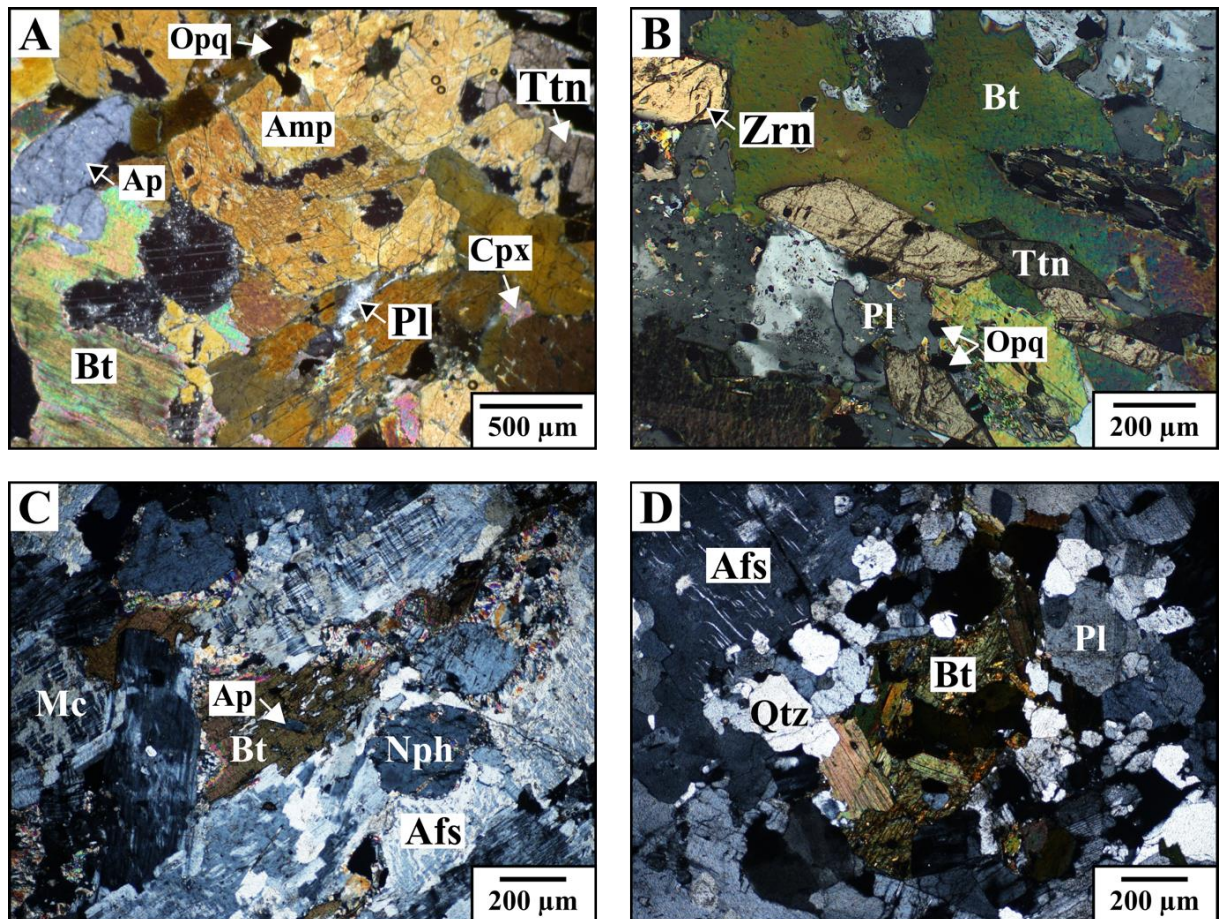
Fig. II.3. Characteristic textural features of the studied rocks. (A) Cumulus amphibole and titanite with intercumulus plagioclase in amphibole- and pyroxene-rich cumulate (VRG6546/b), +N (crossed polarized light). (B) Biotite, zircon, and titanite in syenite (VRG7404), +N. (C) Biotite and nepheline in nepheline syenite (VRG6836), +N. (D) Biotite aggregate in granite (VRG6831), +N. Abbreviations of the rock-forming minerals are after Whitney and Evans (2010)

II.5.4. Granite

Granite (VRG6827, VRG6831, VRG6853) is phaneritic and inequigranular. It is composed of alkaline feldspar (24–45 vol%), plagioclase (21–35 vol%), and quartz (17–31 vol%) (Fig. II.3D). Microcline is often poikilitic and encloses plagioclase, quartz, and biotite. Two generations of plagioclases can be recognized: (a) megacrystalline, zoned, and sericitic; (b) smaller-sized and myrmekitic. Mafic constituents (3–25 vol%) are represented by biotite and amphibole. Altered amphibole is often accompanied by opaque minerals, biotite, and epidote. Secondary rutile and titanite aggregates occur along the cleavage faces of altered biotite. Zircon, titanite, apatite, and magnetite are the most common primary accessory minerals.

II.6. Results

II.6.1. K/Ar geochronology

The results of K/Ar age dating can be found in Fig. II.5 and Table II.2. Amphibole of amphibole- and pyroxene-rich cumulate yielded a K/Ar mean age of 238.6 ± 8.9 Ma. An age of 216.0 ± 8.1 Ma was determined for amphibole of nepheline syenite. K/Ar ages of biotite from granite are 201.4 ± 7.6 and 198.3 ± 7.5 Ma. Amphibole of granite gave K/Ar mean ages of 197.3 ± 7.4 and 196.3 ± 7.4 Ma.

Table II.2. Results of K/Ar dating of amphibole and biotite crystals from the Ditrău Alkaline Massif (Romania)

Sample	Rock type	Locality and GPS coordinates	Studied fraction	K-content (%)	$^{40}Ar_{rad/g}$ (ncm³/g)	$^{40}Ar_{rad}$ (%)	Age (Ma)
VRG6546/b	Amphibole- and pyroxene-rich cumulate	Jolotca, Tarniţa de Sus Creek 46.87454, 25.49871	Amphibole	1.16	$1.15 \cdot 10^{-5}$	78.1	238.6 ± 8.9
VRG6836	Nepheline syenite	Jolotca, Fagului Plat Creek 46.86841, 25.55315	Amphibole	1.62	$1.4450 \cdot 10^{-5}$	94.8	216.0 ± 8.1
VRG6827	Granite	Jolotca, Turcului Creek 46.8706, 25.55029	Amphibole	3.41	$2.7641 \cdot 10^{-5}$	93.6	197.3 ± 7.4
VRG6831	Granite	Jolotca, Turcului Creek 46.88141, 25.55258	Amphibole	1.33	$1.0719 \cdot 10^{-5}$	87.7	196.3 ± 7.4
			Biotite	3.46	$2.8194 \cdot 10^{-5}$	92.4	198.3 ± 7.5
VRG6853	Granite	Jolotca, Creanga Mare Creek 46.8743, 25.59169	Biotite	4.04	$3.3468 \cdot 10^{-5}$	95	201.4 ± 7.6

II.6.2. U–Pb geochronology

The textural homogeneity of the studied titanite and zircon crystals was inspected using CL and BSE images. The ideal spots for analyzes were selected based on these images, in order to avoid crystal parts containing inclusions, different textures, or cracks. CL images usually show normal magmatic zoning of the examined titanite and zircon grains. Older or texturally disparate crystal domains were only observed in the case of zircon samples.

II.6.2.1. Syenite

In situ U–Pb dating was performed on 15 rim and 16 core domains of titanite crystals. The different growth zones did not yield distinguishable ages within uncertainty. The amount of non-radiogenic [206]Pb isotope is high; thus, one can consider the matrix-corrected lower intercept age of 225.3 ± 1.5 Ma, with an MSWD value of 1.1 in the Tera-Wasserburg diagram as a relevant datum (n = 31; Fig. II.4A) and an interpreted main crystallization age of 225.3 ± 2.7 Ma (with 1% external uncertainties; Table II.3).

 In situ U–Pb dates of 32 zircon spots on 12 crystals were measured. The obtained data were filtered according to their discordance (<5%) and resulted in 15 concordant dates, varying between 238.1 and 226.3 Ma. The calculated concordia age is 232.4 ± 2.4 Ma that has a relatively high (14) MSWD value (overdispersion is included in the uncertainty; Vermeesch, 2018; Fig. II.4B). The interpreted main zircon crystallization age is 232.4 Ma, with an uncertainty of ± 3.3 Ma (including 1% external uncertainties; Table II.3).

Table II.3. Summary of the U–Pb titanite and zircon ages of syenite and nepheline syenite from the Ditrău Alkaline Massif (Romania)

Sample	Rock type	Locality and GPS coordinates	Studied fraction	Number of measured data/ concordant data	Lower intercept age (Ma)	MSWD	Concordia age (number of dates included)	MSWD	Interpreted main crystallization age (Ma) with uncertainty (including 1% external uncertainties)
VRG7404	Syenite	Teasc Creek 46.88086, 25.51715	Titanite	30/0	225.3 ± 1.5	1.1	n.d.	n.d.	225.3 ± 2.7
VRG7546	Nepheline syenite	Teasc Creek 46.88461, 25.5132	Titanite	25/0	230.6 ± 2.6	1.5	n.d.	n.d.	230.6 ± 3.5
VRG7425	Syenite	Holoşag Creek 46.87458, 25.53758	Zircon	32/15	n.d.	n.d.	232.4 ± 2.4 (15)	14	232.4 ± 3.3
VRG7546	Nepheline syenite	Teasc Creek 46.88461, 25.5132	Zircon	105/82	n.d.	n.d.	230.6 ± 0.8 (81)	6.9	230.6 ± 2.4

II.6.2.2. Nepheline syenite

The analyzed titanite crystals show around 10% non-radiogenic [206]Pb contents; thus, one can apply the fractionation-corrected lower intercept age of 230.6 ± 2.6 Ma, with an MSWD value of 1.7 in the Tera-Wasserburg diagram as a relevant datum (Fig. II.4C) and an interpreted crystallization age of 230.6 ± 3.5 Ma (n = 25; with external uncertainties; Table II.3).

 In situ U–Pb dating was performed on two grain-size fractions of zircon crystals. The obtained 105 data were filtered according to their discordance (<5%). There was no difference in age between the grain size fractions. The analyzes yielded 82 concordant ages, ranging between 238.7 and 220.1 Ma. One older, xenocrystic date of 757.8 Ma was detected. The concordia age is 230.6 ± 0.8 Ma, with an MSWD of 6.9 (uncertainty includes the overdispersion of MSWD; Vermeesch, 2018; Fig. II.4D). The main zircon crystallization age is 230.6 Ma, with an uncertainty of ± 2.4 Ma (including 1% external uncertainties; Table II.3).
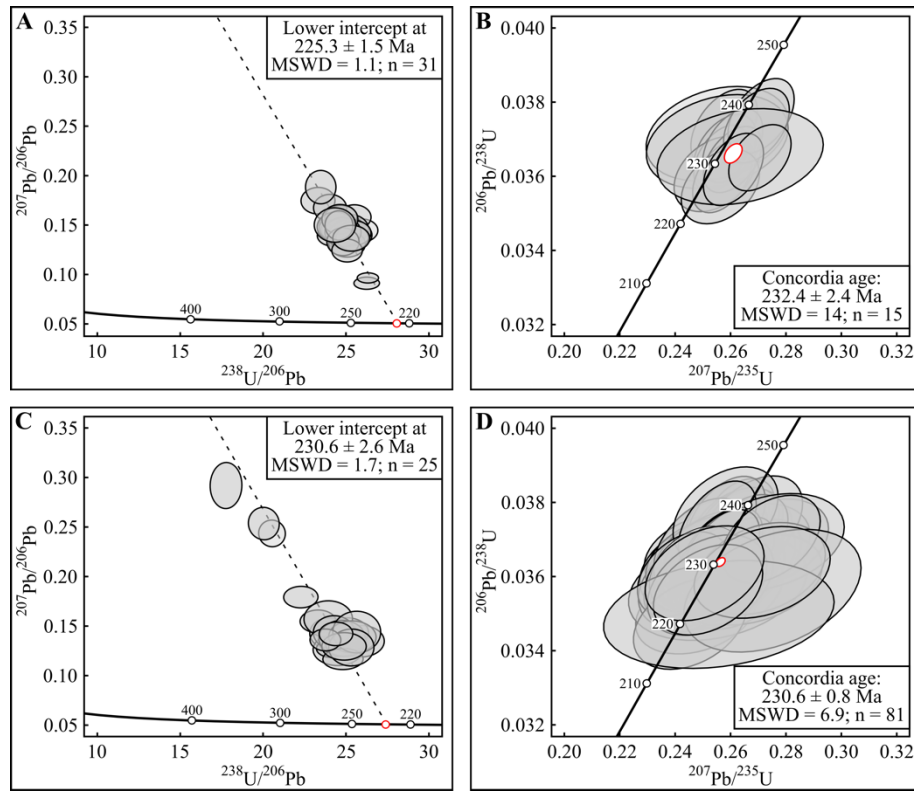
Fig. II.4. Results of U–Pb geochronology. (A) Syenite U–Pb age data of titanite spots in the Tera-Wasserburg concordia plot. (B) Concordant zircon U–Pb isotopic data of syenite in the Wetherill plot with concordia age. (C) Nepheline syenite U–Pb age data of titanite spots in the Tera-Wasserburg concordia plot. (D) Concordant zircon U–Pb isotopic data of nepheline syenite in the Wetherill plot with concordia age

II.7. Discussion

According to our field structural and petrographic observations, the following inferences can be drawn: (a) based on petrographic and genetic aspects, cumulate rocks (e.g., hornblendite, olivine-rich cumulate, amphibole- and pyroxene-rich cumulate, amphibole-rich cumulate), gabbro, and diorite should not be classified into different rock complexes (e.g., Anastasiu and Constantinescu, 1979; Zólya and Zólya, 1985, 1986; Pál-Molnár, 1988). It can be noticed that these rock types occur adjacently (Fig. II.1B) with either abrupt or gradual transition to each other. After Pál-Molnár (2000), the rock association of this structurally and tectonically complex lithostratigraphic unit is referred to as the Tarniţa Complex. Detailed petrogenetic interpretation of this unit can be found in Pál-Molnár et al. (2015a) and Heincz et al. (2018); (b) the gradual transition between diorite, monzodiorite, monzonite, and syenite is difficult to trace in the field; (c) the transition between syenite, quartz syenite, and granite can also be continuous; (d) different-sized metamorphic xenoliths occur in syenite and granite; (e) rocks of the Tarniţa Complex, diorite-syenite and syenite-granite transition zones are crosscut by nepheline syenite; (f) syenite intruded into the Tarniţa Complex; (g) nepheline syenite and rocks of (a)–(f) are crosscut by tinguaite dykes; (h) lamprophyre dykes intersect all other rock types of the massif.

II.7.1. Geochronological data

Comparing the results of previous work with our new K/Ar and U–Pb data (Tables II.1–3), the diversity of the obtained ages, ranging between 238.6 ± 8.9 Ma and 81.3 ± 3.1 (Fig. II.5) can be observed. This phenomenon can be explained by the fact that different authors performed K/Ar analyzes on various minerals with different closure temperatures; however, interpretation of these data should be carried out with caution. Bagdasarian (1972), Streckeisen and Hunziker (1974), Mînzatu and Ardeleanu (1980) as well as Mînzatu et al. (1981) determined whole-rock ages. The results of these analyzes are mostly mixed ages, due to the different closure temperatures and resistance of the minerals. K/Ar data of biotite and feldspars – considering the low closure temperatures of these phases – yield the age of post-magmatic events. This means that the ages obtained from minerals with higher closure temperatures for the K/Ar decay system [i.e., amphibole: 510 ± 25°C (Harrison, 1981); Pál-Molnár and Árva-Sós, 1995; Dallmeyer et al., 1997] and the U–Pb ages of titanite and zircon (Pană et al., 2000; this study) could provide the most relevant information about the timing of the magmatic events. The K/Ar ages of amphiboles yield reliable information solely when the solidus of the crystallizing magma and the closure temperature of amphibole are comparable. It must be noticed that the amphibole of this study, dated by K/Ar method, originates from a cumulate rock that – based on previous thermobarometric calculations of Almási et al. (2015) and Pál-Molnár et al. (2015a) – crystallized at considerably higher temperatures (900–1050°C) than the typical closure temperature of amphibole. Hence, the K/Ar age of the studied amphibole sample displays the minimum crystallization age of the amphibole- and pyroxene-rich cumulate rock. The analyzed titanite and zircon crystallization dates of syenite and nepheline syenite samples are mostly equal within uncertainty and are concordant with the 229.6 +1.7/–1.2 Ma ID-TIMS age of the zircon crystals from a syenite sample published by Pană et al. (2000). This is also in age-agreement with the amphibole data of hornblendite determined by Pál-Molnár and Árva-Sós (1995) and with the amphibole data of gabbro and diorite analyzed by Dallmeyer et al. (1997).

The emplacement sequence of the different rock types of the massif – considering field occurrences and overlapping age data – is as follows: cumulate rocks, diorite, monzodiorite, monzonite, syenite, quartz syenite, granite, nepheline syenite, tinguaite, and lamprophyre.
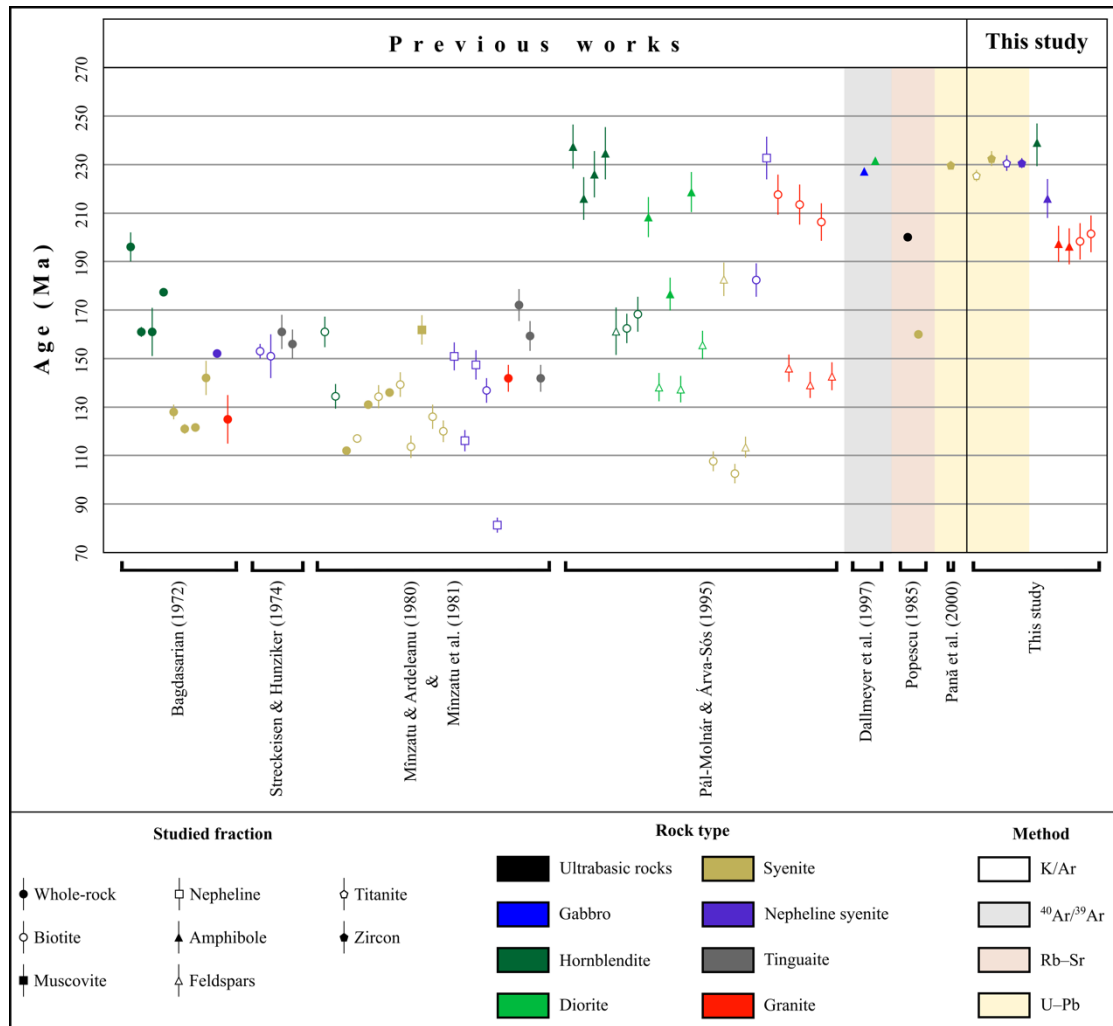
Fig. II.5. Previously published results and our new geochronological data from the Ditrău Alkaline Massif

Taking into account all age data from the examined rock types in this study, they reveal a slightly broad age span, from 238.6 ± 8.9 Ma (amphibole from cumulate rock by K/Ar method) to 196.3 ± 7.4 Ma (amphibole from granite by K/Ar method). Nevertheless, the younger dates are possibly affected by post-magmatic fluids, similarly to those younger ages from previous studies using K/Ar and Rb–Sr methods. Therefore, the lower limit of the magmatic event age is questionable since both the archive data and the new K/Ar ages exhibit wide scattering. The upper limit is also ambiguous, as the highest age value (238.6 ± 8.9 Ma of amphibole from amphibole- and pyroxene-rich cumulate; this study) was determined by K/Ar method and shows a significant error, overlapping the U–Pb ages.

According to these, it can be concluded that the igneous event age could be most plausible between 238.6 ± 8.9 Ma (amphibole from amphibole- and pyroxene-rich cumulate; this study) and 225.3 ± 2.7 Ma (titanite from syenite; this study), keeping in mind that the most significant U–Pb data scatter around ~230 Ma.

Using the methodology we have so far, there is no resolvable age difference between the early emplaced cumulate rocks and the late nepheline syenite. These data contradict the age-

34

range of the multi-stage evolution theory of the DAM proposed by Morogan et al. (2000) and disprove the age-range of the two and multi-stage formation hypothesis of Pál-Molnár and Árva-Sós (1995), Kräutner and Bindea (1998) as well as of Pál-Molnár (2000, 2008).

II.7.2. Palinspastic reconstruction

Based on previous geochemical results (e.g., Morogan et al., 2000; Pál-Molnár, 2000, 2010b; Batki et al., 2014; Pál-Molnár et al., 2015a), the DAM was emplaced in an intra-plate, rift-related tectonic environment. Considering the age and geochemical data, formation of the massif can be attributed to the evolution of Western-Tethys. Several authors (e.g., Kozur, 1991; Stampfli and Borel, 2002, 2004; Hoeck et al., 2009; Pană, 2010) have made attempts to interpret the rifting and subducting events of the separate oceanic basins of Tethys. Contrasting palinspastic reconstructions have been developed due to the complex structure and tectonic evolution of the area. Formation of the Alps and Carpathians is coherent with the evolution of the Meliata-Maliac/Vardar Oceans (Stampfli and Borel, 2002).

According to Stampfli and Borel (2002), the Neotethys started to open in the Late Carboniferous–Early Permian period. This process initiated the drifting of the Cimmerian Block from Pangea and the subduction of Paleotethys in the Middle–Late Triassic period. Slab roll-back of Paleotethys resulted in the formation of back-arc basins along the southern Eurasian margin. Some of these basins evolved into an oceanic basin. Several back-arc basins (e.g., Karakaya, Küre) closed due to the Cimmerian collision in the Jurassic. The Meliata, Maliac, and Pindos oceanic branches remained open until the Late Jurassic. Their subduction initiated the opening of further back-arc basins (e.g., Vardar). Subduction of the Küre Ocean was accompanied by the closure of the Meliata-Maliac Ocean in the Late Triassic–Early Jurassic (Stampfli and Borel, 2002).

Kozur (1991) made two Middle–Late Triassic palinspastic reconstructions for the Eastern Carpathians: (a) the postulated Central Dinaric Ocean was situated between the High Karst Zone and the Lim/Bosnian Zone. The two branches of this ocean were the Hallstatt and Meliata Oceans. The Transylvanian–Pieniny Ocean occupied an adjacent but separate basin; (b) according to the second hypothesis of Kozur (1991), a triple junction was formed in the Eastern Carpathians. One of its branches, the Pieniny Ocean, opened up during the Early Anisian, whereas Meliata evolved in the Middle Anisian. The Transylvanian Ocean extended through the Strandzha Zone to the Pontides. Based on Kozur (1991), the Meliata Ocean closed in the Late Jurassic (Oxfordian); its remnants are represented by obducted nappes enclosing ophiolites.
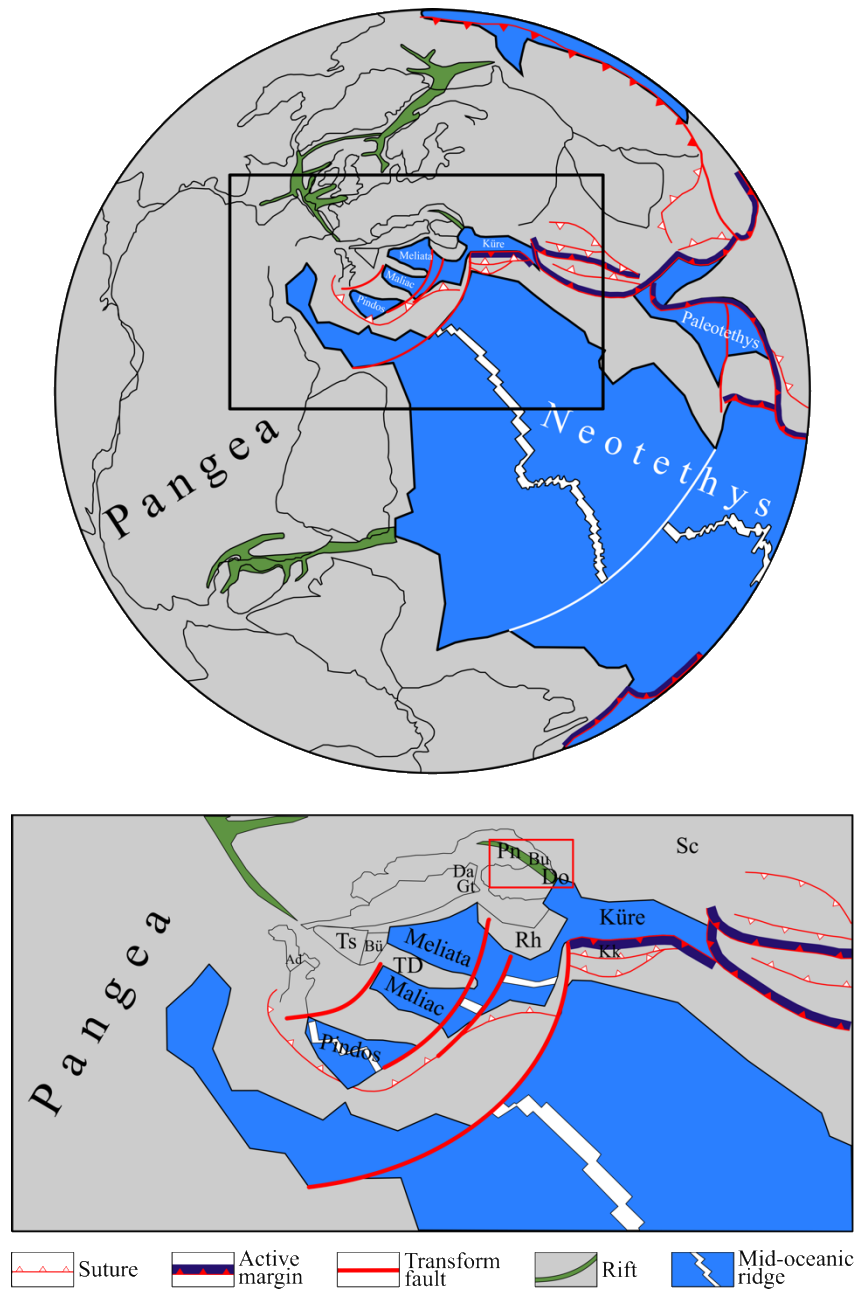
Fig. II.6. Middle–Late Triassic palinspastic reconstruction (modified after Stampfli and Borel, 2002). Legend: Ad – Adria (*s.s.*); Bu – Bucovinian; Bü – Bükk; Da – Dacides; Do – Dobrogea; Gt – Getic; Kk – Karakaya forearc; Pn – Pienniny rift; Rh – Rhodope; Sc – Scythian platform; TD – Trans-Danubian; Ts – Tisia

Middle–Late Triassic ophiolite breccias and olistholites occur in the Late Barremian–Early Albian Wildflysch of Rarău, Hăghimaş and Perşani Mountains (Eastern Carpathians). Hoeck et al. (2009) proposed that these rocks are the remnants of a subducted oceanic crust, formerly located between the Bucovinian, Infrabucovinian, and Northern Apuseni continental panels. Emplacement of the DAM can be attributed to the opening of the oceanic basin. Analogous Middle Triassic intrusions occur in the Southern Alps (Castellarin et al., 1982) and Dinarides (Pamić, 1984). Opening of the Vardar Ocean induced the subduction of the oceanic branch beneath the Northern Apuseni and Infrabucovinian units. The ocean closed in the Late Triassic–Early Jurassic (Hoeck et al., 2009).

Pană (2010) did not agree with the hypothesis of Hoeck et al. (2009), considering that (a) the entire ophiolite suite is not represented, (b) the studied rocks are located in an intra-continental tectonic setting, and (c) the reported age data are not precise enough. Pană (2010) questioned the credibility of the palinspastic reconstruction of Hoeck et al. (2009). According to Hoeck et al. (2009), the Northern Apuseni block was located north of the Meliata Ocean, albeit Triassic sediments and volcanic rocks of the Northern Apuseni Mountains can be correlated with rocks formed south of the Meliata Ocean (Channell and Kozur, 1997). In the absence of geologic evidence, Pană (2010) argued the hypothesis that the oceanic crust subducted beneath the Northern Apuseni and Infrabucovinian continental domains in the Late Triassic–Early Jurassic.

The geochronological data are in correspondence with the reviewed palinspastic reconstructions and petrogenesis of the DAM. Considering this information, the Ditrău Alkaline Massif was formed in an intra-plate, rift-related extensional tectonic setting at the southwestern margin of the East European Craton (Fig. II.6; the postulated area of emplacement is marked by the red rectangle) during the Middle–Late Triassic.

II.8. Concluding remarks

Previous, mostly K/Ar geochronological data of the Ditrău Alkaline Massif have been supplemented and refined by new, more precise K/Ar and U–Pb age data. U–Pb geochronology of accessory minerals is the most reliable method to determine the age of magmatic processes, while post-magmatic thermal events can be traced by the K/Ar decay system.

A K/Ar age of 238.6 ± 8.9 Ma was obtained for amphibole of amphibole- and pyroxene-rich cumulate. Based on *in situ* U–Pb dating, titanite and zircon from syenite were formed at 225.3 ± 2.7 Ma and 232.4 ± 3.3 Ma, respectively. Nepheline syenite yielded an amphibole K/Ar age of 216.0 ± 8.1 Ma as well as titanite and zircon U–Pb ages of 230.6 ± 3.5 and 230.6 ± 2.4 Ma, respectively. K/Ar ages of amphibole and biotite from granite range from 196.3 ± 7.4 to 197.3 ± 7.4 and 198.3 ± 7.5 to 201.4 ± 7.6 Ma, respectively. Considering the new and previous (post-1990) K/Ar and U–Pb data, crystallization of the massif took place between 238.6 ± 8.9 and 225.3 ± 2.7 Ma (noting that the most relevant U–Pb ages scatter around ~230 Ma).

Age data and tectonic analogies suggest a short magmatic span (Middle–Late Triassic, Ladinian–Norian) of the Ditrău Alkaline Massif. The magmatism could be associated with an intra-plate, rift-related extensional tectonic setting at the southwestern margin of the East European Craton.

CHAPTER III

PETROGRAPHIC EVIDENCES OF OPEN-SYSTEM MAGMATIC PROCESSES IN THE FELSIC ROCKS OF THE NORTHERN PART OF THE DITRĂU ALKALINE MASSIF (EASTERN CARPATHIANS, ROMANIA)

Luca Kiri
'Vulcano' Petrology and Geochemistry Research Group, Department of Mineralogy, Geochemistry and Petrology, University of Szeged, Szeged, Hungary
e-mail: kiri.luca@gmail.com

Máté Szemerédi
'Vulcano' Petrology and Geochemistry Research Group, Department of Mineralogy, Geochemistry and Petrology, University of Szeged, Szeged, Hungary;
MTA-ELTE Volcanology Research Group, Budapest, Hungary
e-mail: szemeredi.mate@gmail.com

Elemér Pál-Molnár
'Vulcano' Petrology and Geochemistry Research Group, Department of Mineralogy, Geochemistry and Petrology, University of Szeged, Szeged, Hungary;
MTA-ELTE Volcanology Research Group, Budapest, Hungary
e-mail: palm@geo.u-szeged.hu

Petrographic evidences of open-system magmatic processes in the felsic rocks of the northern part of the Ditrău Alkaline Massif (Eastern Carpathians, Romania)

by: Luca Kiri, Máté Szemerédi, Elemér Pál-Molnár

Abstract

Over the almost 190-years-long research of the Ditrău Alkaline Massif (Eastern Carpathians, Romania), felsic rocks have been regarded as homogeneous, uniform units of the igneous complex. Nevertheless, our detailed textural study revealed that the felsic suite (diorite–alkaline feldspar syenite and nepheline-bearing syenite–granite series), cropping out north of the Jolotca Creek valley is more heterogenous at the micro-scale than previously thought. This heterogeneity partly derives from abundant mafic mineral-rich clusters; nevertheless, felsic minerals also exhibit various, remarkable textural features. Outcrop-to-micro-scale traits of felsic crystal settling, mafic mineral aggregates, and flow fabrics along with metamorphic country rock xenoliths suggest that the studied rocks crystallized under dynamic magmatic conditions. Cumulate formation, shear flow, convection currents as well as various open-system magmatic processes (e.g., magma recharge, magma mixing and mingling, crystal or mush transfer and recycling, country rock assimilation) played a significant role in the petrogenesis of the examined felsic suite.

Based on field observations as well as on the microtextural relationship of the minerals, two major groups of felsic rocks were distinguished: (1) felsic rocks (lacking or containing sparse mafic minerals) spatially associated with mafic rocks and (2) felsic rocks (with mafic minerals and clots) spatially unassociated with mafic rocks. Rocks of the former group are dominated by plagioclase, accompanied by minor alkaline feldspar, biotite, and accessory titanite. Distinct structural and textural features suggest the physical accumulation of the rock-forming phases. Such textural properties can also be observed in some rocks of the second group. Isolated mafic minerals are rather scarce in the latter; nevertheless, different types of aggregates made up of either identical or various mafic phases are more common. Clustered minerals are either intact or show different stages of alteration.

A detailed petrographic study of the above-mentioned peculiarities has been implemented in order to define their potential origin(s) and petrogenetic significance.

III.1. Introduction

The Ditrău Alkaline Massif (DAM) is a unique locality with a presently tilted vertical cross-section of a preceding alkaline magma storage system (Pál-Molnár et al., 2015a), exposing different rock types on a spectrum from ultramafic cumulates to granitoid rocks. Outcrops provide an excellent *in situ* insight into different stages of the evolution of the alkaline igneous suite.

Felsic rocks have been regarded – at both macro and micro-scales – as homogeneous, uniform units of the DAM throughout almost the entire research history of the massif. Recently, some studies (e.g., Batki et al., 2018; Heincz et al., 2018; Ódri et al., 2020) drew attention to distinct structural, textural, and geochemical features, implying open-system processes that had operated during the formation of the examined felsic rocks. The application of *in situ* geochemical analysis made a significant contribution to the appropriate interpretation of these rocks. However, in spite of the new findings of the above-cited articles, several questions regarding the genesis of the felsic suite (e.g., provenance, composition, and evolution of the parental magma) have still remained unanswered.

Pál-Molnár et al. (2015a) revealed that the accumulation of mafic minerals has played a crucial role in the petrogenesis of some rock types of the DAM (e.g., olivine-rich cumulate, amphibole- and pyroxene-rich cumulate, amphibole-rich cumulate). The existence of a hypothetic felsic cumulate pile in the massif has been proposed by Heincz et al. (2018). Furthermore, Ódri et al. (2020) presumed that some felsic rocks (e.g., syenite and quartz syenite) could have been formed by crystal accumulation as well.

According to Chappell et al. (1987), the viscosity of felsic melts does not favor the segregation of crystals. However, a 1–3% volatile-content may decrease the viscosity of felsic magmas so effectively that it allows crystals to settle and accumulate on the floor of a magma chamber (e.g., Dingwell et al., 1985, 1996; Baker, 1996, 1998). Furthermore, crystals could also separate from high-temperature felsic melts with low volatile-content since melt viscosity decreases with increasing temperature (Dingwell et al., 1996; Clemens et al., 1997). Miller and Miller (2002), Wiebe et al. (2002) as well as Collins et al. (2006) recognized that in the case of felsic systems, settling of multi-crystalline aggregates is more effective than sinking of single crystals. Numerous structural and textural attributes may point to the mechanical accumulation of felsic rock-forming minerals (Vernon and Paterson, 2006; Vernon and Collins, 2011).

Rocks of the diorite–alkaline feldspar syenite and nepheline-bearing syenite–granite series not only comprise isolated ferromagnesian phases but also include mafic clots (also known as: aggregates, blobs, clumps, clusters, lumps, nodules) containing multiple crystals of either identical or various ferromagnesian minerals.

Several theories and interpretations can be found in the literature concerning the origin of mafic aggregates: (1) mineral accumulation, (2) magma mixing and mingling, and (3) the involvement of exotic (e.g., crustal or restitic) materials.

Cumulate or chilled-margin phases originating from the border zones of the pluton, incorporated as solid or partly solid enclaves (Wiebe et al., 1997), are also known as cognate (autolith) inclusions (Kumar and Singh, 2014). Such enclaves are cogenetic with the host rock and consist of early-formed – mostly mafic – mineral phases identical to those of the enclosing rock (Hughes, 1982; Wall et al., 1987). Convection currents are highly capable of dragging and transporting crystal clots and fragments. These aggregates could survive the high temperature in the interior of the chamber without being dissolved; thus, they could be preserved as (recrystallized) autolithic enclaves (Bea, 2010). Klaver et al. (2017) defined the term "microcumulate" as a cluster of 5–50 crystals that are only recognizable in thin section. They often exhibit non-equilibrium textures such as reaction-replacement of ferromagnesian minerals along cleavage planes, rims, and fractures.

Mafic microgranular enclaves (MMEs) can be formed by (1) the replenishment of the magma chamber (Frost and Mahood, 1987; Wiebe and Collins, 1998; Vernon and Paterson, 2006; Vernon and Collins, 2011); (2) break-up of a basal sheet in a compositionally layered intrusion (Wiebe et al., 1997); (3) magma mixing and mingling (Kumar and Singh, 2014). Disruption of the enclaves may lead to the formation of mafic clots (Wiebe, 1973). Nevertheless, single crystals or mineral aggregates of more basic composition can also be incorporated into the enclave-bearing felsic magma (Didier, 1987). Micro-enclaves (up to 1 cm) are sub-spherical clusters of ferromagnesian minerals along with titanite and Ca-plagioclase. Convection currents may drag and carry these phases and distribute them throughout the magma storage system. The presence of micro-enclaves and contrasting zoning of neighboring feldspars implies the initial, practically thorough mixing phase (Fernandez and Barbarin, 1991). Interaction between mafic magma-derived crystals (e.g., pyroxene) and a volatile-rich, felsic magma leads to the formation of polycrystalline, amphibole-rich clusters (Vernon, 1984, 1990; Zorpi et al., 1991; Castro and Stephens, 1992). Further hybridization (hydration and mass-transfer of the chemical components) may result in the replacement of amphibole by biotite (Tate et al., 1997; Ubide et al., 2014b).

The residual source material (restite) is a patch of unmelted mafic substance (single crystals or small mineral aggregates) from the source region that got carried by the ascending magma (White and Chappell, 1977). During this process, crystals either remain intact (primary restite; Chappell et al., 1987) or recrystallize due to lower P-T and more hydrous conditions (Wall et al., 1987) in order to reach equilibrium with the host magma (secondary restite).

Restitic minerals can be derived either straight from the source region, following partial melting or from the host magma-induced dismemberment of restite enclaves (Huang et al., 2018). According to Presnall and Bateman (1973), White and Chappell (1977), Chappell (1978) as well as Chappell et al. (1987), many of the amphibole and biotite crystals occurring as clots in granites are products of the reaction between restitic pyroxenes and the host granitic melt.

The detailed petrographic study presented herein is the first step in the revision and reinterpretation of the felsic rocks (diorite–alkaline feldspar syenite and nepheline-bearing syenite–granite suite) occurring in the northern part of the DAM (the region north of the Jolotca Creek, bordered by the Teasc and Rezu Mare Creeks), based on a systematically collected and documented new set of samples. The aim of this paper is to shed light on and emphasize the importance of micro-scale textural features that bear important information on the genesis of the studied rocks. The examined felsic rocks seem to be of more considerable petrographic complexity than presented in previous interpretations. The objective here is to illustrate and describe the diverse petrographic characteristics of the studied felsic rocks and to introduce a preliminary discussion concerning their genetic peculiarities.

III.2. Geologic setting

The Ditrău Alkaline Massif covers an area of approximately 225 km^2 in the Eastern Carpathians, Dacia Mega-Unit (Romania; Fig. III.1A) and makes up the southern and southwestern parts of the Giurgeu Mountains. The DAM comprises various rock types occurring in an intricate structural framework: ultramafic cumulates (olivine-rich cumulate, amphibole- and pyroxene-rich cumulate, amphibole-rich cumulate), alkali gabbro, alkali diorite, monzodiorite, monzonite, monzosyenite, syenite, nepheline syenite, quartz syenite, and alkali granite (Fig. III.1C). The above-mentioned rock bodies are intersected by lamprophyre, syenite, and tinguaite dykes (Pál-Molnár, 2000; Batki et al., 2014; Pál-Molnár et al., 2015a, b).

The igneous event took place during the Middle–Late Triassic (Pál-Molnár et al., 2021) at the southwestern margin of the East European Craton and can be attributed to an extensional, rift-related, intra-plate tectonic environment. The DAM had intruded into the Variscan metamorphic rocks of the Eastern Carpathians, that were exposed to subsequent nappe-forming Alpine tectonic phases (Fig. III.1B). The Cretaceous (Austrian) tectogenesis resulted in an east-verging nappe system. In the literature, it is cited as Median Dacides (Săndulescu, 1984) or Eastern Getides (Balintoni, 1997). The Median Dacides are composed of three Alpine nappes (Infrabucovinian, Subbucovinian, and Bucovinian Nappe) comprising pre-Alpine metamorphic rocks and Permo-Mesozoic cover sequences (Săndulescu, 1984). The Subbucovinian and Bucovinian Nappes are made up of pre-Alpine, petrographically identical tectonic units (Rodna,

Pietrosu Bistriţei, Putna, and Rarău Nappe) of western vergence (Balintoni et al., 1983; Vodă and Balintoni, 1994; Balintoni, 1997).

Within a structural aspect, the DAM forms part of the Bucovinian Nappe (Fig. III.1B) and is directly related to four of its pre-Alpine metamorphic terranes (Bretila, Tulgheş, Negrişoara, and Rebra Lithogroup; Balintoni et al., 2014).

The massif and the Subbucovinian Nappe are divided by a tectonic unconformity since the DAM was uprooted amidst the Alpine tectonic processes and was slit by the Bucovinian shear zone at a depth of approximately 1800–2000 m (Kräutner and Bindea, 1995).
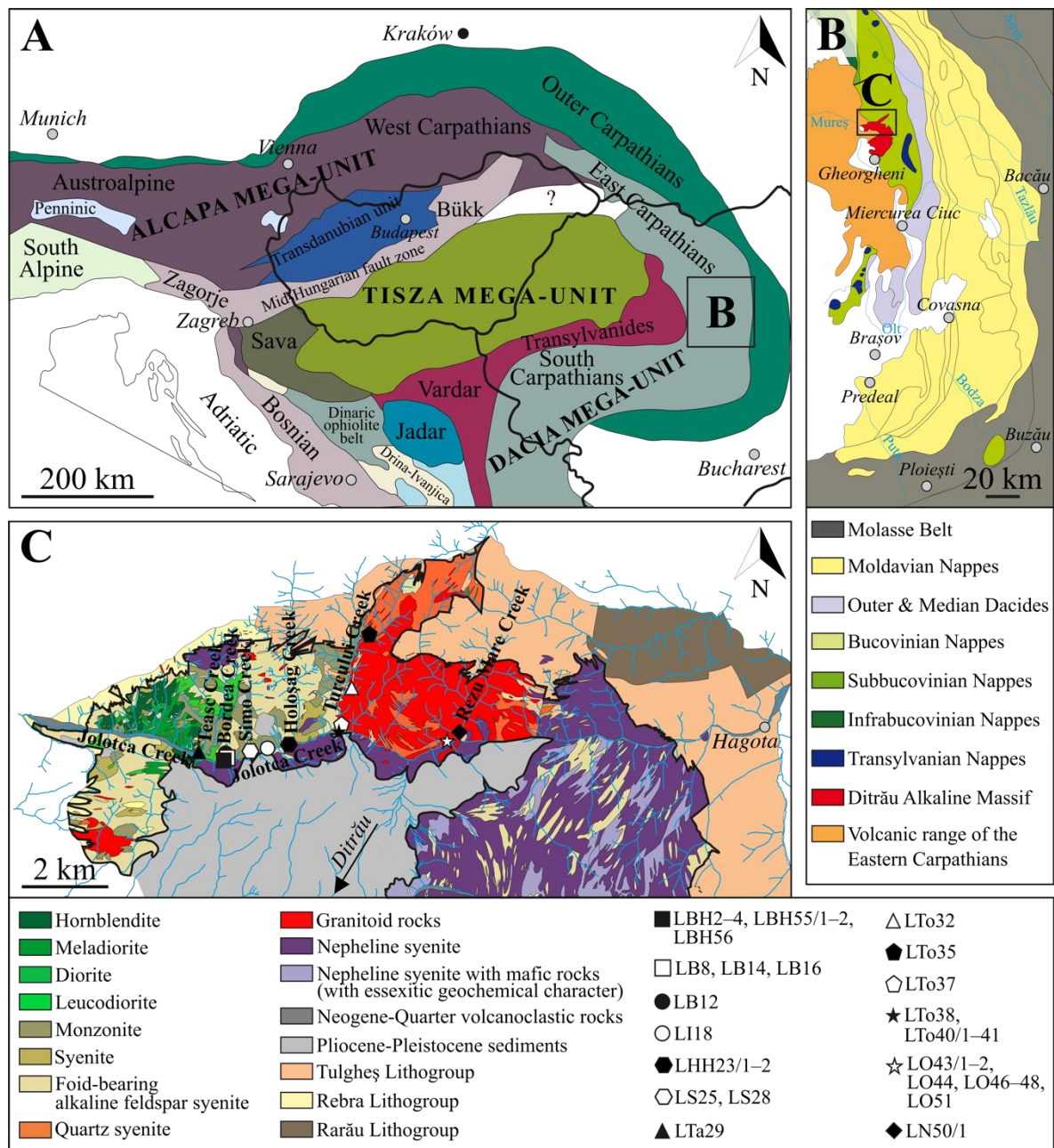
Fig. III.1. (A) Location of the Ditrău Alkaline Massif (DAM) in the structural framework of the Alpine–Carpathian–Dinaric region (after Haas et al., 2010). (B) Position of the DAM in the Alpine structural units of the Eastern Carpathians (Săndulescu et al., 1981, modified). (C) Schematic geologic map of the northern part of the DAM, exhibiting sampling sites (Pál-Molnár et al., 2015a)

III.3. Sampling and analytical techniques

To better understand the felsic rocks and their relationship with other rock types of the Ditrău Alkaline Massif, a set of new, systematically collected and documented samples has been acquired. Fieldwork took place in late 2019 and covered the northern part of the DAM (the area north of Jolotca the Creek, bounded by the Teasc and Rezu Mare Creeks). Exposures are rather poor (Fig. III.2A) due to the dense vegetation and recent recultivation; thus, sampling points were mostly situated in the valleys of creeks and on the hillsides (Figs. III.1C and III.2). Samples were collected from *in situ* outcrops. All characteristic felsic rock types as well as the metamorphic country rocks of the northern area were sampled and the most representative specimens were studied. Samples were named after their sampling locality (i.e., the names of the creeks). Out of the 49 specimens, 46 thin sections were prepared at the Department of Petrology and Geochemistry, Eötvös Loránd University, Budapest, Hungary. Petrographic observations were implemented on both hand specimens and thin sections at the Department of Mineralogy, Geochemistry and Petrology, University of Szeged, Szeged, Hungary. Thin sections were investigated under Olympus BX41 and BrunelSP300P optical microscopes. Mineral phases were determined using a THERMO Scientific DXR Raman microscope. Modal compositions (vol%) in the petrographic descriptions were estimated using the JMicroVision image processing software (Roduit, 2019), by counting 2000 randomly positioned points in each thin section. Backscattered electron (BSE) images were taken with an AMRAY 1830 SEM equipped with an EDAX PV 9800 EDS detector at the Department of Petrology and Geochemistry, Eötvös Loránd University, Budapest, Hungary. BSE imaging was applied to reveal compositional zoning as well as microtextural and reaction relations among the adjacent mineral phases.

III.4. Results

III.4.1. Field observations

The contact between the mafic and felsic rocks cannot be directly traced in the study area due to the adverse exposures and soil formation processes (Fig. III.2A); therefore, their field relationship is not unambiguous.

The macroscopic and microscopic appearances of the studied rocks are remarkably complex. Felsic rocks display various petrographic features (e.g., grain size, type of mafic minerals and/or clots, degree of alteration and/or replacement of the ferromagnesian components, textural orientation) in different parts of the massif. Decimeter–meter-scale mafic microgranular enclaves have not been observed; nevertheless, smaller-sized mafic aggregates (Fig. III.3A–D) and metamorphic country rock xenoliths are common (Figs. III.2D and III.3E,

F). Several late-stage mafic (lamprophyre) and felsic (alkaline feldspar syenite, syenite, monzonite, and quartz syenite) dykes crosscut the felsic igneous bodies (Fig. III.2E).
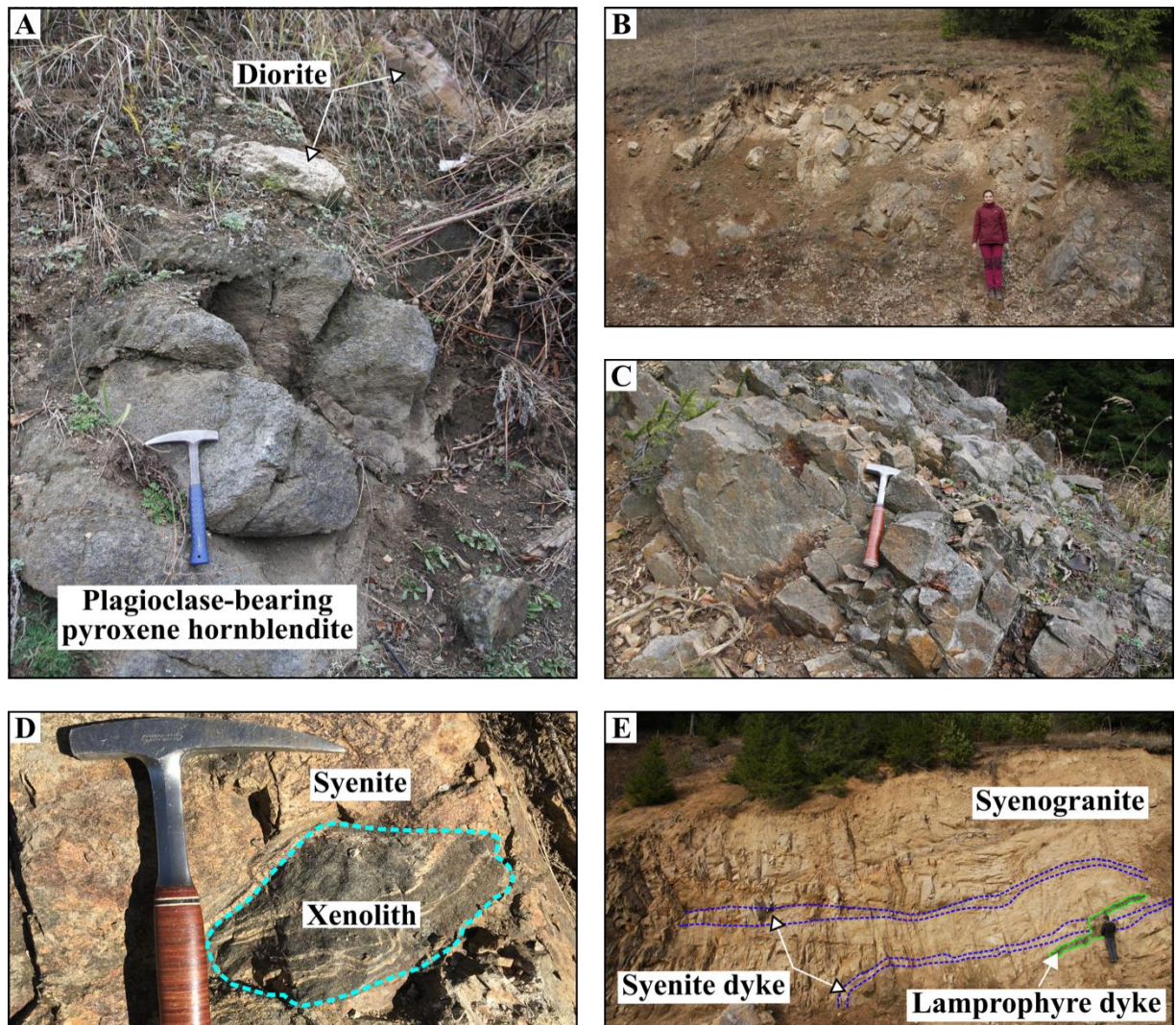
Fig. III.2. Outcrops of the studied felsic rocks. (A) Plagioclase-bearing pyroxene hornblendite overlain by diorite. (B) and (C) Monzonite and monzogranite exposures, respectively. (D) Metamorphic country rock xenolith (marked by the turquoise dashed line), enclosed by syenite. (E) Syenogranite, intruded by syenite and lamprophyre dykes. The former is highlighted by blue, whereas the latter is distinguished by green dashed lines

III.4.2. Petrography

Detailed petrographic description and interpretation of the mafic rocks of the study area are the subject of companion studies (e.g., Pál-Molnár, 2000; Pál-Molnár et al., 2015a). Hence, attributes of the felsic rocks are emphasized and discussed in detail and only the relevant field, mineralogical, and textural observations of the mafic rocks are interpreted in this paper.

Many significant textural characteristics of the studied rocks can only be revealed by classic polarized-light microscopic investigations; thus, the presented descriptions are based on optical microscopic observations. However, features that are controlled by the chemical

composition may only be unraveled by SEM imaging. Hence, the optical microscopic analyzes were complemented by the interpretation of SEM images.

Felsic rocks can be classified into two major groups in line with their spatial occurrence and petrographic features (Fig. III.4).
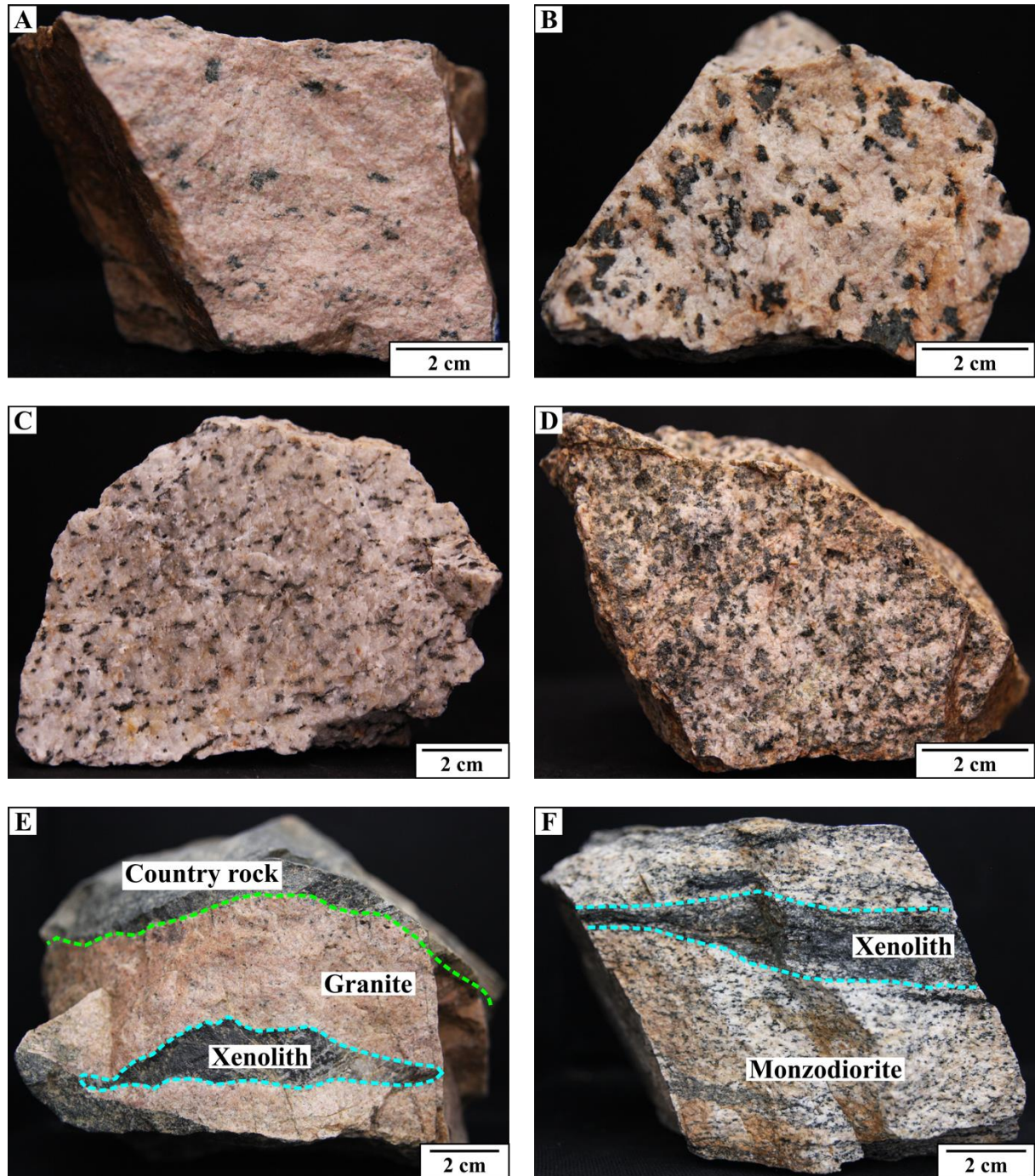
Fig. III.3. Characteristic macroscopic textural features of some of the studied felsic rocks. Mafic clots in (A) monzonite dyke, (B) monzonite, (C) nepheline-bearing syenite, and (D) monzonite. (E) Hornfels xenolith, enclosed by granite along the contact with the metamorphic country rock. (F) Hornfels xenolith in monzodiorite with oriented texture. The margins of the xenoliths are highlighted by turquoise, whereas the contact with the metamorphic wall rock is marked with green dashed lines
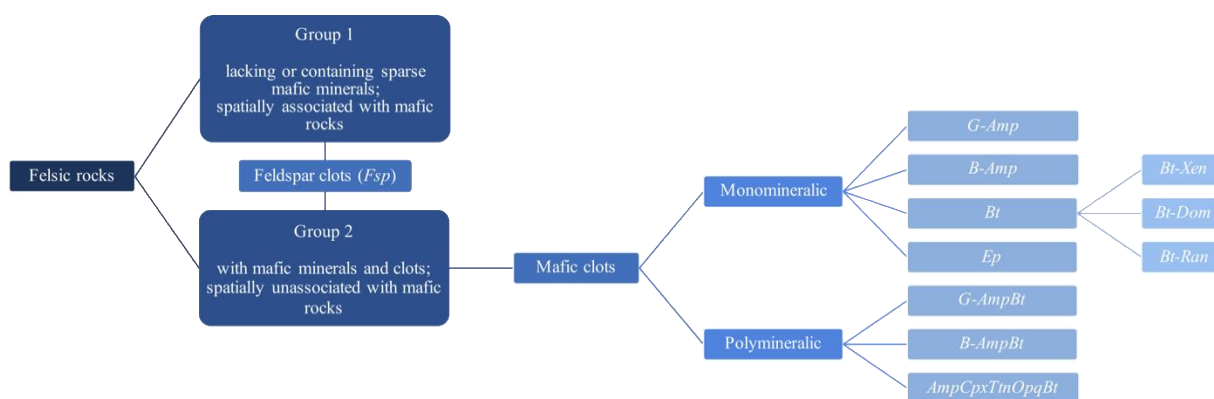
Fig. III.4. Tree diagram illustrating the hierarchy of the studied rocks and the various types of mafic aggregates

III.4.2.1. Group 1 – Felsic rocks (lacking or containing sparse mafic minerals) spatially associated with mafic rocks (hillside west of the Bordea Creek)

The associated mafic rock is composed of plagioclase, green amphibole, biotite, scarce clinopyroxene, and accessory phases (apatite, titanite) and shows evident textural features of mineral accumulation processes (Fig. III.6A). Based on its fabric and paragenesis, the rock can be classified as plagioclase-bearing pyroxene hornblendite.

Felsic rocks of this group (Fig. III.4) are white, medium-to-coarse-grained, phaneritic, inequigranular, and composed mainly of plagioclase, a minor amount of alkaline feldspar, accompanied by biotite flakes in variable amount (up to 9 vol%) (Table III.1). Titanite is the most common accessory mineral. In accordance with their modal composition, the studied felsic rocks can be regarded as diorite (Fig. III.5).
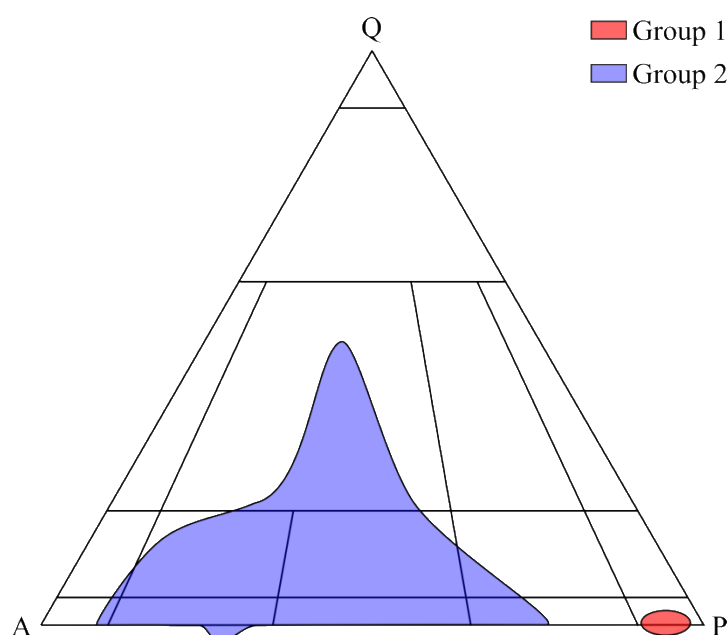
Fig. III.5. QAP diagram illustrating the classification of the studied felsic rocks based on their modal composition (Le Maitre et al., 2002). Abbreviations: Q – quartz, A – alkaline feldspar, P – plagioclase

Table III.1. Sampling locality and modal composition (vol%, without mafic clots) of the investigated felsic rocks of the Ditrău Alkaline Massif (Romania)

Group	Sample	Rock type	Locality and GPS coordinates	Modal composition of the felsic host without mafic clots (vol%)												
				Pl	Afs	Qtz	Neph	Cpx	G-Amp	B-Amp	Act	Bt	Ms	Ttn	Opq	Ep
1	LB8	Diorite	Bordea Creek 46.86246, 25.51698	87	2							9		1		1
	LB16	Diorite with oriented texture	Bordea Creek 46.86235, 25.51704	85	8							4	2			1
2	LBH2	Monzodiorite with oriented texture	Hillside west of the Bordea Creek 46.86200, 25.51558	62	31				3			2		1	<1	
	LBH3	Monzonite	Hillside west of the Bordea Creek 46.86202, 25.51570	51	43							4	<1	<1		1
	LBH4	Monzonite dyke	Hillside west of the Bordea Creek 46.86198, 25.51574	42	56							<1	<1	<1		<1
	LB12	Monzonite	Bordea Creek 46.86376, 25.51694	47	51							2				
	LB14	Monzonite dyke with oriented texture	Bordea Creek 46.86257, 25.51718	46	50							1		1		2
	LI18 fine-grained	Monzonite with oriented texture	Behind the school in Jolotca 46.86448, 25.52762	43	53				1			2		1		
	LI18 coarse-grained	Monzonite	Behind the school in Jolotca 46.86448, 25.52762	50	43				6			<1		<1		
	LHH23/1	Monzonite	Hillside west of the Holoșag Creek 46.86579, 25.53452	56	38							6				
	LHH23/2	Monzonite	Hillside west of the Holoșag Creek 46.86579, 25.53452	42	55							2		<1	<1	
	LS25	Syenite with oriented texture	Simo Creek 46.86425, 25.52344	31	64				<1			4		<1		
	LS28	Nepheline-bearing syenite with oriented texture	Simo Creek 46.86456, 25.52324	25	70		2		1			1		1		
	LTa29	Monzonite	Teasc Creek 46.86344, 25.50844	42	51				2		1	1		2	1	
	LTo32	Monzogranite	Turcului Creek 46.87757, 25.55223	43	31	20			2			4				
	LTo35	Monzogranite	Turcului Creek 46.8887, 25.55766	36	35	24			3			2				
	LTo37	Monzogranite	Turcului Creek 46.86908, 25.54919	32	41	22			<1		4	<1		<1	<1	
	LTo38	Quartz syenite	Turcului Creek 46.86829, 25.54906	11	72	15						2				
	LTo40/1	Monzonite	Turcului Creek 46.86803, 25.54850	34	62	2						<1		<1	1	
	LTo41	Syenite	Turcului Creek 46.86815, 25.54878	24	76											

Table III.1. Continued

Group	Sample	Rock type	Locality and GPS coordinates	Modal composition of the felsic host without mafic clots (vol%)												
				Pl	Afs	Qtz	Neph	Cpx	G-Amp	B-Amp	Act	Bt	Ms	Ttn	Opq	Ep
2	**LO43/1**	Quartz syenite	Jolotca Creek 46.86636, 25.58108	20	72	6				1		<1				
	LO43/2	Quartz monzonite	Jolotca Creek 46.86636, 25.58108	35	45	16			<1	<1		3				
	LO44	Quartz syenite dyke	Jolotca Creek 46.86637, 25.58113	24	56	17		<1		<1		2				
	LO46	Syenite dyke	Jolotca Creek 46.86652, 25.58135	40	50			<1		<1		9	<1			
	LO47	Syenite dyke	Jolotca Creek 46.86653, 25.58107	22	64							6	8			
	LO48	Syenogranite	Jolotca Creek 46.86658, 25.58144	22	56	21				<1		<1			<1	
	LN50/1	Granite + hornfels country rock	Rezu Mare Creek 46.86842, 25.58544	20	28	46						6				
	LO51	Alkaline feldspar syenite dyke with oriented texture	Jolotca Creek 46.86651, 25.58117	8	78							3	11			
	LBH55/1	Monzodiorite with oriented texture + hornfels xenolith	Hillside west of the Bordea Creek 46.86196, 25.51556	71	22							7				
	LBH55/2	Monzodiorite with oriented texture	Hillside west of the Bordea Creek 46.86196, 25.51556	61	30							8	<1			<1
	LBH56	Monzonite	Hillside west of the Bordea Creek 46.86196, 25.51564	35	63							2				

Abbreviations: Act – actinolite (secondary), Afs – alkaline feldspar, B-Amp – blue amphibole, Bt – biotite, Cpx – clinopyroxene, Ep – epidote (secondary), G-Amp – green amphibole, Ms – muscovite (secondary), Neph – nepheline, Opq – opaque minerals, Pl – plagioclase, Qtz – quartz, Ttn – titanite

Idiomorphic–hypidiomorphic plagioclase (400–2.500 μm) is the dominant phase, making up almost 90 vol% of the studied rocks (Fig. III.6A, B). Idiomorphic–hypidiomorphic apatite (90–500 μm) and titanite (80–400 μm) occur as inclusions within. The typical zoning pattern of plagioclase is defined by a variously altered (sericitized), occasionally resorbed, sieve-textured core, mantled by a fresh, inclusion-free, unaltered rim (Fig. III.6C, D). Larger-sized (up to 9 mm), idiomorphic–hypidiomorphic plagioclase megacrysts are also common (Fig. III.6B). Idiomorphic–xenomorphic alkaline feldspar (300–800 μm) often shows a perthitic texture and occurs in a minor amount (2–8 vol%). It fills up the intergranular space between the framework of larger-sized plagioclase crystals; however, it sporadically appears as a rock-forming phase along with plagioclase (Fig. III.6A–C). Feldspars in contact generally have straight crystal faces and are frequently aligned parallel to them; thus, forming aggregates of multiple crystals and defining an oriented texture as well (Fig. III.6A, C). Furthermore, impingement of feldspar grains with separate cores is also prevalent (Fig. III.6D, marked by the red arrow). There are clusters of multiple, molded, sericitized, sieve-textured feldspar crystals that are mantled by a common, inclusion-free overgrowth (Fig. III.6D, marked by the yellow arrow).

Biotite (200–5.000 μm) is hypidiomorphic–xenomorphic (Fig. III.6A, B, D); sagenitic texture as well as idiomorphic–hypidiomorphic apatite (80–300 μm) and titanite inclusions are its common features (Fig. III.6D). Titanite is completely or partially enclosed by biotite and has two generations (90–300 and 600–1.000 μm sized). Biotite occurs sporadically (Fig. III.6B): some domains are completely devoid of it, whereas in other areas it is concentrated into local accumulations of multiple grains (showing no evidence of a touching framework).

Idiomorphic–hypidiomorphic apatite (∼200 μm) and titanite appear along the main rock-forming phases as well (∼1 vol%) (Fig. III.6B). Interstitial titanite has two populations: 200–600 and 900–1.500 μm in size. Secondary minerals are represented by muscovite (0–2 vol%) and epidote (1 vol%). Fine-grained epidote either forms intergrowths with sagenitic biotite or occurs as inclusions. It also fills up the space between feldspars in the form of well-developed crystals or as microcrystalline aggregates (2 vol%) (Fig. III.6A, C). Epidote, along with titanite, is present as vein-filling as well.

The contact between the mafic and felsic rocks in the same outcrop can only be traced in a single hand specimen. Nevertheless, this sample perfectly preserves the continuous transition between the two rock types, forming an interlocking texture. Signs of sharp, abrupt changes or intrusive processes have not been identified (Fig. III.6A).
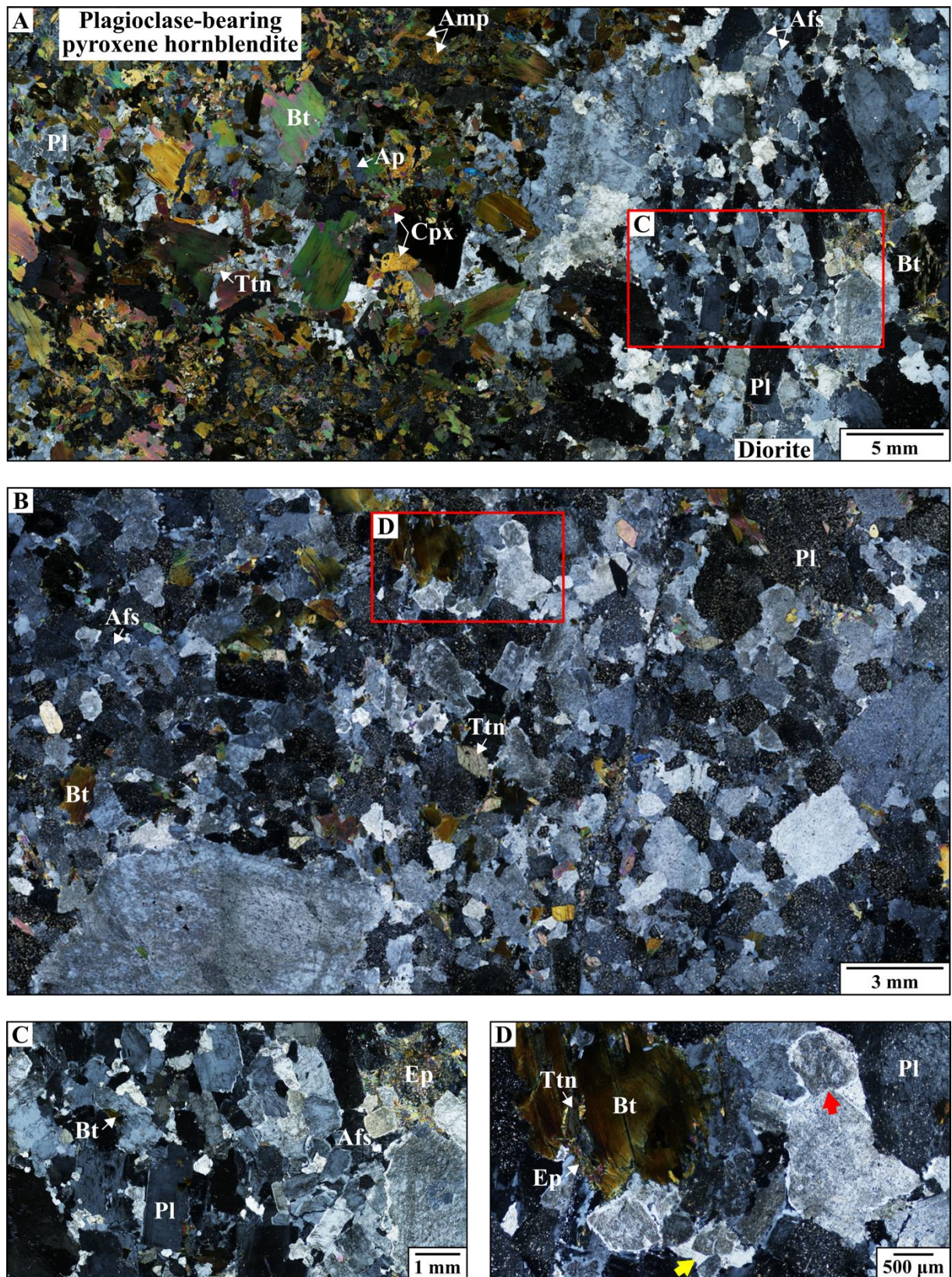
Fig. III.6. Characteristic textural features of the studied felsic rocks belonging to Group 1. (A) Continuous transition between plagioclase-bearing pyroxene hornblendite and the mostly idiomorphic plagioclase-dominated diorite. The latter exhibits an oriented texture, +N (crossed polars). (B) Diorite, containing disseminated biotite and feldspar megacrysts, +N. Note the straight crystal faces of the touching plagioclases. (C) Aggregate of multiple feldspar grains with straight crystal faces in parallel orientation, +N. (D) Two impinged plagioclase crystals (marked by the red arrow) with separate cores. The yellow arrow is pointing at a cluster of multiple, sericitized, and molded cores mantled by a pure rim, +N. Abbreviations of the rock-forming minerals are after Whitney and Evans (2010)

III.4.2.2. Group 2 – Felsic rocks (with mafic minerals and clots) spatially unassociated with mafic rocks (area between the Teasc and Rezu Mare Creeks)

Felsic rocks of this group (Fig. III.4) are white to (pale)pink and have a medium-to-coarse-grained, phaneritic, (in)equigranular texture (some of them contain megacrysts of up to 11 mm) (Fig. III.3A–D). They cover the entire spectrum of felsic rocks from alkaline feldspar syenite to monzodiorite as well as from nepheline-bearing syenite to granite (Fig. III.5). These rocks vary in the modal proportion of felsic minerals and the presence or absence of feldspathoids and quartz (Table III.1). Alkaline feldspar (orthoclase and microcline) commonly exhibits a perthitic microtexture. Most of the plagioclases have a distinct, somewhat resorbed, sericitized, sieve-textured core, rimmed by an inclusion-free mantle. Nevertheless, some rocks contain a minor amount of reverse-zoned feldspar crystals. It is common that smaller plagioclase crystals are enclosed by alkaline feldspar. Plagioclase in contact with alkaline feldspar exhibits irregular grain boundaries. Additional accessory phases (most commonly apatite, titanite, and zircon) are also prevalent.

It is conspicuous that mafic minerals (clinopyroxene, blue and green amphiboles, biotite) tend to occur in different types of clots comprising multiple grains of either identical or disparate ferromagnesian phases, accompanied by minor amounts of feldspars, quartz, accessory and opaque minerals (Figs. III.4 and III.7–9; Table III.2). The aggregated crystals are either completely intact or exhibit different stages of alteration. The number of single mafic minerals occurring in the groundmass varies from sample to sample, however, it is rather limited.

Clots associated with mafic microgranular enclaves have not been identified; however, certain varieties can be unequivocally attributed to metamorphic country rock xenoliths (Fig. III.7E, F)

The type, amount, and form of appearance of the ferromagnesian mineral assemblages could provide important information on the evolution of the encircling felsic rocks and may guide us to better understand their genesis. Thus, rather than describing the mineralogical and textural features of the different host rocks in detail, in the following subsections, we will focus on the petrographic characteristics of the distinct mafic phases. It must be elucidated beforehand that the phrase "groundmass" is applied to the phaneritic, holocrystalline, predominantly felsic mineral-rich domain of the so-called "host rock" enclosing mafic aggregates.

Based on their characteristic petrographic features (e.g., type and texture of the main ferromagnesian components), the clusters can be classified into the following characteristic groups (Fig. III.4; Table III.2).

Table III.2. Type, distinctive features, and mineral assemblages of the mafic aggregates occurring in the felsic rocks of the Ditrău Alkaline Massif (Romania)

Clot type	Sample	Size of the clots (mm)	Shape of the clots	Oriented texture	Modal proportion in the host (vol%)	Grain-size of the host (mm)	Clot-forming minerals (appearance, size [mm] and modal proportion in the aggregates [vol%])								
							Cpx	G-Amp	Act	B-Amp	Bt	Ep	Ttn	Opq	Pl
Monomineralic — *G-Amp*	LBH2 LI18 LTa29 LTo35 LTo37 LO43/2	0.6–6 max. 8		If the host has oriented texture	0.6–13	0.2–4		I–H 0.1–4	± H–X 0.2–1				± IG or RC	± IG or RC	± IG
Monomineralic — *B-Amp*	LO43/1 LO44	1–5			2–3	0.3–3	± H–X (moderately altered) 0.1–0.5 amorphous–prismatic (uralitic pseudomorphs) 0.3–2			I–X 0.1–3					
Monomineralic — *Bt-Xen*	LBH55/1 LBH55/2	2 (width), armoring the xenolith		Parallel to the foliation of the host		max. 0.5 (adjacent to the selvedge); max. 2 (away from the xenolith)					I–H 0.1–2		± IG		
Monomineralic — *Bt-Dom*	LHH23/1	0.6–4 (wispy bands: 0.8–3)	Some are subspherical	In wispy bands	18	0.1–1					I–H 0.1–2 (in clots); 0.08–0.3 (in wispy bands)			± RBt	± IG
Monomineralic — *Bt-Ran*	LHH23/2 LS25 LTo32 LTo35 LTo37 LO46 LO47 LO48 LO51 LBH55/1 LBH55/2 LBH56	0.4–4	Isometric or elongated		0.2–2 max. 5	0.1–3					I–H 0.1–2			± RBt	± IG

53

Table III.2. Continued

| | Clot type | Sample | Size of the clots (mm) | Shape of the clots | Oriented texture | Modal proportion in the host (vol%) | Grain-size of the host (mm) | Clot-forming minerals (appearance, size [mm] and modal proportion in the aggregates [vol%]) | | | | | | | | |
								Cpx	G-Amp	Act	B-Amp	Bt	Ep	Ttn	Opq	Pl
Monomineralic	*Ep*	LBH3 LBH4 LB12 LB14 LTa29 LBH55/1 LBH55/2	0.4–3	Amorphous, isometric or stubby to slightly elongated prismatic	If the host has oriented texture	0.1–6	0.1–2 max. 3						I–X 0.03–1			
Polymineralic	*G-AmpBt*	LBH2 LI18 LS25 LS28 LTa29 LTo32 LTo35 LO43/2	1–3 max. 5	Isometric or stubby to moderately elongated prismatic	If the host has oriented texture	1–6	0.2–3		I–X 0.1–3 39–70	± H–X 0.3–2 max. 17		I–X 0.1–2 30–59		± IG I–X 0.1–0.9 max. 7	± IG	± IG
	B-AmpBt	LO44	2–4	Amorphous or stubby prismatic		0.8	0.3–3				H–X 0.2–2 93	H 0.8–2 7				
	AmpCpxTtnOpqBt	LTa29	5	Stubby to slightly elongated		2	0.2–2 (megacrysts: max. 5)	H–X 0.5–1 11	H 0.05–2 42	H–X 0.07–1 (inclusions in G-Amp); max. 0.6 (patches) 42		± IG	± IG	IG I–H 0.1–1 5	IG	± IG

Abbreviations: Act – actinolite, B-Amp – blue amphibole, Bt – biotite, Cpx – clinopyroxene, Ep – epidote, G-Amp – green amphibole, Opq – opaque minerals, Pl – plagioclase, Ttn – titanite;

I – idiomorphic, H – hypidiomorphic, X – xenomorphic;

IG – intergranular, RBt – along the rims of biotite, RC – along the rims of the clot;

clot name abbreviations can be found in the text

III.4.2.2.1. Monomineralic mafic clots

III.4.2.2.1.1. Green amphibole-rich aggregate (abbreviated as *G-Amp*)

These clusters comprise multiple crystals of intact green amphibole (magnesiohastingsite, determined by Raman spectroscopy; Fig. III.7A, B; Table III.2). If zoned, a brown core is surrounded by a green rim. Amphibole might contain idiomorphic–hypidiomorphic apatite (Fig. III.12A), titanite, and occasionally opaque or zircon inclusions. Titanite and opaque grains are present either in the intergranular space between the amphibole crystals or along the outer rim of the aggregates (Fig. III.7A, B). In certain monzonite and monzogranite samples, the groundmass contains less intact actinolitic amphibole and it also appears in some of the *G-Amp* clots. In case the host rock exhibits an oriented texture, the amphiboles are aligned with their long axes parallel to the foliation. Thus, both the clusters and the minerals in them are oriented (Fig. III.7B). Otherwise, randomly-aligned crystals make up the clumps. Isolated amphibole crystals have a similar color and habit related to their aggregated counterparts (Fig. III.7A, B).

III.4.2.2.1.2. Blue amphibole-rich aggregate (*B-Amp*)

Randomly oriented blue amphibole (riebeckite) crystals make up these clots (Fig. III.7C, D; Table III.2). Most of the grains are entirely intact (Fig. III.7C), whereas others exhibit a spongy texture due to numerous feldspar inclusions (Fig. III.7D). Idiomorphic apatite, idiomorphic–hypidiomorphic opaque minerals, and hypidiomorphic zircon are encircled by blue amphibole.

Although it is not prevalent, a few of the clusters contain moderately decomposed clinopyroxene (aegirine; Fig. III.7D). Amorphous masses as well as prismatic uralitic pseudomorphs after clinopyroxene are present in some of the clumps.

The amount of individually occurring blue amphibole is limited and some of them also show a spongy fabric. Scarce, isolated clinopyroxene may be present in the groundmass.

III.4.2.2.1.3. Biotite-rich aggregate (*Bt*)

Based on their spatial distribution, three subtypes of *Bt* clumps can be distinguished:

(1) metamorphic country rock xenolith-related clots, (2) clusters occurring in distinct domains of the enclosing rock, and (3) randomly dispersed aggregates (Fig. III.4).
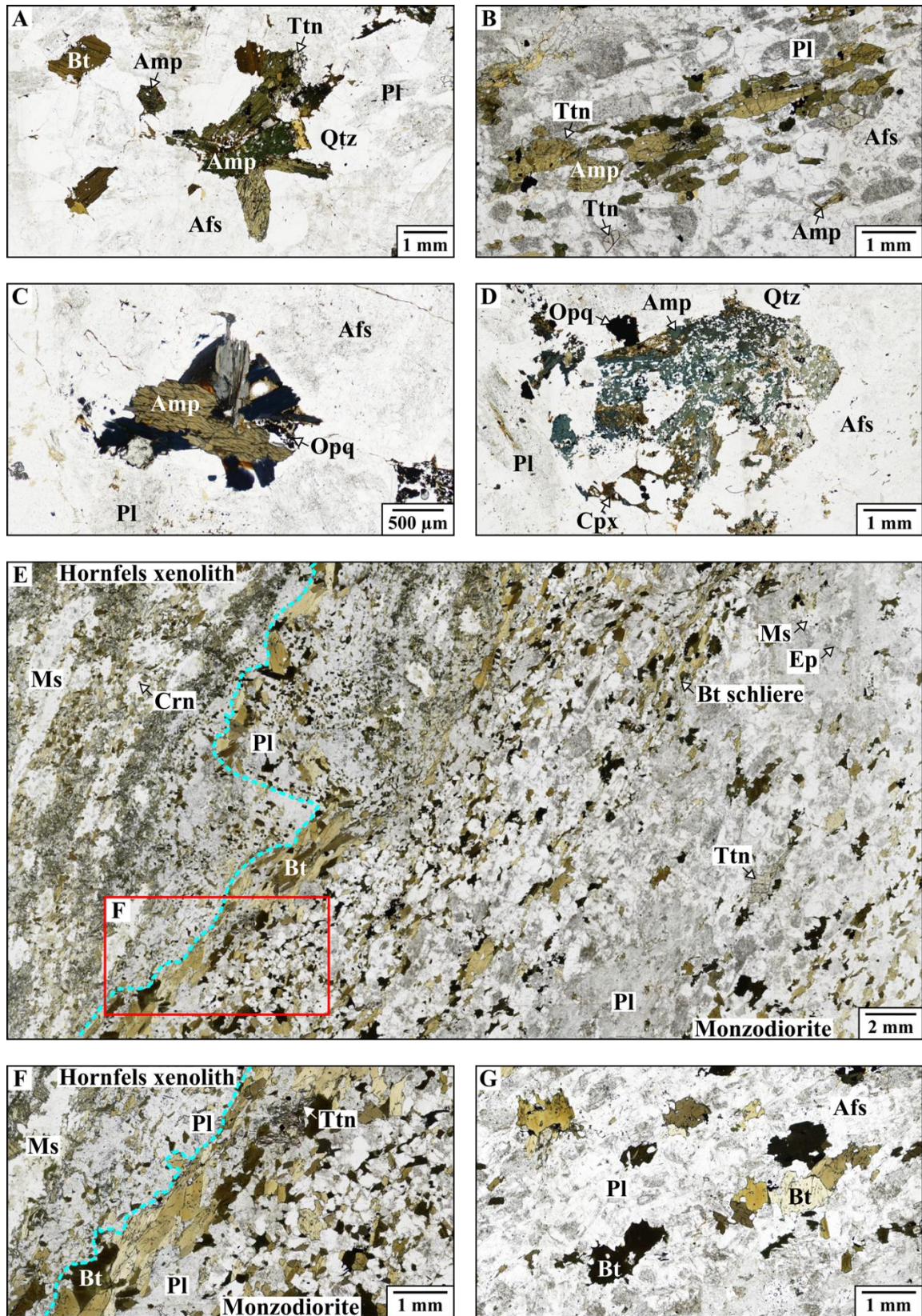
Fig. III.7. Characteristic textural features of the monomineralic mafic clots occurring in the felsic rocks of Group 2. (A) *G-Amp* aggregate, adjoined by isolated amphibole and biotite, 1N (plane-polarized light). (B) Elongated *G-Amp* clump exhibiting oriented texture, 1N. (C) *B-Amp* cluster, 1N. (D) *B-Amp* clot comprising spongy blue amphibole with minor clinopyroxene, 1N. (E) Biotite-rich selvedge (*Bt-Xen*) along the contact of the hornfels xenolith and the monzodiorite host rock, 1N. (F) Texture of the enclosing rock in the proximity of the biotite-dominated fringe (*Bt-Xen*), 1N. (G) Aggregated and isolated groundmass biotite in the monzodiorite host further away from the hornfels xenolith, 1N. Abbreviations of the rock-forming minerals are after Whitney and Evans (2010)

56

III.4.2.2.1.3.1. Metamorphic country rock xenolith-related biotite-rich aggregate (*Bt-Xen*)

This clot type is spatially associated with an approximately 20 cm long, ellipsoidal hornfels xenolith that becomes flattened towards its edges (Figs. III.3F and III.7E, F). It is strongly decomposed and comprises profoundly sericitized plagioclase, – mostly aggregated – intact biotite blades and plates as well as masses of xenomorphic biotite intergrown with epidote. There are bands and almost isometric clumps of randomly-oriented muscovite flakes, some of which enclose xenomorphic remnants of corundum (Fig. III.7E).

The hornfels xenolith is armored by an up to 2 mm wide, discontinuous selvedge (also known as selvage) of moderately to strongly elongated (± minor amount of equant) biotite (Fig. III.7E, F; Table III.2). Sagenitic biotite is also present in a minor amount. Inclusions of biotite are represented by idiomorphic apatite, idiomorphic–hypidiomorphic titanite, and hypidiomorphic zircon. Titanite also occurs in the intergranular space between biotite crystals (Fig. III.7F). In the proximity of the xenolith, biotite of akin properties makes up intermittent mafic bands (schlieren; Fig. III.7E).

The aggregated biotite crystals have straight grain boundaries and either exhibit a shape-preferred orientation (aligned parallel to their long axes and to the orientation of the selvedge and schlieren as well) or lie at high angles to the main foliation (resembling a herringbone pattern) (Fig. III.7E, F). These mafic bands follow the outline of the xenolith and are aligned parallel to the foliation of the enclosing rock.

Adjacent to the selvedge, the plagioclase-dominated monzodiorite host exhibits a honeycomb-like, fine-grained texture with interstitial biotite (Fig. III.7E, F). Further away from the xenolith, the host rock progressively passes into a coarser-grained, oriented texture with more abundant alkaline feldspar. In this domain, clots of equant-to-strongly-elongated, randomly or crystal face-parallel aligned biotite occur (Fig. III.7G); however, mafic schlieren are totally absent. Isolated grains of equidimensional-to-slightly-elongated platy biotite are also common and are aligned parallel to the foliation of the rock (Fig. III.7G). Some of the aggregated and isolated groundmass biotite are embayed by feldspar grains.

III.4.2.2.1.3.2. Biotite-rich aggregate in distinct domains of the host rock (*Bt-Dom*)

Clots of this group are concentrated into certain domains of the monzonite host. There are other areas in the enclosing rock that are entirely devoid of mafic minerals, whereas further zones contain exclusively isolated biotite crystals (Fig. III.8A).

Equant-to-slightly-elongated biotite makes up this clump type (Fig. III.8A–C; Table III.2). Idiomorphic zircon and hypidiomorphic–xenomorphic opaque minerals occur as inclusions. Opaque phases might also be present along the cleavage planes and rims of certain

biotite grains (Figs. III.8B, C and III.12B). Biotite flakes are either randomly oriented or aligned parallel to their crystal faces.

Occasionally, cluster-forming biotite becomes elongated towards the edge of the aggregate. These crystals are accompanied by more prolonged and smaller-sized biotite blades (± mostly equant feldspar and opaque phases); hence, some of the clumps are connected by these sinuous, wispy bands. In some places, these aggregates of elongated biotite grains can be as narrow as a single crystal. The orientation of the prolonged grains (and most of the slightly elongated, clot-forming biotite) coincides with the direction of the mafic bands (Fig. III.8B). A few of the blade-like biotite crystals are rimmed by microcrystalline muscovite. Some of the interconnected clusters resemble a subspherical shape (Fig. III.8C).

Biotite in the host is of similar size and appearance as its aggregated counterparts. Its shape-preferred orientation is not as pronounced; thus, it defines a weak foliation that is parallel to the mafic bands (Fig. III.8A, B). Some biotite crystals (both in the encircling rock and in the clots) are embayed by feldspars.

III.4.2.2.1.3.3. Randomly distributed biotite-rich aggregate (*Bt-Ran*)

Clumps of this group consist of equant to moderately (and minor strongly) elongated biotite crystals (Fig. III.8D; Table III.2). Idiomorphic–hypidiomorphic apatite and zircon along with hypidiomorphic–xenomorphic titanite and opaque minerals are the most common inclusions. In a few instances, opaque phases are dispersed along the cleavage planes and rims of biotite plates. Touching biotite grains have straight crystal faces and are either aligned parallel to them or lie at an angle.

Single biotite of akin characteristics also occurs in the host. Isolated and clot-forming biotite crystals are occasionally embayed by feldspars. Scarce, isolated green or blue amphiboles and clinopyroxene might be present in the groundmass as well.

III.4.2.2.1.4. Epidote-rich aggregate (*Ep*)

The cluster-forming epidote grains are either randomly oriented or aligned parallel to their crystal faces (Fig. III.8E). If the host exhibits an oriented fabric, the long axis of the prolonged aggregates coincides with the direction of the foliation (Table III.2).

Apart from the clumps, epidote might be present as isolated crystals between the main rock-forming minerals or as inclusions within feldspars and biotite. It can also be intergrown with platy groundmass-biotite.

The host is either devoid of or contains a minor amount of single green amphibole.
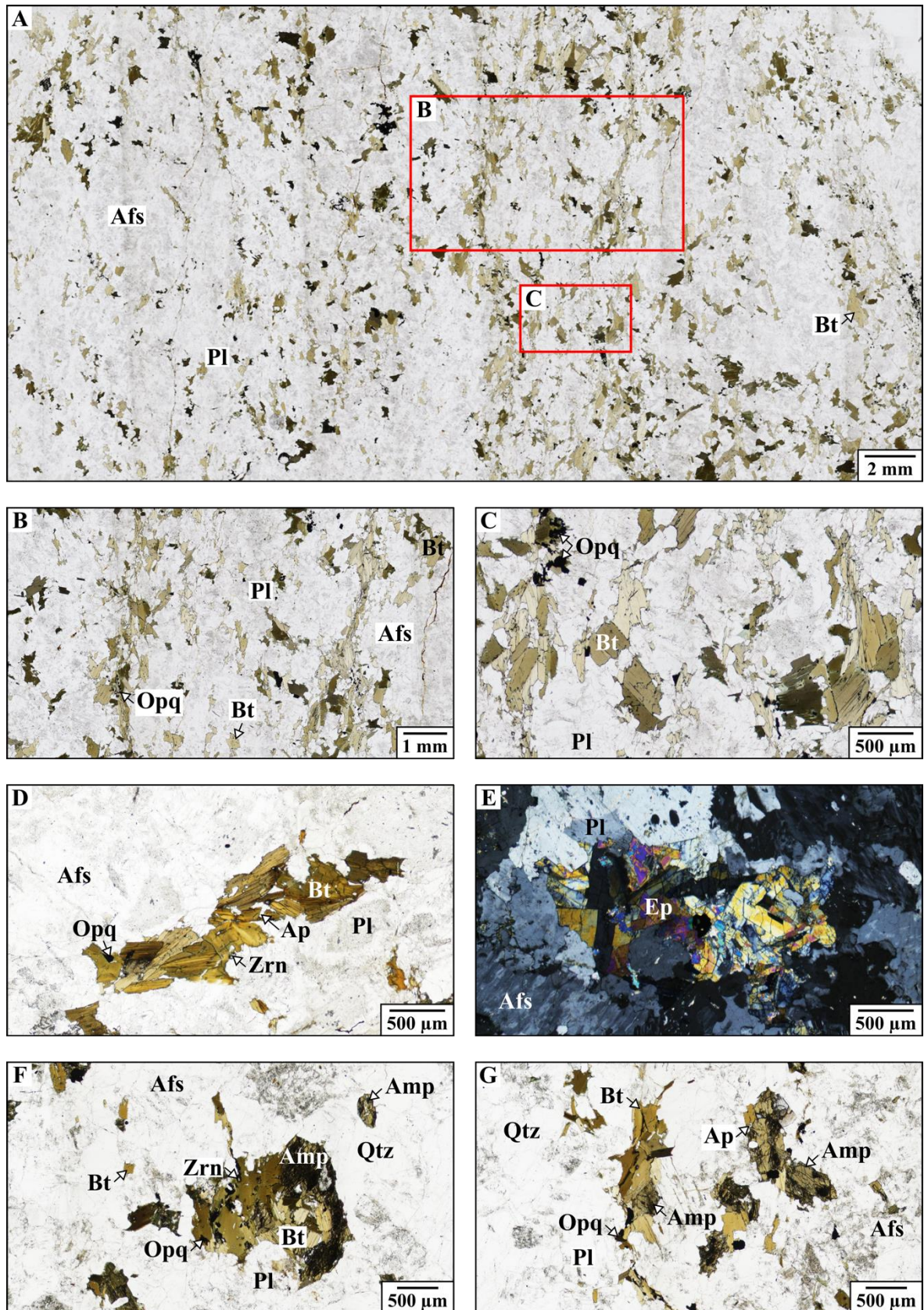
Fig. III.8. Characteristic textural features of the monomineralic and polymineralic mafic clots in the felsic rocks of Group 2. (A) *Bt-Dom* aggregates in distinct domains of the monzonite host, 1N (plane-polarized light). (B) *Bt-Dom* clumps, interconnected by wispy bands made up of elongated, blade-like biotite crystals, 1N. (C) Subspherical *Bt-Dom* cluster on the right side of the photomicrograph, 1N. (D) Slightly elongated, randomly distributed *Bt-Ran* clot, 1N. (E) *Ep* aggregate, +N (crossed polars). (F) Isometric *G-AmpBt* cluster, adjoined by amphibole and biotite of the monzogranite host, 1N. (G) Elongated *G-AmpBt* clump, 1N. Abbreviations of the rock-forming minerals are after Whitney and Evans (2010)

59

III.4.2.2.2. Polymineralic mafic clots

III.4.2.2.2.1. Green amphibole + biotite aggregate (*G-AmpBt*)

Petrographic characteristics of this cluster type can be found in Table III.2. Idiomorphic–hypidiomorphic apatite, titanite, and zircon crystals are enclosed by green amphibole (Fig. III.8F, G). Isolated amphibole crystals might occur in the host rock as well.

Biotite (Fig. III.8F, G) contains idiomorphic–hypidiomorphic apatite, titanite, and zircon along with hypidiomorphic–xenomorphic opaque inclusions (Fig. III.12C). Single biotite plates of akin habit and optical properties may be present in the groundmass as well. Some of them as well as of the clot-forming biotite crystals exhibit a spongy fabric due to abundant feldspar inclusions. A single sample also includes scarce isolated blue amphibole.

Amorphous, isometric, or prismatic aggregates of similar petrographic features, however, with altered versions of the comprising minerals, were also observed (Fig. III.9A, B). There are other decomposed, isometric or prismatic clusters containing remnants of green amphibole (some of them have an actinolitic core), accompanied by chlorite, intact biotite flakes, titanite, and opaque minerals (Fig. III.9C, D). Isometric or prismatic clumps of altered as well as fresh biotite, titanite, and opaque phases associated with minor muscovite and quartz occur in some of the samples (Fig. III.9E). Clots of isometric or prismatic shape comprising decomposed along with intact biotite, epidote, titanite, and opaque minerals were also found (Fig. III.9F).

III.4.2.2.2.2. Blue amphibole + biotite aggregate (*B-AmpBt*)

Petrographic features of this cluster type are summarized in Table III.2. Aggregated blue amphibole (Fig. III.9G) encloses idiomorphic apatite, idiomorphic–hypidiomorphic opaque, and hypidiomorphic zircon crystals. Isolated blue amphibole is rarely present in the groundmass. Blue amphiboles of both the clumps and the host may exhibit a spongy texture, owing to abundant feldspar inclusions (Figs. III.9G and III.12D).

Clot-forming biotite includes idiomorphic apatite, hypidiomorphic zircon, and hypidiomorphic–xenomorphic opaque inclusions. The host rock contains minor single biotite. The amount of isolated clinopyroxene crystals is negligible.

Amorphous or prismatic aggregates of akin petrographic characteristics, albeit comprising altered versions of the cluster-forming phases, were also found (Fig. III.9H). A reaction corona has developed around certain biotite flakes that are in contact with quartz grains of the groundmass. The peripheral area of such textures is composed of fine-grained blue amphibole and/or clinopyroxene, whereas the internal zone is made up of feldspars that are occasionally accompanied by opaque phases (Fig. III.9H). There are other decomposed,

prismatic clusters made up of altered along with intact biotite, titanite, opaque minerals, and clinopyroxene. The latter is present as an inclusion enclosed by biotite, interstitially among the clot-forming biotite crystals as well as along the outline of the aggregates. In the case of the latter, the clinopyroxene rim occurs exclusively in places where the cluster-forming biotite is adjoined by quartz crystals of the syenogranite host rock (Fig. III.9I).

III.4.2.2.2.3. Amphibole + clinopyroxene + titanite + opaque minerals ± biotite aggregate (*AmpCpxTtnOpqBt*)

Amphibole is present in two distinct forms (Table III.2). Magnesiohastingsite with cuspate boundaries (Fig. III.9J) contains idiomorphic– hypidiomorphic apatite and titanite inclusions. The other variety, namely actinolite, is less intact and has a sieved or fibrous texture. It occurs either as numerous tabular or prismatic inclusions within magnesiohastingsite (and thus, producing a poikilitic fabric) or forms adjoining patches (Fig. III.9J). The two amphibole types not only make up the clumps but also occur as single grains in the monzonite host rock.

Pale brown as well as green clinopyroxenes (augite, diopside) are present as crystal fragments (Figs. III.9J and III.12E). In some aggregates, they are encircled by actinolite (Figs. III.9J and III.12F). Isolated clinopyroxene is totally absent from the groundmass. Biotite occurs in a very limited number in the host rock.

III.4.2.2.3. Other peculiar textural features of the felsic rocks belonging to Group 2
III.4.2.2.3.1. Spongy mafic megacrysts

Idiomorphic–hypidiomorphic stubby-to-strongly-elongated prismatic or columnar, occasionally chloritized, randomly distributed biotite megacrysts (up to 14 mm) occur in some of the host rocks. They exhibit a spongy microtexture due to abundant feldspar inclusions (Fig. III.10A).

III.4.2.2.3.2. Feldspar-rich aggregate (*Fsp*)

Not only rocks of Group 1 but also many mafic clot-bearing rocks include clusters of multiple, idiomorphic–hypidiomorphic feldspar crystals that are aligned parallel to their crystal faces and have a separate, sericitized, sieve-textured and/or inclusion-laden core, rimmed by an inclusion-free zone (Fig. III.10B, C, marked by red dashed lines). Some of the feldspar grains in contact exhibit a truncated zoning pattern due to the embayment of one crystal in another. Aggregates of plagioclase crystals also occur as inclusions within groundmass microcline (Fig. III.10C, D, highlighted by red and purple dashed lines, respectively).
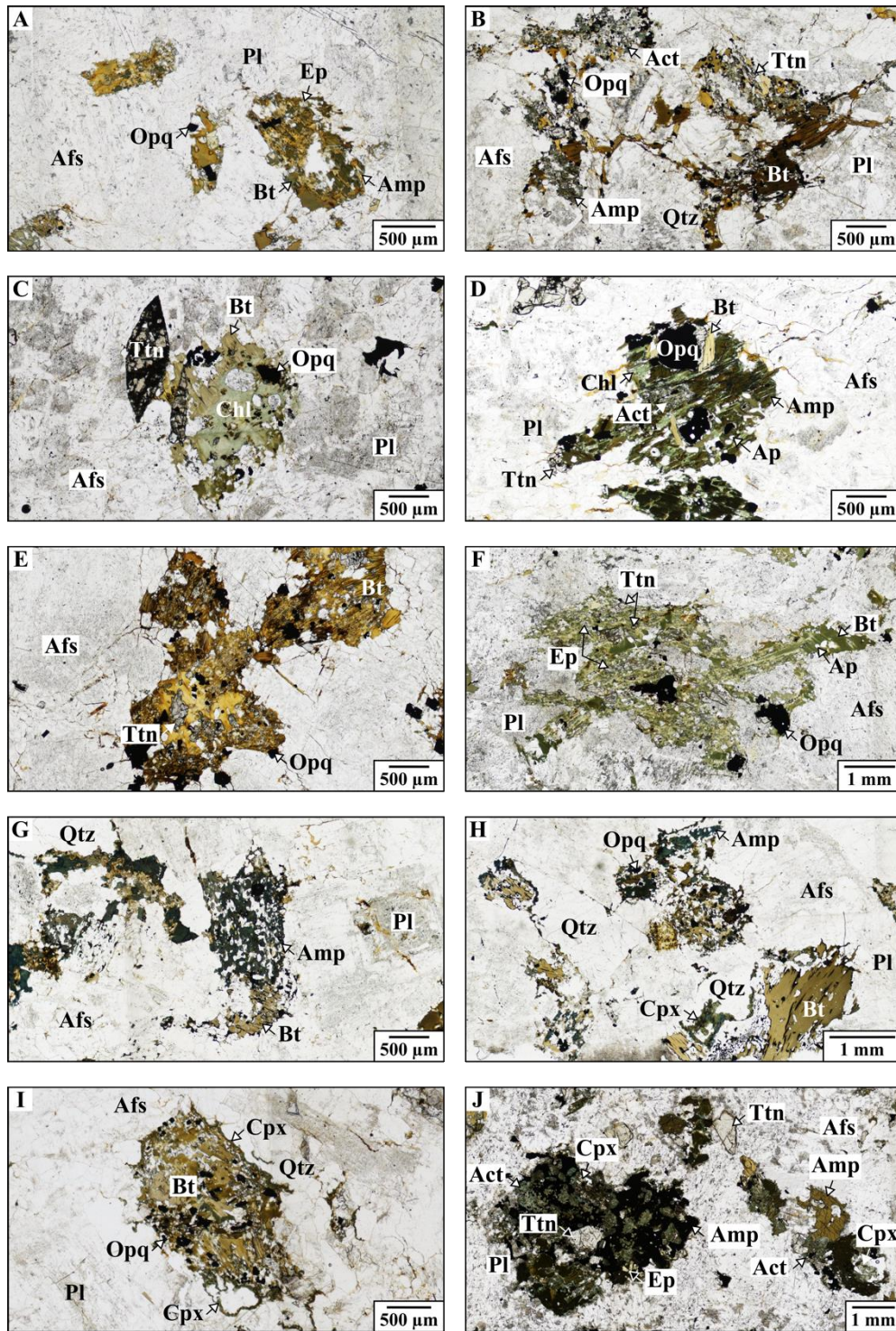
Fig. III.9. Characteristic textural features of the polymineralic as well as of the altered mafic clots in the felsic rocks of Group 2. (A) and (B) Altered clusters composed of green amphibole, biotite, titanite, and opaque minerals, with (B) containing additional actinolite, 1N (plane-polarized light). (C) and (D) Altered clots comprising chlorite, biotite, titanite, and opaque minerals, with (D) including additional green amphibole with an actinolitic core, 1N. (E) Aggregate of decomposed biotite, titanite, and opaque minerals, accompanied by minor muscovite and quartz, 1N. (F) Clump containing decomposed biotite, epidote, titanite, and opaque minerals, 1N. (G) Polymineralic *B-AmpBt* aggregate, 1N. Note the spongy fabric of blue amphibole. (H) Decomposed clusters of blue amphibole, biotite, and clinopyroxene, 1N. Note the presence of a reaction corona in places where biotite is in contact with quartz crystals of the quartz syenite host. (I) Clot composed of altered biotite, clinopyroxene, titanite, and opaque minerals, 1N. Note that clinopyroxene occurs along the periphery of the cluster where biotite is adjoined by quartz crystals of the syenogranite host. (J) Polymineralic *AmpCpxTtnOpqBt* clumps, 1N. Note the two clinopyroxene types (brown and green) occurring in the distinct clots. Abbreviations of the rock-forming minerals are after Whitney and Evans (2010)

III.4.2.2.3.3. Feldspar megacrysts

Idiomorphic–hypidiomorphic alkaline feldspar (orthoclase and microcline) megacrysts (up to 11 mm) appear in the host rocks. Many of them enclose several fine-grained, idiomorphic–hypidiomorphic plagioclase crystals with a separate, sericitized, sieve-textured core, mantled by a fresh rim. The plagioclase inclusions are either randomly oriented or are aligned parallel to the crystal faces of the host mineral. Aggregates of multiple plagioclase grains encircled by alkaline feldspar megacrysts are also common (Fig. III.10E, distinguished by red and purple dashed lines, respectively).

Likewise, (alkaline feldspar)syenite dykes include copious idiomorphic–hypidiomorphic, tabular or columnar, randomly or slightly oriented alkaline feldspar (orthoclase and microcline) megacrysts (Fig. III.10F, highlighted by purple dashed lines). Their size varies between 1 and 4 mm, nevertheless, some of them may reach 8 mm.

III.4.2.2.3.4. Adjacent feldspar crystals with different zoning sequences

The most common zonation pattern of feldspars is represented by a sericitized, sieve-textured, occasionally resorbed core, mantled by an inclusion-free rim (Figs. III.10B–E and III.12G). Rarely, some crystals exhibit complex zoning and the clear rim is succeeded by another sericitized, sieve-textured zone, armored by a pure rim (Figs. III.10G, marked by the red arrow and III.12H).

In a monzonite sample, feldspar grains exhibiting reverse, multiple-zoning (Fig. III.10H, marked by the red arrow) occur along with the more frequent, normal-zoned crystals (Fig. III.10H, marked by the yellow arrow). In this case, an idiomorphic, fresh core is enclosed by a sericitized, sieve-textured sector, followed by a peripheral zone of different width where inclusions are absent (Figs. III.10H, marked by the red arrow and III.12I). Conspicuously, these reverse-zoned crystals are spatially related to mafic clots (i.e., directly attached to the clusters or else, occurring in their proximity), namely to *G-AmpBt* aggregates.
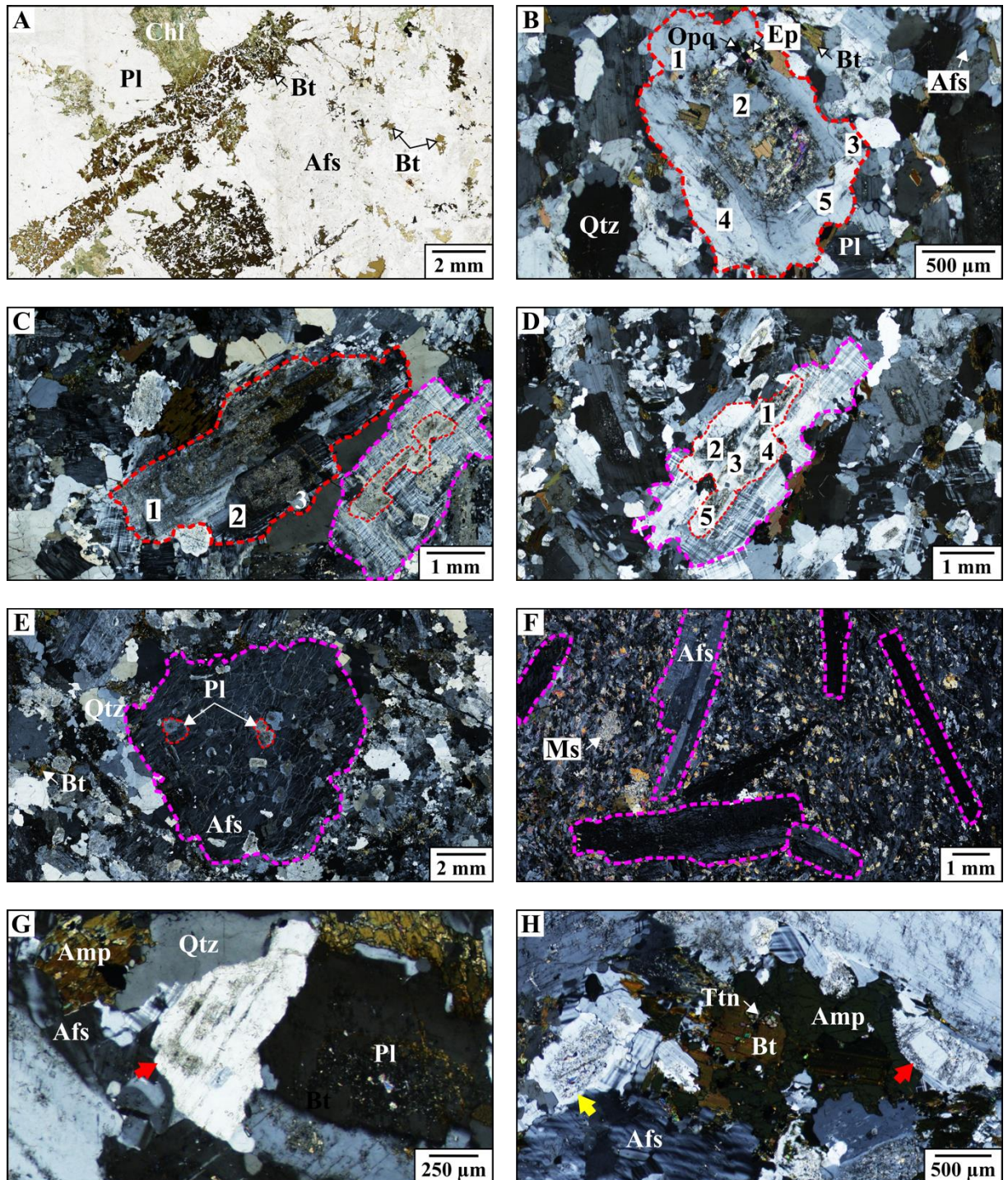
Fig. III.10. Other peculiar features of the felsic rocks of Group 2. (A) Spongy biotite megacrysts, 1N (plane-polarized light). (B) and (C) *Fsp* clusters (highlighted by red dashed lines) consisting of multiple grains (numbered) with separate cores in parallel orientation, with (C) containing additional microcline (marked by the purple dashed line) with plagioclase inclusions in synneusis relation (highlighted by the red dashed line), +N (crossed polars). (D) Microcline (distinguished by the purple dashed line), encircling plagioclase crystals (numbered and highlighted by the red dashed line) in synneusis orientation, +N. (E) Alkaline feldspar megacryst (marked by the purple dashed line), enclosing several separate or aggregated (highlighted by red dashed lines) plagioclase grains with a sericitized, sieve-textured core, +N. (F) Slightly oriented alkaline feldspar megacrysts (distinguished by purple dashed lines) in alkaline feldspar syenite dyke with oriented texture, 1N. (G) Multiple-zoned feldspar crystal (marked by the red arrow), +N. (H) Normal-zoned feldspar (marked by the yellow arrow) adjoined by a reverse-zoned crystal (marked by the red arrow), 1N. Note that the latter is spatially associated with a mafic clot. Abbreviations of the rock-forming minerals are after Whitney and Evans (2010)

III.4.2.2.3.5. Biotite clusters in the metamorphic country rock spatially associated with granite and in the incorporated xenoliths

Approximately 10 cm sized, ellipsoidal, intact country rock xenoliths can be found along the contact of granite and the metamorphic rocks of the Tulgheş Lithogroup (Fig. III.3E). The xenoliths become narrow towards their edges and pass into utmost 800 μm wide, contact zone-parallel bands (Fig. III.11A). Both the hornfels xenoliths and the identical wall rock contain abundant idioblastic–hypidioblastic almandine garnet (up to 600 μm) (Fig. III.11). Approximately 1 cm further away from the contact, max. 1 mm sized garnets occur in the metamorphic country rock (Fig. III.11A). Garnet crystals of the xenoliths are completely intact (Fig. III.11B), whereas in the wall rock, some of them exhibit a reaction texture with biotite.

Another special feature of both the hornfels xenoliths and the country rock is the presence of 0.5–4 mm-sized, isometric or elongated aggregates of randomly oriented, idiomorphic–hypidiomorphic biotite laths and plates (up to 800 μm) along with minor anatase and relict garnet (the latter two occur exclusively in biotite clumps of the wall rock) (Figs. III.11 and III.12J). Some of the biotite crystals are chloritized. Not as abundant as the biotite-rich clusters, however, subspherical, microcrystalline muscovite-rich clots (up to 800 μm) also appear in the metamorphic country rock (Fig. III.11C).
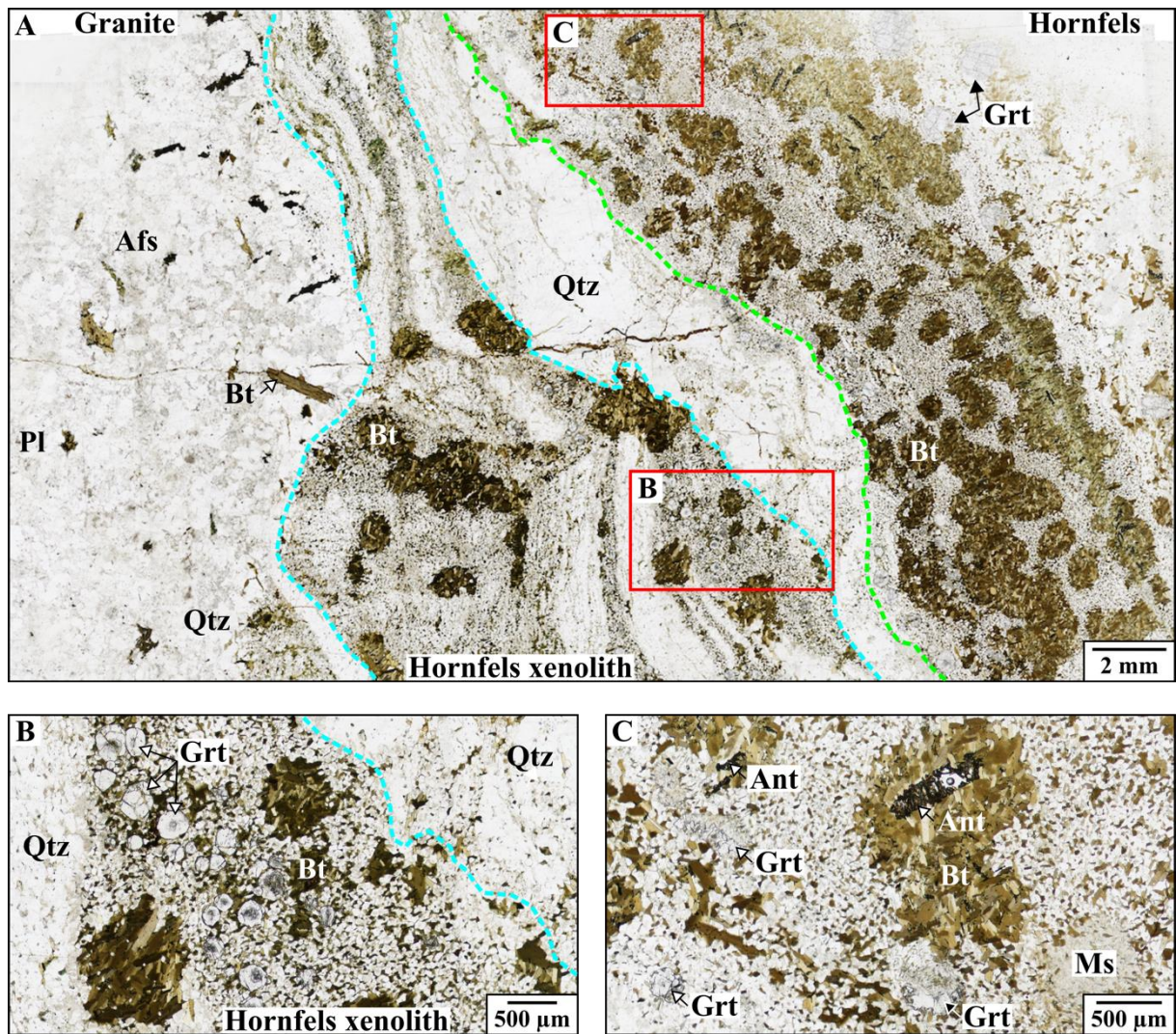
Fig. III.11. Characteristic textural features of the hornfels wall rock and xenolith. (A) The contact of granite and the hornfels country rock, 1N (plane-polarized light). Note that the xenolith passes into a contact-zone parallel band. The margins of the xenolith are highlighted by turquoise, whereas the contact with the country rock is marked by green dashed lines. (B) Biotite-rich aggregates and garnet crystals of the metamorphic xenolith, 1N. The rim of the xenolith is distinguished by the turquoise dashed line. (C) Anatase-bearing biotite-clots and a muscovite-dominated cluster of the metamorphic wall rock, 1N. Abbreviations of the rock-forming minerals are after Whitney and Evans (2010)
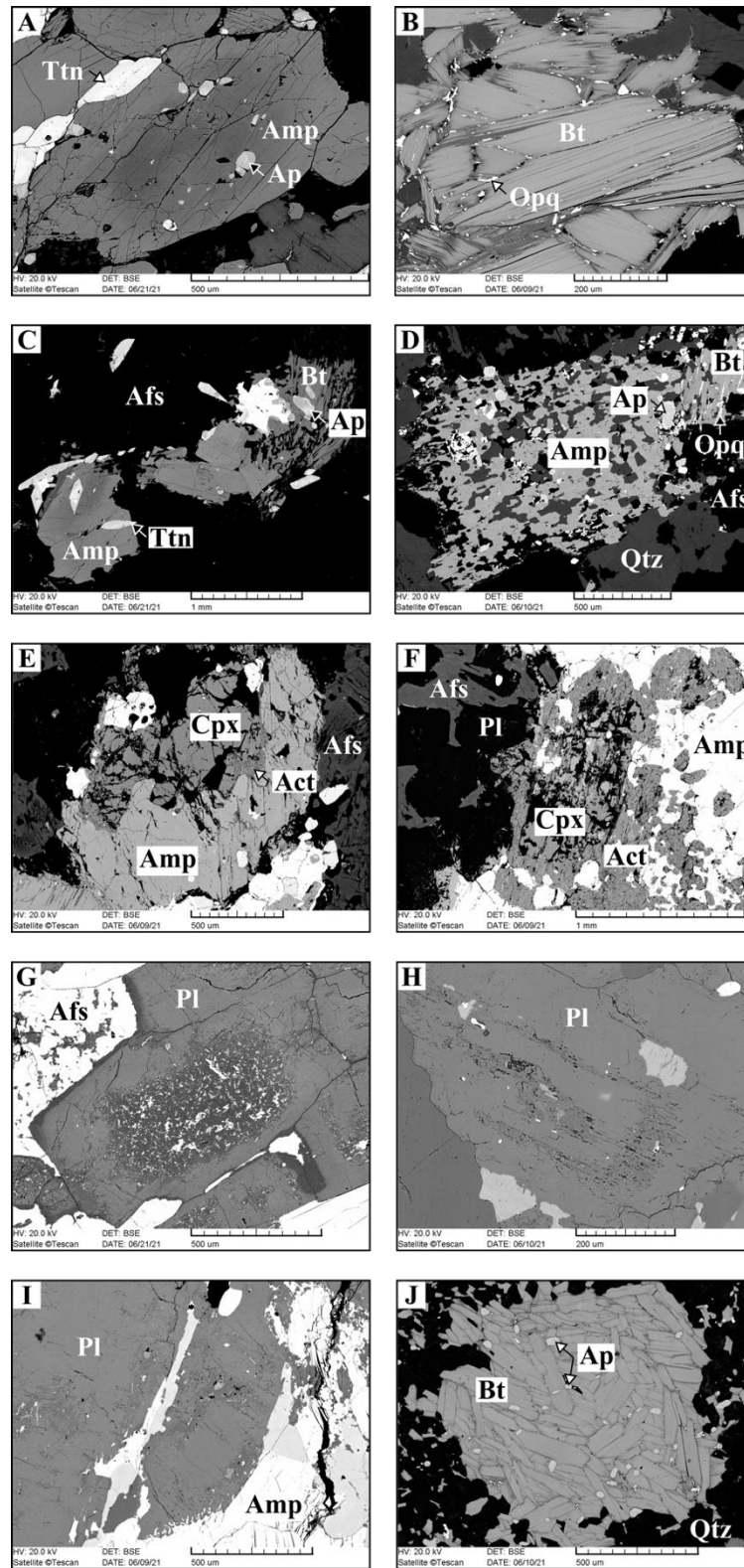
Fig. III.12. SEM images of the clot-forming ferromagnesian minerals and the felsic minerals in the groundmass. (A) Zoned green amphibole crystal with apatite inclusions in a *G-Amp* aggregate. (B) Biotite plates rimmed by opaque minerals in a *Bt-Dom* cluster. (C) *G-AmpBt* clot comprising both zoned and unzoned amphibole crystals. (D) *B-AmpBt* clump with spongy blue amphibole. (E) Green amphibole encircling clinopyroxene with minor actinolite in an *AmpCpxTtnOpqBt* aggregate. (F) Actinolite surrounding clinopyroxene in an *AmpCpxTtnOpqBt cluster*. (G) Typical zoning pattern of groundmass plagioclase with a sericitized core mantled by inclusion-free domains. (H) Multiple-zoned plagioclase exhibiting a sericitized core and zone. (I) Reverse-zoned plagioclase with a pure core encircled by a sericitized domain, followed by a rim where inclusions are absent. (J) Biotite-rich isometric clot in a hornfels xenolith. Abbreviations of the rock-forming minerals are after Whitney and Evans (2010)

III.5. Discussion

III.5.1. Indications of felsic crystal accumulation and other dynamic magma chamber processes from the Ditrău Alkaline Massif

The studied felsic suite of the DAM is considerably more diverse than previously thought. The heterogeneities are generally not of outcrop or macro-scale but rather occur at the micro-scale.

Both types of felsic rocks (Group 1 and 2) contain abundant, idiomorphic–hypidiomorphic, touching feldspar crystals that are aligned parallel to their crystal faces and define a shape-preferred orientation (Fig. III.6A, C). If present, mafic minerals, clots, and schlieren are also arranged accordingly (Fig. III.7B, E, G). Such an arrangement results in strongly foliated igneous rocks, showing no signs of solid-state deformation. Feldspar lamination can be attributed either to gravity-driven compaction or to the magmatic flow-induced shearing of the crystal mush (Ildefonse and Fernandez, 1988; Féménias et al., 2005; Vernon and Paterson, 2006 and references therein).

On a smaller scale, there are examples of aggregates, embedded in the felsic groundmass, comprising multiple feldspar crystals with a separate core and growth zones, adhered in a parallel orientation (Fig. III.10B, C). Furthermore, analogous clusters of smaller-sized plagioclase crystals occur as inclusions within alkaline feldspar of the felsic rocks (Fig. III.10C, D) as well as in alkaline feldspar megacrysts (Fig. III.10E). Such clumps are also known as "chain structure" (Vernon and Collins, 2011) and can be formed by a phenomenon Vogt (1921) described as "synneusis": suspended crystals may be episodically drifted together by turbulent currents (e.g., as a consequence of replenishment) or by gravitational segregation (Brown, 1956; Brothers, 1964; Vance, 1969). Synneusis requires a high melt-to-crystal ratio; thus, it operates mostly in the early stages of crystallization. Based on these findings, feldspar crystals of such clusters – both in the groundmass and as inclusions – represent an earlier generation and may record turbulence due either to the injection of new magma batch(es) (Vance, 1969) or to convection currents. Polycrystalline aggregates of felsic minerals are more capable of settling in viscous (felsic) magmas (Vernon and Collins, 2011) and the abundance of such clots implies physical accumulation.

Some of the feldspars are embayed by another crystal (Fig. III.6D, marked by the red arrow); nevertheless, clusters composed of multiple feldspar grains mutually impinging each other were also observed (Fig. III.6D, marked by the yellow arrow). These crystals exhibit an irregular contact and a locally truncated zoning pattern. The embayed minerals have a separate, sericitized/sieve-textured core, completely isolated by a few, continuous growth-zones. In most cases, the crystals in such a textural relation are mantled by a common, inclusion-free rim (Fig. III.6D). Contact melting and embayment of the accumulated, touching crystals may be related

to the compaction of the crystal mush (Park and Means, 1996; Vernon et al., 2004; Vernon and Collins, 2011). The pure rim is inferred to represent interstitial melts trapped among the accumulated crystals.

The different zonation of adjoining feldspars (Figs. III.10B–E, G, H and III.12G–I) indicates distinctive crystallization and reaction histories. Zoning patterns of feldspars retained disequilibrium textures and thus, recorded evidence of dynamic magmatic events. Most of the feldspars show a common zonation: a sericitized/sieve-textured core is encircled by a pure rim (Figs. III.6C, D, III.10B–E, and III.12G). This texture implies that significant changes occurred in the intensive variables (such as P, T, or aH$_2$O) and/or in the magma composition, which could be related to an interaction with a more primitive magma. Bindea et al. (2020) interpreted the two-feldspar core-mantle textures (albite core rimmed by alkaline feldspar) as a resorption or replacement texture of a formerly-grown plagioclase by a subsequent alkaline feldspar, amidst open-system magmatic circumstances.

Though not as abundant, there are some examples of feldspars exhibiting multiple (Figs. III.10G, marked by the red arrow and III.12H) as well as reverse (Figs. III.10H, marked by the red arrow and III.12I) zoning. In the first case, the core of the crystals is Ca-rich, assumed by its profound sericitization. The core is mantled by a zone with a more sodic composition. It is followed by another domain of calcic spike, which is armored by a Na-rich rim. The calcic core and zone might have originated from a magma of higher temperature and more mafic composition, whereas the sodic areas represent a lower-temperature and relatively felsic environment. The different zones record compositional changes in feldspars that can be attributed to variations in the magmatic conditions and thus, may imply multi-stage mixing events. Nevertheless, such multiple-zoned crystals are relatively scarce. Hence, it is more likely that their texture is the result of a smaller-scale/less-widespread process and indicates crystallization amidst fluctuating parameters (e.g., T and magma composition). Such conditions can easily be conceived during crystal transfer, caused e.g., by turbulent currents. Turbulence is not necessarily independent of magma mixing/mingling; indeed, it is probable that single crystals of both end-members have been dragged by these currents during the invasion of the replenishing magma and became introduced into the new environment characterized by contrasting composition and intensive variables. Subsequent and repeated transport of single crystals from one magma into the other could have resulted in the observed textural features. Nevertheless, chamber-scale convection currents may also carry crystals and circulate them between various domains of the magmatic system defined by different chemical compositions, P, and T. Based on the dimension of the zones with different textures, the transported feldspar

crystals either had not spent much time in either environment before they were introduced into the other one or became notably resorbed in the new setting.

Similarly, reverse zoning of feldspars (Figs. III.10H and III.12I) hints that such crystals originate from an environment of different temperature and/or composition and that their particular textural characteristics were formed by crystal transfer and/or interaction between different magma batches (Wiebe, 1968; Baxter and Feely, 2002; Vernon and Paterson, 2006). Their intact, inclusion-free core implies a more sodic composition. It is succeeded by a relatively wide, extensively sericitized zone of supposedly more Ca-rich chemical composition. Such crystals are mantled by a possibly sodic rim, where inclusions are absent. The core may have originated from the felsic magma and later became introduced into another environment of higher temperature and/or contrasting composition and – based on the dimension of the sericitized domain – spent there a relatively long time before being transported back into its original setting. The outer rim is likely to represent the felsic end-member. The observation that reverse-zoned feldspars are spatially associated with mafic clots further supports the hypothesis that (at least some of) the latter originated from other regions of the magma storage system and/or were introduced into their present setting by magma mixing/mingling. The presence of antecrysts and mantled xenocrysts adjoining their mantle-free equivalents can also be explained by the felsic cumulate hypothesis (Vernon and Collins, 2011).

Based on these observations, the evolution of the investigated felsic rocks was driven by multiple magma chamber processes. Textural features – implying settling of felsic minerals, magmatic flow, strain of the crystal mush, magma mixing/mingling as well as turbulent convection – reveal the dynamic conditions that prevailed in the magmatic system. Crystal accumulation and flow fabrics indicate the presence of heterogeneous domains within the chamber. The former was confined to areas where shear flow and/or convection was limited, whereas the latter occurred in active regions where melt was more abundant. Repeated injection of more primitive magmas into the felsic crystal mush, interaction of the two end-members as well as replenishment-induced convection and stirring, along with temperature and/or density gradient-driven currents also played a crucial role in the development of the observed features.

III.5.2. Mafic clots in the felsic suite of the Ditrău Alkaline Massif: origin and significance

Felsic rocks of Group 2 appear to be homogeneous at the macro-scale (Fig. III.3A–D); however, their microtextural features indicate that they comprise – besides minor isolated ferromagnesian minerals – mafic aggregates of various petrographic characteristics (Figs. III.4 and III.7–9; Table III.2). The observation that such clots are present in practically all of the felsic rocks of Group 2 indicates that cluster-formation was a widespread and common mechanism. They

make a considerable contribution to enhancing the mafic mineral content of the host rocks since not all of the ferromagnesian phases are considered to be of primary, direct magmatic origin.

Synneusis is a generally accepted concept for the genesis of felsic (plagioclase, alkaline feldspar, or quartz) clusters (Vance, 1969); nevertheless, according to Vernon and Collins (2011), mafic clots may be formed by the same process as well. However, it should be noted that mafic clumps could be the products of various alternative mechanisms, details of which will be discussed henceforth.

Carvalho et al. (2017) found that the maficity of diatexite magmas can be significantly increased by the raft and grain-scale disaggregation of mafic schollen. Lavaure and Sawyer (2011) focused particularly on country rock xenoliths and they also found that the dismemberment of these inclusions plays an important role in increasing the modal proportion of ferromagnesian minerals (especially biotite) in the host. Based on the results of Batki et al. (2018), open-system processes such as magma mixing and mingling, crystal transfer as well as recycling were significant in the petrogenesis of some rock types of the DAM (e.g., diorite, ijolite, syenite, tinguaite). The study by Ódri et al. (2020) shed light on the contribution of 20–60% upper crustal material during the evolution of the felsic suite (syenite, quartz syenite, quartz monzonite, granite).

Keeping in mind the above-mentioned information, it is likely that at least some of the mafic clumps are composed of replacive minerals after a precursor phase. Comparing all observed aggregate types, one can notice a continuous transition from almost intact clot-forming crystals through partial to complete replacement (pseudomorphism). Thus, different clusters might represent the distinct stages of substitution of the entrained materials. Some clump types are presumed to be of different origin. Identification of the processes prevailing in the magma storage system is rather challenging and it is assumed that a combination of multiple, complex mechanisms resulted in the formation of the observed features. Figure III.13 is a schematic illustration of how the modal proportion of the ferromagnesian phases could have been modified during these processes.

It is supposed that the base of the magma chamber comprises a mafic cumulate pile that is overlain by a felsic crystal mush. This system is periodically replenished by magma batches of a more primitive composition (Fig. III.13/1).
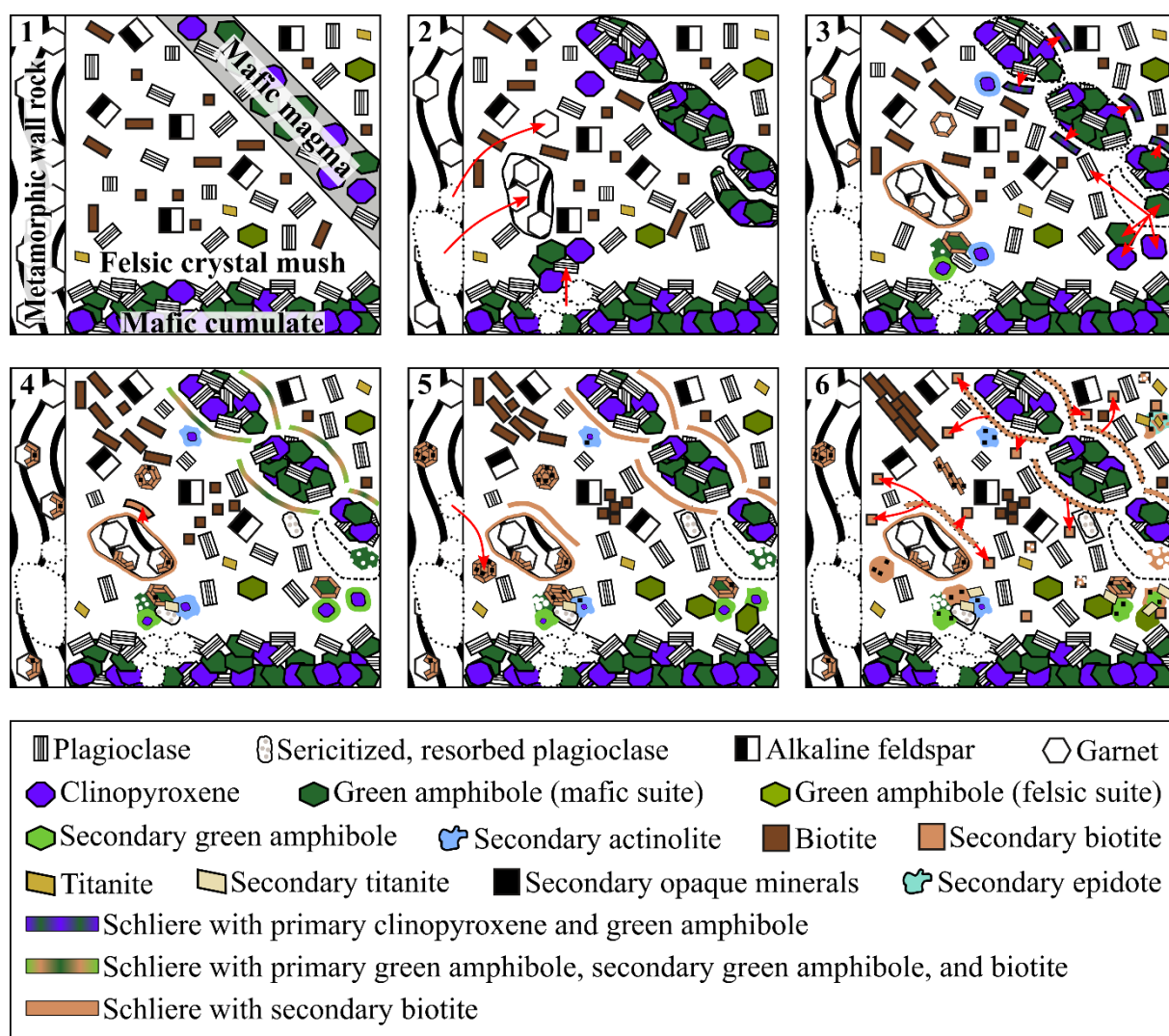
Fig. III.13. Schematic interpretation of the processes involved in the formation of the studied mafic clots. Mechanisms associated with the development of felsic clots and cumulates are not represented for visual clarity. The relative size of the crystals and structural elements is not illustrated to scale. See text for details

Due to the movement of the host magma, coherent magmatic enclaves and isolated ferromagnesian minerals are formed by the disruption of the mafic dyke (Fig. III.13/2). Owing to the interaction with the igneous body, metamorphic wall rock xenoliths and country rock-derived isolated crystals become introduced into the felsic crystal mush. Turbulent currents – induced either by the invasion of the replenishing magma or by thermal and/or density gradients – may drag and deposit mafic cumulus mineral aggregates in the felsic system (Fig. III.13/2).

The flow of the felsic melt leads to the separation of plagioclase from biotite and of elongated biotite crystals from the equant ones. The latter is introduced into the low shear strain (plagioclase-dominated) zones (Fig. III.13/3). Shearing also promotes the disaggregation of the entrained inclusions. Continuous erosion of the incorporated magmatic enclaves and metamorphic xenoliths reduces their dimensions, adds ferromagnesian minerals into the felsic host, and thus, leads to the formation of swarms comprising mafic phases. In this way,

clinopyroxene- and amphibole-bearing short and wide schlieren develop along the edges of the magmatic enclaves. The mafic bands are parallel to the margins of the rafts (Fig. III.13/3). This mechanism strongly increases the maficity of the felsic lithologies. The interaction between the host and the incorporated substances leads to progressive changes in the mineral assemblage of the latter. Following their incorporation into the felsic system, exotic materials become extensively modified and their ferromagnesian constituents are systematically replaced by secondary minerals (Fig. III.13/3). Isolated clinopyroxene crystals begin to be replaced by actinolite (Castro and Stephens, 1992). Garnet crystals are replaced by minor biotite (White et al., 2005) both in the mush and in the xenoliths. Due to the effect of the igneous body, replacive phases may develop in the metamorphic wall rock as well. Country rock xenoliths become completely mantled by a rim of biotite crystals (Fig. III.13/3). The *Bt-Xen* aggregate (Fig. III.7E, F) can be interpreted as a selvedge formed along the interface of the metamorphic xenolith and the host magma due to a chemical reaction between the two phases. The K-content of the host may decrease due to the development of the biotite-dominated fringe. This phenomenon may have an effect on the amount of alkaline feldspar crystallizing from the melt (Kriegsman, 2001) and most possibly that is the reason why alkaline feldspar of the enclosing rock becomes more abundant further away from the enclave. Secondary green amphibole and actinolite, along with biotite are formed after clot-forming cumulus clinopyroxene and green amphibole, respectively. Some of the cumulate-derived amphiboles develop a spongy texture, implying that they are not in equilibrium with their current setting (Fig. III.13/3).

As the magmatic strain increases, schlieren containing minor primary green amphibole along with secondary green amphibole and biotite after clinopyroxene and amphibole, respectively, become elongated. Short and wide, biotite-rich schlieren become detached from the periphery of the metamorphic xenoliths. The incorporated primary minerals are further replaced by secondary phases (Fig. III.13/4). Since clinopyroxene and amphibole can accommodate Ca, Y, and rare earth elements (REEs) in higher concentrations compared to biotite, the formation of secondary biotite after clinopyroxene or amphibole is accompanied by the crystallization of Ca-, Y-, and REE-bearing accessory minerals (Ubide et al., 2014b). This could account for the abundance of apatite, titanite, zircon, and opaque phases occurring both in the interstices and on the margins of the studied clusters (e.g., Figs. III.8D, F, G and III.9D, J). The rims of exotic plagioclase become resorbed in the new environment characterized by different intensive variables and composition. Simultaneously, plagioclase crystals begin to be sericitized (Fig. III.13/4).

Biotite completely replaces amphibole in the magmatic enclave-related schlieren (Fig. III.13/5). Intact growth-zones develop around the resorbed and sericitized plagioclase cores.

Xenolith-related biotite-rich schlieren become elongated. Some garnet crystals (both in the country rock and in the mush) are completely replaced by biotite, forming biotite-rich clumps and such pseudomorphs are further incorporated into the felsic system. The distribution of the different minerals within the rock as well as the extent of the chemical potential gradient and the diffusion coefficient bear a strong influence on the local reactions (Foster, 1986) and this could be the reason why pseudomorphs of garnet occur in the proximity of intact crystals (Figs. III.11 and III.13). Equant biotite crystals of the feldspar-rich domains form aggregates (Fig. III.13/5). By this stage, the plagioclase-rich domain has attained the rigid percolation threshold and thus, shear strain becomes more significant in the mafic mineral-rich bands. In the latter, biotite aggregates are formed initially, followed by imbrication of the elongated crystals. New magmatic amphibole crystallizes on some of the secondary mineral-bearing clots (Fig. III.13/5).

Schlieren are weaker than the feldspar-dominated host rock; hence, the postsub-magmatic strain is more pronounced in the mafic bands, which leads to the development of strongly elongated biotite-rich schlieren (Fig. III.13/6). Development of the *Bt-Dom* clots (Fig. III.8A–C) could be explained by the heterogeneous mineral and shear strain distribution of the magma (Milord and Sawyer, 2003). In domains of a higher magmatic strain, biotite-rich aggregates formed after garnet also become elongated and form schlieren; otherwise, they retain the habit of the preceding crystal (Fig. III.13/6). Schlieren-derived, detached biotite crystals become dispersed; thus, further increasing the maficity of the host. Actinolite and secondary biotite completely replace the isolated clinopyroxene and the spongy green amphibole, respectively (Fig. III.13/6), which implies that the latter was not in equilibrium with the melt. Flow of the host magma might completely disrupt the enclaves and xenoliths as well as the schlieren and then may thoroughly distribute the detached crystals (mostly biotite), developing a homogeneous texture in the host (Fig. III.13/6). Formation of the opaque fringe and inclusions along the cleavage planes of biotite (Figs. III.8B, C and III.12B) can be attributed to temperature-drop and/or deformation. Decreasing temperature, associated with a chemical reaction between biotite and the trapped melt may result in the crystallization of a muscovite rim enveloping biotite as well as the exsolution of opaque phases (Milord and Sawyer, 2003). Primary minerals of the clusters are either completely replaced (e.g., Fig. III.8C, D) or are preserved as crystal relics (e.g., Figs. III.8F, G and III.9J). Complete substitution is inferred to be favored in melt-rich, more hydrous regions of the system. The replacive phases may recrystallize into a larger grain-size in order to decrease the surface area and energy and thus, attain greater stability (Fig. III.13/6).

Some of the *G-AmpBt* aggregates (Fig. III.8F, G) and *Bt-Ran* clusters (Fig. III.8D) perfectly preserve the transition from intact green amphibole (Fig. III.14/1), through biotite

partially replacing and retaining the shape of amphibole (Fig. III.14/2) along with biotite-dominated clumps containing minor amphibole (Fig. III.14/3) to complete replacement by biotite and elongation of the clusters (Fig. III.14/4).
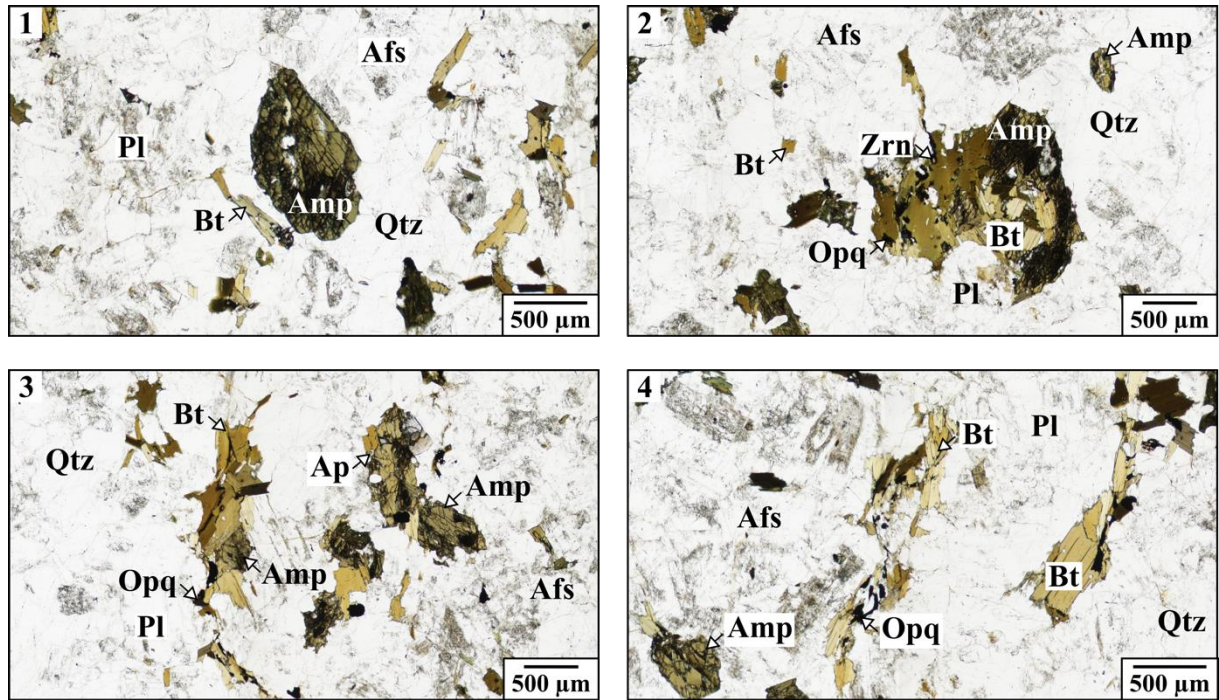
Fig. III.14. Textural changes during the progressive interaction of the incorporated green amphibole with the monzogranite host. (1) Hypidiomorphic, almost intact green amphibole in the host rock, 1N (plane-polarized light). (2) Green amphibole, partially replaced by biotite, with accessory zircon and opaque minerals, 1N. (3) Stubby schliere comprising minor green amphibole and secondary biotite, 1N. (4) Elongated schlieren, made up of biotite with a well-developed shape-preferred orientation completely replacing amphibole, 1N. Abbreviations of the rock-forming minerals are after Whitney and Evans (2010)

Groundmass and clot-forming epidote (Fig. III.8E) is most likely a hydrothermal, secondary phase that formed after amphibole and plagioclase (Bird and Spieler, 2004; Pandit et al., 2014; Kobylinski et al., 2020). Aggregates comprising decomposed mafic phases (Figs. III.9A–F, H, I and III.13/6) are likely to be the products of post-magmatic processes (e.g., hydrothermal or deuteric alteration of the primary ferromagnesian minerals and/or the mafic clusters comprising intact crystals).

It should be noted that some of the ferromagnesian minerals, defined as single mafic phases and considered as original, primary constituents of the felsic host rocks, may not be related to their present enclosing rock, but were derived from the disaggregation of the exotic inclusions, clots and/or the incorporation of single exotic crystals that have been thoroughly dispersed in the felsic system. This hypothesis is supported by the fact that some of the isolated ferromagnesian minerals exhibit irregular grain boundaries as well as a resorbed and spongy fabric, implying that they are not in equilibrium with their current setting (Fig. III.13/3–6).

The origin of isolated blue amphibole along with the different types of clusters containing blue amphibole (*B-Amp*, *B-AmpBt*, and their altered versions; Figs. III.7C, D, III.9G, H, and III.12D) is rather puzzling. Riebeckite is a common, primary mineral in Na-rich alkaline igneous rocks (such as nepheline syenite, syenite, granite); nevertheless, it also occurs in crystalline schists as well as in rocks that were subjected to alkali metasomatism (e.g., fenitization) (Miyashiro, 1957; Verschure and Maijer, 2005; Nesse, 2017). The studied rocks, containing single clinopyroxene along with different types of blue amphibole-laden aggregates, crop out in the proximity of nepheline syenite. Hence, some kind of relationship could be presumed between the clot-bearing rocks and nepheline syenite. Verschure and Maijer (2005) described replacement and corona textures identical to those observed in the studied rocks (Fig. III.9H). Such features can be interpreted as the products of a two-phase fenitization. In the first stage, breakdown of the original amphibole and biotite crystals had been initiated by the metasomatic process, leading to the formation of a reaction corona comprising Na-pyroxene and feldspars (Fig. III.9I). It was followed by a second phase, where, among others, Na-amphibole replaced the formerly generated Na-pyroxene as well as primary amphibole and biotite (Fig. III.9G, H). Na-metasomatism has previously been reported from the DAM, e.g., by Streckeisen (1960), Streckeisen and Hunziker (1974), Jakab et al. (1987), Kräutner and Bindea (1998) as well as by Pál-Molnár (2000). Thus, it could be a plausible mechanism for forming the isolated blue amphiboles and the blue amphibole-bearing clots.

Summarizing our observations, metamorphic country rock xenoliths can be traced along the border zone of the igneous body (Figs. III.2D, III.3E, F, III.7E, F, and III.11A, B); whereas, farther into the center of the pluton, schlieren are more characteristic and different types of mafic clusters are abundant (Figs. III.7A–D, III.8, and III.9). The metamorphic rocks enveloping the DAM as well as the country rock xenoliths contain abundant garnet crystals that are accompanied by aggregates of randomly-oriented biotite laths and plates (Figs. III.11 and III.12J). These clots are identical to the "biotite atolls" described by White et al. (2005) and they have been interpreted as pseudomorphs after garnet. Disaggregation of the enclaves, entrainment of garnet, and its subsequent replacement by biotite (Fig. III.13/2–6) or alternatively, involvement of the previously replaced grains (pseudomorphs; Fig. III.13/5–6) could account for (at least some of) the biotite-rich aggregates observed in the felsic rocks of the DAM.

Origin of the clots in the inner areas of the massif is less clear since, in most cases, secondary minerals replace the primary ones; furthermore, the robust evidence of magma chamber processes has either been obliterated or cannot be observed due to the poor exposures. However, there are a few locations where proofs of open-system magmatic processes (e.g.,

magma mixing/mingling) can be investigated (e.g., Heincz et al., 2018). If such an interaction was involved in the formation of the studied felsic suite and it occurred at the early stages of crystallization, the felsic and mafic end-members could have thoroughly mixed, leading to the complete homogenization of the mafic intrusion. The absence of mafic microgranular enclaves may be explained by this mechanism (Fernandez and Barbarin, 1991). With advanced crystallization of the felsic mush, hybridization of the mafic magma becomes progressively hindered and thus, magma mingling prevails. This process favors the formation of mafic enclaves. Such magma blobs can be distributed in the chamber, e.g., by large-scale convection currents. Enclaves are likely to be disaggregated during their transport or due to the movement of the host magma (Fernandez and Barbarin, 1991). This second hypothesis seems to be more feasible to interpret the lack of the aforementioned structural features, adding that the scarcity of outcrops could also prevent one from recognizing and investigating the magmatic enclaves. Thus, it is likely that some of the mafic aggregates occurring in the studied felsic rocks retain the vestiges of magma mixing/mingling event(s).

Assuming that dynamic conditions prevailed in the magma chamber, thermal and/or density gradient-related convection or replenishment-induced currents could have accounted for crystal/mush transfer and/or recycling that resulted in the formation of certain mafic clusters.

III.6. Concluding remarks

The presence and combination of the observed micro-textural features (e.g., feldspar clots, adjoining feldspars with different zoning sequences, mafic aggregates, metamorphic country rock xenoliths) infer that the studied felsic rocks of the Ditrău Alkaline Massif (Eastern Carpathians, Romania) crystallized under dynamic magmatic conditions. Such circumstances can easily be conceived in an open magma storage system, periodically invaded by new magma batches. Interaction of the distinct magmas resulted in mixing and mingling event(s); furthermore, magmatic stirring was induced by the injection of the replenishing magma. Convection currents may have also developed as a consequence of thermal and/or density gradients. Heterogeneous domains are likely to have been formed within the chamber with regions of limited shear flow and/or convection. This environment favored the accumulation of felsic minerals. Magmatic flow and turbulent currents prevailed in the melt-rich domains.

Felsic rocks of Group 1 (occurring on the hillside west of the Bordea Creek) exhibit distinct textural features characteristic of felsic cumulates. Rocks that had previously been classified into different types might be interpreted as accumulations of felsic minerals in different proportions.

Felsic rocks belonging to Group 2 (exposed between the Teasc and Rezu Mare Creeks) also bear traces of felsic crystal accumulation. Furthermore, they enclose different types of mafic aggregates. Mafic clots could have been formed by several mechanisms. However, based on their modal compositions and textural features, complemented by the results of former studies, some of the clusters are potential polycrystalline pseudomorphs after antecrysts and/or xenocrysts that were incorporated either by an interaction between different magma batches, by crystal transfer/recycling, and/or by wall rock contamination. Aggregates show the different stages of replacement of the precursor phase(s). Certain biotite-rich clumps could have been formed by a chemical reaction between the metamorphic wall rock xenoliths and the host as well as by the heterogeneous distribution of shear strain in the crystal mush. Some of the clusters comprising decomposed mafic minerals could be related to late-stage or post-magmatic modification of the ferromagnesian phases and/or mafic aggregates.

Crystal accumulation, crystal transfer/recycling, magma mixing and mingling as well as the incorporation of exotic materials cannot be proved by macroscopic and microscopic structural and textural features alone. Hence, recent data of the ongoing mineral-scale geochemical analyzes will be applied to unravel further details of the presumed open-system magmatic processes to understand more about the genesis of the felsic suite of the Ditrău Alkaline Massif.

CHAPTER IV

BULK-ROCK AND MINERAL-SCALE GEOCHEMICAL EVIDENCE OF OPEN-SYSTEM MAGMATIC PROCESSES IN THE FELSIC ROCKS OF THE NORTHERN PART OF THE DITRĂU ALKALINE MASSIF (EASTERN CARPATHIANS, ROMANIA)

Luca Kiri
'Vulcano' Petrology and Geochemistry Research Group, Department of Mineralogy, Geochemistry and Petrology, University of Szeged, Szeged, Hungary
e-mail: kiri.luca@gmail.com

Máté Szemerédi
'Vulcano' Petrology and Geochemistry Research Group, Department of Mineralogy, Geochemistry and Petrology, University of Szeged, Szeged, Hungary;
HUN-REN-ELTE Volcanology Research Group, Budapest, Hungary
e-mail: szemeredi.mate@gmail.com

Saskia Erdmann
Université d'Orléans, CNRS/INSU – ISTO – BRGM, UMR 7327, Orléans, France. 1A Rue 13 de la Ferollerie Campus Géosciences, 45100 Orléans, France
e-mail: saskia.erdmann@cnrs-orleans.fr

Anikó Batki
'Vulcano' Petrology and Geochemistry Research Group, Department of Mineralogy, Geochemistry and Petrology, University of Szeged, Szeged, Hungary;
HUN-REN-ELTE Volcanology Research Group, Budapest, Hungary
e-mail: batki@geo.u-szeged.hu

Elemér Pál-Molnár
'Vulcano' Petrology and Geochemistry Research Group, Department of Mineralogy, Geochemistry and Petrology, University of Szeged, Szeged, Hungary;
HUN-REN-ELTE Volcanology Research Group, Budapest, Hungary
e-mail: palm@geo.u-szeged.hu

Bulk-rock and mineral-scale geochemical evidence of open-system magmatic processes in the felsic rocks of the northern part of the Ditrău Alkaline Massif (Eastern Carpathians, Romania)

by: Luca Kiri, Máté Szemerédi, Saskia Erdmann, Anikó Batki, Elemér Pál-Molnár

Abstract

The felsic suite in the northern part of the Ditrău Alkaline Massif has previously been considered as a homogeneous, uniform unit of the igneous complex. However, these felsic rocks exhibit remarkable diversity at the micro-scale. Petrographic observations were complemented by bulk-rock and mineral-scale geochemical data to further support this hypothesis.

Whole-rock composition of the studied rocks validates the presence of two, compositionally-different felsic cumulate piles in the massif (characterized by $Eu/Eu^* = 2.5$–6.7, $\Sigma REE = 125$–206 ppm and $Eu/Eu^* = 1.0$–1.1, $\Sigma REE = 358$–688 ppm, respectively). Mineral chemical data (amphibole, clinopyroxene, and plagioclase) were acquired from crystals of different textural positions (clot-forming and isolated) to understand which of the ferromagnesian minerals and plagioclase have the highest potential for recognizing distinct magmatic environments and open-system magmatic processes. The composition of clinopyroxenes (diopside with mg# = 0.77 and 0.85, respectively) overlaps with the formerly published data. Moreover, a new, cumulus-phase occurrence of the clinopyroxenes with a convex REE pattern has been identified. Abrupt changes of the Ba, Sr, TiO_2, and ΣREE concentrations in different domains of the zoned amphibole crystals and variations in the MgO, FeO, TiO_2, Sr, Ba, La, Ce, and anorthite content in plagioclase crystals, together with the bulk-rock data, point to the hybrid nature of the majority of the investigated rocks.

Our recent geochemical data support the previous, predominantly petrography-based assumptions, that the felsic suite in the northern area of the massif was formed in a dynamic, open-system magmatic environment, wherein crystal settling, magma mixing, crystal/mush transfer and recycling as well as country rock assimilation prevailed.

IV.1. Introduction

Many plutonic rocks are partial cumulates or were formed by open-system igneous processes. Therefore, it is difficult, if not impossible, to evaluate the evolution of their parental melt from bulk-rock data (Deering and Bachmann, 2010; Coint et al., 2013). In contrast, mineral textures and composition – particularly mineral-scale trace element composition and compositional variation – record igneous processes more accurately (e.g., crystal transfer and recycling, fractional crystallization, magma mingling and mixing), including the associated heterogeneity of the magmatic system (Słaby et al., 2007, 2011; Coint et al., 2013; Barnes et al., 2016). During magma mixing or crystal recycling, the crystallizing minerals come into contact with magmas of distinct physicochemical properties (Słaby et al., 2007), which then create a subtle-to-drastic, crystal-scale variation (Barnes et al., 2016): complex growth and/or disequilibrium textures and zones with different geochemical compositions are formed within individual crystals (Hibbard, 1981; Baxter and Feely, 2002; Perugini et al., 2006; Kahl et al., 2011, 2015, 2017; Gros et al., 2020). Shifts in the major and trace element concentrations across a single crystal can be used as a proxy to track changes in the melt composition or in other intensive parameters (e.g., pressure and temperature; Słaby et al., 2007, 2011; Coint et al., 2013). In mafic-to-moderately evolved metaluminous-to-peralkaline granitic magmas, clinopyroxene and/or amphibole are common liquidus or near-liquidus phases (e.g., Scaillet et al., 2016; Huang et al., 2019), which incorporate a large spectrum of trace elements that range from large ion lithophile over rare earth to high field strength elements (LILEs, REEs, HFSEs, respectively; e.g., Naney, 1983; Marks et al., 2004). In combination, both minerals may record near-liquidus to near-solidus evolution of magmas, which thus reflect their relatively large stability fields and refractory nature (slow diffusivities for the key compositional constituents; e.g., Costa, 2021). Therefore, amphibole and clinopyroxene chemistry can be applied to unravel the igneous evolution and, ideally, the composition of the parental melt (e.g., Piwinskii, 1968; Naney, 1983; Schmidt, 1992; Marks et al., 2004; Ubide et al., 2014a). Similarly, plagioclase crystallizes over an extensive spectrum of magma compositions as well as over a large range of temperatures (e.g., Wiebe, 1968; Anderson, 1984; Blundy and Wood, 1991; Putirka, 2005). Although the concentration of trace elements and the type of trace elements that are incorporated by plagioclase are significantly lower than in clinopyroxene and amphibole crystals, some of the elements (e.g., Sr and Ba) are particularly useful for deciphering igneous processes (Blundy and Shimizu, 1991; Ginibre et al., 2002; Grogan and Reavy, 2002). Intra-crystalline diffusion and thus equilibration of major elements and several trace elements (e.g., Sr, Ba, REEs) is slow, and their concentration commonly records the compositional and other changes of intensive parameters of the host magmas precisely (e.g., pressure and temperature; Smith et al., 2009).

The main objective of this research was to discern which of the studied mafic minerals (magmatic and secondary amphibole as well as clinopyroxene) and plagioclase have the highest potential to distinguish different igneous environments and to reveal open-system magmatic processes. New mineral major and trace element data along with whole-rock compositions are presented to further understand the petrogenesis of the felsic suite in the northern part of the Ditrău Alkaline Massif (DAM), thereby complementing previous field and petrographic observations.

IV.2. Geologic setting

The DAM is situated in the Eastern Carpathians (Romania) and belongs to the Dacia Mega-Unit (Fig. IV.1A, B). It forms the southwestern and southern areas of the Giurgeu Mountains and extends over an area of ca. 225 km^2. The massif consists of different rock types in a spectrum from ultramafic cumulates to granitoid rocks (Streckeisen and Hunziker, 1974; Jakab, 1998; Kräutner and Bindea, 1998; Morogan et al., 2000; Pál-Molnár, 2000; Batki et al., 2014; Pál-Molnár et al., 2015a, b; Fig. IV.1C).

In the Middle–Late Triassic, an igneous event occurred near the southwestern margin of the East European Craton in an intra-plate, rift-related, extensional tectonic regime. Recent geochronological data suggest a brief magmatic period (Ladinian–Norian) for the formation of the DAM (e.g., Pál-Molnár et al., 2021; Klötzli et al., 2022). The Variscan metamorphic rocks of the Eastern Carpathians had been penetrated by the alkaline magmas of the DAM and were collectively subjected to consecutive nappe-forming Alpine tectonic processes (Fig. IV.1B). An eastward-verging nappe system was established as a result of the Cretaceous (Austrian) tectogenesis. It is referred to as either Eastern Getides (Balintoni, 1997) or Median Dacides (Săndulescu, 1984). The Infrabucovinian, Subbucovinian, and Bucovinian Nappes (with pre-Alpine metamorphic rocks and Permo-Mesozoic cover series) make up the Median Dacides (Săndulescu, 1984). Pre-Alpine, petrographically-analogous tectonic units occur in the Subbucovinian and Bucovinian Nappes. The DAM is structurally associated with the Bucovinian Nappe (Fig. IV.1B) and juxtaposed with four of its pre-Alpine metamorphic terranes (Bretila, Tulgheş, Negrişoara, and Rebra Lithogroup; Balintoni et al., 2014). A tectonic discontinuity separates the DAM from the Subbucovinian Nappe because the massif was uprooted during the Alpine tectonic events and was thus split by the Bucovinian shear zone (Kräutner and Bindea, 1995).
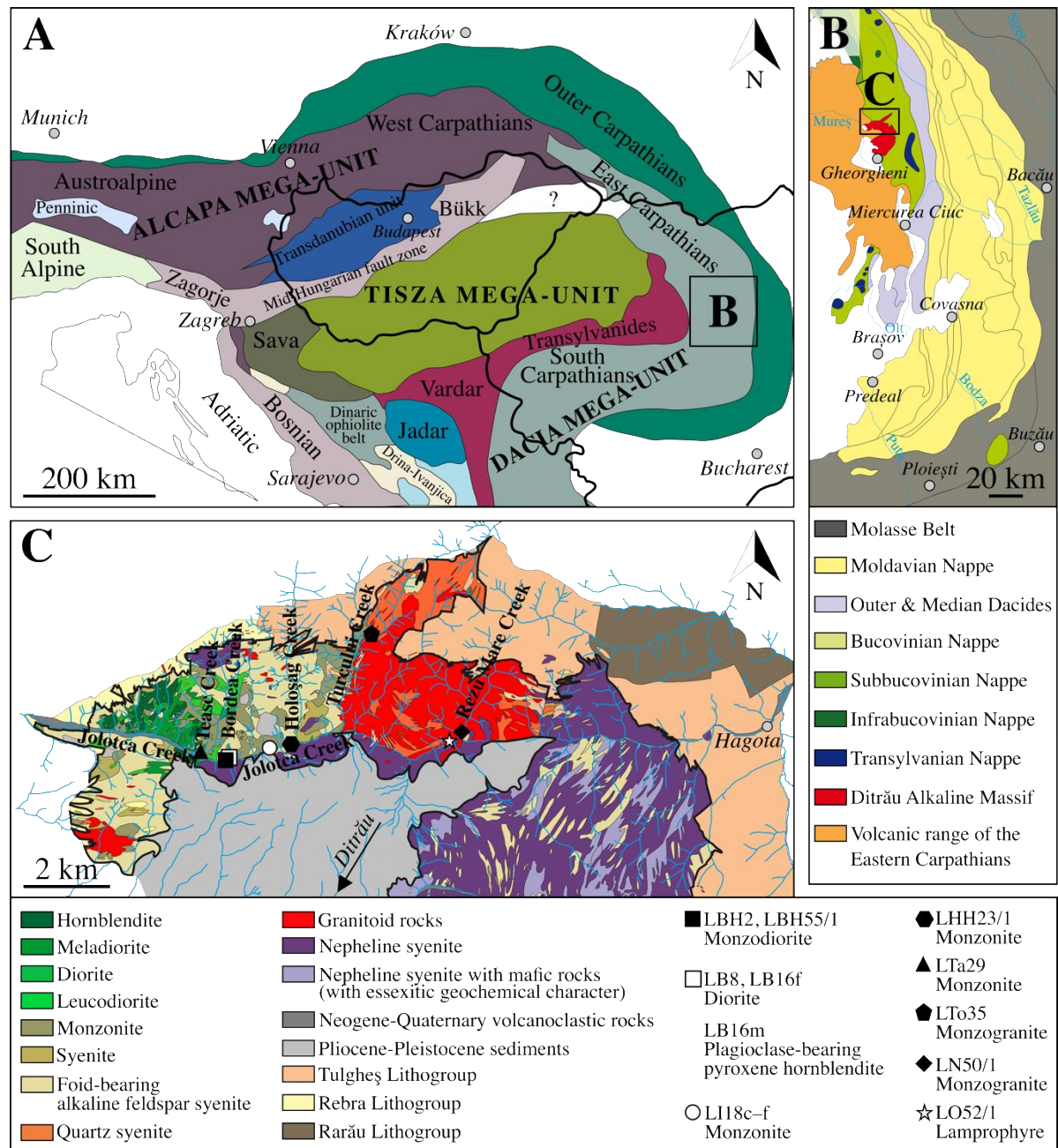
Fig. IV.1. (A) Position of the Ditrău Alkaline Massif in the Alpine-Carpathian-Dinaric realm (modified after Haas et al., 2010). (B) Location of the massif in the Alpine tectonic units of the Eastern Carpathians (modified after Săndulescu et al., 1981). (C) Sampling sites of various rock types (details in the legend) in the schematic geological map of the northern part of the massif (modified after Pál-Molnár et al., 2015a)

In the northern part of the DAM, from west to east, the massif comprises a sequence of ultramafic and mafic cumulates that grade into gabbro, diorite (*s.l.*), monzonite, syenite, quartz syenite, and granite (Fig. IV.1C). Nepheline syenite forms an extensive area in the central and eastern parts of the massif, associated with minor syenite and granite (Pál-Molnár, 2000; Pál-Molnár et al., 2015a, b). The spatially-related (ultra)mafic rocks [hornblendite, gabbro, and diorite (*s.l.*)] in the northwestern part of the massif form a lithostratigraphic unit of a complex structure (referred to as the Tarnița Complex; Pál-Molnár, 2000). Apart from the mingling structures of different diorite types (*s.l.*) (Fig. IV.2A) near the confluence of the Pietrăriei de

Sus and Jolotca Creeks (Heincz et al., 2018), no other intrusive contacts were found in this region. Mingling structures of diorite (*s.l.*) and nepheline syenite can be studied in the outcrops along the Ditrău–Hagota road (central part of the DAM), evidenced by mafic enclaves (Fig. IV.2B) and large mafic (Fig. IV.2C) as well as felsic cumulate fragments (Fig. IV.2D). The rocks of the massif are crosscut by lamprophyre, (nepheline)syenite, ijolite, and tinguaite dykes (Pál-Molnár, 2000; Batki et al., 2014; Pál-Molnár et al., 2015a, b; Fig. IV.2A, E). Wall rock xenoliths are present along the contact between syenite, monzogranite, and the metamorphic country rocks (e.g., Kräutner and Bindea, 1995; Kiri et al., 2022; Fig. IV.3C). Based on amphibole thermobarometry, the (ultra)mafic cumulates are lower-crust derived (Pál-Molnár et al., 2015a); whereas, granite was emplaced at middle-to-upper-crustal depths (Pál-Molnár et al., 2015b). P–T conditions for the formation of other lithologies are not available (e.g., monzonite and syenite).
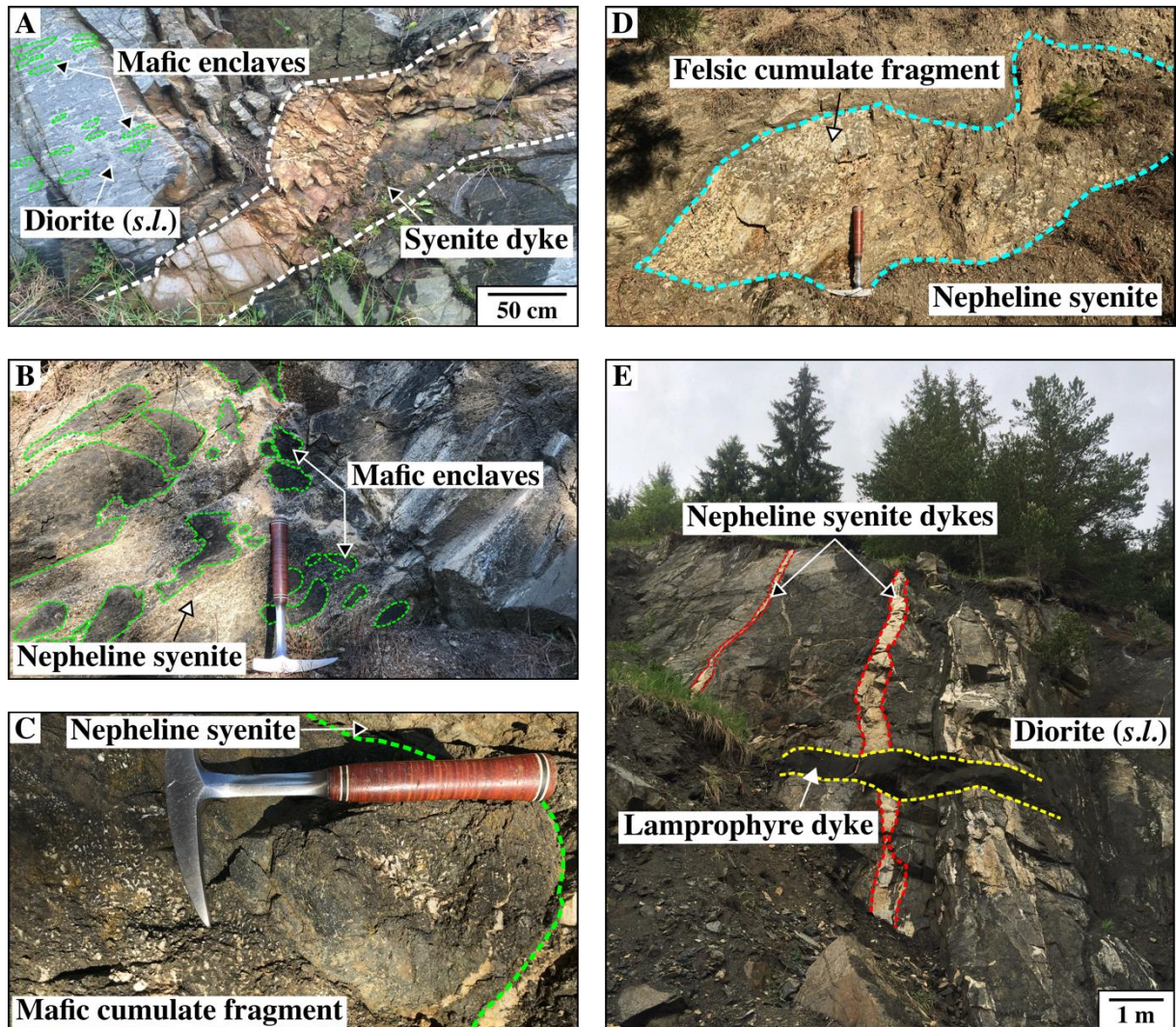
Fig. IV.2. Field evidence for interactions between different magma batches. (A) Syenite dyke, crosscutting the host rock and the mafic enclaves in the Tarnița Complex. (B) Mafic enclaves, (C) mafic cumulate fragment, (D) felsic cumulate fragment, and (E) nepheline syenite and lamprophyre dykes in outcrops along the Ditrău–Hagota road

Previous studies have interpreted the felsic suite of the northern part of the DAM as a homogeneous, uniform unit of the massif (e.g., Jakab, 1998; Kovács and Pál-Molnár, 2005). Nevertheless, recent investigations have suggested that the felsic rocks were formed in an open-system magmatic environment (e.g., Batki et al., 2018; Heincz et al., 2018; Ódri et al., 2020; Kiri et al., 2022). A detailed petrographic study of the felsic suite in the northern area of the DAM revealed microtextural features (e.g., mafic clots, plagioclase crystals in synneusis relation, adjacent plagioclase feldspars with disparate zoning patterns, country rock xenoliths) indicative of dynamic magmatic conditions (e.g., crystal transfer and recycling, cumulate formation, magma mixing and mingling as well as wall rock assimilation; Kiri et al., 2022). However, the sparse geochemical data for the felsic rocks (e.g., Batki et al., 2018; Ódri et al., 2020) and the lacking mineral-scale compositional data needed to be supplemented to validate this concept.

Batki et al. (2018) distinguished two parental magmas based on the composition of clinopyroxene populations from olivine-rich and pyroxene-rich cumulates, diorite, syenite, nepheline syenite, camptonite and tinguaite dykes, along with ijolite enclaves: Magma1 (M1) of basanitic composition, parental to (ultra)mafic cumulates and rocks of the Tarnița Complex along with Magma2 (M2) that evolved to a phonolitic composition. Interaction between the two magmas was evidenced by the presence of green clinopyroxene antecrysts in diorite, syenite, and tinguaite. However, the evolution of the felsic suite [e.g., the open-system processes involved in the formation of syenite (crustal assimilation, magma mixing) and its genetic relation to the other rock types of the massif] remained partly unresolved (Batki et al., 2018).

IV.3. Materials and analytical methods

IV.3.1. Samples

The detailed description of the sampling area along with the macroscopic and microscopic characteristics of the collected rocks can be found in Kiri et al. (2022) since only a brief summary is presented here (Table IV.1; Supplementary Table IV.1). In line with the classification schemes used in previous studies (e.g., Pál-Molnár et al., 2015a; Heincz et al., 2018; Kiri et al., 2022), the nomenclature used in this paper is based on the modal composition of the studied rocks to ensure comparability. Two groups of felsic rocks were identified in accordance with their field occurrences and microtextures: Group 1 – felsic rocks (diorite) with a minor mafic mineral content, spatially associated with mafic cumulates (plagioclase-bearing pyroxene hornblendite) and Group 2 – felsic rocks (monzodiorite, monzogranite, monzonite, nepheline-bearing syenite, quartz monzonite, quartz syenite, syenite, syenogranite) which comprise mafic minerals and aggregates and are not spatially associated with mafic cumulates

(Kiri et al., 2022). Plagioclase (85–87 vol%) predominates in the rocks of the first group; whereas, biotite (4–9 vol%), alkaline feldspar (2–8 vol%), and titanite (max. 1 vol%) occur in minor amounts (Fig. IV.3A). Structural and textural characteristics of the rock-forming minerals [e.g., impinging plagioclase feldspars with separate cores, clusters of multiple plagioclase crystals in parallel orientation ("chain structure"; Vernon and Collins, 2011); Fig. IV.4A, B] imply that these rocks were formed by crystal accumulation. In the rocks of Group 2, the felsic rock-forming minerals are represented by plagioclase (8–71 vol%), alkaline feldspar (22–78 vol%), and quartz (0–46 vol%) (Fig. IV.3B–D). Discrete, primary mafic minerals are rare (amphibole: max. 6 vol%; biotite: max. 9 vol%); however, various clusters (max. 18 vol%) which comprise either one or multiple mafic mineral types are prevalent (Fig. IV.4E–H; Supplementary Table IV.1). Titanite is the most common accessory mineral (max. 2 vol%). Some of the rocks in the second group also exhibit textural traits that are analogous to those of Group 1, thus, indicating crystal accumulation (Fig. IV.4C, D).

Exposures are rare due to recent recultivation and dense vegetation. Hence, the samples were collected from *in situ* outcrops on the hillsides and in the valleys of creeks.

The rocks to be analyzed for bulk rock and/or mineral compositions (Table IV.1) were selected according to the following criteria: (a) to include the most important felsic rock types (diorite, monzodiorite, monzogranite, monzonite) as well as ferromagnesian minerals (amphibole and clinopyroxene) from mafic rocks (plagioclase-bearing pyroxene hornblendite and lamprophyre) for comparison, which are all typical of the northern area of the massif; (b) to represent all textural types; and (c) to include all textural-mineralogical mafic and felsic (feldspar-rich) crystal-clot varieties.

Table IV.1. Nomenclature, sampling locations, main petrographic features, and whole-rock major and trace element compositions of the studied rocks from the Ditrău Alkaline Massif (Romania)

Sample	LBH2	LB8	LB16f (felsic part)	LB16m (mafic part)	LI18f (fine-grained)	LI18c (coarse-grained)	LHH23/1	LTa29	LTo35	LN50/1	LO52/1	LBH55/1
Rock type (modal composition and texture)	MDo	D	Do	PlPxH	Mo	M	M	M	MG	MG	L	MDo
Rock type (total alkali *vs*. SiO₂)	M	S	S	-	M	S	M	M	QM	G	-	M
Rock type (calculated cation norms)	FMD	FMD	FMD	-	FM	FM	FS	FM	QM	MG	-	FM
Locality and GPS coordinates	Hillside west of the Bordea Creek 46.86200, 25.51558	Bordea Creek 46.86246, 25.51698	Bordea Creek 46.86235, 25.51704	Bordea Creek 46.86235, 25.51705	Behind the school in Jolotca 46.86448, 25.52762	Behind the school in Jolotca 46.86448, 25.52762	Hillside west of the Holoşag Creek 46.86579, 25.53452	Teasc Creek 46.86344, 25.50844	Turcului Creek 46.8887, 25.55766	Rezu Mare Creek 46.86842, 25.58544	Jolotca Creek 46.86653, 25.58137	Hillside west of the Bordea Creek 46.86196, 25.51556
Rock group	2	1	1	-	2	2	2	2	2	2	-	2
Mineral assemblage (primary) and modal composition (vol%)	Pl (62) Afs (31) Amp (3) Bt (2) Ttn (1) Opq (<1)	Pl (87) Afs (2) Bt (9) Ttn (1)	Pl (85) Afs (8) Bt (4)	Pl (61) Cpx (4) Amp (5) Bt (30)	Pl (43) Afs (53) Amp (1) Bt (2) Ttn (1)	Pl (50) Afs (43) Amp (6) Bt (<1) Ttn (<1)	Pl (56) Afs (38) Bt (6)	Pl (42) Afs (51) Amp (2) Bt (1) Ttn (2)	Pl (36) Afs (35) Qtz (24) Amp (3) Bt (2)	Pl (20) Afs (28) Qtz (46) Bt (6)	Pl (60) Cpx (2) Amp (21) Bt (15) Ttn (2)	Pl (71) Afs (22) Bt (7)

Major elements (wt%)

	LBH2	LB8	LB16f	LB16m	LI18f	LI18c	LHH23/1	LTa29	LTo35	LN50/1	LO52/1	LBH55/1
SiO₂	53.43	62.60	60.74	n.d.	57.71	58.74	55.65	55.69	63.72	75.68	n.d.	57.19
TiO₂	2.06	0.48	0.66	n.d.	0.83	1.02	1.13	1.69	0.74	0.13	n.d.	0.77
Al₂O₃	18.02	20.52	21.65	n.d.	20.08	19.27	18.94	18.55	17.01	12.84	n.d.	21.13
Fe₂O₃	8.50	2.02	2.13	n.d.	5.01	4.47	8.22	6.64	4.18	1.77	n.d.	4.90
MnO	0.22	0.03	0.03	n.d.	0.16	0.14	0.18	0.12	0.09	0.03	n.d.	0.08
MgO	1.74	0.57	0.53	n.d.	0.61	0.78	2.62	1.48	0.92	0.15	n.d.	0.96
CaO	5.77	2.19	3.09	n.d.	3.44	3.31	1.14	4.56	2.06	0.54	n.d.	2.84
Na₂O	6.14	9.54	8.53	n.d.	6.31	6.00	6.44	5.44	4.72	4.11	n.d.	6.77
K₂O	2.46	0.91	1.49	n.d.	4.11	4.99	3.55	4.00	4.84	4.24	n.d.	3.64
P₂O₅	0.35	0.05	0.07	n.d.	0.12	0.19	<0.01	0.30	0.22	0.02	n.d.	0.28
Cr₂O₃	0.00	0.00	0.00	n.d.	<0.002	<0.002	0.02	<0.002	<0.002	0.00	n.d.	<0.002
LOI	0.80	0.80	0.70	n.d.	0.80	0.50	1.70	0.80	1.20	0.40	n.d.	1.00
Total	99.57	99.83	99.74	n.d.	99.43	99.64	99.71	99.59	99.79	99.92	n.d.	99.76
mg#	0.29	0.36	0.33	n.d.	0.19	0.26	0.39	0.31	0.30	0.14	n.d.	0.28

Normative minerals (wt%)

	LBH2	LB8	LB16f	LB16m	LI18f	LI18c	LHH23/1	LTa29	LTo35	LN50/1	LO52/1	LBH55/1
Ne	2.04	1.58	2.45	n.d.	3.05	2.52	0.37	0.41	0.00	0.00	n.d.	3.68
Ol	1.38	0.99	0.93	n.d.	0.74	0.71	4.57	1.94	0.00	0.00	n.d.	1.68

Table IV.1. Continued

Sample	LBH2	LB8	LB16f (felsic part)	LB16m (mafic part)	LI18f (fine-grained)	LI18c (coarse-grained)	LHH23/1	LTa29	LTo35	LN50/1	LO52/1	LBH55/1
D.I.	79.50	95.25	94.98	n.d.	90.22	89.84	81.46	84.76	90.2	96.62	n.d.	89.56

Trace elements (ppm)

	LBH2	LB8	LB16f	LB16m	LI18f	LI18c	LHH23/1	LTa29	LTo35	LN50/1	LO52/1	LBH55/1
Be	6.00	2.00	2.00	n.d.	8.00	2.00	2.00	2.00	6.00	12.00	n.d.	2.00
Sn	3.00	<1	<1	n.d.	3.00	2.00	<1	2.00	3.00	2.00	n.d.	<1
W	0.70	<0.5	<0.5	n.d.	0.60	<0.5	0.50	<0.5	1.60	2.00	n.d.	1.50
Sc	3.00	<1	<1	n.d.	1.00	2.00	1.00	3.00	3.00	<1	n.d.	3.00
V	92.00	21.00	22.00	n.d.	32.00	36.00	46.00	87.00	33.00	<8	n.d.	98.00
Co	10.20	3.60	5.90	n.d.	3.50	4.00	9.20	10.30	5.00	1.00	n.d.	7.70
Ni	<20	<20	<20	n.d.	<20	<20	40.00	<20	<20	<20	n.d.	<20
Ga	22.50	16.10	19.20	n.d.	25.30	21.00	22.60	18.10	22.30	22.00	n.d.	21.10
Rb	45.90	20.20	30.30	n.d.	80.60	99.00	103.00	46.90	156.60	143.00	n.d.	102.60
Sr	1404.00	1238.90	1676.30	n.d.	2455.10	1587.70	412.50	2040.10	557.50	44.80	n.d.	1171.60
Y	42.20	7.30	11.10	n.d.	32.40	29.30	3.80	32.50	20.60	23.70	n.d.	6.40
Zr	523.40	64.70	135.30	n.d.	913.60	459.30	1009.40	248.70	483.00	126.90	n.d.	179.30
Nb	245.80	36.60	56.80	n.d.	206.00	138.30	36.00	186.00	87.90	114.40	n.d.	39.80
Cs	0.70	<0.1	0.30	n.d.	1.40	0.90	1.00	0.30	2.80	1.90	n.d.	0.80
Ba	1009.00	856.00	770.00	n.d.	1978.00	1943.00	636.00	2561.00	912.00	86.00	n.d.	1494.00
La	174.50	25.60	38.70	n.d.	233.50	104.60	60.30	125.70	41.00	16.40	n.d.	73.60
Ce	311.00	43.20	67.50	n.d.	328.90	184.30	48.20	228.50	90.70	33.40	n.d.	89.80
Pr	29.60	4.35	6.79	n.d.	27.76	18.29	2.67	22.79	7.78	4.05	n.d.	6.82
Nd	96.40	14.90	22.70	n.d.	83.00	61.20	6.10	75.90	27.70	15.10	n.d.	19.90
Sm	13.77	2.38	3.60	n.d.	10.90	9.19	0.44	10.83	5.16	3.75	n.d.	2.36
Eu	4.07	0.90	1.20	n.d.	3.28	2.70	0.96	3.25	1.52	0.67	n.d.	1.75
Gd	10.49	1.89	2.94	n.d.	7.86	7.32	0.43	8.35	4.49	4.01	n.d.	1.89
Tb	1.54	0.27	0.43	n.d.	1.12	1.08	0.06	1.21	0.68	0.73	n.d.	0.20
Dy	8.12	1.54	2.25	n.d.	6.18	5.59	0.50	6.36	4.01	4.81	n.d.	1.18
Ho	1.47	0.24	0.40	n.d.	1.13	1.10	0.13	1.17	0.74	0.93	n.d.	0.22
Er	4.13	0.67	1.16	n.d.	3.43	3.22	0.47	3.49	2.24	3.08	n.d.	0.59
Tm	0.56	0.09	0.15	n.d.	0.46	0.40	0.08	0.41	0.32	0.46	n.d.	0.09
Yb	3.39	0.53	0.82	n.d.	2.99	2.65	0.70	2.63	2.27	2.94	n.d.	0.66
Lu	0.45	0.06	0.10	n.d.	0.48	0.39	0.14	0.30	0.33	0.45	n.d.	0.10
Hf	12.90	1.50	2.90	n.d.	16.50	9.30	19.10	6.70	10.60	5.50	n.d.	3.40
Ta	15.50	3.10	4.70	n.d.	11.00	7.80	0.70	12.50	5.80	13.20	n.d.	1.20
Th	16.10	3.40	10.90	n.d.	40.90	11.00	1.70	9.30	16.50	61.00	n.d.	8.20
U	3.80	0.80	3.90	n.d.	6.00	2.40	0.90	1.50	3.20	9.80	n.d.	1.50
ΣREE	1493.09	209.03	360.81	n.d.	1888.00	1040.67	1189.56	970.79	794.14	376.42	n.d.	429.10
(La/Sm)$_N$	7.91	6.72	6.71	n.d.	13.38	7.11	85.58	7.25	4.96	2.73	n.d.	19.48
(Gd/Yb)$_N$	2.50	2.89	2.90	n.d.	2.13	2.23	0.50	2.57	1.60	1.10	n.d.	2.32
Eu/Eu*	1.03	1.29	1.12	n.d.	1.08	1.00	6.73	1.04	0.96	0.53	n.d.	2.53

Rock type abbreviations:
D – diorite,
Do – diorite with oriented texture,
FM – foid-bearing monzonite,
FMD – foid-bearing monzodiorite,
FS – foid-bearing syenite,
G – granite,
L – lamprophyre,
M – monzonite,
Mo – monzonite with oriented texture,
MDo – monzodiorite with oriented texture,
MG – monzogranite,
PlPxH – plagioclase-bearing pyroxene hornblendite,
QM – quartz monzonite,
S – syenite
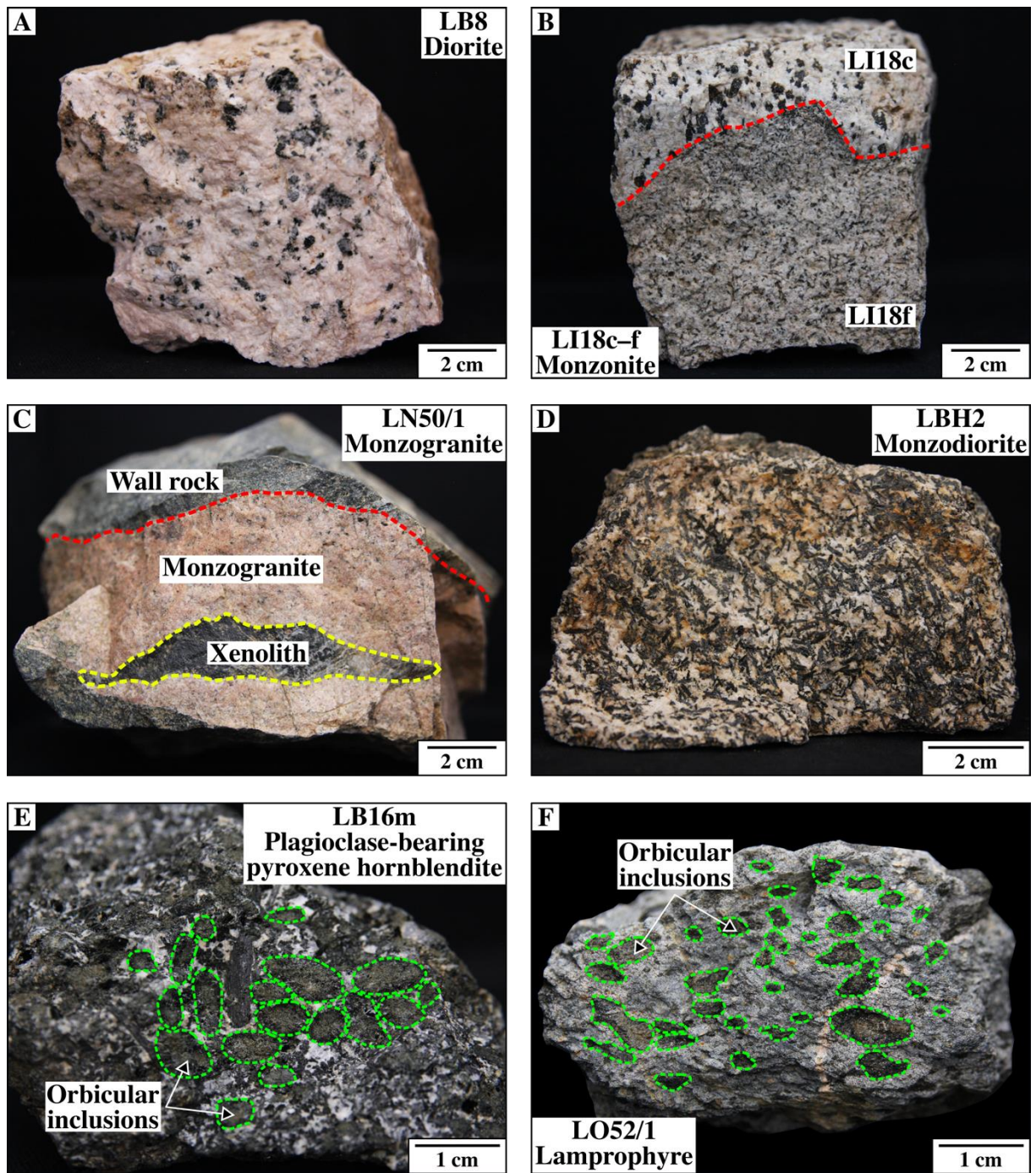
Fig. IV.3. Macroscopic textural characteristics of the studied rocks. (A) Disseminated biotite flakes in diorite. (B) Contact (highlighted by the red dashed line) between monzonite and monzonite dyke. (C) Hornfels xenolith in monzogranite. The margin of the xenolith is marked in yellow, while the contact of monzogranite and the metamorphic wall rock is highlighted by the red dashed line. (D) Isolated and clot-forming amphibole crystals in monzodiorite. (E) and (F) Orbicular inclusions with a clinopyroxene core rimmed by amphibole and biotite of the host (marked by green dashed lines) in plagioclase-bearing pyroxene hornblendite and lamprophyre, respectively
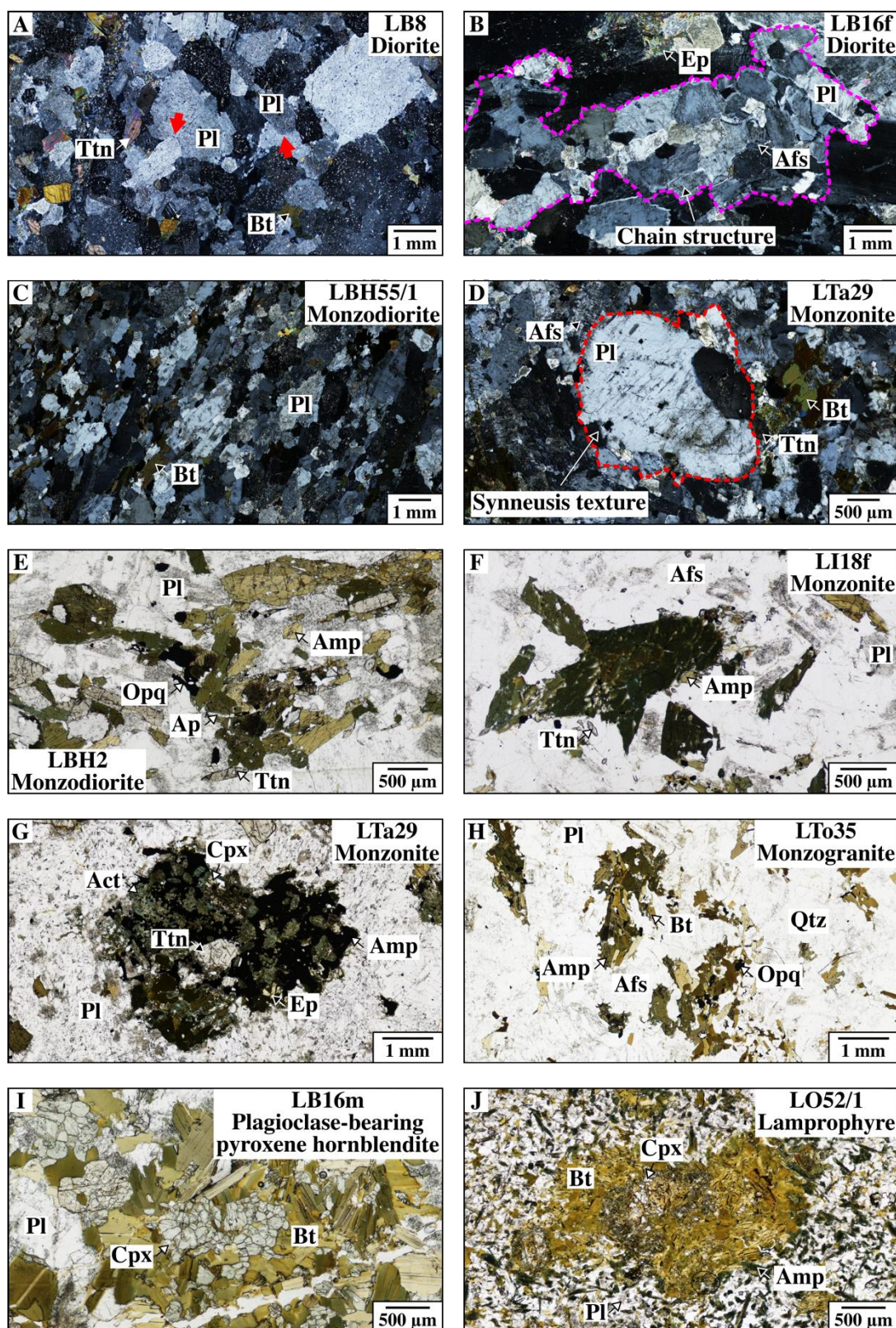
Fig. IV.4. Characteristic micro-scale textural features of the studied rocks. (A) Impinging plagioclase crystals (marked by red arrows), +N (crossed polars). (B) Chain structure of plagioclase crystals in parallel orientation (the aggregate is highlighted by the pink dashed line), +N. (C) Parallelly-aligned biotite and plagioclase, +N. (D) Plagioclase megacryst with smaller-sized grains in synneusis relation (the cluster is highlighted by the red dashed line), +N. (E) and (F) Amphibole aggregates, 1N (plane-polarized light). (G) Polymineralic *AmpCpxTtnOpqBt* aggregate, 1N. (H) *AmpBt* clusters, 1N. (I) and (J) Orbicular inclusions with a clinopyroxene core rimmed by amphibole and biotite crystals, 1N. Clot type abbreviations: *AmpBt* – amphibole + biotite cluster, *AmpCpxTtnOpqBt* – amphibole + clinopyroxene + titanite + opaque minerals ± biotite aggregate. The names of the minerals were abbreviated following the classification scheme of Whitney and Evans (2010)

IV.3.2. Bulk-rock major and trace element analyzes

The representative felsic rock samples were powdered and analyzed at the Bureau Veritas Mineral Laboratories (ACMELabs, Vancouver, Canada). The whole-rock composition of plagioclase-bearing pyroxene hornblendite and lamprophyre was not determined (they were only characterized petrographically), as comprehensive data for similar rock types are readily available in previous research (e.g., Batki et al., 2014; Pál-Molnár et al., 2015a). Major element concentrations were determined by ICP-ES (detection limit: 0.01–0.04 wt%), whereas trace element compositions were measured using ICP-MS. Samples were split and a 0.2 g sample was used for $LiBO_2/Li_2B_4O_7$ fusion decomposition for ICP-ES and a 0.2 g sample for ICP-MS. The STD SO-19 and QUARTZ_KRA (pure quartz) internal geological reference materials were applied to control the analytical accuracy (better than ± 1.5%). Duplicate samples were used in each analytical set to verify the precision (better than 0.5% for the repeated measurements). After ignition at 1000°C for 4 hours, the weight difference was applied to calculate the loss on ignition (LOI).

IV.3.3. *In situ* mineral major and trace element analyzes

Mineral major and trace element concentrations were determined on crystals from polished thin sections (30 μm thickness). Minerals selected for analysis were those that are common in almost all rock types of the northern part of the massif (amphibole, clinopyroxene, and plagioclase) – including amphibole and clinopyroxene crystals of plagioclase-bearing pyroxene hornblendite (LB16m) and lamprophyre (LO52/1) (Figs. IV.3E, F and IV.4I, J) that were measured for comparison. Mafic and felsic minerals in different textural positions (occurring as isolated crystals in the "groundmass" as well as clot-forming minerals) were selected to track any compositional differences. It must be elucidated that the term "groundmass" used in this paper refers to the main mass of the host rock: the holocrystalline, phaneritic, and generally felsic mineral-rich domain that encircles mafic crystal clusters.

Zonation and compositional variation of the minerals were investigated optically (by transmitted light and back-scattered electron microscopy) and characterized quantitatively (by SEM BSE, EMPA, and LA-ICP-MS). An AMRAY 1830 SEM coupled with an EDAX PV 9800 EDS detector at the Department of Petrology and Geochemistry, Eötvös Loránd University, Budapest, Hungary was applied to acquire backscattered electron images (Fig. IV.5). The BSE images along with microphotographs were implemented to reveal compositional zonation and to determine the position of the analytical spots. In the absence of optical and SEM zoning, the analytical points (core, transition, rim) were located based on geometric parameters.
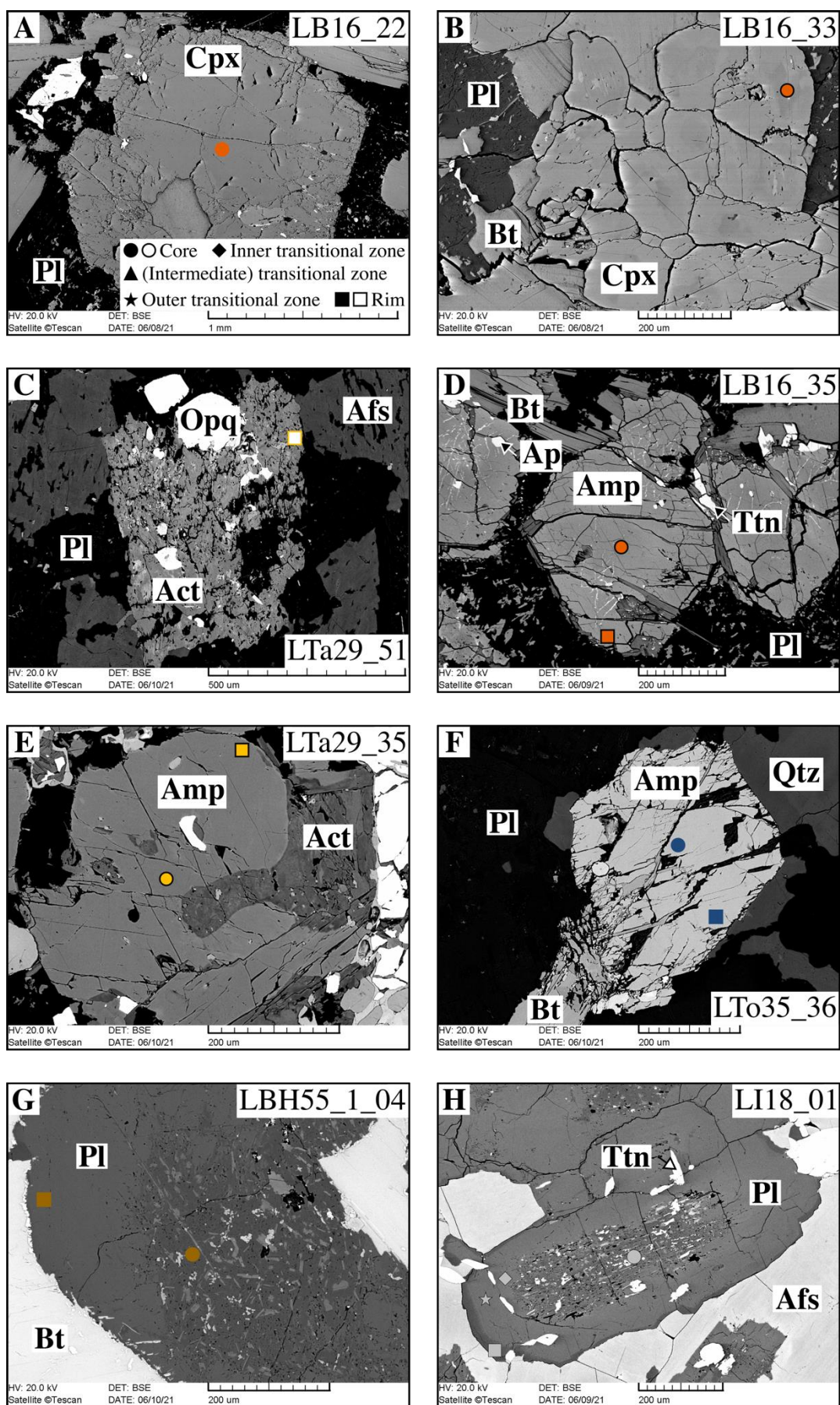
Fig. IV.5. Representative SEM images of the studied crystals, showing where the individual analyzes were performed. Symbols with black rim mark analyzes on clot-forming crystals. (A) and (B) Groundmass and orbicular inclusion-derived clinopyroxene, respectively. (C) Groundmass actinolite. (D) and (E) Clot-forming amphibole. (F) Isolated amphibole. (G) Reversely-zoned and (H) complexly-zoned plagioclase crystal

Both major- and minor element concentrations of minerals were determined by electron microprobe in wavelength dispersive mode, carried out at the Institut des Sciences de la Terre d'Orléans – Centre National de la Recherche Scientifique (ISTO-CNRS), Orléans, France, using a Cameca SX Five electron microprobe, operated at an acceleration voltage of 15 kV and a beam current of 10 nA, utilizing a focused beam. The elements analyzed for all sample phases (10 and 5 seconds counting times on peaks and background, respectively) were Si, Ti, Al, Mg, Mn, Fe, Ca, Na, and K, which are reported as oxide concentrations, with Fe recorded as FeO. Calibration standards were natural and synthetic mineral phases (albite: Si, Na; Al_2O_3: Al; andradite: Ca; Fe_2O_3: Fe; $MnTiO_3$: Mn, Ti; olivine: Mg; orthoclase: K), of which albite, andradite, and olivine were also repeatedly analyzed as quality control.

Trace element concentrations (including REE) were determined by LA-ICP-MS, employing a RESOlution SE laser ablation system connected to an Agilent 8900 QQQ inductively-coupled plasma mass spectrometer at the Institut des Sciences de la Terre d'Orléans – Centre National de la Recherche Scientifique (ISTO-CNRS), Orléans, France. The same spots were analyzed as for the EMPA. Ablations were performed with a round laser beam of different diameters (amphibole: 20 and 30 μm; clinopyroxene: 30 μm; plagioclase: 20, 30, and 50 μm) with a frequency of 10 Hz and a fluence of 4 J cm^{-2} on the sample surface. Ablations were carried out in a mixed Ar (~0.9 l/min) and He (~400 ml/min) atmosphere. The ICP-MS was operated at 1480 W. For the mafic minerals and plagioclase, 33 and 22 isotope concentrations were measured, respectively, each with a dwell time of 10 ms. Three analyzes of the external standard NIST610 were followed by the analysis of the quality control reference materials NIST612 and BCR-2G as well as twelve analyzes of samples unknown in sequences of 100–200 points. Each analysis comprised a measurement of 20 s gas blank before 30 s laser ablation and a 10 s washout at the end. The ablation signals were individually screened for contaminated analyzes. To determine trace element concentrations off-line, the Glitter software (van Achterbergh et al., 2001) was used with a linear extrapolation across external standards and SiO_2 determined by electron microprobe as the internal standard. Reference material compositions are the preferred values provided at GeoReM (http://georem.mpch-mainz.gwdg.de/).

IV.4. Results

IV.4.1. Whole-rock major and trace element data

Results of the bulk-rock geochemical analyzes can be found in Table IV.1. Based on their Chemical Index of Alteration (CIA; Nesbitt and Young, 1982), the studied samples were either subjected to no weathering or weak weathering. The SiO_2 composition of the analyzed rocks covers a wide spectrum (53.4–75.7 wt%; Fig. IV.6A). Due to their high Na_2O+K_2O content (ranging from 8.4 to 10.9 wt%), the studied rocks are classified as alkaline. In the TAS diagram, the samples are aligned along a single compositional array, which involves the monzonite, syenite, and quartz monzonite compositional fields. The only exception is sample LN50/1 (monzogranite), which deviates from this trend (Fig. IV.6A).

Although feldspathoids were not identified during our petrographic investigations, CIPW norm calculations imply that most of the analyzed rocks – with the exception of the quartz-bearing samples LTo35 and LN50/1 (monzogranites) – are nepheline-normative (0.4–3.7 vol%) and their composition plots in the "foid-bearing" field in the cation norm classification diagram (Streckeisen and Le Maitre, 1979; Fig. IV.6B; Table IV.1).

There is a negative correlation between the concentration of SiO_2 and Fe_2O_3, MgO, TiO_2, MnO, and CaO (Fig. IV.6D–H). In contrast, the data points for Na_2O and K_2O are scattered (Fig. IV.6I, J).

The differentiation index (D.I., the sum of normative quartz, albite, orthoclase, nepheline, kaliophilite, and leucite; Cross et al., 1902) varies from 79.5 [LBH2 (monzodiorite)] to 96.6 [LN50/1 (monzogranite)] (Table IV.1).

Three trends can be identified according to the chondrite-normalized REE patterns of the rocks (Fig. IV.7A, C, E): (a) LHH23/1 (monzonite) and LBH55/1 (monzodiorite) show a strong enrichment in light rare earth elements (LREEs) and a slight enrichment in heavy rare earth elements (HREEs) (Table IV.1). These samples have the highest positive Eu anomaly (Eu/Eu* = 2.5–6.7; Fig. IV.7A); (b) the majority of the analyzed samples [LB8 and LB16f (diorites), LI18c–f and LTa29 (monzonites) and LTo35 (monzogranite)] have overlapping, parallel REE patterns (Fig. IV.7C) and an insignificant Eu anomaly (Eu/Eu* ~1). Samples LB8 and LB16f (diorites) are the exceptions since they have a slight positive Eu/Eu* value (1.1 and 1.3, respectively). The rocks of this trend differ only in their ΣREE concentration (104–523 ppm). Similarly to the rocks of trend (a), the latter are also characterized by a marked enrichment in LREEs and a minor increase in the HREE content (Table IV.1); whereas (c) sample LN50/1 (monzogranite) has a distinct negative Eu anomaly (Eu/Eu* = 0.53; Fig. IV.7E). It shows a modest enrichment in both LREEs and HREEs (Table IV.1).
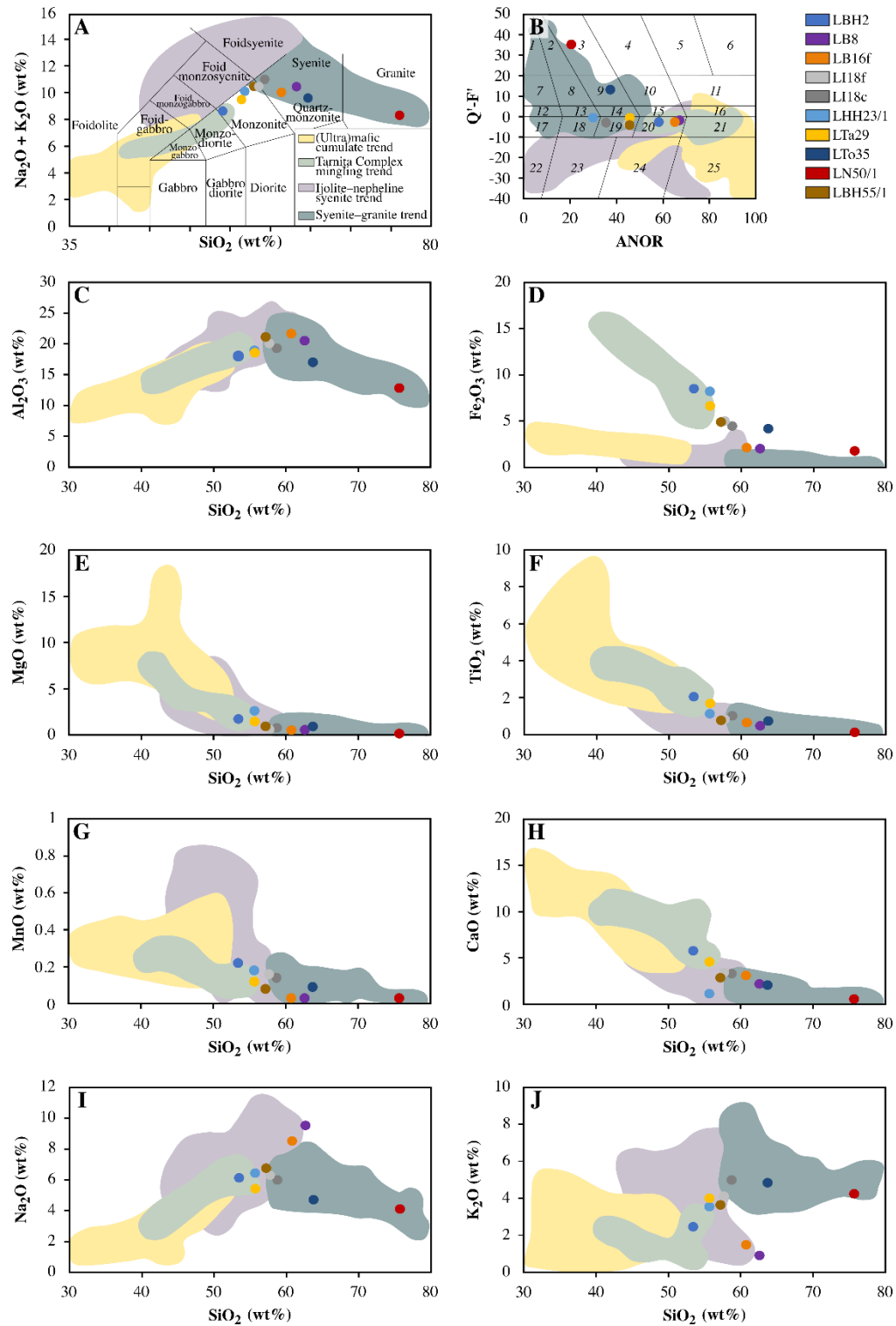
Fig. IV.6. (A) Classification of the examined rocks based on the total alkali versus SiO_2 diagram (after Le Maitre et al., 2002). (B) Classification of the studied rocks in the cation norm diagram for plutonic rocks (after Streckeisen and Le Maitre, 1979). Field numbers of the diagram: 1 – alkali feldspar granite, 2 – syenogranite, 3 – monzogranite, 4 – granodiorite, 5 – tonalite, 6 – calcic tonalite, 7 – quartz alkali feldspar syenite, 8 – quartz syenite, 9 – quartz monzonite, 10 – quartz monzodiorite/monzogabbro, 11 – quartz diorite/quartz gabbro, 12 – alkali feldspar syenite, 13 – syenite, 14 – monzonite, 15 – monzodiorite/monzogabbro, 16 – diorite/gabbro, 17 – foid-bearing alkali feldspar syenite, 18 – foid-bearing syenite, 19 – foid-bearing monzonite, 20 – foid-bearing monzodiorite/monzogabbro, 21 – foid-bearing diorite/gabbro, 22 – foid syenite, 23 – foid monzosyenite, 24 – foid monzodiorite/monzogabbro, 25 – foid diorite/gabbro. (C) to (J) Major element oxides plotted against SiO_2 for the analyzed samples. Whole-rock data from Kovács and Pál-Molnár (2005), Batki et al. (2014, 2018), Pál-Molnár et al. (2015a, b), and Pál-Molnár (2021) are given for comparison, highlighted by the colored fields. Symbol colors are the same for the samples in all figures, which are given in (B)

The same three trends can be distinguished in the chondrite-normalized spider diagrams (Fig. IV.7B, D, F): the rocks of trend (a) are characterized by elevated La, Sr, Zr, Hf, and Eu contents. Negative anomalies occur in Ta, Nd, Sm, and Tb (Fig. IV.7B); the rocks belonging to trend (b) show a slight positive anomaly in Nb and Ta (with some samples showing a positive Zr and Hf anomaly as well) and a negative anomaly in U, Nd, and Tm (Fig. IV.7D); while trend (c) has positive Ta and Hf along with negative Nb, Sr, and Eu anomalies (Fig. IV.7F).
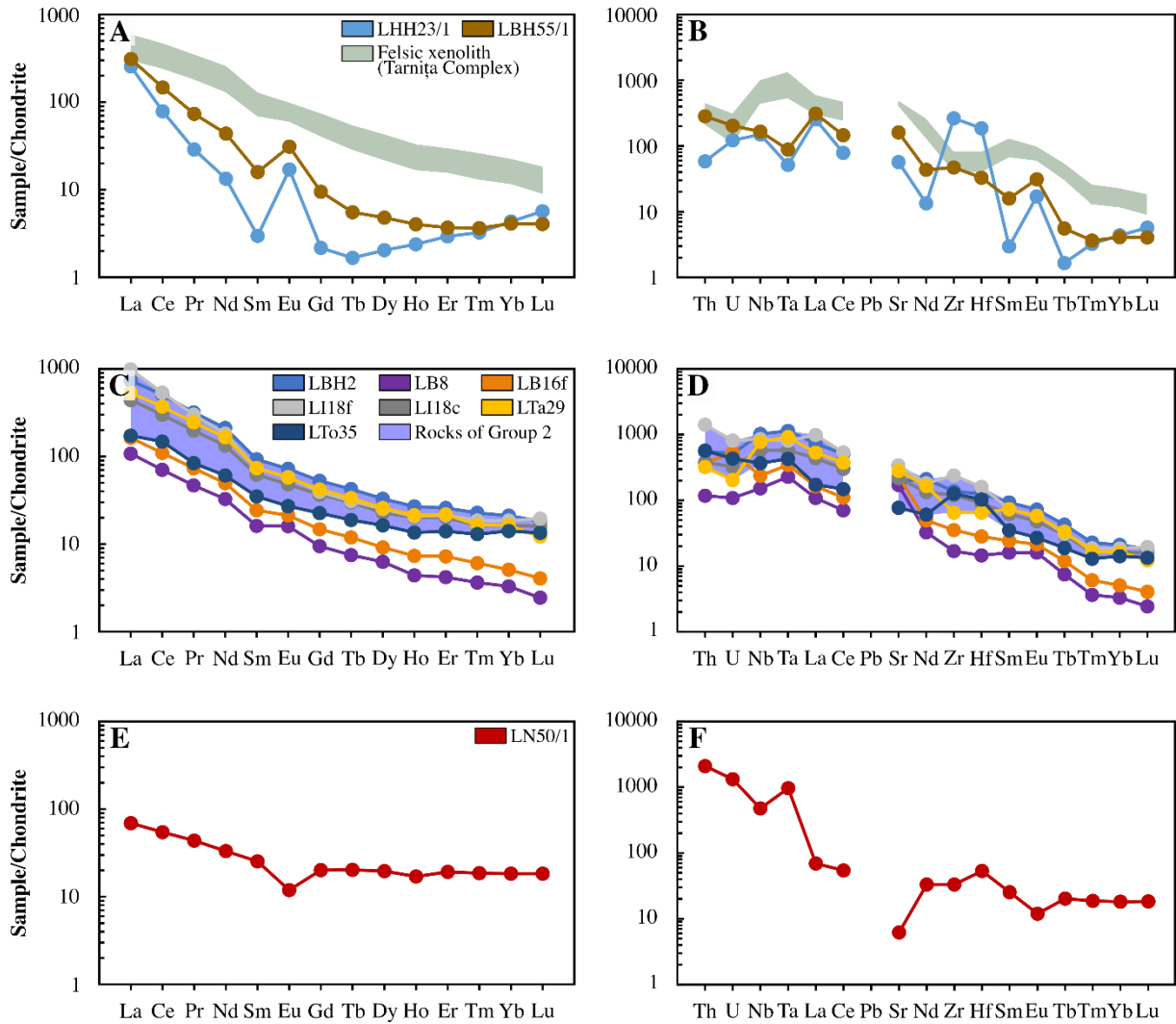
Fig. IV.7. Chondrite-normalized REE diagrams (left) and multielement spider diagrams (right) for the analyzed rocks. For comparison, the shaded fields in (A) and (B) cover the whole-rock compositions of felsic xenoliths in the Tarnița Complex from Pál-Molnár (2021). The colored fields in (C) and (D) represent the bulk-rock compositions of Group 2 rocks from this study. The normalizing values are after Sun and McDonough (1989)

IV.4.2. Mineral textures and chemistry

IV.4.2.1. Clinopyroxene

The most important textural features of the studied clinopyroxene crystals are summarized in Supplementary Table IV.2. The analyzed clinopyroxenes were classified according to Morimoto et al. (1988) (Supplementary Fig. IV.1). Supplementary Table IV.3 contains the major and trace element compositions of the analyzed crystals.

Clinopyroxenes of different textural positions in LB16m (plagioclase-bearing pyroxene hornblendite) have distinct geochemical compositions (Fig. IV.8; Supplementary Fig. IV.1): (a) groundmass clinopyroxene (Fig. IV.5A) is aluminian diopside ($Wo_{48}En_{37}Fs_{15}$; mg# = 0.77) with a convex REE pattern (Fig. IV.8A). It is characterized by high Zr and Hf concentrations and low Sm, Eu, and Tb contents (Fig. IV.8B). Clot-forming clinopyroxene in LTa29 (monzonite; Fig. IV.4G) exhibits an overlapping composition (Fig. IV.8A, B; Supplementary Fig. IV.1); (b) clinopyroxene in the center of the orbicular inclusions (Figs. IV.4I and IV.5B) is diopside ($Wo_{48}En_{41}Fs_{11}$; mg# = 0.85). Its REE pattern is concave (Fig. IV.8C); Sm, Eu, and Tb are present in high concentrations (Fig. IV.8D). Groundmass clinopyroxene and clinopyroxene in the center of the orbicular inclusions in LO52/1 (lamprophyre; Fig. IV.4J) are of comparable composition (Fig. IV.8C, D; Supplementary Fig. IV.1).
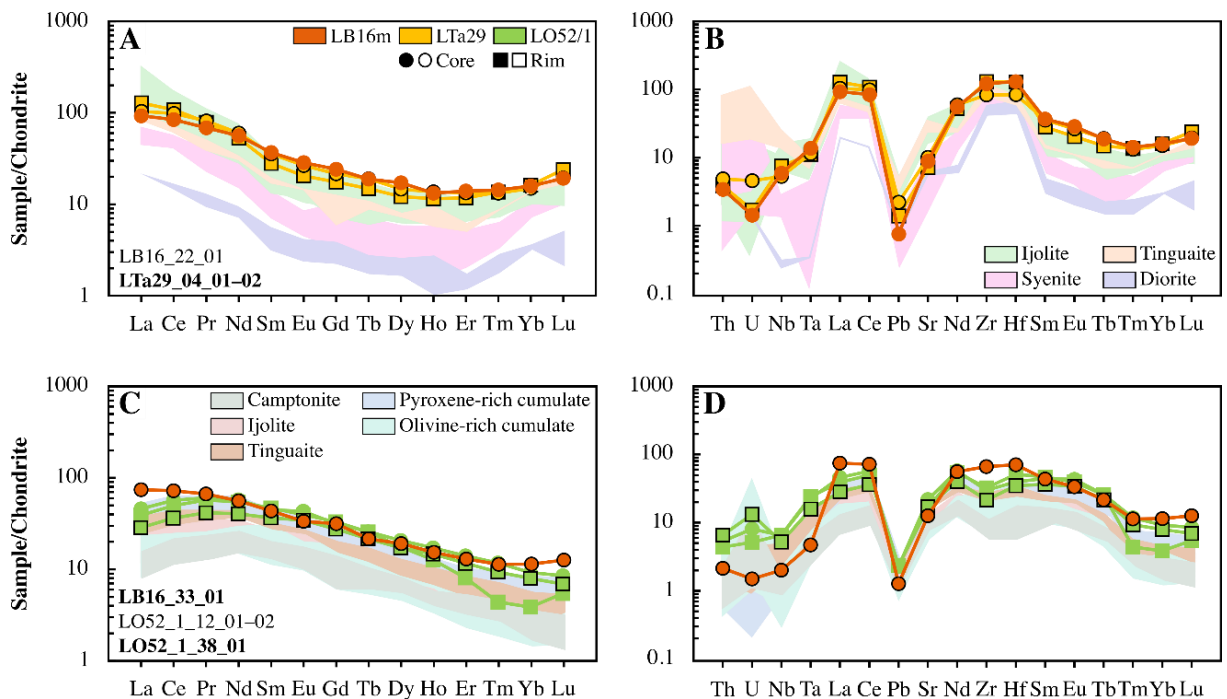
Fig. IV.8. Chondrite-normalized REE diagrams (left) and multielement spider diagrams (right) for the selected, representative clinopyroxene compositions. (A) and (B) Groundmass clinopyroxene in LB16m (plagioclase-bearing pyroxene hornblendite) and clot-forming clinopyroxene in LTa29 (monzonite). (C) and (D) Orbicular inclusion-derived clinopyroxene in LB16m (plagioclase-bearing pyroxene hornblendite) along with isolated and orbicular inclusion-derived clinopyroxene in LO52/1 (lamprophyre). For comparison, the shaded fields show the compositional trends of clinopyroxenes from Batki et al. (2014, 2018) and Pál-Molnár et al. (2015a). The normalizing values are according to Sun and McDonough (1989)

IV.4.2.2. Amphiboles

Based on their textural characteristics and geochemical composition, the examined amphiboles can be categorized as primary and secondary.

The analyzed actinolite crystals are characterized by Si > 7.3 and exhibit depletions in Na, K, Fe, and Ti, thereby implying that they were produced by subsolidus reactions (Leake, 1978; Chivas, 1981; Hendry et al., 1985).

Supplementary Table IV.4 provides a summary of the textural characteristics of the investigated actinolites (Fig. IV.5C). The nomenclature of Leake et al. (1997) was applied to classify the analyzed crystals. Major and trace element compositions of the studied actinolites from sample LTa29 (monzonite) are listed in Supplementary Table IV.5.

Actinolite is characterized by a mg# varying between 0.40 and 0.76 and the amount of Al^{IV} is 0.0–0.7 atoms per formula unit (apfu) (Supplementary Fig. IV.2). The chondrite-normalized REE pattern of actinolite exhibits a marked enrichment in LREEs and a slighter enrichment in HREEs (Fig. IV.9; Supplementary Table IV.5). The REE as well as the trace element patterns of the analyzed crystals, mostly overlap, with a general enrichment in Zr and Hf and a negative anomaly in U and Pb (Fig. IV.9); however, there are some clot-forming crystals with a pronounced negative Eu anomaly (Fig. IV.9C) or with elevated U and Pb contents (Fig. IV.9D).
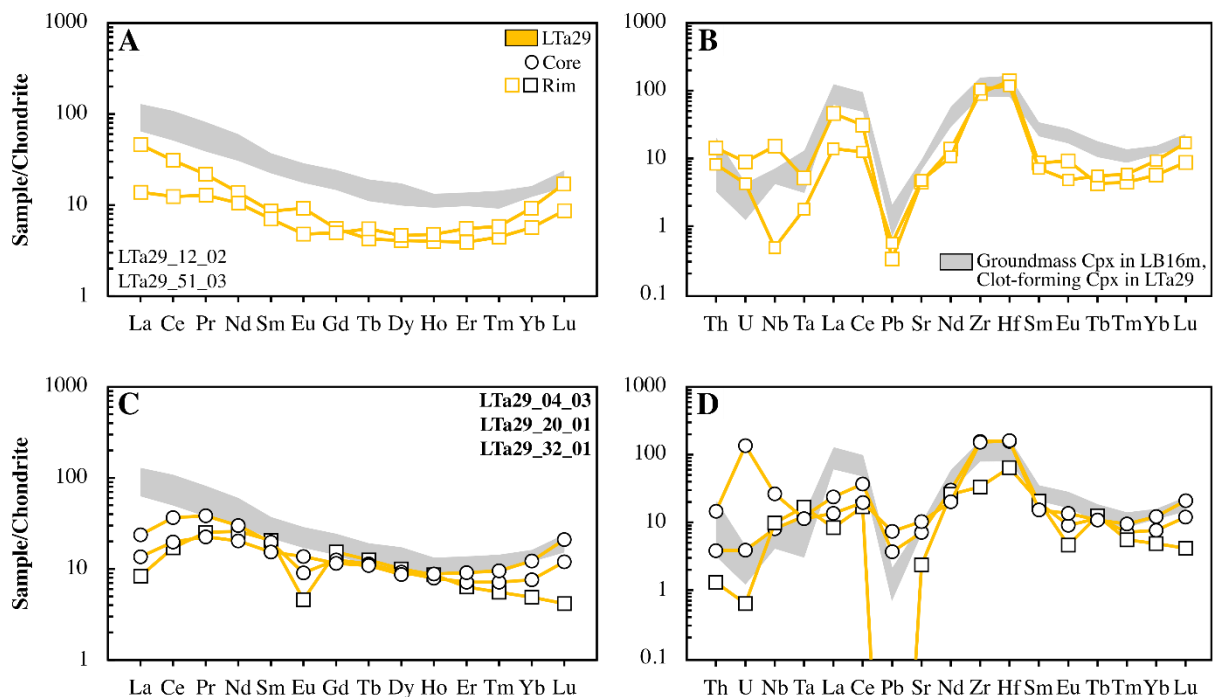
Fig. IV.9. Chondrite-normalized REE diagrams (left) and multielement spider diagrams (right) for the analyzed actinolite crystals from sample LTa29 (monzonite). (A) and (B) Compositions of the isolated, groundmass actinolite crystals. (C) and (D) Compositions of the clot-forming actinolites. The shaded fields show the compositional trends of groundmass clinopyroxene in LB16m (plagioclase-bearing pyroxene hornblendite) and clot-forming clinopyroxene in LTa29 (monzonite) for comparison. The normalizing values are according to Sun and McDonough (1989)

The other group of the analyzed crystals generally has a maximum Si < 7.3 and they are not depleted in elements, such as Na, K, Ti, and Fe, classifying them as truly magmatic (Leake, 1978).

The major textural features of the studied magmatic amphiboles are listed in Supplementary Table IV.6. The analyzed crystals were classified according to Leake et al. (1997). Major and trace element compositions of the magmatic amphiboles are summarized in Supplementary Table IV.7.

The studied magmatic amphiboles exhibit significant intercrystalline variations in their major and trace element concentrations and can be classified into three separate types in line with their composition.

Type I is represented by the isolated and clot-forming amphibole (hastingsite) of LB16m (plagioclase-bearing pyroxene hornblendite; Fig. IV.5D). The mg# (0.5–0.6) and Al^{IV} (1.8–2.0 apfu) composition of the crystals show limited variations (Supplementary Fig. IV.2). Amphiboles of this group have straight REE patterns with a continuous decrease from LREEs to HREEs (Fig. IV.10A). Minor negative Eu (Eu/Eu^* min. 0.77) and Tm together with significant negative U and Pb anomalies are the characteristic features of this group (Fig. IV.10B). Based on their major and trace element compositions (Figs. IV.10A, B and IV.11; Supplementary Fig. IV.2), groundmass and megacrystic amphiboles (Fe-kaersutite and Mg-hastingsite + Fe-pargasite, respectively) of sample LO52/1 (lamprophyre) can also be ascribed to this group.

The second amphibole type (Type II) is represented by hastingsite [LBH2 (monzodiorite), LI18c–f (monzonites)], Mg-hastingsite and Fe-pargasite [LTa29 (monzonite); Fig. IV.5E]. The mg# varies between 0.2 and 0.5 and the amount of tetrahedral aluminium is 1.8–2.2 apfu, making it indistinguishable from Type I amphiboles (Supplementary Fig. IV.2). Nevertheless, this amphibole variety is characterized by a convex, U-shaped REE pattern with a marked enrichment in LREEs and a relatively limited increase in the HREE concentration (Supplementary Table IV.7). Amphiboles of this group show negative anomalies in U, Ta, and Pb along with positive anomalies in Nb, Zr, and Hf (Fig. IV.10C–H).

The third amphibole type (Type III) is characteristic of sample LTo35 (monzogranite) exclusively (Fig. IV.5F). It is Fe-hornblende with limited variations in the mg# (0.37–0.39) and Al^{IV} (1.3–1.4 apfu) concentrations, forming a unique group in the mg# *vs*. Al^{IV} diagram (Supplementary Fig. IV.2). It has a distinct, seagull-shaped REE pattern with a marked negative Eu anomaly (Fig. IV.10I). Pb and Zr also exhibit negative anomalies (Fig. IV.10J). Certain elements, for example, Nb, Ta, Nd, Sm, and Tb, are present in anomalously high concentrations (Figs. IV.10J and IV.11B).
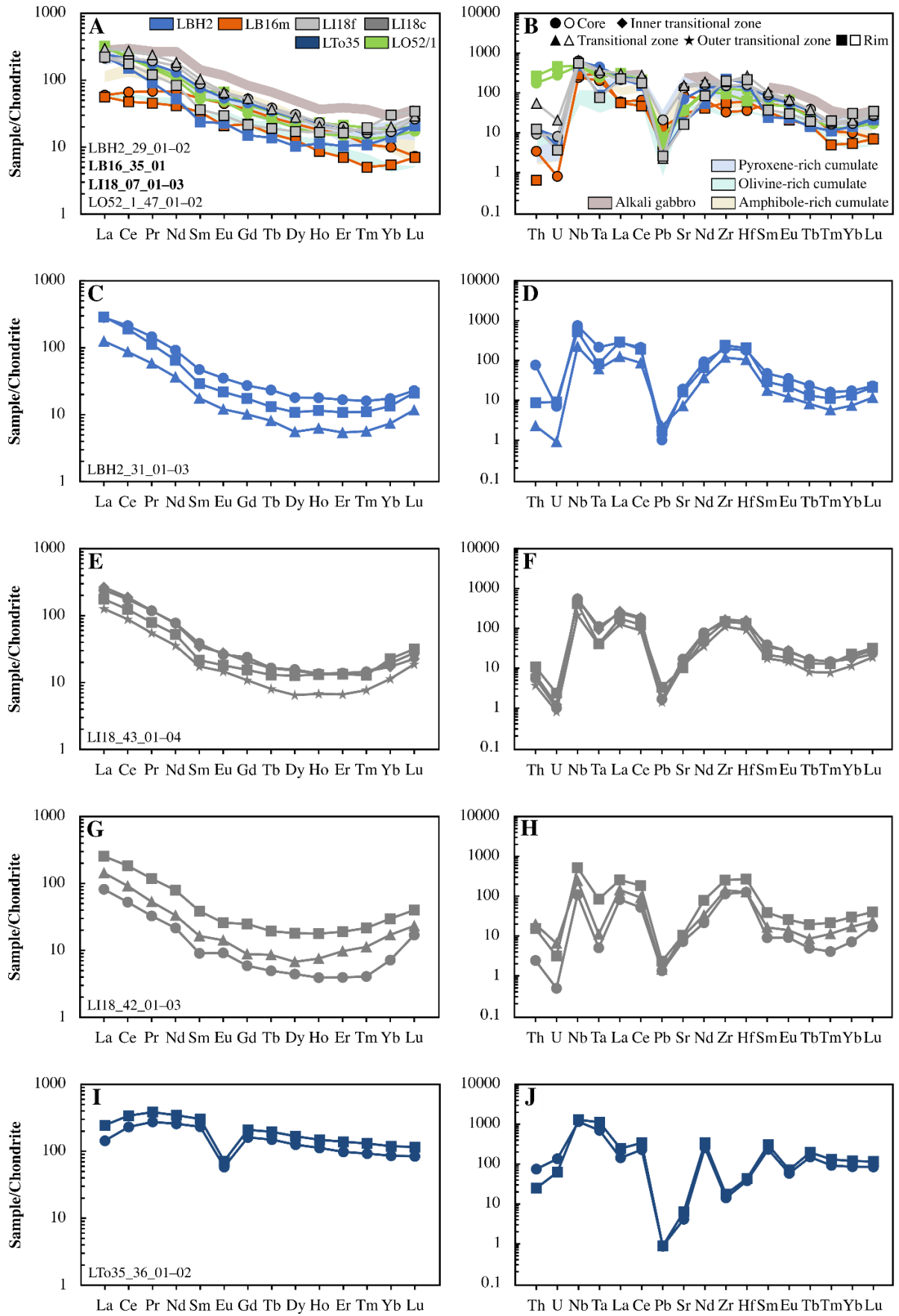
Fig. IV.10. Chondrite-normalized REE diagrams (left) and multielement spider diagrams (right) for the representative magmatic amphibole crystals. Symbols with a black rim mark data of the clot-forming crystals. The shaded fields show the compositional trends of cumulus amphibole (Pál-Molnár et al., 2015a) and amphibole of alkali gabbro (Morogan et al., 2000) for comparison. The normalizing values are according to Sun and McDonough (1989)

In addition, complexly-zoned amphibole crystals with zones characterized by different REE and trace element patterns and element concentrations are also present in the studied rocks (Figs. IV.10 and IV.11).
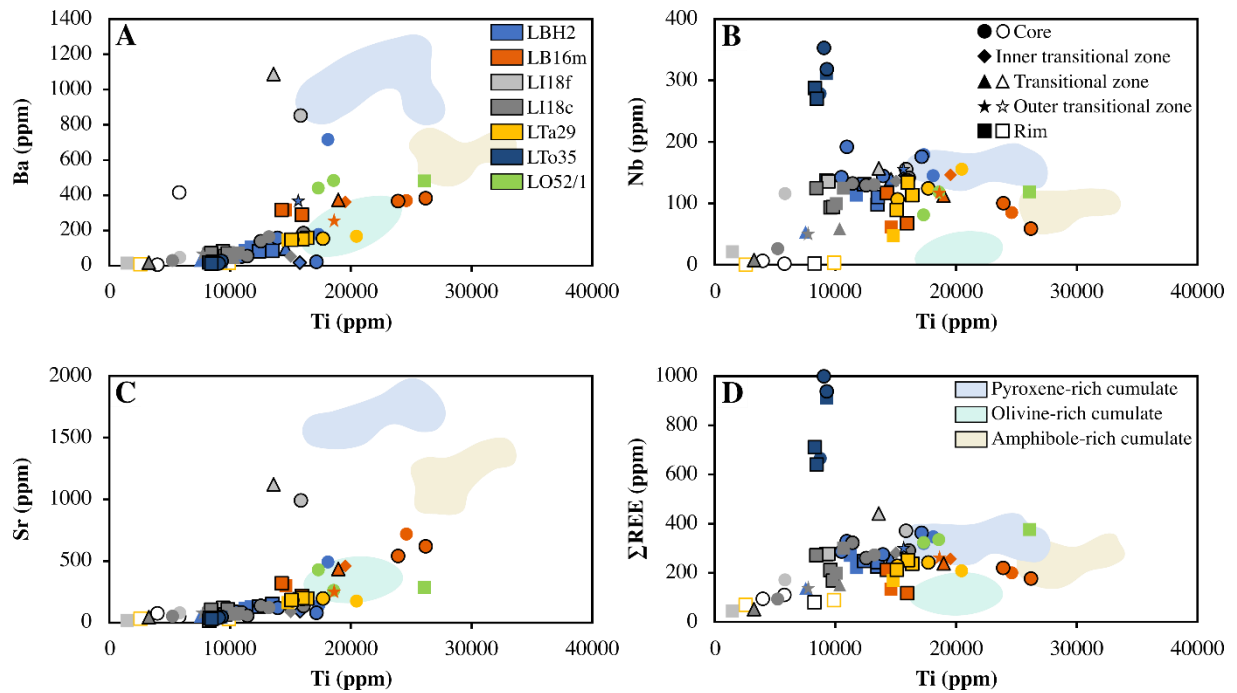
Fig. IV.11. Trace element compositions of the analyzed amphibole crystals. Actinolite data are marked by empty symbols. Data of the aggregated crystals are identified by symbols with a black rim. The shaded fields show the compositional trends of cumulus amphibole (Pál-Molnár et al., 2015a) and amphibole of alkali gabbro (Morogan et al., 2000) for comparison. The normalizing values are according to Sun and McDonough (1989)

IV.4.2.3. Plagioclase

The main textural characteristics of the analyzed plagioclase crystals are summarized in Supplementary Table IV.8. The studied rocks are made up of plagioclase of variable composition (albite and oligoclase; Supplementary Fig. IV.3; Supplementary Table IV.9). It has to be noted that in some zones, the concentration of the analyzed rare earth elements was below the detection limit of the analyzes, resulting in the anomalously low ΣREE value of these domains.

Clear groundmass plagioclase (Type I) in sample LBH2 (monzodiorite) shows no compositional zonation: its core and rim have similar major and trace element concentrations. Both zones have high Eu/Eu[*] values (core: 3.7 and rim: 5.3; Fig. IV.12A; Supplementary Table IV.9).

The normally-zoned plagioclase (Type II) megacryst in LTa29 (monzonite) has the highest anorthite content among the analyzed plagioclase samples (Fig. IV.13A, B; Supplementary Fig. IV.3; Supplementary Table IV.9). The different zones are characterized by distinct REE concentrations (Fig. IV.12B).

Groundmass plagioclase with a sericitized core (Fig. IV.5G) in LBH55/1 (monzodiorite) exhibits reverse zoning (Type III): its rim is relatively enriched in anorthite, FeO, and TiO_2 (Fig. IV.13A, B) and exhibits a marked positive Eu anomaly (Fig. IV.12C; Supplementary Table IV.9).

The complexly-zoned groundmass plagioclase with a sericitized core (Fig. IV.5H) in LI18f (monzonite) is characterized by two (inner and outer) transitional zones that are relatively enriched in An content, FeO, TiO_2, and Ba (Fig. IV.13; Supplementary Table IV.9). The REEs exhibit a continuous decrease from the core towards the rim (Fig. IV.12D).

The core and the outer transitional zone of the complexly-zoned plagioclase with a clear core in LI18f (monzonite) exhibit elevated anorthite and FeO contents, whereas the inner transitional zone and the rim are characterized by lower anorthite and FeO concentrations (Fig. IV.13A; Supplementary Table IV.9). The inner transitional zone is the most enriched in REEs and shows no Eu anomaly (Fig. IV.12E).
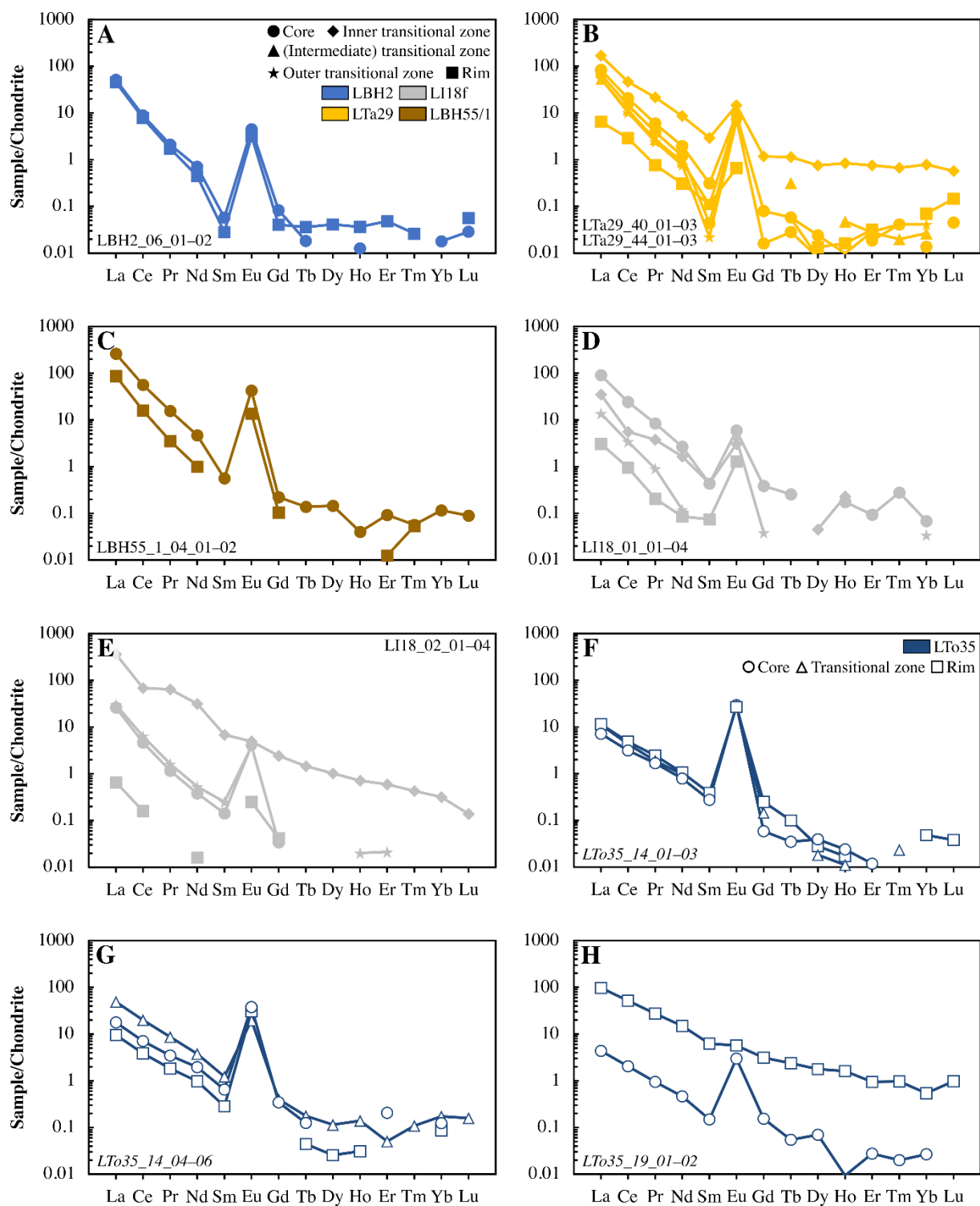
Fig. IV.12. Chondrite-normalized REE patterns of the analyzed isolated plagioclase crystals. (A) Clear, unzoned plagioclase. (B) Normally-zoned megacryst. (C) Reversely-zoned plagioclase with a sericitized core. (D) Complexly-zoned plagioclase with a strongly sericitized core. (E) Complexly-zoned plagioclase with a clear core. (F) Large, complexly-zoned plagioclase crystal with an inclusion-rich and strongly sericitized core, in synneusis. (G) Smaller-sized, normally-zoned plagioclase with a sericitized core, in synneusis. (H) Clear, unzoned plagioclase crystal, in synneusis. The normalizing values are according to Sun and McDonough (1989)

The aggregated plagioclase crystals occurring in synneusis relation exhibit distinct zoning patterns.

The complexly-zoned crystals are characterized by a transitional zone with the highest anorthite content and the highest concentrations of TiO_2, La, and Ce (Fig. IV.13B, D; Supplementary Table IV.9). There is no systematic difference in the REE patterns of the zones (Fig. IV.12F).

The normally-zoned crystals have a core with the highest anorthite content as well as Sr and Ba concentrations among the aggregated crystals (Fig. IV.13B, C; Supplementary Fig. IV.3; Supplementary Table IV.9). The transitional zone is the most enriched in REEs (Fig. IV.12G).

The clear and unzoned crystals have a core and a rim with overlapping compositions (Supplementary Table IV.9); nevertheless, the core is characterized by a distinct positive Eu anomaly and significantly lower REE concentrations (Fig. IV.12H).
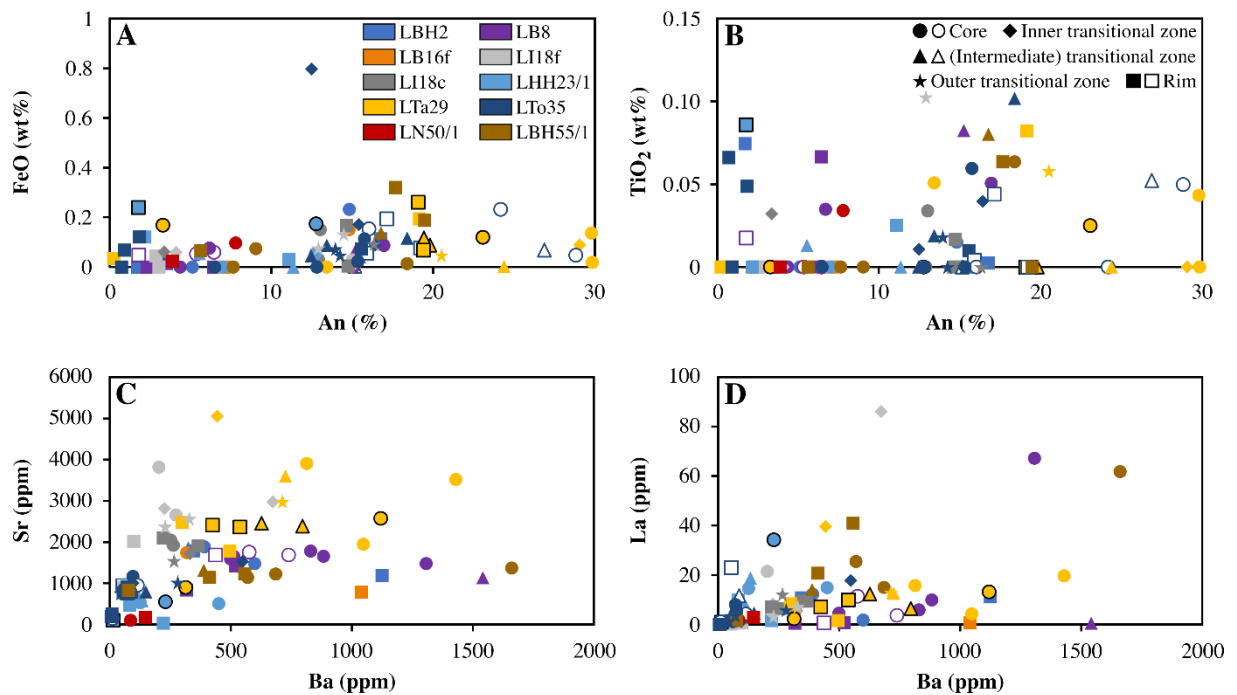
Fig. IV.13. Major and trace element compositions of the analyzed plagioclase crystals. The compositions of plagioclase crystals in synneusis are identified by empty symbols. Data of clot-forming plagioclase are marked by symbols with a black rim

IV.5. Discussion

In the following, results of the whole-rock analyzes along with clinopyroxene, amphibole, and plagioclase data will be interpreted in combination with microtextures and field observations. The aim is to provide an insight into the igneous history of the DAM and to identify the key processes during the evolution of the felsic suite in the northern part of the massif.

IV.5.1. Interpretation of the whole-rock major and trace element data

When combining our new bulk-rock data with the previously-published data sets in the TAS diagram, bulk-rock compositions of the recently analyzed samples partly overlap with and connect the trends of the rocks formed by magma mingling in the Tarniṭa Complex [diorite (*s.l.*), monzodiorite, and monzonite] and those of the syenite–granite series (Fig. IV.6A).

Based on their mineralogy and microtextures (Figs. IV.3A and IV.4A, B), LB8 and LB16f (diorites) were regarded as felsic cumulates (Group 1; Kiri et al., 2022). However, these samples are characterized by only a slightly positive Eu anomaly (Eu/Eu* = 1.3 and 1.1, respectively) along with a high differentiation index (D.I. = 95.3 and 95.0, respectively; Table IV.1). Furthermore, their REE patterns overlap with those of the other analyzed samples [Group 2 (Kiri et al., 2022): LBH2 (monzodiorite), LI18c–f and LTa29 (monzonites), and LTo35 (monzogranite)]; the only difference is the Eu anomaly and a slight depletion in HREEs (Fig. IV.7C). Therefore, based on their bulk-rock geochemical compositions, LB8 and LB16f (diorites) cannot be distinguished from the above-listed samples. The advanced cumulate (Kumar and Singh, 2014) nature of LB8 and LB16f (diorites) may explain the observed geochemical features.

Nevertheless, samples LHH23/1 (monzonite) and LBH55/1 (monzodiorite) (Group 2; Kiri et al., 2022) exhibit a different trend (Fig. IV.7A). Their high Eu/Eu* (6.7 and 2.5, respectively), in accordance with the low REE concentrations (ΣREE = 125 and 206 ppm, respectively), elevated La and Sr contents (Table IV.1), high abundance and the microtextures of plagioclase (e.g., chain structure, impingement; Kiri et al., 2022; Fig. IV.4C) point to the less-differentiated, early felsic cumulate nature of these rocks (Kumar and Singh, 2014). Based on the felsic xenoliths in the Tarniṭa Complex, Heincz et al. (2018) hypothesized the existence of a felsic cumulate pile in the DAM. Nevertheless, their bulk-rock composition (Pál-Molnár, 2021) is completely different from that of LHH23/1 (monzonite) and LBH55/1 (monzodiorite) (Fig. IV.7A, B). This implies that samples LHH23/1 (monzonite) and LBH55/1 (monzodiorite) represent the felsic cumulate phase of a magma that is different from that of the parental magma of the Tarniṭa Complex (Magma1; Batki et al., 2018).

The negative Eu anomaly (Eu/Eu* = 0.5) of sample LN50/1 (monzogranite; Fig. IV.7E) indicates that it crystallized from a highly differentiated (D.I. = 96.6), evolved melt or from an expelled residual liquid. The low REE concentration (ΣREE = 114 ppm) can be attributed to crustal assimilation (Kumar and Singh, 2014) and this is strongly supported by the oxygen isotope data of Ódri et al. (2020).

IV.5.2. Implications from the clinopyroxene data

Batki et al. (2018) identified two distinct parental magmas based on the compositions of the clinopyroxene populations: Magma1 (M1), with a basanitic composition, was identified as the parental magma of the (ultra)mafic cumulates in the Tarnița Complex, whereas Magma2 (M2) evolved to a phonolitic composition, giving rise to nepheline syenite.

Isolated clinopyroxene of LB16m (plagioclase-bearing pyroxene hornblendite; Fig. IV.5A) as well as clustered clinopyroxene of LTa29 (monzonite; Fig. IV.4G) exhibit a convex REE pattern (Fig. IV.8A) and a trace element composition (Fig. IV.8B) similar to that of the green clinopyroxene crystals (classified as Type II) reported from ijolite and tinguaite dykes as well as from diorite and syenite (Batki et al., 2018). They are considered to be antecrysts in the tinguaite dykes, diorite, and syenite (Batki et al., 2018). Nevertheless, LB16m (plagioclase-bearing pyroxene hornblendite) has a microtexture typical of cumulates and the isolated clinopyroxene is present as a primary, cumulus mineral (autocryst). Its composition does not overlap with that of the M1-derived clinopyroxene in the orbicular inclusions (Fig. IV.8; Supplementary Fig. IV.1). Thus, LB16m (plagioclase-bearing pyroxene hornblendite) represents the cumulate phase of a different parental magma (M2; Batki et al., 2018) from which the Type II diopsides crystallized.

The clinopyroxene of the orbicular inclusions in LB16m (plagioclase-bearing pyroxene hornblendite; Fig. IV.5B) and LO52/1 (lamprophyre), along with the sparse isolated crystals of LO52/1, have a concave REE pattern (Fig. IV.8C). Pál-Molnár et al. (2015a) reported similar clinopyroxene compositions from the olivine-rich as well as from the pyroxene-rich cumulates. The clinopyroxene described from the camptonite and tinguaite dykes, pyroxene-rich hornblendite, and ijolite enclave has very similar geochemical features (Batki et al., 2018; Fig. IV.8C, D). According to the classification of Batki et al. (2018), these clinopyroxenes are primitive diopsides (classified as Type I) that crystallized in a closed system from Magma1. However, in LB16m (plagioclase-bearing pyroxene hornblendite) and LO52/1 (lamprophyre), such primitive diopside crystals are present in the orbicular inclusions (Figs. IV.3E, F, IV.4I, J, and IV.5B). The fact that these diopsides occur in the aggregates, being mantled by amphibole and biotite crystals of the host, strongly implies their antecrystic origin. Periodic replenishment

of M1 triggered the transport of the previously-crystallized clinopyroxenes into a new magmatic environment. Lamprophyres are feasible candidates for transporting these crystals. Mechanical break-up of the inclusions led to the fragmentation of the aggregates and the scant occurrence of isolated clinopyroxene crystals in the lamprophyres.

The interaction between M1 and M2 magmas (Batki et al., 2018) is supported by the observation that orbicular inclusions with primitive diopside crystals from M1 magma were found in the M2 magma-derived LB16m rock (plagioclase-bearing pyroxene hornblendite; Figs. IV.3E, IV.4I, IV.5B, and IV.8C–H). Clinopyroxenes of M2 were also mobilized and distributed throughout the magmatic system. This resulted in the formation of mafic mineral aggregates, some of which still preserve relics of antecrystic clinopyroxene (Batki et al., 2018; Kiri et al., 2022; Figs. IV.4G and IV.14H). Actinolite (Fig. IV.5C) is characterized by high mg# values (0.4–0.8) that overlap with those of the Type II diopsides (mg# = 0.6–0.9). The REE and trace element patterns of actinolite (both groundmass and aggregated) in LTa29 (monzonite) are similar to those of the groundmass clinopyroxene in LB16m (plagioclase-bearing pyroxene hornblendite) and the aggregated diopside in LTa29 (monzonite) (Fig. IV.9). This suggests that the antecrystic clinopyroxene was replaced by actinolite at lower temperatures (e.g., Vernon, 1984, 1990; Castro and Stephens, 1992; Hibbard, 1995; Choe and Jwa, 2004; Fig. IV.14G, H).

IV.5.3. Implications from the amphibole data

The most important features of the analyzed amphibole crystals and their interpretation are summarized in Fig. IV.14.

The intra-crystalline major and trace element compositions of Type I amphiboles are practically identical and uniform in both LB16m (plagioclase-bearing pyroxene hornblendite; Fig. IV.5D) and LO52/1 (lamprophyre). Their REE and trace element patterns as well as trace element compositions completely overlap with those of the amphibole in olivine-rich, pyroxene-rich, and amphibole-rich cumulates (Pál-Molnár et al., 2015a) as well as in alkali gabbro (Morogan et al., 2000) (Figs. IV.10A, B and IV.11). This means that although M1 and M2 magmas can be distinguished on the basis of clinopyroxene data, amphiboles do not show such systematic differences in their composition. Thus, the M1 and M2-derived cumulus amphibole crystals (Type I; Fig. IV.14A) are indiscernible from each other.

Type II amphiboles are represented by groundmass amphibole in LI18f, clot-forming amphibole in LI18c as well as isolated and aggregated amphiboles in LTa29 (monzonites) (Fig. IV.14B). Although their major element composition is less distinct from that of the Type I amphiboles (Supplementary Fig. IV.2), they are characterized by a convex REE pattern. The homogeneous internal texture and composition of these amphiboles suggest that they formed

from the magma that currently hosts them (Barnes et al., 2016) and were not involved in crystal transfer and/or recycling.

Groundmass and clot-forming amphiboles of LTo35 (monzogranite; Figs. IV.4H, IV.5F, and IV.14C), which belong to Type III, form a distinct group in the mg# *vs*. Al^{IV} diagram (Supplementary Fig. IV.2). Amphiboles of both textural positions exhibit a distinct, seagull-shaped REE pattern (Fig. IV.10I). The marked negative Eu anomaly (Eu/Eu* = min. 0.2) and the highest ΣREE concentration (1000 ppm) of all analyzed crystals (Supplementary Table IV.7) indicate that these amphiboles are late crystallization products (Kumar and Singh, 2014). Depletions in Pb, Zr, and Eu (Fig. IV.10J) suggest that this amphibole variety was formed after alkaline feldspar, zircon, and plagioclase, respectively (Marks et al., 2004; Barnes et al., 2016; Tang et al., 2020). The homogeneous intra-crystalline composition (Fig. IV.10I, J) infers that the amphiboles of this group were not involved in crystal transfer/recycling.

Some crystals show variable intra-crystalline zoning patterns and trace element concentrations (Figs. IV.10A–H and IV.11; Supplementary Fig. IV.2), implying their different origins and crystallization under various circumstances. The REE patterns and the trace element compositions of the core as well as the core and transitional zone of some amphibole crystals in samples LBH2 (monzodiorite) and LI18f (monzonite) overlap with those of the Type I amphiboles of cumulate origin (Figs. IV.10A, B and IV.11). Nevertheless, their rims are characterized by a different, convex REE pattern (Fig. IV.10A), which is typical of the Type II amphiboles. This implies that the cores and the transitional zone originated from the cumulate pile of either M1 or M2 (Wiebe et al., 1997; Klaver et al., 2017) and were dragged either by convection currents or by dykes (e.g., LI18f) that deposited them in their current, relatively more felsic environment (Bea, 2010), where the rims were formed (Barnes et al., 2017) (Fig. IV. 14D). Compositions of the core of the LBH2_31 (Fig. IV.10C, D; Supplementary Table IV.7) along with the core and inner transitional zone of the LI18_43 amphibole crystals (Fig. IV.10E, F; Supplementary Table IV.7) suggest that they were derived from a relatively mafic environment. Nevertheless, the absolute content of Ba, Sr, and TiO$_2$ does not approach that of the mafic cumulate-derived amphibole (Fig. IV.11A, C; Supplementary Table IV.7). Although these domains originated from a mafic magma, they represent its more evolved stage. On the other hand, the transitional zone in LBH2_31 and the outer transitional domain in LI18_43 show an abrupt decrease in the TiO$_2$, Sr, and Ba content (Fig. IV.11A, C; Supplementary Table IV.7) and imply interaction (mixing) with a more evolved magma (Barnes et al., 2017). The rims are characterized by an intermediate composition representing the present host (Figs. IV.10C, E and IV.14E). In contrast, LI18_42 in LI18c (monzonite) shows a continuous increase in ΣREE (Fig. IV.10G), Ba, Sr, and TiO$_2$ from the core to the rim; nevertheless, their absolute

concentrations are rather low (Fig. IV.11A, C, D; Supplementary Table IV.7). This suggests that the core crystallized from a felsic magma and the outer zones were formed under the influx of a magma with a slightly more mafic composition (Fig. IV.14F).

IV.5.4. Implications from the plagioclase data

The key characteristics of the examined plagioclase crystals and their interpretation are summarized in Fig. IV.14.

Regardless of their textural position (isolated or clustered), plagioclase crystals in the studied felsic rocks (even in single samples) exhibit a wide range of different zonation patterns (Fig. IV.12; Supplementary Fig. IV.3).

Ca-rich zones in feldspars (e.g., LI18_01_02–03 and LI18_02_03; Supplementary Fig. IV.3; Supplementary Table IV.9) denote a shift in their composition as a result of changing physicochemical conditions (e.g., in the melt composition and/or temperature). This can be related to the transport of individual crystals into a new magmatic environment (recycling) or to the change of the physicochemical parameters around the crystal itself (Nixon and Pearce, 1987; Barbarin, 1990; Hattori and Sato, 1996; Grogan and Reavy, 2002; Kahl et al., 2011, 2015, 2017). Intermittent recharge of mafic magmas results in the coupled increase in the MgO, FeO, TiO_2, Sr, Ba, La, Ce, and anorthite content of plagioclase (Hattori and Sato, 1996; Słaby et al., 2002, 2007, 2011; Smith et al., 2009). Nevertheless, no evidence of such a process has been identified (e.g., mafic microgranular enclave swarms in the felsic suite in the northern part of the DAM) and none of the analyzed plagioclase compositional zones show such systematic, concurrent geochemical trends (Fig. IV.13; Supplementary Table IV.9). This inconsistency could be explained by the nature of the interacting end-members. Differentiation may fractionate mafic magmas towards intermediate, so that the concentration of the above-mentioned elements gradually decreases. Mixing with a differentiated, more evolved mafic magma – which still preserves some of its typical mafic features (e.g., high mg#, Ba, Sr, and TiO_2 contents; Coint et al., 2013) – could result in the observed geochemical patterns. Composition of the rims corresponds to that of their respective, evolved hybrid host (Figs. IV.12D, E and IV.14L, M).

Synneusis texture (Fig. IV.4D) indicates a period of turbulence and stirring in the system (Brown, 1956; Brothers, 1964; Vance, 1969; Grogan and Reavy, 2002). Plagioclase crystals occurring in synneusis relation (e.g., LTo35_14 and LTo35_19) are characterized by different zoning patterns (Fig. IV.12F–H; Supplementary Fig. IV.3; Supplementary Table IV.9), proving their distinct origin and crystallization history within the magmatic system (Fig. IV.14N).

	Amp type	Zonation	Texture	Features	Occurrence	Interpretation
A	Type I	Unzoned		Idiomorphic–hypidiomorphic	Ol-, Px-, Amp-rich cumulate; M2-cumulate	Cumulus phase, crystallized from M1/M2
B	Type II	Unzoned		Idiomorphic–hypidiomorphic	Monzonite, monzodiorite	Phenocryst (s.s.), crystallized from the hybrid magma
C	Type III	Unzoned		Idiomorphic–hypidiomorphic	Monzo-granite	Phenocryst (s.s.), crystallized from the fractionated hybrid magma
D	Composite	Zoned		Idiomorphic	Monzonite, monzodiorite	Core: cumulus phase from M1/M2; rim: hybrid magma
E	Composite	Complex		Idiomorphic–hypidiomorphic	Monzonite, monzodiorite	Core: fractionated foidgabbro; transition: syenite; rim: hybrid magma
F	Composite	Complex		Hypidiomorphic	Monzonite	Core: syenite magma; transition, rim: fractionated foidgabbro
G	Actinolite	Unzoned		Xenomorphic	Monzonite	Secondary, after Cpx (Type II)
H	Mafic clot	-		Stubby-to-slightly elongated; size: ~5 mm; minerals: Cpx (Type II), Amp (Type II and Act)	Monzonite	Amp (Type II and Act) on Cpx (Type II) antecryst nucleus

	Pl type	Zonation	Texture	Features	Occurrence	Interpretation
I	Type I	Unzoned		Hypidiomorphic–xenomorphic	Monzonite, monzodiorite	Phenocryst (s.s.), crystallized from the hybrid magma
J	Type II	Normal		Idiomorphic–hypidiomorphic; clear or sericitized core	Diorite (s.l.), monzonite, monzogranite	Core: fractionated foidgabbro; rim: (fractionated) hybrid magma
K	Type III	Reverse		Idiomorphic–hypidiomorphic; sericitized core	Monzonite, monzodiorite	Core: syenite magma; rim: fractionated foidgabbro
L	Composite	Complex		Idiomorphic–hypidiomorphic; sericitized core	Diorite (s.l.), monzonite, monzodiorite, monzogranite	Core: syenite magma; transition: fractionated foidgabbro; rim: hybrid magma
M	Composite	Complex		Idiomorphic–hypidiomorphic; clear core, clear or sericitized inner transition ± hybrid rim	Monzonite, monzogranite	Core+outer transition: fractionated foid-gabbro; inner transition+rim: hybrid
N	Felsic clot	-		Stubby-to-elongated; size: max. 5 mm; minerals: Pl (Type I and II)	Monzogranite	Crystals from different regions of the system in synneusis orientation
O	Felsic cumulate I	-		Whole-rock composition shows no Eu-anomaly	Tarniţa Complex	Xenolith, entrained in solid state; felsic cumulate of M1
P	Felsic cumulate II	-		Whole-rock composition shows marked positive Eu-anomaly	Bordea Creek, Holoşag Creek	Felsic cumulate of M2

Fig. IV.14. Summary of the analyzed amphibole and plagioclase crystals with respect to their zonation, texture, and occurrence as well as the interpretation of their origin and crystallization history. Abbreviations: Act – actinolite, Amp – amphibole, Cpx – clinopyroxene, Ol – olivine, Pl – plagioclase, Px – pyroxene; M1 – Magma1, M1a – Magma1a, M2 – Magma2, M2a – Magma2a, M2b – Magma2b, referring to the magmatic environments in the Ditrău Alkaline Massif

IV.5.5. Implications for the evolution of the Ditrău Alkaline Massif

The rocks of the DAM were formed by the emplacement and interaction of different magma batches in an open-system igneous environment (e.g., Batki et al., 2018; Heincz et al., 2018; Ódri et al., 2020; Fig. IV.15). The clinopyroxene-based study of Batki et al. (2018) has confirmed the presence of two, compositionally-different parental magmas and associated evolutional trends. Magma1 of basanitic composition (Batki et al., 2018) fractionated towards a monzodioritic/monzonitic composition. Not only mafic but also felsic roof cumulates were formed from this magma (Pál-Molnár et al., 2015a; Heincz et al., 2018; Fig. IV.15A, B, I). Intermittent replenishment by magmas of higher temperature and less-evolved composition produced mafic microgranular enclaves in the Tarnița Complex. Concurrent turbulence dragged and dispersed the felsic cumulate fragments into the lower part of the system (Heincz et al., 2018; Figs. IV.14O and IV.15J).

The evolution of Magma2 resulted in the formation of a phonolitic magma, parental to nepheline syenite (Batki et al., 2018; Fig. IV.15D). Bulk-rock composition of the Magma1-derived felsic xenoliths in the Tarnița Complex (Pál-Molnár, 2021) is completely different from that of LHH23/1 (monzonite) and LBH55/1 (monzodiorite) (Fig. IV.7A, B). This implies that these samples were formed concurrently from Magma2 in those areas where convection was restricted and the thermal and compositional gradients diminished (Figs. IV.14P and IV.15C).

The composition of groundmass clinopyroxene in LB16m (plagioclase-bearing pyroxene hornblendite; Fig. IV.8A, B) and the texture of the rock (Fig. IV.3E) imply that this sample could be the so-far unrecognized cumulate phase of M2 (Batki et al., 2018; Fig. IV.15C). Orbicular inclusions of LB16m (Figs. IV.3E and IV.4I) contain clinopyroxene crystals (Fig. IV.5B) of a composition overlapping with that of the cumulus clinopyroxene of M1 (Fig. IV.8C, D). This suggests that an interaction between the two magma bodies took place in the deeper sections of the igneous system (Fig. IV.15C, D). Tinguaite with ijolite enclaves was formed by magma mingling of the fractionated derivatives of M1 and M2 (Fig. IV.15E–G).

During the emplacement of M2 magma, excess heat caused partial melting in the country rocks, which resulted in the formation of syenitic magma (Hildreth and Moorbath, 1988; Bergantz, 1989; Fig. IV.15H). As Ódri et al. (2020) suggested, the proportion of the upper crustal material could be approximately 20–25% in syenite. Abundant syenite dykes (e.g., crosscutting the Tarnița Complex; Fig. IV.2A) support the presence of the syenitic magma.

Closed-system processes

A Basanitic parental melt (Batki et al., 2014)

M1

Fractional crystallization + accumulation (Pál-Molnár et al., 2015a)

Base of the system

Magma1 (early camptonitic magma)

Ol-rich cumulate

B Basanitic parental melt (Batki et al., 2014)

M1

Fractional crystallization $F_{max} = 46.8$ (Batki et al., 2014)

M1a

Fractional crystallization + accumulation (Pál-Molnár et al., 2015a)

Base of the system

Magma1 (early camptonitic magma)

Magma1a (fractionated camptonitic magma)

Px-rich cumulate

Open and closed-system processes

C Basanitic parental melt (Pál-Molnár, 2021)

M2

Fractional crystallization + accumulation

Base of the system

+

Roof of the system

Magma2

Pl-bearing Px and Amp-rich cumulate ± M1-derived Cpx

Pl-rich felsic cumulate

D M1   M2

Fractionation

M2a

Fractionation

M2b

M1 recharge & recycling

Magma2a (ijolitic magma)

Magma2b (phonolitic magma)

Open-system processes

E M2   M1a

M2 recharge & recycling

F M1a   M2b

M1a recharge & recycling

G Tinguaite with ijolite enclaves

M2a   M2b

Magma mingling

H M2   Crust

20-25% crustal assimilation (Ódri et al., 2020)

Syenitic magma

I Basanitic parental melt (Pál-Molnár, 2021)

Tarniţa Complex

Fractional crystallization + accumulation

+

Roof of the system

Foidgabbro

Fractionated foidgabbro

Pl-rich felsic cumulate of M1

J Foidgabbro with (ultra)mafic & felsic enclaves

M1 + M2 recharge & recycling

K Fractionated foidgabbro

Syenitic

Syenitic magma recharge & recycling

Magma mixing

Felsic hybrids

Monzodiorite, monzonite

Fractional crystallization + up to 65% crustal assimilation (Ódri et al., 2020)

Granite

Fig. IV.15. Schematic emplacement model for the Ditrău Alkaline Massif (modified after Batki et al., 2018). The relative size of the structural and textural elements is not illustrated to scale. Mineral illustrations and abbreviations of the magmatic environments can be found in Fig. IV.14. and in Batki et al. (2018). See text for details

In the TAS diagram, bulk-rock compositions of the recently-analyzed samples partly overlap with and connect the trends of the rocks formed by magma mingling in the Tarnița Complex and those of the syenite–granite series (Fig. IV.6A). There is a distinct, widespread group of amphiboles (Type II) occurring in almost all of the analyzed felsic samples (Figs. IV.5E and IV.14B). However, these rocks also contain zoned amphibole crystals (Fig. IV.14D) and the composition of their core resembles that of the amphibole in cumulate rocks (Type I) of either M1 (Pál-Molnár et al., 2015a) or M2 (Fig. IV.10A, B), whereas the composition of their rims overlaps with that of the Type II amphiboles. The amphibole and plagioclase crystals are diverse in terms of their size along with their inter- and intra-crystalline zoning patterns (Figs. IV.10, IV.11, IV.12, and IV.13; Supplementary Figs. IV.2 and IV.3). These features indicate the hybrid nature of the studied rocks (Słaby et al., 2007; Barnes et al., 2016) and strongly suggest that they were formed by the interaction (magma mixing) of the syenitic magma and the fractionated (most likely intermediate) derivative of M1 (Fig. IV.15K), with the latter still preserving some of its pristine mafic features (e.g., relatively high mg#, TiO_2, Sr, and Ba contents; Coint et al., 2013). The interaction between the end-members with comparable rheological properties, temperature, and relatively similar, felsic composition resulted in thorough mixing rather than mingling (Sparks and Marshall, 1986; Bateman, 1995; Poli et al., 1996; Ubide et al., 2014b). This could explain the absence of mafic microgranular enclaves and other, outcrop and macro-scale evidence of open-system igneous processes in the northern part of the massif (between the Tarnița and Turcului Creeks). This region [exemplified by samples LBH2 (monzodiorite), LI18c–f, and LTa29 (monzonites)] represents the early stage of the interaction (Bateman, 1995) and/or the structurally-higher section of the hybrid zone, where low crystallinity and convection favored thorough mixing. Along the Ditrău–Hagota road (central part of the DAM), magma mingling is exposed, which is evidenced by mafic enclaves and large mafic as well as felsic cumulate blocks (Fig. IV.2B–D). This was formed subsequently in the thermal history of the massif (Bateman, 1995) and/or it could be the lower part of the hybrid zone, where the locked crystal mush hindered magmatic stirring and resulted in structural inhomogeneities.

Fractionation of the hybrid magma (Campos et al., 2002) resulted in the formation of amphibole autocrysts/phenocrysts of uniform composition (Type II; Fig. IV.14B). Their homogeneous internal texture and composition (Fig. IV.5E) imply that they were formed from the magma currently hosting them (Barnes et al., 2016) and that they were not involved in crystal transfer and/or recycling.

Amphiboles of LTo35 (monzogranite; Figs. IV.4H, IV.5F, IV.10I, J, and IV.14C; Supplementary Fig. IV.2) crystallized from an evolved magma batch that developed from

further fractionation of the hybrid magma (Campos et al., 2002) and simultaneous assimilation of additional crustal material (Fig. IV.15K). The latter is supported by the findings of Ódri et al. (2020), according to which quartz monzonite contains 50% lower crustal material, while granite is characterized by 35–65% upper crustal contribution.

The intrusion of lamprophyre, ijolite, tinguaite, and (nepheline)syenite dykes (Fig. IV.2A, E) marked the last stage of the igneous activity. They represent M1, M2, and the syenitic melt respectively.

IV.6. Concluding remarks

Previously, the felsic rocks of the northern part of the Ditrău Alkaline Massif (Eastern Carpathians, Romania) were regarded as a homogeneous, uniform assemblage. However, there is a great micro-scale diversity (e.g., mafic clots, felsic aggregates, distinct zonation patterns of adjacent plagioclase crystals) in the felsic suite north of the Jolotca Creek valley.

The whole-rock major and trace element data support the previous hypotheses deduced from petrographic observations and prove the existence of two, compositionally different felsic cumulate piles in the DAM.

Bulk-rock data, amphibole, and plagioclase compositions attest to the hybrid nature of the majority of the felsic rocks occurring in the northern part of the massif. Crystal transfer and recycling as well as hybridization were unraveled by the unique compositions in the different zones of amphibole and plagioclase crystals. All these features suggest that the studied rocks were formed by the mixing of magmas with relatively similar composition, temperature, and rheological properties.

<h1 style="text-align:center">CHAPTER V</h1>

<h2 style="text-align:center">CONCLUSIONS</h2>

The felsic rocks in the northern part of the Ditrău Alkaline Massif (DAM) were studied in this doctoral research. Field, macroscopic, and microscopic petrographic observations, bulk-rock and mineral-scale major and trace element data, amphibole and biotite K/Ar along with titanite and zircon U–Pb ages were utilized to unravel the genesis and evolution of the investigated felsic suite and to locate the geodynamic environment wherein the DAM was formed.

The exhumed magma storage system of the DAM is a unique natural laboratory where the products of open- and closed-system igneous processes characteristic of trans-crustal magmatic systems can be directly accessed and studied.

The massif has been in the focus of research over the past 190 years and multiple hypotheses have emerged regarding its genesis, source region, evolution, timing, and paleogeographic environment (e.g., Streckeisen, 1938, 1960; Anastasiu and Constantinescu, 1979; Pál-Molnár and Árva-Sós, 1995; Kräutner and Bindea, 1998; Morogan et al., 2000; Pál-Molnár, 2000; Pană et al., 2000). The felsic rocks in the northern part of the massif (north of the Jolotca Creek valley) were mostly regarded as a homogeneous, uniform unit of the DAM. Recent structural, bulk-rock and mineral chemical major and trace element data revealed that these rocks are more heterogeneous than previously thought and that open-system processes (e.g., country rock assimilation, crystal transfer and recycling, along with magma mingling and mixing) were involved in their genesis (e.g., Batki et al., 2018; Heincz et al., 2018; Ódri et al., 2020). These findings put a pressing need for the re-examination of the felsic suite of the DAM.

The timing of the igneous event is crucial to understand the geodynamic context, the tectonic framework of the massif, and the emplacement sequence of the different magmas. The reviously published age data (K/Ar ages of whole-rock samples, alkaline feldspar, amphibole, biotite, muscovite, nepheline, nepheline + sodalite, and plagioclase as well as Rb–Sr bulk-rock, $^{40}Ar/^{39}Ar$ amphibole, and U–Pb zircon ages) had to be revised and supplemented by new data acquired by state-of-the-art dating techniques to determine the age and time span of the alkaline magmatism. K/Ar geochronology was performed on amphibole crystals of amphibole- and pyroxene-rich cumulate (238.6 ± 8.9 Ma), nepheline syenite (216.0 ± 8.1 Ma), and granite (197.3 ± 7.4 and 196.3 ± 7.4 Ma). Biotite from granite yielded K/Ar mean ages of 201.4 ± 7.6 and 198.3 ± 7.5 Ma. The U–Pb crystallization age of titanite from syenite is 225.3 ± 2.7 Ma, while, the crystallization age of zircon is 232.4 ± 3.3 Ma. Titanite and zircon from nepheline syenite yielded U–Pb crystallization ages of 230.6 ± 3.5 Ma and 230.6 ± 2.4 Ma, respectively.

The archive data, complemented by our recent K/Ar and U–Pb ages, cover a broad time interval from 238.6 ± 8.9 to 81.3 ± 3.1 Ma. Due to their low closure temperature, the K/Ar ages of biotite and feldspar can only be used for the timing of post-magmatic processes. Some authors (Bagdasarian, 1972; Streckeisen and Hunziker, 1974; Mînzatu and Ardeleanu, 1980; Mînzatu et al., 1981) used whole-rock samples; therefore, the results of their analyzes can be regarded as mixed ages owing to the distinct resistance and closure temperatures of the rock-forming minerals. With this in mind, the U–Pb ages of titanite and zircon and the K/Ar data of amphibole (with some restrictions) should be considered when it comes to the timing of the magmatic event. Both the previous and the recent K/Ar data are scattered, making the lower limit of the igneous event age ambiguous. The oldest age data is 238.6 ± 8.9 Ma, determined by K/Ar method on amphibole from amphibole- and pyroxene-rich cumulate. It shows a considerable error coincident with the U–Pb data. Considering the recent and post-1990 K/Ar and U–Pb results, the magmatic event could be dated between 238.6 ± 8.9 Ma (amphibole from amphibole- and pyroxene-rich cumulate) and 225.3 ± 2.7 Ma (titanite from syenite). These data disprove the age and time range of the multi-phase evolution hypothesis of Pál-Molnár and Árva-Sós (1995), Kräutner and Bindea (1998), Morogan et al. (2000), and Pál-Molnár (2000, 2008) and infer a brief magmatic activity, without a significant time gap between the formation of the early emplaced (ultra)mafic cumulates and the subsequent intrusion of the felsic suite (e.g., syenite, granite, and nepheline syenite).

Previous geochemical analyzes (e.g., Morogan et al., 2000; Pál-Molnár, 2000, 2010b; Batki et al., 2014; Pál-Molnár et al., 2015b), combined with the geochronological data, are in line with the palinspastic reconstructions and imply that the DAM was emplaced at the southwestern margin of the East European Craton and its genesis is related to the rifting of the oceanic basins of the Western-Tethys in the Middle–Late Triassic (Ladinian–Norian) (e.g., Kozur, 1991; Stampfli and Borel, 2002, 2004; Hoeck et al., 2009; Pană, 2010).

Recently, Klötzli et al. (2022) published *in situ* zircon SIMS U–Pb ages of nepheline syenite from different regions of the DAM. Based on the petrochronological and geochemical data, three intrusion events were distinguished: 232.1 ± 0.8 Ma (Ghiduț suite), 230.7 ± 0.2 Ma (Ditrău suite), and 224.9 ± 1.1 Ma (Lăzarea suite), supporting the theory that the DAM was built incrementally by the emplacement of multiple magma pulses. Klötzli et al. (2022) emphasized that there is no evidence of magmatic or hydrothermal activity younger than 215 ± 1 Ma. These geochronological data correspond well with our results and support our interpretation that the massif is the product of a brief igneous event.

Additional fieldwork and sampling were inevitable since the locations of previous sampling sites could not be retraced in the absence of GPS data. A set of new samples were

collected during two field campaigns in 2019 and 2021, focusing on the felsic rocks of the DAM. Not only their GPS coordinates but also their field and structural relations with other rock types (e.g., mafic rocks, metamorphic country rocks, mafic and felsic dykes) of the massif were documented. Detailed petrographic investigations were implemented on hand specimens and on thin sections from the northern part of the massif. Mineral phases were analyzed by Raman and scanning electron microscopy.

The relationship between the mafic and felsic rocks is not apparent, as it cannot be traced in the field due to poor exposures. Mafic microgranular enclaves have not been observed in the studied area; however, wall rock xenoliths and aggregates of mafic minerals are common and dykes (e.g., lamprophyre, alkaline feldspar syenite, syenite, and tinguaite) crosscutting the felsic rocks are prevalent.

The studied rocks seem to be uniform at the macro-scale; nevertheless, most of their significant textural characteristics can be revealed under the microscope. At this scale, the felsic rocks exhibit a substantial petrographic heterogeneity (including grain size, type of ferromagnesian minerals and their occurrence in mafic clusters, and textural orientation).

The studied felsic rocks were categorized into two groups based on their spatial occurrence and petrographic characteristics. Felsic rocks of Group 1, occurring on the hillside west of the Bordea Creek, are spatially associated with mafic rocks (plagioclase-bearing pyroxene hornblendite) and they are either devoid of or contain a minor amount of mafic minerals (biotite). Idiomorphic–hypidiomorphic plagioclase with a sieve-textured, variably sericitized core and an intact rim is the dominant rock-forming mineral, accompanied by minor perthitic alkaline feldspar, biotite, and accessory titanite. Plagioclase crystals are aligned parallel to their straight crystal faces, making up aggregates of multiple grains and defining a shape-preferred orientation. Feldspar-rich clusters ("chain structure"; Vernon and Collins, 2011) are formed by gravitational segregation (Brown, 1956; Brothers, 1964; Vance, 1969) or synneusis (when suspended crystals get episodically drifted together by turbulent currents; Vogt, 1921; Vance, 1969). Polycrystalline felsic crystal clusters are more prone to settling in felsic and viscous magmas (Vernon and Collins, 2011) and their abundance implies gravitational accumulation. Gravity-driven compaction or magmatic flow-induced shearing may have resulted in feldspar lamination (Ildefonse and Fernandez, 1988; Féménias et al., 2005; Vernon and Paterson, 2006 and references therein). Impinging plagioclase crystals with separate cores are also common, implying compaction of the crystal mush (Park and Means, 1996; Vernon et al., 2004; Vernon and Collins, 2011).

Felsic rocks of Group 2, cropping out in the area between the Teasc and Rezu Mare Creeks, are spatially unassociated with mafic rocks. They are made up of felsic minerals

(alkaline and plagioclase feldspars ± quartz ± feldspathoids) in variable amounts. Feldspars are characterized by similar textural features as in the rocks of Group 1. Amphibole, biotite, and clinopyroxene are mostly present in different types of mafic aggregates. Subordinate accessory and opaque phases, feldspars, and quartz also occur in the clusters. The clot-forming minerals are either intact or show different extents of alteration. Clusters related to mafic microgranular enclaves have not been recognized; nevertheless, some of the aggregates can be attributed to metamorphic wall rock xenoliths. Single, isolated ferromagnesian minerals of the "groundmass" (the phaneritic, holocrystalline, felsic mineral-rich domain of the host rock) are represented in limited amounts. Based on the type and textural features of the mafic components, the clots were classified as monomineralic (green amphibole-, blue amphibole-, biotite-, and epidote-rich aggregates) and polymineralic (green amphibole + biotite; blue amphibole + biotite; amphibole + clinopyroxene + titanite + opaque minerals ± biotite aggregate). Mafic clusters can be produced by cumulate formation and recirculation (Wiebe et al., 1997; Bea, 2010; Klaver et al., 2017), synneusis (Vogt, 1921; Vance, 1969), and by the disaggregation of mafic microgranular enclaves and country rock xenoliths (Lavaure and Sawyer, 2011; Carvalho et al., 2017), resulting in the entrainment of exotic minerals. It is likely that some of the aggregates are made up of minerals that partially or completely replace the primary antecrysts and/or xenocrysts. Rocks of the second group also contain spongy mafic megacrysts, feldspar megacrysts, and adjoining feldspar crystals with different zonation patterns. The latter points to the distinct crystallization and reaction histories of feldspars, involving mixing with a more primitive mafic magma and crystal recycling between different environments (Wiebe, 1968; Baxter and Feely, 2002; Vernon and Paterson, 2006).

The combined occurrence of the observed microtextural characteristics implies that the studied felsic rocks were formed under dynamic, open-system magmatic conditions, wherein convection, country rock assimilation, crystal or mush transfer and/or recycling, cumulate formation, incorporation of exotic materials, magma recharge, magma mixing and mingling as well as shear flow prevailed.

The field, macroscopic and microscopic structural and textural observations had to be supported by whole-rock (ICP-ES and ICP-MS) and mineral-scale (SEM BSE, EMPA, and LA-ICP-MS) major and trace element analyzes to better understand the open-system igneous mechanisms that formed the studied felsic rocks and to decipher their relationship with the previously defined igneous environments [Magma1 of basanitic composition, parental to (ultra)mafic cumulates and rocks of the Tarnița Complex; Magma2 that evolved to a phonolitic composition and produced nepheline syenite (Batki et al., 2018)]. For this purpose, the most common felsic rock types (diorite, monzodiorite, monzogranite, monzonite) of the northern part

of the massif were selected for analysis. The selected samples covered all textural variations and all mineralogical-textural felsic and mafic aggregate types. Amphibole, clinopyroxene, and plagioclase were selected for mineral chemical analysis since they occur in practically every rock type in the northern area of the DAM. For comparison, the compositions of amphibole and clinopyroxene crystals of lamprophyre and plagioclase-bearing pyroxene hornblendite were analyzed. Mafic and felsic minerals in various textural positions (aggregated and isolated single crystals of the groundmass) were included to determine whether they exhibit any compositional variation.

The bulk-rock major and trace element compositions support the previous interpretations deduced from the petrographic features and confirm the presence of two felsic cumulate piles of different compositions. Diorite samples of Group 1 – formerly classified as felsic cumulates based on their mineralogy and microtextures – exhibit a slightly positive Eu anomaly (Eu/Eu* = 1.1–1.3) and a high differentiation index (D.I. = 95.0–95.3). Their REE patterns overlap with those of the majority of Group 2 rocks. They only differ in their Eu anomaly and the concentration of HREEs, making them indistinguishable from the rocks of Group 2. Nevertheless, certain monzonite and monzodiorite samples of Group 2 are characterized by different trends, with a marked positive Eu anomaly (Eu/Eu* = 2.5–6.7) and a low REE content (ΣREE = 125–206 ppm). Additionally, many of their abundant plagioclase crystals are impinged or occur in chain structures. These features suggest that these rocks are early felsic cumulates (Kumar and Singh, 2014). Their whole-rock composition does not overlap with that of the previously described, Magma1-derived felsic xenoliths of the Tarnița Complex (Heincz et al., 2018; Pál-Molnár, 2021), evidencing that they represent the felsic cumulate phase of a different parental magma (Magma2).

The studied plagioclase-bearing pyroxene hornblendite contains clinopyroxenes in two different textural configurations. Clinopyroxene crystals in the center of the orbicular inclusions of plagioclase-bearing pyroxene hornblendite exhibit a concave REE pattern (typical of Magma1-derived clinopyroxenes; Batki et al., 2018) and are mantled by amphibole and biotite of the host rock, suggesting their antecrystic origin. Unlike the (ultramafic)cumulates of Magma1 (Batki et al., 2018), the studied plagioclase-bearing pyroxene hornblendite contains isolated clinopyroxene cumulus crystals characterized by a convex REE pattern, typical of clinopyroxenes crystallized from Magma2 (Batki et al., 2018). Thus, the studied plagioclase-bearing pyroxene hornblendite could be the so-far unrecognized mafic cumulate of Magma2. The presence of Magma1-derived pyroxene inclusions in plagioclase-bearing pyroxene hornblendite proves that Magma1 and Magma2 interacted in the deeper regions of the igneous system. The mobilization and redistribution of Magma2-derived clinopyroxenes produced

mafic crystal clusters, some of which still retain fragments of antecrystic clinopyroxene (Batki et al., 2018). The high mg# (0.4–0.8) along with the REE and trace element patterns of groundmass and clot-forming actinolites imply that these are replacive minerals after clinopyroxene antecrysts.

In the TAS diagram, whole-rock compositions of the recently analyzed samples partially overlap with and connect the trends of the rocks formed by magma mingling in the Tarnița Complex [diorite (*s.l.*), monzodiorite, and monzonite] and those of the syenite–granite series. Amphibole and plagioclase crystals are diverse in size and are characterized by variable intra-crystalline zoning patterns and trace element contents, indicating their distinct origins and crystallization histories, which involve crystal transfer and recycling as well as magma mixing, hybridization, and fractionation (Słaby et al., 2007; Barnes et al., 2016).

Variations in the Ba, Sr, and TiO_2 concentrations of zoned amphiboles (Barnes et al., 2017) and in the MgO, FeO, TiO_2, Sr, Ba, La, Ce, and anorthite contents of plagioclase crystals (Hattori and Sato, 1996; Słaby et al., 2002, 2007, 2011; Smith et al., 2009) imply magma mixing with a differentiated (evolved) mafic magma, that still preserved some of its typical mafic features (e.g., high mg#, Ba, Sr, and TiO_2 concentrations; Coint et al. 2013). This magma is represented by the fractionated (most likely intermediate) derivative of Magma1. The other magma involved in the interaction is syenite, formed by crustal assimilation of Magma2. The interplay between magmas with similar temperature, rheological properties, and felsic composition induced thorough mixing rather than mingling (Sparks and Marshall, 1986; Bateman, 1995; Poli et al., 1996; Ubide et al., 2014b). This could be the reason why outcrop and macro-scale evidence of open-system magmatic processes (e.g., mafic microgranular enclaves) are absent in the northern part of the massif (between the Tarnița and Turcului Creeks).

Amphibole autocrysts with uniform composition and homogeneous internal texture were formed by fractionation of the hybrid magma (Campos et al., 2002). These features indicate that they were not involved in crystal transfer and that they were formed from the magma currently hosting them (Barnes et al., 2016).

Further fractionation of the hybrid magma (Campos et al., 2002) and simultaneous assimilation (Ódri et al., 2020) led to the formation of granite. Amphibole crystals with a marked negative Eu anomaly (Eu/Eu* = min. 0.2) and a high ΣREE concentration (1000 ppm) crystallized from this evolved magma batch.

The last stage of the igneous activity is marked by the intrusion of lamprophyre, ijolite, tinguaite, and (nepheline)syenite dykes, representing Magma1, Magma2, and the syenitic melt, respectively.

SUMMARY

Introduction and the aims of the study

The Ditrău Alkaline Massif (DAM; Eastern Carpathians, Romania) is a Middle–Late Triassic igneous complex (Pál-Molnár et al., 2021) that formed in an intra-plate, rift-related, extensional tectonic environment (e.g., Morogan et al., 2000; Pál-Molnár, 2000, 2010b; Batki et al., 2014; Pál-Molnár et al., 2015b). The massif is made up of a wide variety of rock types, ranging from ultramafic cumulates to granitoid rocks, crosscut by lamprophyre, syenite, and tinguaite dykes (Pál-Molnár, 2000; Batki et al., 2014; Pál-Molnár et al., 2015a, b). It is a remarkable natural site for studying the open- and closed-system magmatic processes of trans-crustal igneous systems. Rare earth element (REE) mineralization makes the massif one of the potential, economically viable deposits in Europe (Honour et al., 2018).

Numerous and often conflicting theories and genetic models have emerged during the 190-years-long scientific exploration of the massif (e.g., Streckeisen, 1938, 1960; Kräutner and Bindea, 1998; Morogan et al., 2000; Pál-Molnár, 2000). Researchers attempted to unravel the timing of the igneous event and to determine the emplacement sequence of the different magma batches (e.g., Streckeisen, 1952, 1954; Pál-Molnár and Árva-Sós, 1995; Kräutner and Bindea, 1998; Pană et al., 2000). Early on in the study of the massif, Streckeisen (1954), Kräutner and Bindea (1998) as well as Morogan et al. (2000) emphasized the importance of open-system igneous processes in the evolution of the DAM. Some details of these mechanisms have been unraveled by recent structural observations, bulk-rock and mineral-scale geochemical data (e.g., Batki et al., 2018; Heincz et al., 2018; Ódri et al., 2020). With a few exceptions (e.g., Streckeisen, 1954; Kräutner and Bindea, 1998; Morogan et al., 2000), the felsic rocks in the northern area of the DAM have generally been regarded as homogeneous, uniform units. Clinopyroxene antecrysts were described from diorite and syenite (Batki et al., 2018), raising the importance of re-examining the felsic rocks.

The PhD research focuses on the felsic suite exposed in the northern area of the DAM. The objectives were the following: (1) the revision of the previous geochronological data and to implement them with new K/Ar and U–Pb radiometric ages; (2) the detailed petrographic examination of the systematically collected and documented new set of felsic rock samples; (3) the whole-rock and mineral-scale geochemical analysis (including major and trace elements) of the samples; (4) to come up with a conceptual evolution model by integrating all recently obtained knowledge about the massif.

Applied methods

The most conventional methods (field observations, macroscopic and microscopic petrography, whole-rock and mineral-scale major and trace element geochemistry, K/Ar and U–Pb geochronology) were applied in the study of the felsic rocks cropping out in the northern part of the DAM.

Age determination was performed on a previously collected, archive set of samples. K/Ar geochronology was implemented on separated amphibole and biotite crystals by a digital flame photometer and a magnetic mass spectrometer at the HUN-REN Institute for Nuclear Research, Debrecen, Hungary. Titanite and zircon crystals were separated for U–Pb geochronology by standard gravity and magnetic separation methods. Backscattered electron (BSE) and cathodoluminescence (CL) imaging were performed at the Department of Petrology and Geochemistry, Eötvös Loránd University, Budapest, Hungary and at the Department of Geosciences, Johann Wolfgang Goethe University, Frankfurt, Germany. *In situ* U–Pb age determinations were carried out at the GÖochron Laboratories, Georg-August University of Göttingen, Göttingen, Germany, utilizing an excimer laser and a Thermo Finnigan Element2 sector field mass spectrometer.

A new set of samples was collected in two sampling campaigns in 2019 and 2021. Documentation involved the registration of GPS coordinates and the relationship of the felsic rocks with other rock types (e.g., country rocks, dykes, mafic rocks). Thin sections were prepared at the Department of Petrology and Geochemistry, Eötvös Loránd University, Budapest, Hungary. Petrographic observations were performed using Brunel SP300P and Olympus BX41 optical microscopes at the Department of Mineralogy, Geochemistry and Petrology, University of Szeged, Szeged, Hungary. A THERMO Scientific DXR Raman microscope was also utilized to determine certain mineral phases. Compositional zonation and microtextural relations were revealed by BSE imaging, using an AMRAY 1830 SEM equipped with an EDAX PV 9800 EDS detector at the Department of Petrology and Geochemistry, Eötvös Loránd University, Budapest, Hungary.

The samples selected for bulk-rock geochemistry were prepared and analyzed at the Bureau Veritas Mineral Laboratories (ACMELabs) in Vancouver, Canada. Major element concentrations were determined by ICP-ES; whereas, trace elements (including rare earth elements) were analyzed by ICP-MS.

The major and trace element compositions of single minerals were determined from polished thin sections of 30 μm thickness. Amphibole, clinopyroxene, and plagioclase were selected for analysis since they occur in nearly all rock types in the northern part of the massif. Amphibole and clinopyroxene from lamprophyre and plagioclase-bearing pyroxene

hornblendite were also analyzed for comparison. To determine whether there are any compositional variations, ferromagnesian and felsic minerals in various textural positions [including aggregated minerals and single crystals occurring in the "groundmass" (the phaneritic, holocrystalline, felsic mineral-rich domain of the so-called host rock)] were investigated. Major- and minor-element compositions of the minerals were analyzed at the Institut des Sciences de la Terre d'Orléans – Centre National de la Recherche Scientifique (ISTO-CNRS), Orléans, France, utilizing a Cameca SX Five electron microprobe. The same spots were measured during the trace element (including rare earth elements) analyzes as for the EMPA. Trace element concentrations were also determined at the Institut des Sciences de la Terre d'Orléans– Centre National de la Recherche Scientifique (ISTO-CNRS), Orléans, France by LA-ICP-MS, using a RESOlution SE laser ablation system connected to an Agilent 8900 QQQ inductively coupled plasma mass spectrometer.

New scientific results

The integrated investigation of the felsic rocks cropping out in the northern part of the Ditrău Alkaline Massif has provided significant novel results regarding the age, time span, and paleotectonic environment of the igneous event, the textural heterogeneity of the felsic rocks, the complex history of the constituent mafic and felsic minerals, the evolution of the felsic suite, and the genesis of the massif.

T1 Felsic rocks of the Ditrău Alkaline Massif were formed by a short-lived igneous event in the Middle–Late Triassic.

The age and time span of the felsic magmatism were specified by new K/Ar (amphibole: nepheline syenite and granite; biotite: granite) and U–Pb ages (titanite and zircon: nepheline syenite and syenite), combined with the thoroughly revised archive age data. Titanite and zircon from syenite yielded U–Pb ages of 225.3 ± 2.7 Ma and 232.4 ± 3.3 Ma, respectively. Amphibole from nepheline syenite formed at 216.0 ± 8.1 Ma; whereas, U–Pb ages of titanite and zircon are 230.6 ± 3.5 and 230.6 ± 2.4 Ma, respectively. K/Ar ages of amphibole and biotite from granite range from 196.3 ± 7.4 to 197.3 ± 7.4 and 198.3 ± 7.5 to 201.4 ± 7.6 Ma, respectively. Considering new and previous (post-1990) K/Ar and U–Pb data, there is no resolvable age difference between the early emplaced mafic cumulates and the felsic rocks. These findings disprove the age and time span of the previous, multi-phase evolution theories (e.g., Pál-Molnár and Árva-Sós, 1995; Kräutner and Bindea, 1998; Morogan et al., 2000; Pál-Molnár, 2000, 2008) and infer that the Ditrău Alkaline Massif is the product of a relatively short-lived igneous event.

T2 The felsic suite, cropping out in the northern part of the Ditrău Alkaline Massif, is more heterogeneous at the micro-scale than previously presumed.

Felsic rocks have been mostly regarded as homogeneous, uniform units of the magmatic complex. However, a detailed textural study has revealed that the felsic rocks occurring north of the Jolotca Creek valley exhibit considerable micro-scale heterogeneity. The studied rocks were categorized into two groups based on their field occurrence and microtexture: Group 1 – lacking or containing scant ferromagnesian minerals, spatially associated with mafic rocks and Group 2 – containing mafic minerals and clusters, spatially unassociated with mafic rocks. All rocks of Group 1 and some of Group 2 bear micro-scale traces of the gravitational accumulation of felsic minerals and the compaction of the crystal mush [e.g., feldspar lamination, feldspar-rich aggregates (chain structure), mutually impinging crystals].

T3 The mafic minerals of Group 2 rocks generally occur in different types of clots comprising multiple grains of either identical or disparate ferromagnesian phases.

The microtextural heterogeneity of the rocks from Group 2 partly derives from the presence of different types of mafic mineral clusters with various petrographic features. Monomineralic (green amphibole-, blue amphibole-, biotite-, and epidote-rich) and polymineralic (green amphibole + biotite; blue amphibole + biotite; amphibole + clinopyroxene + titanite + opaque minerals ± biotite) aggregates were distinguished in the studied felsic rocks. Some of the clots are made up of replacive minerals after a precursor phase (antecryst and/or xenocryst) and the different clusters exhibit distinct stages of substitution of the entrained materials. The presence of aggregates contributes significantly to the increased modal proportion of ferromagnesian minerals in the host rocks. Clots associated with mafic microgranular enclaves have not been observed; however, certain types are associated with metamorphic country rock xenoliths. The amount of isolated mafic minerals is rather limited.

T4 The accumulation of both mafic and felsic crystals played a significant role in the formation of the Ditrău Alkaline Massif.
T4a A new mafic cumulate type was revealed by the trace element composition of cumulus clinopyroxene.

Clot-forming clinopyroxenes with a convex REE pattern have previously been reported as antecrysts, among others, in diorite and syenite. Clinopyroxenes of identical composition were described for the first time as cumulus minerals (autocrysts) from plagioclase-bearing pyroxene hornblendite, which represents the cumulate phase of the parental melt of nepheline syenite. Mobilization and redistribution of clinopyroxene crystals of this type resulted in the formation

of mafic mineral clusters in the felsic rocks, some of which still preserve relics of antecrystic clinopyroxene.

T4b Two types of felsic cumulates of different origins were distinguished by their whole-rock major and trace element composition.

Certain monzonite and monzodiorite samples of Group 2 are characterized by a high Eu/Eu^* value (2.5–6.7), low ΣREE (125–206 ppm) as well as elevated La and Sr concentrations. These features, combined with the high abundance and microtexture of plagioclase (e.g., chain structure, impingement), suggest that these rocks are less differentiated, early felsic cumulates. Based on their mineralogy, microtexture, and geochemical properties, the felsic xenoliths of the Tarnița Complex were previously described as felsic cumulates. Nevertheless, the whole-rock composition of these enclaves differs from that of the Group 2 monzonite and monzodiorite, implying that they are felsic cumulates of different parental magmas.

T5 A nomenclature based on the bulk-rock composition of the studied rocks can be misleading due to cumulate formation and the incorporation of exotic materials.

Most of the examined rocks are cumulates or partial cumulates, characterized by the accumulation of felsic minerals in varying modal proportions. In addition, some of the samples contain polycrystalline clusters of mafic minerals with antecrysts. It has been pointed out that the whole-rock data should be treated with caution, as cumulate formation (both mafic and felsic) and the incorporation of crystals of different origins have a significant impact on the modal mineralogy and subsequently on the overall composition of the rocks. These findings challenge the conventional use of nomenclature based on the bulk-rock composition and demonstrate that the integration of microtextural investigations and mineral-scale geochemical analyzes is crucial for selecting an appropriate nomenclature for the studied rocks and also for understanding the processes that occur during pluton emplacement.

T6 A conceptual evolution model was created by integrating all available knowledge about the Ditrău Alkaline Massif.

The rocks of the DAM were formed by the emplacement and interplay of multiple magma batches derived from two different parental magmas in an open-system magmatic environment.

Two types of felsic cumulates with distinct whole-rock compositions were formed in regions where convection was limited. Not only felsic but also (ultra)mafic cumulates were produced. The latter can be distinguished by the composition of cumulus clinopyroxene; however, cumulus amphibole crystals exhibit overlapping geochemical features. Orbicular

inclusions with primitive clinopyroxene crystals in their core occur in plagioclase-bearing pyroxene hornblendite, suggesting that the two parental magmas have already interacted in the deeper part of the igneous system. Whereas, tinguaite with ijolite enclaves was formed by mingling of the fractionated derivatives of the parental magmas.

The syenitic magma was formed by crustal assimilation of the parental melt of nepheline syenite during its emplacement.

Bulk-rock compositions of the recently analyzed felsic rocks partially overlap with and connect the trends of the syenite–granite series and those of the rocks formed by magma mingling in the Tarnița Complex [diorite (*s.l.*), monzodiorite, and monzonite]. Amphibole and plagioclase crystals are characterized by variable intra-crystalline zoning patterns and element contents (particularly Ba, Sr, and TiO_2 as well as MgO, FeO, TiO_2, Sr, Ba, La, and Ce, respectively) and are diverse in terms of their size. These features imply that the studied felsic rocks have a hybrid origin and were formed by mixing of the syenitic magma and the fractionated (most likely intermediate) derivative of the basanitic parental magma. The interaction between magmas of comparable temperature, rheological properties, and composition favored thorough mixing rather than mingling. This explains the lack of outcrop-to-macro-scale evidence (e.g., mafic microgranular enclaves) of open-system magmatic processes in the northern part of the DAM (between the Tarnița and Turcului Creeks).

Further fractionation of the hybrid magma and simultaneous crustal assimilation resulted in the formation of granite.

The last stage of the igneous event was marked by the intrusion of lamprophyre, ijolite, tinguaite, and (nepheline)syenite dykes.

ÖSSZEGZÉS

Bevezetés és célkitűzések

A Ditrói Alkáli Masszívum (DAM; Keleti-Kárpátok, Románia) egy középső-késő triász korú (Pál-Molnár et al., 2021) magmás komplexum, amely lemezen belüli, riftesedő, extenziós tektonikai környezetben alakult ki (pl. Morogan et al., 2000; Pál-Molnár, 2000, 2010b; Batki et al., 2014; Pál-Molnár et al., 2015b). A masszívum változatos kőzettani felépítésű, folyamatos átmenetet mutat az ultramafikus kumulátumoktól a granitoid kőzetekig. A DAM kőzeteit lamprofír, szienit és tinguait telérek járják át (Pál-Molnár, 2000; Batki et al., 2014; Pál-Molnár et al., 2015a, b). A DAM kiváló lehetőséget nyújt a kérget átszelő (*trans-crustal*) magmás rendszerek nyílt és zárt rendszerű magmás folyamatainak tanulmányozására. A ritkaföldfém (RFF) ércesedésnek köszönhetően a masszívum Európa egyik potenciális, gazdaságilag hasznosítható RFF-lelőhelye (Honour et al., 2018).

A masszívum 190 éves kutatástörténete során számos, gyakran egymásnak ellentmondó keletkezési modell látott napvilágot (pl. Streckeisen, 1938, 1960; Kräutner és Bindea, 1998; Morogan et al., 2000; Pál-Molnár, 2000). A DAM-hoz kapcsolódó korábbi kutatások során több kísérletet is tettek a magmás esemény korának megállapítására és a különböző „magmacsomagok" (*magma batches*) benyomulási sorrendjének meghatározására (pl. Streckeisen, 1952, 1954; Pál-Molnár és Árva-Sós, 1995; Kräutner és Bindea, 1998; Panǎ et al., 2000). A kutatás korai szakaszában Streckeisen (1954), Kräutner és Bindea (1998), valamint Morogan et al. (2000) is kihangsúlyozta a nyílt rendszerű magmás folyamatok szerepét a masszívum kőzeteinek kialakulásában. E folyamatok bizonyos részleteit a közelmúltbeli szerkezeti megfigyelések, valamint teljes kőzet- és ásványgeokémiai adatok (pl. Batki et al., 2018; Heincz et al., 2018; Ódri et al., 2020) segítségével sikerült feltárni. Néhány kivételtől eltekintve (pl. Streckeisen, 1954; Kräutner és Bindea, 1998; Morogan et al., 2000), a DAM északi területén felszínre bukkanó felzikus kőzeteket homogénnek és egységesnek tekintették. Batki et al. (2018) klinopiroxén antikristályokat írt le többek között dioritból és szienitből, felvetve a felzikus kőzetek újraértelmezésének szükségességét.

A doktori kutatás középpontjában a DAM északi részén feltáruló felzikus kőzetek állnak. A tanulmány célja: (1) a korábbi geokronológiai adatok felülvizsgálata, valamint új K/Ar és U–Pb radiometrikus korokkal történő kiegészítése; (2) a szisztematikusan begyűjtött és dokumentált új felzikus kőzetminták részletes petrográfiai vizsgálata; (3) a minták teljes kőzet- és ásványgeokémiai fő- és nyomelem összetételének meghatározása; (4) egy elméleti fejlődési modell kidolgozása a masszívummal kapcsolatos valamennyi újonnan szerzett ismeret alapján.

Alkalmazott vizsgálati módszerek

A DAM északi részén felszínre bukkanó felzikus kőzetek vizsgálata során a magmás kőzetek tanulmányozására általánosan használt módszereket (terepi megfigyelések, makroszkópos és mikroszkópos petrográfia, teljes kőzet- és ásvány fő- és nyomelem geokémia, K/Ar és U–Pb geokronológia) alkalmaztam.

A kormeghatározás egy korábban begyűjtött, archív mintasorozat kőzetein készült. A K/Ar kormeghatározást szeparált amfibol és biotit kristályokon, digitális lángfotométerrel és mágneses tömegspektrométerrel végezték a debreceni HUN-REN Atommagkutató Intézetben. Az U–Pb kormeghatározás standard gravitációs és mágneses módszerekkel szeparált titanit és cirkon kristályokon történt. A visszaszórt elektron (BSE) és katódlumineszcens (CL) képalkotást a budapesti Eötvös Loránd Tudományegyetem Kőzettani és Geokémiai Tanszékén és a frankfurti Johann Wolfgang Goethe Egyetem Földtudományi Tanszékén végezték el. Az *in situ* U–Pb kormeghatározást a göttingeni Georg-August Egyetem GÖochron Laboratóriumában, excimer lézer és Thermo Finnigan Element2 szektoros tömegspektrométer segítségével végezték el.

Az új mintasorozat kőzeteit 2019-ben és 2021-ben, két terepbejárás során gyűjtöttem be. A dokumentálás magában foglalta a GPS-koordináták, valamint a felzikus kőzetek és más kőzettípusok (pl. mellékkőzetek, telérek és mafikus kőzetek) terepi viszonyának rögzítését is. A vékonycsiszolatok a budapesti Eötvös Loránd Tudományegyetem Kőzettani és Geokémiai Tanszékén készültek el. A petrográfiai megfigyeléseket Brunel SP300P és Olympus BX41 optikai mikroszkópokkal végeztem a Szegedi Tudományegyetem Ásványtani, Geokémiai és Kőzettani Tanszékén. Egyes ásványfázisok meghatározásához a tanszéken rendelkezésre álló THERMO Scientific DXR Raman mikroszkópot használtam. Az összetételi zonációt és a mikroszöveti kapcsolatokat BSE képalkotással vizsgáltam egy EDAX PV 9800 EDS detektorral felszerelt AMRAY 1830 pásztázó elektronmikroszkóp (SEM) segítségével a budapesti Eötvös Loránd Tudományegyetem Kőzettani és Geokémia Tanszékén.

A teljes kőzet geokémiai vizsgálatra kiválasztott mintákat a vancouveri Bureau Veritas Mineral Laboratories (ACMELabs) elemezte. A főelemek koncentrációját ICP-ES eljárással határozták meg, míg a nyomelemeket (beleértve a ritkaföldfémeket is) ICP-MS módszerrel elemezték.

Az egyes ásványok fő- és nyomelem összetételét 30 μm vastagságú, polírozott vékonycsiszolatokból határoztam meg. Amfibol, klinopiroxén és plagioklász kristályok összetételét elemeztem, mivel ezek az ásványok szinte minden, a masszívum északi részén előforduló kőzettípusban jelen vannak. A lamprofir, valamint a plagioklász-tartalmú piroxén hornblendit amfibol és klinopiroxén kristályainak összetételét az összehasonlítás érdekében

vizsgáltam. Az „alapanyagban" [*groundmass;* az ún. befogadó kőzet (*host rock*) fanerokristályos, holokristályos, felzikus ásványokban gazdag tartományában] megjelenő izolált szemcséket, valamint az ásványaggregátumokat felépítő mafikus és felzikus ásványokat is elemeztem annak feltárására, hogy a különböző szöveti helyzetben előforduló kristályok összetételében mutatkozik-e eltérés. Az ásványok főelem összetételét az Orléans-i Földtudományi Intézet – Francia Nemzeti Tudományos Kutatóközpont, Cameca SX Five elektronmikroszondájával (EMPA) vizsgáltam. A nyomelemek (beleértve a ritkaföldfémeket is) elemzése során ugyanazokban a pontokban határoztam meg az ásványok összetételét, mint az EMPA mérések esetében. A nyomelem koncentrációkat szintén az Orléans-i Földtudományi Intézet – Francia Nemzeti Tudományos Kutatóközpontjában, LA-ICP-MS segítségével vizsgáltam, egy RESOlution SE lézerablációs rendszerrel, amelyhez egy Agilent 8900 QQQ induktív csatolású plazma tömegspektrométert csatlakoztattak.

Az eredmények tézisszerű összefoglalása

A Ditrói Alkáli Masszívum északi részén előforduló felzikus kőzetek integrált vizsgálata jelentős új eredményekkel szolgált a magmás esemény korát és időtartamát, a felzikus kőzetek szöveti heterogenitását, a kőzetalkotó mafikus és felzikus ásványok komplex történetét, a felzikus kőzetegyüttes fejlődését, valamint a masszívum kőzeteit létrehozó folyamatokat illetően.

T1 A Ditrói Alkáli Masszívum felzikus kőzetei egy rövid magmás eseményhez köthetően, a középső–késő triászban alakultak ki.

A felzikus magmatizmus korát és időtartamát új K/Ar (amfibol: nefelinszienit és gránit; biotit: gránit) és U–Pb (titanit és cirkon: nefelinszienit és szienit) korok alapján, valamint az archív koradatok újraértelmezésével pontosítottam. A szienitből származó titanit és cirkon U–Pb kora 225,3 ± 2,7, illetve 232,4 ± 3,3 millió év. A nefelinszienit amfiboljának K/Ar módszerrel meghatározott kora 216,0 ± 8,1 millió év; míg a titanit és a cirkon U–Pb kora 230,6 ± 3,5, illetve 230,6 ± 2,4 millió év. A gránitból származó amfibol és biotit K/Ar kora 196,3 ± 7,4 és 197,3 ± 7,4 millió év, illetve 198,3 ± 7,5 és 201,4 ± 7,6 millió év között változik. Az új és archív (1990 utáni) K/Ar és U–Pb koradatok figyelembevételével megállapítottam, hogy nincs jelentős időbeli eltérés a korai mafikus kumulátumok és a felzikus kőzetek kialakulása között. Ezek az eredmények cáfolják a korábbi, többfázisú fejlődési modelleket (pl. Pál-Molnár és Árva-Sós, 1995; Kräutner és Bindea, 1998; Morogan et al., 2000; Pál-Molnár, 2000, 2008) és arra utalnak, hogy a Ditrói Alkáli Masszívum egy viszonylag rövid időtartamú magmás esemény eredménye.

T2 A Ditrói Alkáli Masszívum északi részén felszínre bukkanó felzikus kőzetek a korábbi feltételezésekkel ellentétben jelentős mikroléptékű heterogenitást mutatnak.

A felzikus kőzeteket eddig többnyire a magmás komplexum homogén, egységes részének tekintették. A kőzetek részletes mikroszöveti vizsgálatával azonban bizonyítottam, hogy az Orotva-patak völgyétől északra előforduló felzikus kőzetek jelentős mikroléptékű heterogenitást mutatnak. A vizsgált kőzeteket két csoportba soroltam a terepi előfordulásuk és mikroszöveti bélyegeik alapján: 1. csoport – egyáltalán nem, vagy csak kis mennyiségben tartalmaz mafikus ásványokat, térben a mafikus kőzetekkel együtt fordul elő, illetve 2. csoport – mafikus ásványokat és ásványaggregátumokat tartalmaz, térben a mafikus kőzetektől függetlenül fordul elő. Az 1. csoport valamennyi kőzetében és a 2. csoport kőzeteinek némelyikében a felzikus ásványok akkumulációjának és a kristálykása kompakciójának mikroléptékű nyomai fedezhetők fel [pl. a földpátok irányított elrendeződése (*feldspar lamination*), földpát-gazdag aggregátumok („lánc szerkezet"; *chain structure*), egymásba ékelődő kristályok (*impingement*)].

T3 A 2. csoportba tartozó kőzetek mafikus ásványai általában különböző típusú aggregátumokban fordulnak elő, amelyek több, azonos vagy eltérő mafikus ásványszemcséből épülnek fel.

A 2. csoportba tartozó kőzetek mikroszöveti heterogenitása részben a petrográfiailag eltérő, különböző típusú mafikus kristálycsomók (*mafic aggregates/clots/clusters*) jelenlétéből ered. A vizsgált felzikus kőzetekben monomineralikus (zöld amfibol-, kék amfibol-, biotit- és epidot-gazdag) és polimineralikus (zöld amfibol + biotit; kék amfibol + biotit; amfibol + klinopiroxén + titanit + opak ásványok ± biotit) aggregátumokat különböztettem meg. Az ásványhalmazok egy része a prekurzor fázist (ante- és/vagy xenokristály) helyettesítő ásványokból áll és a különböző aggregátumok a bekebelezett szemcsék helyettesítésének különböző fázisait mutatják. A kristálycsomók jelenléte jelentősen megnöveli a mafikus ásványok modális részarányát a befogadó kőzetben. Mafikus finomszemcsés keveredési kőzetzárványokhoz (*mafic microgranular enclave*) kapcsolódó aggregátumokat nem azonosítottam; bizonyos típusok azonban metamorf mellékkőzet zárványokhoz köthetően fordulnak elő. Az „alapanyagban" önállóan előforduló mafikus ásványok mennyisége elhanyagolható.

T4 A mafikus és felzikus kristályok akkumulációja egyaránt jelentős szerepet játszott a Ditrói Alkáli Masszívum kialakulásában.

T4a A kumulusz klinopiroxén nyomelem összetétele alapján egy új mafikus kumulátum típus különböztethető meg.

Az ásványhalmazokban előforduló, konvex RFF-lefutású klinopiroxéneket korábban többek között diorit és szienit antekristályaként írták le. Azonos összetételű klinopiroxéneket azonosítottam kumulusz fázisként (autokristály) plagioklász-tartalmú piroxén hornblenditben, amely a nefelinszienit szülőolvadékának kumulátum fázisát képviseli. A klinopiroxén kristályok mobilizációjával magyarázható a felzikus kőzetek mafikus ásványaggregátumainak kialakulása, amelyek közül néhányban még felfedezhetők a klinopiroxén antekristályok maradványai.

T4b A felzikus kumulátumok két különböző eredetű típusa különböztethető meg a teljes kőzet fő- és nyomelem összetételük alapján.

A 2. csoport bizonyos monzonit és monzodiorit mintáit nagy Eu/Eu*-érték (2,5–6,7), kis ΣREE (125–206 ppm), valamint nagy La- és Sr-koncentráció jellemzi. Ezek a tulajdonságok, valamint a plagioklász jelentős modális részaránya és mikroszövete (pl. lánc szerkezet, egymásba ékelődő szemcsék) arra utalnak, hogy ezek a kőzetek kevésbé differenciált, korai felzikus kumulátumok. Ásványos összetételük, mikroszövetük és geokémiai jellemzőik alapján a Tarnița Komplexum felzikus xenolitjait korábban felzikus kumulátumokként írták le. Azonban ezeknek a kőzetzárványoknak a teljes kőzet összetétele eltér a 2. csoportba sorolt monzonit és monzodiorit összetételétől, amelyből arra következtettem, hogy különböző szülőmagmák felzikus kumulátumait képviselik.

T5 A vizsgált kőzetek teljes kőzet összetételen alapuló nevéktana félrevezető lehet a kumulátum képződés és a magmás rendszer eltérő régióiból származó ásványok bekebelezése miatt.

A vizsgált kőzetek többsége kumulátum vagy részleges kumulátum, amelyeket a felzikus ásványok élterő modális részarányú felhalmozódása jellemez. Ezen kívül néhány minta mafikus ásványok aggregátumait tartalmazza, amelyek némelyikében még azonosítható a prekurzor antekristály. Rámutattam, hogy a teljes kőzet összetételre vonatkozó adatokat kellő körültekintéssel kell kezelni, mivel a kumulátum képződés (mind a mafikus, mind a felzikus) és a különböző eredetű kristályok bekebelezése (*entrainment*) jelentős hatással van a kőzetek modális ásványos és ezen keresztül a teljes kőzet geokémiai összetételére. Ezek az eredmények megkérdőjelezik a hagyományos, teljes kőzet összetételen alapuló nevéktan használatát és

bizonyítják, hogy a mikroszöveti vizsgálatok és az ásványgeokémiai elemzések együttes értelmezése elengedhetetlen a kőzetek megfelelő nevéktanának kiválasztásához, valamint a plutonok kialakulása során lejátszódó folyamatok megértéséhez.

T6 A Ditrói Alkáli Masszívum elméleti fejlődéstörténeti modelljének felállítása a rendelkezésre álló ismeretek alapján.

A DAM kőzeteit két, különböző szülőmagmából származó magmacsomagok benyomulása és kölcsönhatása alakította ki egy nyílt rendszerű magmás környezetben.

Kétféle, eltérő összetételű felzikus kumulátum alakult ki a magmatározó azon régióiban, ahol a konvekció korlátozott volt. Nemcsak felzikus, hanem (ultra)mafikus kumulátumok is keletkeztek. Utóbbiak a kumulusz klinopiroxén összetétele alapján különböztethetők meg; a kumulusz amfibol kristályok azonban hasonló geokémiai jellemzőket mutatnak. A plagioklász-tartalmú piroxén hornblenditben előforduló, a magjukban primitív klinopiroxén kristályokat tartalmazó kerekded zárványok (*orbicular inclusions*) jelenléte arra utal, hogy a két szülőmagma már a magmás rendszer mélyebb régióiban is kölcsönhatásba lépett egymással. Az ijolitos kőzetzárványokat tartalmazó tinguait a szülőmagmák frakcionált olvadékainak keveredésével (*magma mingling*) jött létre.

A szienit magma a nefelinszienit szülőolvadékának kéregasszimilációjával keletkezett.

A tanulmányban vizsgált felzikus kőzetek teljes kőzet összetétele részben átfed a szienit–gránit sorozat és a Tarnița Komplexum magmakeveredéssel keletkezett kőzeteinek [diorit (*s.l.*), monzodiorit és monzonit] összetételével és összeköti azok trendjeit. A változatos szemcseméretű amfibol- és plagioklász kristályokat eltérő zonáció és elemkoncentráció (különösen a Ba, Sr és TiO_2, illetve a MgO, FeO, TiO_2, Sr, Ba, La, Ce esetében) jellemzi. Ezek a tulajdonságok arra utalnak, hogy a vizsgált felzikus kőzetek hibrid eredetűek, a szienit magma és a bazanitos szülőmagma frakcionált (valószínűleg intermedier) olvadékának kölcsönhatásából keletkeztek. A hasonló hőmérsékletű, reológiai tulajdonságú és összetételű magmák közötti kölcsönhatás magmaelegyedésnek (*magma mixing*) kedvezett. Ezzel magyarázható, hogy a DAM északi részén (a Tarnița- és a Török-patak közötti területen) nem fedezhetők fel nyílt rendszerű magmás folyamatokra utaló, feltárás- és makroléptékű szerkezeti elemek (pl. mafikus finomszemcsés keveredési kőzetzárványok).

A gránitok a hibrid magma további frakcionációjával és az ezzel egyidőben végbemenő kéregasszimilációval alakultak ki.

A magmás esemény utolsó szakaszát a lamprofír, ijolit, tinguait és (nefelin)szienit telérek benyomulása jellemezte.

I would like to give a toast to the international group of *Fellow PhD Students* at the Department of Mineralogy, Geochemistry and Petrology, University of Szeged, Szeged, Hungary, for their great company and support, for the countless (and sometimes endless) coffee and lunch breaks, and for all the fun activities inside and outside the PhD room.

I thank the *Staff of the Department of Mineralogy, Geochemistry and Petrology*, University of Szeged, Szeged, Hungary, for the friendly and supportive daily work environment.

I am extremely grateful to my *Family*, especially my *Parents* for their eternal love, support, and encouragement. They provided a stable background so that all I had to worry (a lot) about was my studies and research. This PhD Dissertation is as much their accomplishment as it is mine. I will never forget the seemingly infinite summer vacations I spent abroad with my *Dad* in the shadow of the land drilling rigs. I have fond memories of the rock and fossil hunts that later gave place to crossing high mountain passes, both on foot and in *Trusty Thalia*, the best expedition vehicle ever. I suspect, I got infected with geology then and there; although, it was successfully incubated for a long time. My *Mom* – the Superhost of the well-reviewed Mama Hotel in my hometown of Sándorfalva – deserves a great deal of thanks for always being by my side. I am obliged for her emotional support and for keeping me grounded. She allowed me to follow my instincts regarding my studies, even though this field was not the initial plan. *Mátyás Pányoki* should not go unmentioned, as he never failed to cheer me up and was always ready to do something crazy.

I am grateful to the *Lost Dot* Team (with *Anna Haslock* at the helm) and *Nelson Trees* as well as the ultracycling community of *The Transcontinental Race* and *Silk Road Mountain Race*. I have gained a lot of inspiration, confidence, and courage from the stories of the riders (especially *Jenny Tough*), the locals, and the fellow control point volunteers.

Oddly enough, I would also like to praise *myself* for being brave enough to start this project and then see it through to completion. This entire journey, from my first days as a PhD student to pressing "send" on the third manuscript (twice), has nourished my personal growth and accompanied me through more than five years of my life and everything it has thrown at me. It has been uncomfortable in many ways and I am proud of myself for committing to the challenge every day.

Finally, here is to all the *toxic, negative people* I have come across so far (there have been a lot). They subtly sowed the seeds of doubt but deep inside I always knew I had much more to give and it spurred me on in a certain way. In the back of my mind, there was always that thing of trying to prove them wrong and it has become my greatest motivation to complete my PhD studies.

REFERENCES

Aleinikoff, J.N., Wintsch, R.P., Tollo, R.P., Unruh, D.M., Fanning, C.M., Schmitz, M.D. (2007). Ages and origins of rocks of the Killingworth dome, south-central Connecticut: implications for the tectonic evolution of southern New England. American Journal of Science, 307, 63–118.

Almási, E.E., Batki, A., Kiss, B. (2015). Amfibolok petrogenetikai jelentősége a Ditrói alkáli masszívum ultramafikus kumulátumkőzeteiben (Petrogenetic significance of amphiboles in the ultramafic rocks of the Ditrău Alkaline Massif). Földtani Közlöny, 145(3), 229–246 (in Hungarian).

Anastasiu, N., Constantinescu, E. (1979). Structura și petrogeneza masivului alcalin de la Ditrău (Structure and petrogenesis of the Ditrău Alkaline Massif). Raport geologic final. Arhiva IPEG "Harghita", Miercurea-Ciuc, manuscript (in Romanian).

Anderson, A.T. (1984). Probable relation between plagioclase zoning and magma dynamics, Fuego Volcano, Guatemala. American Mineralogist, 69, 660–676.

Annen, C., Blundy, J.D., Leuthold, J., Sparks, R.S.J. (2015). Construction and evolution of igneous bodies: Towards an integrated perspective of crustal magmatism. Lithos, 230, 206–221.

Bachmann, O., Bergantz, G.W. (2004). On the origin of crystal-poor rhyolites: extracted from batholithic crystal mushes. Journal of Petrology, 45, 1565–1582.

Bagdasarian, G.P. (1972). Despre vîrsta absolută a unor roci eruptive și metamorfice din masivul Ditrău și Munții Banatului din Romănia (About the absolute age of some eruptive and metamorphic rocks from the Ditrău massif and Banat Mountains in Romania). Studii și Cercetări Geologie, Geofizică, Geografie, Seria Geologie, 17(1), 13–21 (in Romanian).

Baker, D.R. (1996). Granitic melt viscosities and configurational entropy models for their calculations. American Mineralogist, 81, 126–134.

Baker, D.R. (1998). Granitic melt viscosity and dike formation. Journal of Structural Geology, 20, 1395–1404.

Balintoni, I. (1997). Geotectonica terenurilor metamorfice din România (Geotectonics of metamorphic terrains in Romania). Carpatica, Cluj Napoca, 176 p (in Romanian).

Balintoni, I., Balica, C. (2013). Carpathian peri-Gondwanan terranes in the East Carpathians (Romania): a testimony of an Ordovician, North-African orogeny. Gondwana Research, 23(3), 1053–1070.

Balintoni, I., Balica, C., Ducea, H., Horst-Peter, H. (2014). Peri-Gondwanan terranes in the Romanian Carpathians: a review of their spatial distribution, origin, provenance, and evolution. Geoscience Frontiers, 5(3), 395–411.

Balintoni, I., Gheuca, I., Vodă, Al. (1983). Pânze de încălecare Alpine și Hercinice din zona sudică și centrală a Zonei Cristalino Mezozoice din Carpații Orientali. (Alpine and Hercynian overthrust nappes from central and southern areas of the East Carpathians Crystalline Mesozoic Zone). Anuarul Instutului de Geologie și Geofizică al României, 60, 15–22 (in Romanian).

Balogh, K. (1985). K/Ar dating of Neogene volcanic activity in Hungary: experimental technique, experiences and methods of chronological studies. Atomki Közlemények, 27(3), 277–288.

Barbarin, B. (1990). Plagioclase xenocrysts and mafic magmatic enclaves in some granitoids of the Sierra Nevada Batholith, California. Journal of Geophysical Research, 95(B11), 17747–17756.

Barnes, C.G., Berry, R., Barnes, M.A., Ernst, W.G. (2017). Trace element zoning in hornblende: Tracking and modeling the crystallization of a calc-alkaline arc pluton. American Mineralogist, 102, 2390–2405.

Barnes, C.G., Memeti, V., Coint, N. (2016). Deciphering magmatic processes in calc-alkaline plutons using trace element zoning in hornblende. American Mineralogist, 101, 328–342.

Bateman, R. (1995). The interplay between crystallization, replenishment and hybridisation in large felsic magma chambers. Earth-Science Reviews, 39, 91–106.

Batki, A., Pál-Molnár, E., Bárdossy, A. (2004). Occurrence and petrology of lamprophyres from the northern part of the Ditrău Alkaline Massif, Eastern Carpathians, Romania. Acta Mineralogica-Petrographica, 45(2), 21–28.

Batki, A., Pál-Molnár, E., Dobosi, G., Skelton, A. (2014). Petrogenetic significance of ocellar camptonite dykes in the Ditrău Alkaline Massif, Romania. Lithos, 200–201, 181–196.

Batki, A., Pál-Molnár, E., Jankovics, M.É., Kerr, A.C., Kiss, B., Markl, G., Heincz, A., Harangi, Sz. (2018). Insights into the evolution of an alkaline magmatic system: An in situ trace element study of clinopyroxenes from the Ditrău Alkaline Massif, Romania. Lithos, 300–301, 51–71.

Baxter, S., Feely, M. (2002). Magma mixing and mingling textures in granitoids: examples from the Galway Granite, Connemara, Ireland. Mineralogy and Petrology, 76, 63–74.

Bea, F. (2010). Crystallization dynamics of granite magma chambers in the absence of regional stress: Multiphysics modeling with natural examples. Journal of Petrology, 51(7), 1541–1569.

Bergantz, G.W. (1989). Underplating and partial melting: Implications for melt generation and extraction. Science, 245, 1093–1095.

Bindea, G., Nakano, S., Makino, K. (2020). Multi-stage reorganizations of feldspars in felsic rocks of the Ditrău Alkaline Intrusive Complex, Romania. Carpathian Journal of Earth and Environmental Sciences, 15(2), 491–514.

Bird, D.K., Spieler, A.R. (2004). Epidote in geothermal systems. Reviews in Mineralogy and Geochemistry, 56, 235–300.

Blundy, J.D., Shimizu, N. (1991). Trace element evidence for plagioclase recycling in calc-alkaline magmas. Earth and Planetary Science Letters, 102, 178–197.

Blundy, J.D., Wood, B.J. (1991). Crystal-chemical controls on the partitioning of Sr and Ba between plagioclase feldspar, silicate melts, and hydrothermal solutions. Geochimica et Cosmochimica Acta, 55, 193–209.

Brothers, R.N. (1964). Petrofabric analyses of Rhum and Skaergaard layered rocks. Journal of Petrology, 6, 255–274.

Brown, G.M. (1956). The layered ultrabasic rocks of Rhum, Inner Hebrides. Philosophical Transactions of the Royal Society of London, Series B, Biological Sciences, 240, 1–53.

Burchardt, S. (Ed.) (2018). Volcanic and igneous plumbing systems: Understanding magma transport, storage and evolution in the Earth's crust. Elsevier, Amsterdam, 341 p.

Campos, T.F.C., Neiva, A.M.R., Nardi, L.V.S. (2002). Geochemistry of the Rio Espinharas hybrid complex, northeastern Brazil. Lithos, 64, 131–153.

Carvalho, B.B., Sawyer, E.W., Janasi, V.A. (2017). Enhancing maficity of granitic magma during anatexis: entrainment of infertile mafic lithologies. Journal of Petrology, 58(7), 1333–1362.

Cashman, K.V., Sparks, R.S.J., Blundy, J.D. (2017). Vertically extensive and unstable magmatic systems: A unified view of igneous processes. Science, 355, eaag3055.

Castellarin, A., Lucchini, F., Rossi, P.L., Sartori, R., Simboli, G., Sommavilla, E. (1982). Note geologiche sulle intrusioni di Predazzo e dei M. Manzoni (Geological notes on the Predazzo and M. Manzoni intrusions). In: Castellarin, A., Vai, G.B. (Eds.): Guida alla geologia del Sudalpino Centro-Orientale. Guide Geol. Reg. Societa Geologica Italiana, Bologna, pp. 211–219 (in Italian).

Castro, A., Stephens, W.E. (1992). Amphibole-rich polycrystalline clots in calc-alkaline granitic rocks and their enclaves. Canadian Mineralogist, 30, 1093–1112.

Channell, J.E.T., Kozur, H.W. (1997). How many oceans? Meliata, Vardar and Pindos oceans in Mesozoic Alpine paleogeography. Geology, 25, 183–186.

Chappell, B.W. (1978). Granitoids from the Moonbi district, New England Batholith, eastern Australia. Journal of the Geological Society of Australia, 25, 267–284.

Chappell, B.W., White, A.J.R., Wyborn, D. (1987). The importance of residual source material (restite) in granite petrogenesis. Journal of Petrology, 28(6), 1111–1138.

Cherniak, D.J. (1993). Lead diffusion in titanite and preliminary results on the effects of radiation damage on Pb transport. Chemical Geology, 110, 177–194.

Cherniak, D.J., Watson, E.B. (2001). Pb diffusion in zircon. Chemical Geology, 172, 5–24.

Chivas, A.R. (1981). Geochemical evidence for magmatic fluids in porphyry copper mineralization. Contributions to Mineralogy and Petrology, 78, 389–403.

Choe, W.H., Jwa, Y.J. (2004). Petrological and geochemical evidences for magma mixing in the Palgongsan Pluton. Geosciences Journal, 8(4), 343–354.

Clemens, J.D., Petford, N., Mawer, C.K. (1997). Ascent mechanisms of granitic magmas: Causes and consequences. In: Holness, M.B. (Ed.): Deformation-enhanced fluid transport in the Earth's crust and mantle. Mineralogical Society Series, Chapman and Hall, London, 8, pp. 145–172.

Codarcea, Al., Codarcea, D.M., Ianovici, V. (1957). Structura geologică a masivului de roci alcaline de la Ditrău (Geological structure of the Ditrău alkali rock massif). Buletin Științific R. P. R. Geologie, Geografie, 2(3–4), 385–446 (in Romanian).

Codarcea, Al., Ianovici, V., Iova, I., Lupan, S., Papacostea, C. (1958). Elemente rare în masivul de la Ditrău (Rare elements in the Ditrău massif). Com. Acad. R. P. R., 8(3), 321–326 (in Romanian).

Cohen, K.M., Finney, S.C., Gibbard, P.L., Fan, J.-X. (2013, updated). The ICS International Chronostratigraphic Chart. Episodes, 36, 199–204.

Coint, N., Barnes, C.G., Yoshinobu, A.S., Barnes, M.A., Buck, S. (2013). Use of trace element abundances in augite and hornblende to determine the size, connectivity, timing, and evolution of magma batches in a tilted batholith. Geosphere, 9(6), 1747–1765.

Coleman, D.S., Gray, W., Glazner, A.F. (2004). Rethinking the emplacement and evolution of zoned plutons: geochronologic evidence for incremental assembly of the Tuolumne Intrusive Suite, California. Geology, 32(5), 433–436.

Collins, W.J., Wiebe, R.A., Healy, B., Richards, S.W. (2006). Replenishment, crystal accumulation and floor aggradation in the megacrystic Kameruka Suite, Australia. Journal of Petrology, 47, 2073–2104.

Costa, F. (2021). Clocks in magmatic rocks. Annual Review of Earth and Planetary Sciences, 49, 231–252.

Cross, W., Iddings, J.P., Pirrson, L.V., Washington, H.S. (1902). A quantitative chemicomineralogical classification and nomenclature of igneous rocks. Journal of Geology, 10, 555–590.

Cruden, A.R., Weinberg, R.F. (2018). Mechanisms of magma transport and storage in the lower and middle crust – Magma segregation, ascent and emplacement. In: Burchardt, S. (Ed.): Volcanic and igneous plumbing systems: Understanding magma transport, storage and evolution in the Earth's crust. Elsevier, Amsterdam, pp. 13–53.

Dallmeyer, D.R., Kräutner, H.G., Neubauer, F. (1997). Middle-late Triassic $^{40}Ar/^{39}Ar$ hornblende ages for early intrusions within the Ditrău alkaline massif, Rumania: implications for Alpine rifting in the Carpathian orogen. Geologica Carpathica, 48, 347–352.

Deering, C.D., Bachmann, O. (2010). Trace element indicators of crystal accumulation in silicic igneous rocks. Earth and Planetary Science Letters, 297, 324–331.

Didier, J. (1987). Contribution of enclave studies to the understanding of origin and evolution of granitic magmas. Geologische Rundschau, 76(1), 41–50.

Didier, J., Barbarin, B. (Eds.) (1991). Enclaves and Granite Petrology. Developments in Petrology, vol. 13, Elsevier, Amsterdam, 626 p.

Dingwell, D.B., Romano, C., Hess, K.-U. (1996). The effect of water on the viscosity of a haplogranitic melt under P-T-X conditions relevant to silicic volcanism. Contributions to Mineralogy and Petrology, 124, 19–28.

Dingwell, D.B., Scarfe, C.M., Cronin, D.J. (1985). The effect of fluorine on viscosities in the system $Na_2O–Al_2O_3–SiO_2$: implications for phonolites, trachytes and rhyolites. American Mineralogist, 70, 80–87.

Dodson, M.H., McClelland-Brown, E. (1985). Isotopic and palaeomagnetic evidence for rates of cooling, uplift and erosion. Geological Society London Memoirs, 10(1), 315–325.

Fall, A., Bodnar, R.J., Szabó, Cs., Pál-Molnár, E. (2007). Fluid evolution in the nepheline syenites of the Ditrău Alkaline Massif, Transylvania, Romania. Lithos, 95, 331–345.

Féménias, O., Coussaert, N., Brassinnes, S., Demaiffe, D. (2005). Emplacement processes and cooling history of layered cyclic unit II-7 from the Lovozero alkaline massif (Kola Peninsula, Russia). Lithos, 83, 371–393.

Fernandez, A.N., Barbarin, B. (1991). Relative rheology of coeval mafic and felsic magmas: nature of resulting interaction process. Shape and mineral fabrics of mafic microgranular enclaves. In: Didier, J., Barbarin, B. (Eds.): Enclaves and granite petrology. Developments in Petrology, Elsevier, Amsterdam, 13, pp. 263–276.

Foster, C.T. (1986). Thermodynamic models of reactions involving garnet in a sillimanite/staurolite schist. Mineralogical Magazine, 50, 427–439.

Frei, D., Gerdes, A. (2009). Precise and accurate in situ U-Pb dating of zircon with high sample throughput by automated LASF-ICP-MS. Chemical Geology, 261(3–4), 261–270.

Frost, T.P., Mahood, G.A. (1987). Field, chemical and physical constraints on mafic-felsic interaction in the Lamarck Granodiorite, Sierra Nevada, California. Geological Society of America Bulletin, 99, 272–291.

Ginibre, C., Worner, G., Kronz, A. (2002). Minor- and trace-element zoning in plagioclase: implications for magma chamber processes at Parinacota volcano, northern Chile. Contributions to Mineralogy and Petrology, 143, 300–315.

Glazner, A.F., Bartley, J.M., Coleman, D.S., Gray, W., Taylor, R.Z. (2004). Are plutons assembled over millions of years by amalgamation from small magma chambers? GSA Today, 14(4/5), 4–12.

Grogan, S.E., Reavy, R.J. (2002). Disequilibrium textures in the Leinster Granite Complex, SE Ireland: evidence for acid-acid magma mixing. Mineralogical Magazine, 66(6), 929–939.

Gros, K., Słaby, E., Birski, L., Kozub-Budzyń, G., Sláma, J. (2020). Geochemical evolution of a composite pluton: insight from major and trace element chemistry of titanite. Mineralogy and Petrology, 114, 375–401.

Haas, J., Budai, T., Csontos, L., Fodor, L., Konrád, Gy. (2010). Pre-Cenozoic geological map of Hungary 1:500 000. Geological Institute of Hungary, Budapest.

Harrison, T.M. (1981). Diffusion of ^{40}Ar in hornblende. Contributions to Mineralogy and Petrology, 78, 324–331.

Harrison, T.M., McDougall, I. (1980). Investigations of an intrusive contact, northwest Nelson, New Zealand, II. Diffusion of radiogenic and excess ^{40}Ar in hornblende revealed by ^{40}Ar/^{39}Ar age spectrum analysis. Geochimica et Cosmochimica Acta, 44, 2005–2020.

Hart, S.R. (1961). The use of hornblendes and pyroxenes for K-Ar dating. Journal of Geophysical Research, 66(9), 2995–3001.

Hattori, K., Sato, H. (1996). Magma evolution recorded in plagioclase zoning in 1991 Pinatubo eruption products. American Mineralogist, 81, 982–994.

Heincz, A., Pál-Molnár, E., Kiss, B., Batki, A., Almási, E.E., Kiri, L. (2018). Nyílt rendszerű magmás folyamatok: magmakeveredés, kristálycsere, kumulátum recirkuláció nyomai a Ditrói Alkáli Masszívumban (Orotva, Románia) [Open-system magmatic processes: magma mingling, crystal transfer and cumulate recycling in the Ditrău Alkaline Massif (Jolotca, Romania)]. Földtani Közlöny, 148(2), 125–142 (in Hungarian).

Hendry, D.A.F., Chivas, A.R., Long, J.V.P., Reed, S.J.B. (1985). Chemical differences between minerals from mineralizing and barren intrusions from some North American porphyry copper deposits. Contributions to Mineralogy and Petrology, 89, 317–329.

Hibbard, M.J. (1981). The magma mixing origin of mantled feldspars. Contributions to Mineralogy and Petrology, 76, 158–170.

Hibbard, M.J. (Ed.) (1995). Petrography to petrogenesis. Prentice Hall, Englewood Cliffs, New Jersey, 587 p.

Hildreth, W. (1979). The Bishop Tuff: evidence for the origin of compositional zonation in silicic magma chambers. Geological Society of America Special Papers, 180, 43–76.

Hildreth, W., Moorbath, S. (1988). Crustal contributions to arc magmatism in the Andes of Central Chile. Contributions to Mineralogy and Petrology, 98, 455–489.

Hoeck, V., Ionescu, C., Balintoni, I., Koller, F. (2009). The Eastern Carpathians „ophiolites" (Romania): Remnants of a triassic ocean. Lithos, 108, 151–171.

Holness, M.B., Stock, M.J., Geist, D. (2019). Magma chambers versus mush zones: constraining the architecture of sub-volcanic plumbing systems from microstructural analysis of crystalline enclaves. Philosophical Transactions of The Royal Society A, 377:20180006.

Honour, V.C., Goodenough, K.M., Shaw, R.A., Gabudianu, I., Hirtopanu, P. (2018). REE mineralisation within the Ditrău Alkaline Complex, Romania: Interplay of magmatic and hydrothermal processes. Lithos, 314–315, 360–381.

Huang, F., Scaillet, B., Wang, R., Erdmann, S., Chen, Y., Faure, M., Liu, H., Xie, L., Wang, B., Zhu, J. (2019). Experimental constraints on intensive crystallization parameters and fractionation in A-type granites: a case study on the Qitianling Pluton, South China. Journal of Geophysical Research, Solid Earth, 124, 10132–10152.

Huang, X.-D., Lu, J.-J., Sizaret, S., Wang, R.-C., Wu, J.-W., Ma, D.-S. (2018). Reworked restite enclave: petrographic and mineralogical constraints from the Tongshanling intrusion, Nanling Range, South China. Journal of Asian Earth Sciences, 166, 1–18.

Hughes, C.J. (Ed.) (1982). Igneous Petrology. Developments in Petrology, Elsevier, Amsterdam, 7, 551 p.

Ildefonse, B., Fernandez, A. (1988). Influence of the concentration of rigid markers in a viscous medium on the production of preferred orientations. An experimental contribution: 1. Non coaxial strain. Bulletin of the Geological Institutions of the University of Uppsala, 14, 55–60.

Jackson, M.D., Blundy, J., Sparks, R.S.J. (2018). Chemical differentiation, cold storage and remobilization of magma in the Earth's crust. Nature, 564, 405–409.

Jackson, S.E., Pearson, N.J., Griffin, W.L., Belousova, E.A. (2004). The application of laser ablation-inductively coupled plasma-mass spectrometry to in situ U–Pb zircon geochronology. Chemical Geology, 211, 47–69.

Jakab, Gy. (1998). Geologia Masivului alcalin de la Ditrău (Geology of the Alkaline Massif of Ditrău). Pallas-Akademia, Miercurea-Ciuc (in Romanian).

Jakab, Gy., Garbaşevschi, N., Balla, Z., Zakariás, L., Péter, J., Strungaru, T., Hereda, N., Sileanu, T., Aronescu, M., Postolache, C., Mocanu, V., Teulea, G., Hannich, D., Tiepac, I. (1987). Sinteza datelor obţinute prin prospecţiuni geologice complexe, lucrări miniere şi foraje, executate pentru minereuri de metale rare şi disperse, feroase şi neferoase în masivul de roci alcaline de la Ditrău, jud. Hargita (Synthesis of data obtained from complex geological prospecting, mining and drilling for rare and dispersed ferrous and non-

ferrous metal ores in the Ditrău alkaline massif). Arhiva IPEG „Harghita”, Miercurea-Ciuc, manuscript (in Romanian).

Jerram, D.A., Dobson, K.J., Morgan, D.J., Pankhurst, M.J. (2018). In: Burchardt, S. (Ed.): Volcanic and igneous plumbing systems: Understanding magma transport, storage and evolution in the Earth's crust. Elsevier, Amsterdam, 192–229.

Kahl, M., Chakraborty, S., Costa, F., Pompilio, M. (2011). Dynamic plumbing system beneath volcanoes revealed by kinetic modelling and the connection to monitoring data: An example from Mt. Etna. Earth and Planetary Science Letters, 308, 11–22.

Kahl, M., Chakraborty, S., Pompilio, M., Costa, F. (2015). Constraints on the nature and evolution of the magma plumbing system of Mt. Etna volcano (1991–2008) from a combined thermodynamic and kinetic modelling of the compositional record of minerals. Journal of Petrology, 56(10), 2025–2068.

Kahl, M., Viccaro, M., Ubide, T., Morgan, D.J., Dingwell, D.B. (2017). A branched magma feeder system during the 1669 eruption of Mt. Etna: evidence from a time-integrated study of zoned olivine phenocryst populations. Journal of Petrology, 58(3), 443–472.

Kennedy, A.K., Kamo, S.L., Nasdala, L., Timms, N.E. (2010). Grenville skarn titanite: potential reference material for SIMS U–Th–Pb analysis. Canadian Mineralogist, 48, 1423–1443.

Kiri, L. (2018). Magmakeveredés nyomai a Ditrói Alkáli Masszívum szienit kőzeteiben (Traces of magma mixing and mingling in syenites of the Ditrău Alkaline Massif). Masters Thesis, University of Szeged, Szeged, 85 p (in Hungarian).

Kiri, L., Szemerédi, M., Pál-Molnár, E. (2022). Petrographic evidences of open-system magmatic processes in the felsic rocks of the northern part of the Ditrău Alkaline Massif (Eastern Carpathians, Romania). Central European Geology, 65(1), 49–76.

Klaver, M., Matveev, S., Berndt, J., Lissenberg, C.J., Vroon, P.Z. (2017). A mineral and cumulate perspective to magma differentiation at Nisyros volcano, Aegean arc. Contributions to Mineralogy and Petrology, 172, 95.

Klötzli, U., Burda, J., Li, Q.-L., Liu, Y., Jakab, Gy., Ionescu, L., Tibuleac, P. (2022). Petrochronological evidence for a three-stage magmatic evolution of the youngest nepheline syenites from the Ditrău Alkaline Massif, Romania. Minerals, 12(5), 657.

Kobylinski, C., Hattori, K., Smith, S., Plouffe, A. (2020). Protracted magmatism and mineralized hydrothermal activity at the Gibraltar Porphyry copper-molybdenum deposit, British Columbia. Economic Geology, 115(5), 1119–1136.

Koch, A. (1876). Erdély keleti részének némely geológiai viszonyai (Geology of Eastern Transylvania). Előadás, Kolozsvári orv. term. tud. társulat 1876. évi értesítője (in Hungarian).

Koch, A. (1879). A ditrói szyenittömzs kőzettani és hegyszerkezeti viszonyairól (Petrology and structure of the Ditrău syenite massif). Magyar Tudományos Akadémia, Értekezések, 9(2) (in Hungarian).

Kovács, G., Pál-Molnár, E. (2005). A Ditrói alkáli masszívum granitoid kőzeteinek petrogenezise [Petrogenesis of the granitoid rocks of the Ditrău Alkaline Massif (Transylvania, Romania)]. Földtani Közlöny, 135(1), 121–143 (in Hungarian).

Kozur, H. (1991). The evolution of the Meliata-Hallstatt ocean and its significance for the early evolution of the Eastern Alps and Western Carpathians. Palaeogeography, Palaeoclimatology, Palaeoecology, 87, 109–135.

Kräutner, H.G. (1996–1997). Alpine and pre-Alpine terranes in the Romanian Carpathians and Apuseni Mountains. In: Papanikolaou, D. (Ed.): Terrane maps and terrane descriptions. IGCP Project No. 276. Annales Geologiques des Pays Helleniques, Athens, pp. 331–400.

Kräutner, H.G., Bindea, G. (1995). The Ditrău alkaline intrusive complex and its geological environment. Romanian Journal of Mineralogy, 77(3), 1–44.

Kräutner, H.G., Bindea, G. (1998). Timing of the Ditrău alkaline intrusive complex (Eastern Carpathians, Romania). Slovak Geological Magazine, 4, 213–221.

Kräutner, H.G., Kräutner, Fl., Tănăsescu, A., Neacşu, V. (1976). Interpretation des âges radiometriques K–Ar pour les roches métamorphiques régénérées. Un exemple – les Carpates Orientales (Interpretation of radiometric K-Ar ages for metamorphic rocks. An example – the Eastern Carpathians). Analele Institutului de Geologie, 50, 167–229 (in French).

Kriegsman, L.M. (2001). Partial melting, partial melt extraction and partial back reaction in anatectic migmatites. Lithos, 56, 75–96.

Kumar, S., Singh, R.N. (Eds.) (2014). Modelling of magmatic and allied processes. Springer International Publishing, Switzerland, 246 p.

Lavaure, S., Sawyer, E.W. (2011). Source of biotite in the Wuluma Pluton: replacement of ferromagnesian phases and disaggregation of enclaves and schlieren. Lithos, 125, 757–780.

Le Maitre, R.W., Streckeisen, A., Zanettin, B., Le Bas, M.J., Bonin, B., Bateman, P., Bellieni, G., Dudek, A., Efremova, S., Keller, J., Lameyre, J., Sabine, P.A., Schmid, R., Sørensen, H., Woolley, A.R. (Eds.) (2002). Igneous rocks: A classification and glossary of terms. Recommendations of the IUGS Subcommission on the Systematics of Igneous Rocks. Cambridge University Press, Cambridge, 236 p.

Leake, B.E. (1978). Nomenclature of amphiboles. American Mineralogist, 63, 1023–1052.

Leake, B.E., Woolley, A.R., Arps, C.E.S., Birch, W.D., Gilbert, M.C., Grice, J.D., Hawthorne, F.C., Kato, A., Kisch, H.J., Krivovichev, V.G., Linthout, K., Laird, J., Mandarino, J.A., Maresch, W.V., Nickel, E.H., Rock, N.M.S., Schumacher, J.C., Smith, D.C., Stephenson, N.C.N., Ungaretti, L., Whittaker, E.J.W., Youzhi, G. (1997). Nomenclature of amphiboles: report on the Subcommittee on Amphiboles of the International Mineralogical Association, Commission on New Minerals and Mineral Names. American Mineralogist, 82, 1019–1037.

Lilienbach, L. (1833). Journal d'un voyage géologique fait en travers toute la chaíne des Carpathes, en Bucovine, en Transylvanie et dans le Marmarosch (Diary of a geological journey through the whole Carpathian chain, in Bucovina, Transylvania and Maramureș). Mémoires de la Société géologique de France, 1, 237–316 (in French).

Marks, M., Halama, R., Wenzel, T., Markl, G. (2004). Trace element variations in clinopyroxene and amphibole from alkaline to peralkaline syenites and granites: implications for mineral–melt trace-element partitioning. Chemical Geology, 211, 185–215.

Marsh, B. (2004). A magmatic mush column rosetta stone: the McMurdo Dry Valleys of Antarctica. Eos, Transactions American Geophysical Union, 85(47), 497–502.

Miller, C.F., Miller, J.S. (2002). Contrasting stratified plutons exposed in tilt blocks, Eldorado Mountains, Colorado River Rift, NV, USA. Lithos, 61, 209–224.

Milord, I., Sawyer, E.W. (2003). Schlieren formation in diatexite migmatite: examples from the St Malo migmatite terrane, France. Journal of Metamorphic Geology, 21, 347–362.

Mînzatu, S., Ardeleanu, P. (1980). Raport: Cercetări radiometrice de detaliu în masivul Ditrău. (Detailed radiometric research in the Ditrău massif). Arhiva IPEG „Harghita", Miercurea-Ciuc, manuscript (in Romanian).

Mînzatu, S., Văjdea, E., Romanescu, O., Iosipcenco, N. (1981). Vârste K-Ar din masivul Ditrău (K-Ar ages of the Ditrău massif). Arhiva IGG, Bucuresti, manuscript (in Romanian).

Miyashiro, A. (1957). The chemistry, optics and genesis of the alkali-amphiboles. Journal of the Faculty of Science, University of Tokyo, Section II, Pt. 1(11), 57–73.

Morgan, S. (2018). Pascal's principle, a simple model to explain the emplacement of laccoliths and some mid-crustal plutons. In: Burchardt, S. (Ed.): Volcanic and igneous plumbing systems: Understanding magma transport, storage and evolution in the Earth's crust. Elsevier, Amsterdam, 139–165.

Morimoto, N., Fabries, J., Ferguson, A.K., Ginzburg, I.V., Ross, M., Seifert, F.A., Zussman, J., Aoki, K., Gottardi G. (1988). Nomenclature of pyroxenes. American Mineralogist, 73, 1123–1133.

Morogan, V., Upton, B.G.J., Fitton, J.G. (2000). The petrology of the Ditrău alkaline complex, Eastern Carpathians. Mineralogy and Petrology, 69, 227–265.

Naney, M.T. (1983). Phase equilibria of rock-forming ferromagnesian silicates in granitic systems. American Journal of Science, 283, 993–1033.

Nesbitt, H.W., Young, G.M. (1982). Early Proterozoic climates and plate motions inferred from major element chemistry of lutites. Nature, 299, 715–717.

Nesse, W.D. (Ed.) (2017). Introduction to mineralogy. Oxford University Press, 3rd edition, 512 p.

Nixon, G.T., Pearce, T.H. (1987). Laser-interferometry study of oscillatory zoning in plagioclase: The record of magma mixing and phenocryst recycling in calc-alkaline magma chambers, Iztaccihuatl volcano, Mexico. American Mineralogist, 72, 1144–1162.

Odin, G.S. and 35 Collaborators (1982). Interlaboratory standards for dating purposes. In: Odin, G.S. (Ed.): Numerical dating in stratigraphy. Wiley and Sons, Chichester, pp. 123–149.

Ódri, Á., Harris, C., Le Roux, P. (2020). The role of crustal contamination in the petrogenesis of nepheline syenite to granite magmas in the Ditrău Complex, Romania: evidence from O-, Nd-, Sr- and Pb-isotopes. Contributions to Mineralogy and Petrology, 175, 100.

Pál-Molnár, E. (1988). Studiul mineralogic şi petrologic al complexului Jolotca din masivul alcalin de la Ditrău, cu privire specială asupra mineralelor purtătoare de fier (Mineralogical and petrological study of the Jolotca

complex in the Ditrău alkaline massif, with special emphasis on iron-bearing minerals). Masters Thesis, Babeş-Bolyai University, Cluj-Napoca, Romania, 127 p (in Romanian).

Pál-Molnár, E. (1994a). A Ditrói szienitmasszívum kialakulása a földtani megismerés tükrében. (Formation of the Ditrău syenite massif in view of geological aspects). A Magyar Tudományos Akadémia Szegedi Akadémiai Bizottságának Kiadványai, Szeged, 85 p (in Hungarian).

Pál-Molnár, E. (1994b). Adalékok a Ditrói szienitmasszívum szerkezeti és kőzettani ismeretéhez. (Contributions to the structural and petrological features of the Ditrău syenite massif) MTA SzAB Competition, manuscript (in Hungarian).

Pál-Molnár, E. (2000). Hornblendites and diorites of the Ditró Syenite Massif. Department of Mineralogy, Geochemistry and Petrology, University of Szeged, Szeged, 172 p.

Pál-Molnár, E. (2008). Mezozoos alkáli magmatizmus a Kárpát régióban: a Ditrói Alkáli Masszívum petrogenezise (Mesosoic alkaline magmatism in the Carpathians: Petrogenesis of the Ditrău Alkaline Massif). OTKA final report, 80 p (in Hungarian).

Pál-Molnár, E. (2010a). Rock-forming minerals of the Ditrău Alkaline Massif. In: Szakáll, S., Kristály, F. (Eds.): Mineralogy of Székelyland, Eastern Transylvania, Romania. Csík County Nature and Conservations Society, Sfântu Gheorghe–Miercurea-Ciuc–Târgu Mureş, pp. 63–88.

Pál-Molnár, E. (2010b). Geology of Székelyland. In: Szakáll, S., Kristály, F. (Eds.): Mineralogy of Székelyland, Eastern Transylvania, Romania. Csík County Nature and Conservations Society, Sfântu Gheorghe–Miercurea-Ciuc–Târgu Mureş, pp. 33–43.

Pál-Molnár, E. (2021). Zárt és nyílt rendszerű magmás folyamatok a Ditrói Alkáli Masszívumban (Closed and open-system igneous processes in the Ditrău Alkaline Massif). MTA Doctoral Dissertation, Hungarian Academy of Sciences, 136 p (in Hungarian).

Pál-Molnár, E., Árva-Sós, E. (1995). K/Ar radiometric dating on rocks from the northern part of the Ditró syenite massif and its petrogenetic implications. Acta Mineralogica-Petrographica, Szeged, 36, 101–116.

Pál-Molnár, E., Batki, A., Almási, E.E., Kiss, B., Upton, B.G.J., Markl, G., Odling, N., Harangi, Sz. (2015a). Origin of mafic and ultramafic cumulates from the Ditrău Alkaline Massif, Romania. Lithos, 239, 1–18.

Pál-Molnár, E., Batki, A., Ódri, Á., Kiss, B., Almási, E.E. (2015b). Geochemical implications of the magmatic origin of granitic rocks from the Ditrău Alkaline Massif (Eastern Carpathians, Romania). Geologia Croatica, 68(1), 51–66.

Pál-Molnár, E., Kiri, L., Lukács, R., Dunkl, I., Batki, A., Szemerédi, M., Almási, E.E., Sogrik, E., Harangi, Sz. (2021). Timing of magmatism of the Ditrău Alkaline Massif, Romania – A review based on new U-Pb and K/Ar data. Central European Geology, 64(1), 18–37.

Pamić, J. (1984). Triassic magmatism of the Dinarides in Yugoslavia. Tectonophysics, 109, 273–307.

Pană, D. (2010). Discussion of "The Eastern Carpathians 'ophiolites' (Romania): Remnants of a Triassic ocean" [Lithos, 108, 151–171]. Lithos, 115, 279–282.

Pană, D., Balintoni, I., Heaman, L. (2000). Precise U–Pb zircon dating of the Syenite Phase from the Ditrău Alkaline Igneous Complex. Studia Universitatis Babeş-Bolyai, Geologia, 45(1), 79–90.

Pandit, D., Panigrahi, M.K., Moriyama, T. (2014). Constrains from magmatic and hydrothermal epidotes on crystallization of granitic magma and sulfide mineralization in Paleoproterozoic Malanjkhand Granitoid, Central India. Chemie der Erde, 74, 715–733.

Park, Y., Means, W.D. (1996). Direct observation of deformation processes in crystal mushes. Journal of Structural Geology, 18, 847–858.

Perugini, D., Petrelli, M., Poli, G. (2006). Diffusive fractionation of trace elements by chaotic mixing of magmas. Earth and Planetary Science Letters, 243, 669–680.

Piwinskii, A.J. (1968). Experimental studies of igneous rock series central Sierra Nevada batholith, California. Journal of Geology, 76, 548–570.

Poli, G., Tommasini, S., Halliday, A.N. (1996). Trace elements and isotopic exchange during acid-basic magma interaction processes. Transactions of the Royal Society of Edinburgh: Earth Sciences, 87, 225–232.

Popescu, G. (1985). Date geocronologice Rb-Sr pe roci din Masivul Ditrău (Rb–Sr geochronological data on rocks of the Ditrău Massif). Arhiva GEOLEX „Harghita", Miercurea-Ciuc, manuscript (in Romanian).

Presnall, D.C., Bateman, P.C. (1973). Fusion relations in the system $NaAISi_3O_8$-$CaAl_2Si_2O_8$-$KAlSi_3O_8$-SiO_2-H_2O and generation of granitic magmas in the Sierra Nevada Batholith. Geological Society of America Bulletin, 84, 3182–3202.

Purdy, J.W., Jäger, E. (1976). K-Ar ages on rock forming minerals from the Central Alps. Memorie degli Istituti di Geologia e Mineralogia dell'Università di Padova, vol. XXX, 31 p.

Putirka, K.D. (2005). Igneous thermometers and barometers based on plagioclase+liquid equilibria: Tests of some existing models and new calibration. American Mineralogist, 90, 336–346.

Reinhardt, M. (1911). Sur l'âge de l'intrusion du syénite néphélinique de Ditró, Transylvanie (On the age of the intrusion of nepheline syenite from Ditrău, Transylvania). Comptes -rendus de l'Institute Géologique de Roumanie, 2, 116 (in French).

Roduit, N. (2019). JMicroVision: image analysis toolbox for measuring and quantifying components of high-definition images. Version 1.3.1. https://jmicrovision.github.io

Săndulescu, M. (Ed.) (1984). Geotectonica Romăniei (Geotectonics of Romania). Editura Technică, 336 p (in Romanian).

Săndulescu, M., Kräutner, H.G., Balintoni, I., Russo-Săndulescu, M., Micu, M. (Eds.) (1981). The structure of the East Carpathians (Moldavia – Maramures Area). Guide Exc. B1, XII Congress of the Carpathian Balkan Geological Association. Institute of Geology and Geophysics, Bucureşti, 92 p.

Scaillet, B., Holtz, F., Pichavant, M. (2016). Experimental constraints on the formation of silicic magmas. Elements, 12(2), 109–114.

Schmidt, M.W. (1992). Amphibole composition in tonalite as a function of pressure: an experimental calibration of the Al-in-hornblende barometer. Contributions to Mineralogy and Petrology, 110, 304–310.

Schoene, B., Schaltegger, U., Brack, P., Latkoczy, C., Stracke, A., Günther, D. (2012). Rates of magma differentiation and emplacement in a ballooning pluton recorded by U–Pb TIMS-TEA, Adamello Batholith, Italy. Earth and Planetary Science Letters, 355–356, 162–173.

Słaby, E., Galbarczyk-Gasiorowska, L., Baszkiewicz, A. (2002). Mantled alkali-feldspar megacrysts from the marginal part of the Karkonosze granitoid massif (SW Poland). Acta Geologica Polonica, 52(4), 501–519.

Słaby, E., Seltmann, R., Kober, B., Müller, A., Galbarczyk-Gasiorowska, L., Jeffries, T. (2007). LREE distribution patterns in zoned alkali feldspar megacrysts from the Karkonosze pluton, Bohemian Massif – implications for parental magma composition. Mineralogical Magazine, 71(2), 193–217.

Słaby, E., Śmigielski, M., Śmigielski, T., Domonik, A., Simon, K., Kronz, A. (2011). Chaotic three-dimensional distribution of Ba, Rb, and Sr in feldspar megacrysts grown in an open magmatic system. Contributions to Mineralogy and Petrology, 162, 909–927.

Sláma, J., Košler, J., Condon, D.J., Crowley, J.L., Gerdes, A., Hanchar, J.M., Horstwood, M.S.A., Morris, G.A., Nasdala, L., Norberg, N., Schaltegger, U., Schoene, B., Tubrett, M.N., Whitehouse, M.J. (2008). Plešovice zircon – A new natural reference material for U–Pb dating and Hf isotopic microanalyses. Chemical Geology, 249(1–2), 1–35.

Smith, V.C., Blundy, J.D., Arce, J.L. (2009). A temporal record of magma accumulation and evolution beneath Nevado de Toluca, Mexico, preserved in plagioclase phenocrysts. Journal of Petrology, 50(3), 405–426.

Solano, J.M.S., Jackson, M.D., Sparks, R.S.J., Blundy, J. (2014). Evolution of major and trace element composition during melt migration through crystalline mush: implications for chemical differentiation in the crust. American Journal of Science, 314, 895–939.

Spandler, C., Hammerli, J., Sha, P., Hilbert-Wolf, H., Hu, Y., Roberts, E., Schmitz, M. (2016). MKED1: A new titanite standard for in situ analysis of Sm-Nd isotopes and U-Pb geochronology. Chemical Geology, 425, 110–126.

Sparks, R.S.J., Annen, C., Blundy, J.D., Cashman, K.V., Rust, A.C., Jackson, M.D. (2019). Formation and dynamics of magma reservoirs. Philosophical Transactions: Mathematical, Physical and Engineering Sciences, 25 February 2019, vol. 377, no. 2139, Theo Murphy meeting issue: Magma reservoir architecture and dynamics, 1–30.

Sparks, R.S.J., Marshall L.A. (1986). Thermal and mechanical constraints on mixing between mafic and silicic magmas. Journal of Volcanology and Geothermal Research, 29, 99–124.

Stampfli, G.M. (2000). Tethyan oceans. In: Bozkurt, E., Winchester, J.A., Piper, J.D.A. (Eds.): Tectonics and magmatism in Turkey and surrounding area. Geological Society of London, Special Publication, 173, pp. 1–23.

Stampfli, G.M., Borel, G.D. (2002). A plate tectonic model for the Paleozoic and Mesozoic constrained by dynamic plate boundaries and restored synthetic oceanic isochrons. Earth and Planetary Science Letters, 196, 17–33.

Stampfli, G.M., Borel, G.D. (2004). The TRANSMED Transects in space and time: constraints on the paleotectonic Evolution of the Mediterranean domain. In: Cavazza, W., Roure, F., Spakman, W., Stampfli, G.M., Ziegler, P.A. (Eds.): The TRANSMED Atlas. The Mediterranean Region from crust to mantle. Springer, Berlin, Heidelberg, pp. 53–90.

Streckeisen, A. (1938). Das Nephelinsyenit-Massiv von Ditro in Rumänien als Beispiel einer kombinierten Differentiation und Assimilation (The nepheline syenite massif of Ditrău in Romania as an example of combined differentiation and assimilation). Verhandlungen der Schweizerische Naturforschende Gesellschaft, 159–161 (in German).

Streckeisen, A. (1952). Das Nephelinsyenit-Massiv von Ditro (Siebenbürgen), I. Teil (The nepheline syenite massif of Ditrău, Part I). Schweizerische Mineralogische und Petrographische Mitteilungen, 32, 251–309 (in German).

Streckeisen, A. (1954). Das Nephelinsyenit-Massiv von Ditro (Siebenbürgen), II. Teil (The nepheline syenite massif of Ditrău, Part II). Schweizerische Mineralogische und Petrographische Mitteilungen, 34, 336–409 (in German).

Streckeisen, A. (1960). On the structure and origin of the Nephelinsyenite Complex of Ditro (Transylvania, Roumania). Rep. 21th IGC, 13, 228–238.

Streckeisen, A., Hunziker, I.C. (1974). On the origin of the Nephelinsyenit Massif of Ditró (Transylvania, Romania). Schweizerische Mineralogische und Petrographische Mitteilungen, 54, 59–77.

Streckeisen, A., Le Maitre, R.W. (1979). A chemical approximation to the modal QAPF classification of the igneous rocks. Neues Jahrbuch für Mineralogie, Abhandlungen, 136, 169–206.

Sun, S., McDonough, W.F. (1989). Chemical and isotopic systematics of oceanic basalts: implications for mantle composition and processes. Geological Society, London, Special Publications, 42, 313–345.

Tang, G.-J., Wang, Q., Wyman, D.A., Dan, W., Ma, L., Zhang, H.-X., Zhao, Z.H. (2020). Petrogenesis of the Ulungur Intrusive Complex, NW China, and implications for crustal generation and reworking in accretionary orogens. Journal of Petrology, 61, 2.

Tate, M.C., Clarke, D.B., Heaman, L.M. (1997). Progressive hybridisation between Late Devonian mafic-intermediate and felsic magmas in the Meguma Zone of Nova Scotia, Canada. Contributions to Mineralogy and Petrology, 126, 401–415.

Ubide, T., Galé, C., Arranz, E., Lago, M., Larrea, P. (2014a). Clinopyroxene and amphibole crystal populations in a lamprophyre sill from the Catalonian Coastal Ranges (NE Spain): a record of magma history and a window to mineral-melt partitioning. Lithos, 184–187, 225–242.

Ubide, T., Galé, C., Larrea, P., Arranz, E., Lago, M., Tierz, P. (2014b). The relevance of crystal transfer to magma mixing: a case study in composite dykes from the Central Pyrenees. Journal of Petrology, 55(8), 1535–1559.

Ubide, T., Neave, D.A., Petrelli, M., Longpré, M.-A. (2021). Crystal archives of magmatic processes. Frontiers of Earth Science, 9:749100.

van Achterbergh, E., Ryan, C.G., Jackson, S.E., Griffin, W.L. (2001). Data reduction software for LA-ICP-MS. In: Sylvester, P.J. (Ed.): Laser Ablation-ICP-Mass spectrometry in the earth sciences: principles and applications, short course series, 29. Mineralogical Association of Canada, St. John's, Newfoundland, 239–243.

Vance, J.A. (1969). On synneusis. Contributions to Mineralogy and Petrology, 24, 7–29.

Vermeesch, P. (2018). IsoplotR: a free and open toolbox for geochronology. Geoscience Frontiers, 9, 1479–1493.

Vernon, R.H. (1984). Microgranitoid enclaves in granites–globules of hybrid magma quenched in a plutonic environment. Nature, 309, 438–439.

Vernon, R.H. (1990). Crystallization and hybridism in microgranitoid enclave magmas: Microstructural evidence. Journal of Geophysical Research, 95, 17849–17859.

Vernon, R.H., Collins, W.J. (2011). Structural criteria for identifying granitic cumulates. Journal of Geology, 119, 127–142.

Vernon, R.H., Johnson, S.E., Melis, E.A. (2004). Emplacement-related microstructures in the margin of a deformed pluton: the San José tonalite, Baja California, México. Journal of Structural Geology, 26, 1867–1884.

Vernon, R.H., Paterson, S.R. (2006). Mesoscopic structures resulting from crystal accumulation and melt movement in granites. Transactions of the Royal Society of Edinburgh: Earth Sciences, 97(4), 369–381.

Verschure, R.H., Maijer, C. (2005). A new Rb-Sr isotopic parameter for metasomatism, Δt, and its application in a study of pluri-fenitized gneisses around the Fen ring complex, South Norway. Norges Geologiske Undersøkelse Bulletin, 445, 45–71.

Vodă, A., Balintoni, I. (1994). Corelari lithostratigrafice în cristalinul Carpaților Orientali (Lithostratigraphic correlations in the Eastern Carpathians). Studia Universitates Babeş-Bolyai, Geologia, 39, 61–66 (in Romanian).

Vogt, J.H.L. (1921). The physical chemistry of the crystallization and magmatic differentiation of the igneous rocks. Journal of Geology, 29(5), 426–443.

Wall, V.J., Clemens, J.D., Clarke, D.B. (1987). Models for granitoid evolution and source compositions. Journal of Geology, 95, 731–749.

White, A.J.R., Chappell, B.W. (1977). Ultrametamorphism and granitoid genesis. Tectonophysics, 43, 7–22.

White, R.W., Pomroy, N.E., Powell, R. (2005). An in situ metatexite-diatexite transition in upper amphibolite facies rocks from Broken Hill, Australia. Journal of Metamorphic Geology, 23, 579–602.

Whitney, D.L., Evans, B.W. (2010). Abbreviations for names of rock-forming minerals. American Mineralogist, 95, 185–187.

Wiebe, R.A. (1968). Plagioclase stratigraphy; a record of magmatic conditions and events in a granite stock. American Journal of Science, 266, 690–703.

Wiebe, R.A. (1973). Relations between coexisting basaltic and granitic magmas in a composite dike. American Journal of Science, 273, 130–151.

Wiebe, R.A., Blair, K.D., Hawkins, D.P., Sabine, C.P. (2002). Mafic injections, in situ hybridization, and crystal accumulation in the Pyramid Peak granite, California. Bulletin of the Geological Society of America, 114, 909–920.

Wiebe, R.A., Collins, W.J. (1998). Depositional features and stratigraphic sections in granitic plutons: implications for the emplacement and crystallization of granitic magma. Journal of Structural Geology, 20(9/10), 1273–1289.

Wiebe, R.A., Smith, D., Sturm, M., King, E.M., Seckler, M.S. (1997). Enclaves in the Cadillac Mountain Granite (Coastal Maine): samples of hybrid magma from the base of the chamber. Journal of Petrology, 38(3), 393–423.

Wiedenbeck, M., Allé, P., Corfu, F., Griffin, W.L., Meier, M., Oberli, F., von Quadt, A., Roddick, J.C., Spiegel, W. (1995). Three natural zircon standards for U-Th-Pb, Lu-Hf trace element and REE analyses. Geostandards Newsletter, 19, 1–23.

Xie, L., Evans, N., Yang, Y., Huang, C., Yang, J. (2018). U-Th-Pb geochronology and simultaneous analysis of multiple isotope systems in geological samples by LA-MC-ICP-MS. Journal of Analytical Atomic Spectrometry, 33(10), 1600–1615.

Zincenco, D. (1991). Masivul alcalin Ditrau: Contribuția datelor Rb-Sr și K-Ar la petrologia și cronologia masivului (The Ditrau alkaline massif: Contribution of Rb-Sr and K-Ar data to the petrology and timing of the massif). Arhiva Soc. Prosp., București, manuscript (in Romanian).

Zincenco, D., Petrescu, M., Popescu, C., Prodănescu, I., Zincenco, C. (1994). Vârsta și petrologia masivului Ditrău: Roci din faciesul învelitor (Age and petrology of the Ditrău massif: Rocks of the enveloping facies). Arhiva Soc. Prosp., București, manuscript (in Romanian).

Zólya, L., Zólya, É.G. (1985). Raport geologic de prospecțiuni geologice de mare detaliu, sc. 1:5000, executată în perimetrul Putna Întunecoasă Vest (A geological study based on geological mapping carried out in 1:5000 scale in the area of the Putna Întunecoasă West Creek). Arhiva IPEG „Harghita", Miercurea-Ciuc, manuscript (in Romanian).

Zólya, L., Zólya, É.G. (1986). Raport geologic privind lucrările de prospecțiuni geologice de mare detaliu, sc. 1:5000, executată în perimetrul Putna Tilalmas-Holoșag, zona Jolotca (A geological study based on geological mapping carried out in 1:5000 scale in the area of the Tilalmas-Holoșag Creeks, Jolotca area). Arhiva IPEG „Harghita", Miercurea-Ciuc, manuscript (in Romanian).

Zorpi, M.J., Coulon, C., Orsini, J.B. (1991). Hybridization between felsic and mafic magmas in calc-alkaline granitoids — a case study in northern Sardinia, Italy. Chemical Geology, 92, 45–86.

SUPPLEMENTARY FIGURES
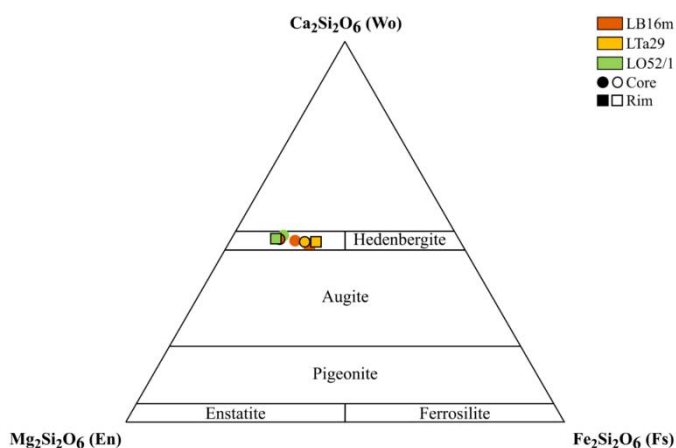
Supplementary Fig. IV.1. Compositional variation of the analyzed clinopyroxenes in terms of the En–Fs–Wo end-members (Morimoto et al., 1988). The clot-forming and orbicular inclusion-derived clinopyroxene data are marked with symbols with a black rim
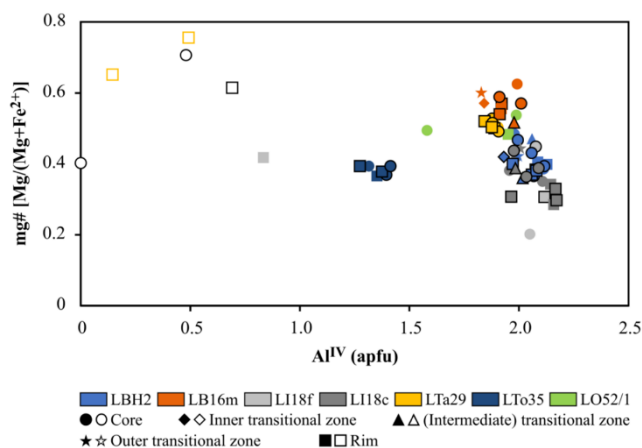
Supplementary Fig. IV.2. Compositional variation of the analyzed amphiboles in terms of their mg# and Al^{IV} concentration. Actinolite data are marked by empty symbols. The compositions of the clot-forming crystals are identified by symbols with a black rim
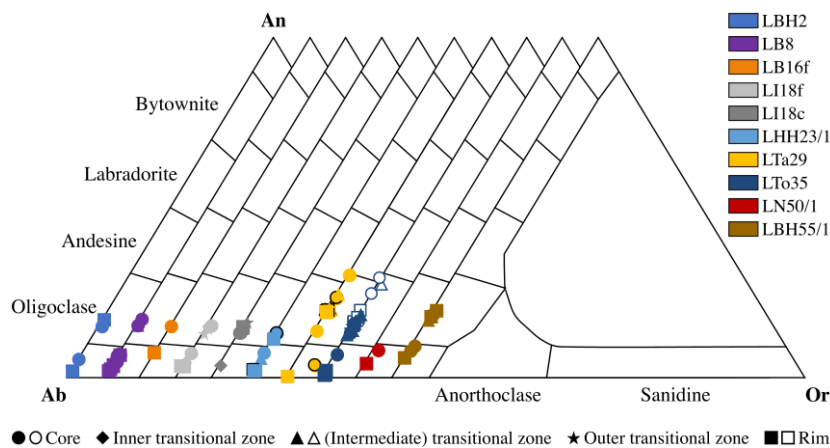
Supplementary Fig. IV.3. Compositional variation of the analyzed plagioclase crystals in terms of the Ab–An–Or end-members. Data of plagioclase in synneusis are marked by empty symbols. The composition of the clot-forming crystals is identified by symbols with a black rim

SUPPLEMENTARY TABLES

Supplementary Table II.1. Results of U–Pb dating of titanites and zircons from syenite from the Ditrău Alkaline Massif (Romania)

Rock Nr.	Spot Nr.	Studied fraction	U (ppm)	Pb (ppm)	207Pb/235U	±1σ (%)	206Pb/238U	±1σ (%)	rho	207Pb/206Pb	±1σ (%)	207Pb/235U (Ma)	±2σ (Ma)	206Pb/238U (Ma)	±2σ (Ma)	207Pb/206Pb (Ma)	±2σ (Ma)	Disc. (%)	206Pb/238U (Ma)	±2σ (Ma)
												Isotopic data			Ages				RDC age	
VRG7404	136	Titanite (core)	23	135	0.72685	3.7	0.03653	1.6	0.42	0.14433	3.4	554.7	32.0	231.3	7.1	2279.8	58.4	58.3	n.d.	n.d.
	137		25	110	0.75060	3.5	0.03912	1.6	0.45	0.13916	3.1	568.6	30.6	247.4	7.6	2216.9	54.5	56.5	n.d.	n.d.
	138		24	134	0.73909	4.4	0.03820	1.5	0.35	0.14033	4.1	561.9	38.0	241.7	7.1	2231.3	71.1	57.0	n.d.	n.d.
	139		23	118	0.79848	3.9	0.03866	1.8	0.45	0.14982	3.5	596.0	35.6	244.5	8.5	2343.9	60.2	59.0	n.d.	n.d.
	143		23	118	0.77044	3.8	0.03878	1.4	0.37	0.14408	3.6	580.0	34.3	245.3	6.9	2276.9	61.9	57.7	n.d.	n.d.
	144		24	116	0.80808	3.6	0.03705	1.6	0.45	0.15820	3.2	601.4	33.0	234.5	7.4	2436.6	55.1	61.0	n.d.	n.d.
	145		25	189	0.72811	3.4	0.03788	1.4	0.41	0.13939	3.1	555.4	29.4	239.7	6.6	2219.7	54.3	56.8	n.d.	n.d.
	146		22	112	0.97697	3.6	0.04056	1.8	0.49	0.17471	3.2	692.1	36.6	256.3	8.8	2603.3	53.2	63.0	n.d.	n.d.
	147		22	133	0.76930	4.2	0.03853	1.8	0.43	0.14482	3.8	579.4	37.0	243.7	8.5	2285.7	65.0	57.9	n.d.	n.d.
	148		21	130	0.74806	4.7	0.03774	1.8	0.38	0.14376	4.3	567.1	41.1	238.8	8.2	2273.1	74.9	57.9	n.d.	n.d.
	149		22	129	0.71685	4.2	0.03714	1.8	0.43	0.13998	3.8	548.8	36.3	235.1	8.3	2227.0	66.8	57.2	n.d.	n.d.
	150		19	119	0.74282	4.3	0.03785	1.8	0.43	0.14235	3.9	564.0	37.6	239.5	8.7	2256.1	67.5	57.5	n.d.	n.d.
	151		19	126	0.78341	3.8	0.03881	1.7	0.46	0.14641	3.4	587.4	34.1	245.4	8.3	2304.5	58.2	58.2	n.d.	n.d.
	152		21	142	0.75546	4.6	0.03755	1.9	0.41	0.14592	4.2	571.4	40.6	237.6	8.8	2298.7	72.3	58.4	n.d.	n.d.
	153		23	100	0.90703	3.8	0.03936	1.7	0.46	0.16712	3.4	655.5	36.8	248.9	8.4	2529.0	56.8	62.0	n.d.	n.d.
	154		26	119	0.83752	3.3	0.03831	1.6	0.48	0.15856	2.9	617.8	31.2	242.3	7.6	2440.4	50.2	60.8	n.d.	n.d.
	155	Titanite (external rim zone)	19	124	0.73359	4.4	0.03749	2.0	0.46	0.14192	3.9	558.7	37.7	237.2	9.3	2250.9	67.1	57.5	n.d.	n.d.
	156		20	131	0.68042	4.5	0.03771	1.8	0.40	0.13086	4.1	527.0	37.5	238.6	8.4	2109.5	72.9	54.7	n.d.	n.d.
	157		20	128	0.72551	3.9	0.03708	1.6	0.41	0.14191	3.5	553.9	33.4	234.7	7.3	2250.7	61.4	57.6	n.d.	n.d.
	158		19	119	0.75104	4.6	0.03814	1.8	0.40	0.14282	4.2	568.8	40.2	241.3	8.7	2261.7	72.6	57.6	n.d.	n.d.
	159		18	122	0.79154	4.6	0.03882	1.9	0.41	0.14789	4.2	592.0	42.1	245.5	9.1	2321.8	73.0	58.5	n.d.	n.d.
	163		23	121	0.82517	4.3	0.03842	1.8	0.41	0.15577	3.9	610.9	39.9	243.0	8.4	2410.3	67.0	60.2	n.d.	n.d.
	164		68	409	0.45308	3.0	0.03603	1.2	0.39	0.09120	2.8	379.4	19.1	228.2	5.3	1450.8	52.7	39.9	n.d.	n.d.
	165		21	132	1.04638	4.0	0.04026	1.6	0.40	0.18850	3.7	727.1	42.1	254.4	8.0	2729.2	60.9	65.0	n.d.	n.d.
	166		21	132	0.70461	4.1	0.03727	1.6	0.40	0.13712	3.8	541.5	35.0	235.9	7.6	2191.2	66.2	56.4	n.d.	n.d.
	167		19	148	0.69969	4.6	0.03817	1.6	0.35	0.13295	4.3	538.6	38.7	241.5	7.7	2137.3	75.3	55.2	n.d.	n.d.
	168		19	126	0.79403	4.3	0.03852	1.4	0.33	0.14950	4.1	593.5	39.5	243.7	6.8	2340.3	70.6	58.9	n.d.	n.d.
	169		25	183	0.64632	4.1	0.03778	1.5	0.37	0.12409	3.8	506.2	32.6	239.0	7.1	2015.9	67.1	52.8	n.d.	n.d.
	170		22	165	0.70375	4.3	0.03734	1.8	0.42	0.13669	3.9	541.0	36.1	236.3	8.3	2185.7	67.8	56.3	n.d.	n.d.
	171		76	405	0.47834	2.4	0.03593	1.0	0.42	0.09657	2.2	396.9	15.7	227.5	4.5	1558.9	41.0	42.7	n.d.	n.d.
	173		19	121	0.80402	5.2	0.03884	2.1	0.41	0.15015	4.8	599.1	47.9	245.6	10.3	2347.7	81.9	59.0	n.d.	n.d.

Supplementary Table II.1. Continued

Rock Nr.	Spot Nr.	Studied fraction	U (ppm)	Pb (ppm)	$^{207}Pb/^{235}U$	±1σ (%)	$^{206}Pb/^{238}U$	±1σ (%)	rho	$^{207}Pb/^{206}Pb$	±1σ (%)	$^{207}Pb/^{235}U$ (Ma)	±2σ (Ma)	$^{206}Pb/^{238}U$ (Ma)	±2σ (Ma)	$^{207}Pb/^{206}Pb$ (Ma)	±2σ (Ma)	Disc. (%)	$^{206}Pb/^{238}U$ (Ma)	±2σ (Ma)
																				RDC age
	186		110	90	0.26723	2.9	0.03563	0.9	0.31	0.05440	2.7	240.5	12.3	225.7	3.9	387.8	61.5	6.2	228.0	5.5
	187		613	1014	0.35413	1.4	0.03677	0.7	0.49	0.06986	1.2	307.8	7.6	232.8	3.2	924.2	26.1	24.4	233.9	5.0
	188		269	453	0.35170	2.2	0.04026	0.8	0.36	0.06336	2.0	306.0	11.6	254.4	3.9	720.5	43.5	16.9	256.2	5.8
	189		143	163	0.50105	2.2	0.03831	0.9	0.38	0.09485	2.1	412.4	15.2	242.4	4.1	1525.1	39.2	41.2	244.6	5.9
	190		63	29	0.25208	4.0	0.03671	1.1	0.28	0.04980	3.9	228.3	16.6	232.4	5.2	185.9	90.3	-1.8	235.1	6.4
	191		76	37	0.27668	2.8	0.03580	1.0	0.36	0.05604	2.6	248.0	12.5	226.8	4.5	454.2	58.7	8.6	229.4	5.8
	192		527	1503	0.26969	1.6	0.03744	0.7	0.45	0.05224	1.4	242.4	6.9	236.9	3.3	296.1	32.8	2.3	238.1	5.1
	193		550	1240	0.25668	1.6	0.03649	0.7	0.41	0.05102	1.5	232.0	6.7	231.0	3.0	241.6	34.0	0.4	232.2	4.9
	194		455	923	0.25928	1.5	0.03662	0.7	0.45	0.05136	1.3	234.1	6.3	231.8	3.1	256.9	31.2	1.0	233.1	5.0
	195		52	21	0.26020	4.6	0.03607	1.2	0.25	0.05232	4.5	234.8	19.5	228.4	5.3	299.3	102.4	2.7	231.3	6.6
	196		66	33	0.51201	3.2	0.03880	1.2	0.37	0.09571	3.0	419.8	22.0	245.4	5.7	1542.2	55.8	41.5	248.2	7.1
	197		65	27	0.31322	3.5	0.03551	1.1	0.32	0.06398	3.3	276.7	17.0	224.9	4.9	741.0	70.2	18.7	227.6	6.2
	198		588	476	0.25556	1.5	0.03578	0.7	0.44	0.05180	1.3	231.1	6.2	226.6	2.9	276.6	31.2	1.9	227.9	4.8
	199		145	110	0.29792	2.0	0.03829	0.9	0.43	0.05643	1.8	264.8	9.4	242.2	4.1	469.3	40.6	8.5	244.5	5.9
	203		52	22	1.02762	2.5	0.04170	1.1	0.43	0.17871	2.3	717.7	26.0	263.4	5.6	2641.0	38.2	63.3	266.5	7.2
VRG7425	204	Zircon	784	1286	0.25988	1.5	0.03602	0.7	0.45	0.05232	1.3	234.6	6.1	228.1	2.9	299.6	30.1	2.7	229.1	4.9
	205		539	1703	0.26807	1.6	0.03719	0.7	0.42	0.05228	1.5	241.1	7.0	235.4	3.1	297.7	34.2	2.4	236.5	5.0
	206		406	866	0.29035	1.7	0.03628	0.7	0.44	0.05805	1.5	258.8	7.7	229.7	3.3	531.7	33.1	11.3	231.1	4.9
	207		237	336	0.26695	2.0	0.03549	0.7	0.38	0.05456	1.8	240.3	8.4	224.8	3.3	394.2	40.7	6.4	226.6	4.8
	208		63	31	0.25580	3.8	0.03823	1.2	0.31	0.04853	3.6	231.3	15.7	241.8	5.5	125.4	85.0	-4.6	244.7	7.0
	209		251	247	0.25428	2.1	0.03544	0.8	0.35	0.05204	2.0	230.0	8.8	224.5	3.3	287.0	46.1	2.4	226.3	5.1
	210		626	849	0.26920	1.5	0.03631	0.6	0.42	0.05377	1.4	242.1	6.5	229.9	2.9	361.4	31.2	5.0	231.1	4.6
	211		59	23	0.32810	4.1	0.03641	1.2	0.29	0.06536	4.0	288.1	20.8	230.5	5.3	786.1	83.3	20.0	233.3	6.7
	212		228	150	0.25211	2.2	0.03576	0.8	0.35	0.05113	2.1	228.3	9.2	226.5	3.5	246.8	48.5	0.8	228.4	5.2
	213		293	182	0.27302	1.8	0.03559	0.8	0.43	0.05563	1.6	245.1	7.8	225.5	3.4	437.7	36.3	8.0	227.2	5.1
	214		74	48	0.72322	2.9	0.03765	1.2	0.42	0.13931	2.6	552.6	24.9	238.3	5.7	2218.7	46.0	56.9	240.9	6.9
	215		153	297	0.35895	2.4	0.03658	0.8	0.35	0.07118	2.2	311.4	12.9	231.6	3.8	962.5	45.9	25.6	233.6	5.3
	216		58	22	0.25210	4.0	0.03649	1.1	0.28	0.05011	3.9	228.3	16.6	231.0	5.2	200.1	90.0	-1.2	233.8	6.3
	217		1464	3459	0.25582	1.3	0.03640	0.6	0.45	0.05098	1.2	231.3	5.6	230.5	2.8	239.8	28.1	0.4	231.0	4.6
	277		133	130	0.30481	2.5	0.03862	1.0	0.39	0.05724	2.3	270.1	12.1	244.3	4.7	500.8	51.9	9.6	246.6	6.3
	278		1336	2526	0.26004	1.4	0.03635	0.6	0.46	0.05189	1.2	234.7	5.7	230.1	2.9	280.5	28.1	1.9	230.8	4.6
	279		512	770	0.25622	1.7	0.03709	0.8	0.45	0.05010	1.6	231.6	7.3	234.8	3.7	199.9	36.5	-1.4	236.1	5.3

Supplementary Table II.2. Results of U–Pb dating of titanites and zircons from nepheline syenite from the Ditrău Alkaline Massif (Romania)

Rock Nr.	Spot Nr.	Studied fraction	Isotopic data										Ages							RDC age	
			U (ppm)	Pb (ppm)	207Pb/235U	±1σ (%)	206Pb/238U	±1σ (%)	rho	207Pb/206Pb	±1σ (%)		207Pb/235U (Ma)	±2σ (Ma)	206Pb/238U (Ma)	±2σ (Ma)	207Pb/206Pb (Ma)	±2σ (Ma)	Disc. (%)	206Pb/238U (Ma)	±2σ (Ma)
VRG7546	212		66	155	1.54659	2.8	0.04607	1.6	0.59	0.24346	2.2		949.1	34.5	290.4	9.3	3142.8	36.5	69.4	n.d.	n.d.
	213		31	120	0.77526	4.9	0.03948	2.0	0.41	0.14243	4.4		582.8	43.6	249.6	9.8	2257.0	76.7	57.2	n.d.	n.d.
	214		40	158	0.71918	4.2	0.03807	2.1	0.50	0.13701	3.7		550.2	36.2	240.9	10.0	2189.8	63.9	56.2	n.d.	n.d.
	215		39	165	0.67799	5.3	0.03652	2.2	0.41	0.13464	4.8		525.6	43.7	231.2	9.8	2159.5	84.1	56.0	n.d.	n.d.
	216		37	143	0.74720	4.7	0.03777	2.1	0.45	0.14347	4.2		566.6	41.6	239.0	9.9	2269.6	73.4	57.8	n.d.	n.d.
	217		41	137	0.86524	3.6	0.04055	1.9	0.53	0.15474	3.1		633.0	34.4	256.3	9.7	2399.0	52.6	59.5	n.d.	n.d.
	218		38	137	1.64935	3.3	0.04719	1.9	0.60	0.25350	2.6		989.3	41.6	297.2	11.3	3206.8	41.9	70.0	n.d.	n.d.
	219		25	127	0.67242	5.8	0.03860	2.5	0.42	0.12634	5.3		522.2	48.0	244.2	11.8	2047.7	93.2	53.2	n.d.	n.d.
	223		24	137	0.71374	5.1	0.03837	2.1	0.42	0.13492	4.6		547.0	43.6	242.7	10.2	2163.1	81.1	55.6	n.d.	n.d.
	224		55	223	0.74245	3.6	0.03774	1.6	0.46	0.14266	3.2		563.8	31.0	238.8	7.7	2259.8	54.7	57.6	n.d.	n.d.
	225		75	289	0.68795	3.2	0.03925	1.5	0.48	0.12712	2.8		531.6	26.7	248.2	7.5	2058.5	49.9	53.3	n.d.	n.d.
	226		27	121	0.70438	5.1	0.03791	2.1	0.41	0.13477	4.6		541.4	43.2	239.8	9.9	2161.1	81.2	55.7	n.d.	n.d.
	227	Titanite	24	130	0.85630	5.4	0.03958	2.5	0.46	0.15689	4.8		628.1	51.3	250.3	12.2	2422.5	81.8	60.2	n.d.	n.d.
	228		24	134	0.77055	5.3	0.03900	2.1	0.40	0.14330	4.8		580.1	47.2	246.6	10.3	2267.5	83.5	57.5	n.d.	n.d.
	229		20	117	0.72592	5.8	0.03821	2.3	0.39	0.13780	5.4		554.2	50.6	241.7	10.9	2199.7	93.6	56.4	n.d.	n.d.
	230		50	160	0.68620	4.1	0.03795	1.9	0.46	0.13113	3.6		530.5	34.3	240.1	9.0	2113.2	64.2	54.7	n.d.	n.d.
	231		37	138	0.71482	5.3	0.03725	2.3	0.45	0.13916	4.7		547.6	45.0	235.8	10.9	2216.9	81.9	56.9	n.d.	n.d.
	232		32	128	0.61333	4.2	0.03810	2.0	0.46	0.11676	3.7		485.7	32.9	241.0	9.3	1907.3	67.6	50.4	n.d.	n.d.
	233		22	120	2.14270	3.9	0.05327	2.2	0.55	0.29170	3.3		1162.7	55.2	334.6	14.2	3426.7	51.5	71.2	n.d.	n.d.
	234		21	118	0.73199	6.4	0.03692	2.3	0.36	0.14380	6.0		557.7	55.5	233.7	10.5	2273.5	102.8	58.1	n.d.	n.d.
	235		21	114	0.66111	6.3	0.03738	2.2	0.34	0.12829	5.9		515.3	51.6	236.5	10.1	2074.7	104.5	54.1	n.d.	n.d.
	236		31	122	0.67883	4.9	0.03804	2.2	0.45	0.12944	4.4		526.1	41.0	240.6	10.6	2090.4	77.6	54.3	n.d.	n.d.
	237		50	167	1.04936	3.1	0.04245	1.9	0.60	0.17929	2.5		728.6	32.7	268.0	9.8	2646.4	42.0	63.2	n.d.	n.d.
	238		50	173	0.74667	3.7	0.03987	1.6	0.44	0.13581	3.3		566.3	32.3	252.1	7.9	2174.5	58.2	55.5	n.d.	n.d.
	239		47	169	0.75969	3.8	0.03881	1.7	0.44	0.14197	3.4		573.8	33.3	245.5	8.0	2251.4	58.7	57.2	n.d.	n.d.
	2		163	123	0.29791	3.1	0.03647	1.1	0.35	0.05924	2.9		264.8	14.4	230.9	4.9	575.8	63.0	12.8	233.0	6.3
	8		719	588	0.25134	1.7	0.03622	0.7	0.38	0.05032	1.6		227.7	7.1	229.4	3.0	209.7	37.5	-0.8	230.6	4.9
	9		396	183	0.25785	2.6	0.03641	0.8	0.30	0.05136	2.5		232.9	10.8	230.6	3.5	257.0	56.8	1.0	232.1	5.2
	10		260	115	0.25341	2.6	0.03638	1.0	0.38	0.05051	2.4		229.3	10.5	230.4	4.4	218.7	55.0	-0.5	232.2	5.9
	11		758	481	0.25583	2.0	0.03731	0.8	0.38	0.04973	1.8		231.3	8.2	236.1	3.5	182.5	43.0	-2.1	237.3	5.4
	12		122	87	0.35852	3.5	0.03783	1.4	0.39	0.06873	3.3		311.1	19.1	239.4	6.6	890.6	67.5	23.0	241.7	7.7
	13	Zircon	815	825	0.25133	1.9	0.03642	0.7	0.37	0.05005	1.8		227.7	7.9	230.6	3.2	197.4	41.8	-1.3	231.7	4.9
	14		273	411	0.39439	2.4	0.04008	1.0	0.43	0.07136	2.1		337.6	13.6	253.4	5.1	967.8	43.9	24.9	255.1	6.5
	15		2338	4194	0.25599	1.4	0.03642	0.6	0.40	0.05098	1.3		231.4	6.0	230.6	2.7	239.8	30.8	0.4	230.9	4.6
	16		632	830	0.30083	2.1	0.03800	0.7	0.33	0.05740	2.0		267.1	10.0	240.5	3.3	507.1	44.2	10.0	241.7	5.1
	17		513	370	0.25407	1.8	0.03636	0.9	0.47	0.05067	1.6		229.9	7.5	230.3	3.9	226.0	37.6	-0.2	231.6	5.6
	18		346	190	0.23856	2.3	0.03601	0.8	0.35	0.04804	2.1		217.2	9.0	228.1	3.6	101.3	51.0	-5.0	229.7	5.2
	19		58	19	0.27159	5.7	0.03527	1.6	0.28	0.05585	5.5		244.0	24.8	223.4	7.1	446.4	121.3	8.4	226.2	8.0
	20		58	22	0.25220	5.1	0.03528	1.4	0.28	0.05185	4.9		228.4	21.1	223.5	6.3	278.6	113.1	2.1	226.2	7.2

Supplementary Table II.2. Continued

Rock Nr.	Spot Nr.	Studied fraction	U (ppm)	Pb (ppm)	$^{207}Pb/^{235}U$	±1σ (%)	$^{206}Pb/^{238}U$	±1σ (%)	rho	$^{207}Pb/^{206}Pb$	±1σ (%)	$^{207}Pb/^{235}U$ (Ma)	±2σ (Ma)	$^{206}Pb/^{238}U$ (Ma)	±2σ (Ma)	$^{207}Pb/^{206}Pb$ (Ma)	±2σ (Ma)	Disc. (%)	$^{206}Pb/^{238}U$ (Ma)	±2σ (Ma)
													Ages						RDC age	
VRG7546	21	Zircon	614	566	0.28735	2.0	0.03626	0.7	0.35	0.05747	1.8	256.5	8.9	229.6	3.1	509.7	40.5	10.5	230.9	4.9
	22		428	336	0.24654	2.3	0.03588	0.8	0.35	0.04983	2.1	223.8	9.2	227.3	3.6	187.1	49.8	-1.6	228.7	5.2
	27		303	235	0.34566	2.3	0.03696	0.8	0.35	0.06783	2.2	301.5	12.3	234.0	3.8	863.3	45.9	22.4	235.7	5.3
	28		145	84	0.83472	2.0	0.04177	1.2	0.62	0.14493	1.6	616.2	18.8	263.8	6.4	2287.0	28.2	57.2	266.2	7.6
	29		684	358	0.26225	1.7	0.03752	0.6	0.36	0.05069	1.6	236.5	7.1	237.4	2.8	227.0	36.4	-0.4	238.7	4.8
	30		883	534	0.26774	1.8	0.03691	0.7	0.37	0.05260	1.7	240.9	7.8	233.7	3.1	311.8	38.6	3.0	234.7	5.0
	31		187	97	0.25814	2.9	0.03574	1.0	0.36	0.05238	2.7	233.2	12.1	226.4	4.7	302.0	61.8	2.9	228.4	5.8
	32		410	245	0.25477	2.3	0.03615	0.7	0.32	0.05111	2.2	230.4	9.5	229.0	3.3	245.7	50.3	0.6	230.5	4.9
	33		321	213	0.24952	2.6	0.03669	0.9	0.33	0.04932	2.4	226.2	10.5	232.3	3.9	163.0	57.1	-2.7	234.0	5.6
	34		356	321	0.25461	2.6	0.03638	0.7	0.26	0.05075	2.5	230.3	10.6	230.4	3.0	229.6	57.5	0.0	232.0	4.9
	35		329	318	0.25435	2.4	0.03601	0.9	0.35	0.05123	2.3	230.1	10.1	228.1	3.8	251.1	52.7	0.9	229.7	5.5
	36		182	158	0.24532	3.5	0.03471	1.0	0.29	0.05125	2.6	222.8	14.0	220.0	4.3	252.2	76.9	1.2	221.9	5.7
	37		295	375	0.24633	2.8	0.03531	0.9	0.34	0.05060	2.6	223.6	11.2	223.7	4.2	222.6	60.5	0.0	225.3	5.4
	38		205	215	0.29938	2.8	0.03565	0.8	0.30	0.06091	2.6	265.9	12.9	225.8	3.7	636.0	56.6	15.1	227.7	5.1
	39		978	796	0.26487	1.8	0.03655	0.7	0.36	0.05255	1.7	238.6	7.7	231.5	3.0	309.3	38.4	3.0	232.4	4.9
	40		1064	845	0.25724	1.6	0.03617	0.7	0.41	0.05157	1.5	232.4	6.8	229.1	3.0	266.4	34.5	1.4	230.0	4.9
	41		779	825	0.25774	1.6	0.03640	0.7	0.47	0.05135	1.4	232.8	6.5	230.5	3.4	256.7	32.1	1.0	231.6	4.9
	42		167	39	0.27072	3.2	0.03657	1.0	0.32	0.05369	3.1	243.3	14.0	231.5	4.7	358.1	69.3	4.8	233.7	6.0
	47		213	58	0.24678	3.2	0.03625	0.9	0.28	0.04936	3.1	224.0	13.1	229.6	4.2	165.2	72.7	-2.5	231.6	5.6
	48		65	23	0.26598	4.4	0.03566	1.5	0.33	0.05410	4.1	239.5	18.7	225.9	6.5	375.1	92.6	5.7	228.6	7.7
	49		65	26	0.28945	4.6	0.03597	1.2	0.26	0.05835	4.5	258.1	21.2	227.9	5.4	542.9	97.9	11.7	230.6	6.6
	50		235	191	0.25644	2.5	0.03552	0.8	0.33	0.05236	2.4	231.8	10.4	225.0	3.6	301.2	54.3	2.9	226.8	5.1
	51		571	720	0.25764	2.0	0.03677	0.7	0.36	0.05082	1.9	232.8	8.5	232.8	3.3	232.5	44.1	0.0	234.0	5.0
	52		551	677	0.24864	2.0	0.03646	0.7	0.34	0.04946	1.9	225.5	8.0	230.9	3.0	169.6	43.6	-2.4	232.1	4.9
	53		306	147	0.25863	2.5	0.03588	0.8	0.30	0.05227	2.4	233.6	10.6	227.3	3.5	297.1	55.3	2.7	229.0	5.2
	54		315	198	0.24386	2.1	0.03561	0.9	0.40	0.04966	1.9	221.6	8.5	225.6	3.8	179.0	45.6	-1.8	227.3	5.5
	55		133	51	0.25036	3.7	0.03603	1.1	0.29	0.05039	3.6	226.9	15.2	228.2	4.9	213.2	82.7	-0.6	230.5	6.2
	56		577	1293	0.26913	2.1	0.03632	0.8	0.39	0.05373	1.9	242.0	9.0	230.0	3.7	359.8	43.8	4.9	231.2	5.2
	57		219	189	0.25893	2.7	0.03533	0.9	0.34	0.05315	2.5	233.8	11.3	223.8	4.0	335.4	57.7	4.3	225.7	5.4
	58		429	253	0.25053	2.1	0.03627	0.9	0.44	0.05010	1.9	227.0	8.7	229.7	4.2	199.6	44.4	-1.2	231.2	5.5
	59		216	197	0.25083	3.0	0.03587	0.9	0.30	0.05071	2.9	227.3	12.4	227.2	4.1	227.8	67.2	0.0	229.1	5.5
	60		361	220	0.25474	2.0	0.03617	0.8	0.37	0.05107	1.9	230.4	8.4	229.1	3.4	244.2	43.8	0.6	230.7	5.2
	61		519	375	0.25554	2.1	0.03596	0.7	0.33	0.05154	2.0	231.1	8.7	227.7	3.1	265.1	45.9	1.4	229.1	4.9
	62		384	256	0.27256	2.3	0.03625	0.7	0.33	0.05452	2.2	244.7	10.0	229.6	3.4	392.8	48.6	6.2	231.1	4.9
	66		27	12	1.10886	4.5	0.12338	1.3	0.30	0.06518	4.7	757.6	48.7	750.0	19.1	780.2	90.6	1.0	757.8	22.1
	67		303	166	0.24457	2.6	0.03599	0.8	0.31	0.04927	2.5	222.2	10.5	228.0	3.6	161.0	58.5	-2.6	229.7	5.2
	68		483	803	0.25976	1.8	0.03710	0.7	0.42	0.05077	1.6	234.5	7.5	234.9	3.4	230.6	37.6	-0.2	236.2	5.0
	69		248	170	0.24450	3.1	0.03592	1.0	0.31	0.04936	2.9	222.1	12.4	227.6	4.3	164.8	68.8	-2.5	229.4	5.8
	70		69	28	0.28168	4.8	0.03614	1.5	0.30	0.05652	4.6	252.0	21.6	228.9	6.6	472.9	101.7	9.2	231.6	7.8
	71		126	70	0.26269	3.5	0.03634	1.1	0.33	0.05242	3.3	236.8	14.7	230.1	5.1	303.9	74.9	2.8	232.4	6.3

151

Supplementary Table II.2. Continued

Rock Nr.	Spot Nr.	Studied fraction	U (ppm)	Pb (ppm)	207Pb/235U	±1σ (%)	206Pb/238U	±1σ (%)	rho	207Pb/206Pb	±1σ (%)	207Pb/235U	±2σ (Ma)	206Pb/238U	±2σ (Ma)	207Pb/206Pb	±2σ (Ma)	Disc. (%)	206Pb/238U	±2σ (Ma)
	72		967	1462	0.25258	1.7	0.03593	0.8	0.44	0.05098	1.5	228.7	7.0	227.6	3.4	239.8	35.8	0.5	228.5	5.2
	73		296	284	0.26067	2.4	0.03706	0.8	0.34	0.05101	2.3	235.2	10.2	234.6	3.8	241.2	52.6	0.3	236.3	5.3
	74		143	51	0.24486	3.3	0.03552	1.2	0.37	0.04999	3.0	222.4	13.1	225.0	5.3	194.6	70.9	-1.2	227.2	6.5
	75		696	688	0.26251	1.9	0.03601	0.7	0.39	0.05287	1.7	236.7	7.9	228.1	3.3	323.3	39.2	3.6	229.2	4.9
	76		149	28	0.24971	3.7	0.03543	1.1	0.29	0.05111	3.5	226.3	15.0	224.5	4.7	245.7	81.1	0.8	226.7	6.1
	77		890	424	0.24788	1.7	0.03577	0.7	0.41	0.05025	1.6	224.9	7.0	226.6	3.2	206.6	37.0	-0.8	227.7	4.8
	78		446	121	0.25187	2.0	0.03572	0.8	0.38	0.05113	1.9	228.1	8.3	226.3	3.5	246.9	43.6	0.8	227.8	5.1
	79		378	102	0.26057	2.2	0.03704	0.9	0.38	0.05102	2.1	235.1	9.5	234.5	4.0	241.6	48.0	0.3	236.1	5.7
	80		517	711	0.24154	2.1	0.03541	0.7	0.35	0.04947	1.9	219.7	8.1	224.3	3.2	170.2	45.0	-2.1	225.6	4.8
	81		859	922	0.26900	1.8	0.03631	0.7	0.37	0.05372	1.7	241.9	7.7	230.0	3.0	359.5	37.9	4.9	231.0	4.9
	82		810	882	0.25301	1.8	0.03571	0.7	0.39	0.05137	1.7	229.0	7.5	226.2	3.2	257.6	39.1	1.2	227.3	4.8
	347		788	843	0.25886	1.9	0.03673	1.0	0.50	0.05112	1.7	233.7	8.0	232.5	4.3	246.3	38.5	0.5	233.6	6.0
	348		220	104	0.26570	2.6	0.03712	1.1	0.42	0.05192	2.3	239.3	11.0	234.9	5.0	282.0	53.9	1.8	236.9	6.4
	349		540	409	0.25685	2.1	0.03729	1.0	0.46	0.04995	1.8	232.1	8.6	236.0	4.5	192.9	43.0	-1.7	237.4	6.0
	350		538	443	0.25604	2.0	0.03610	0.9	0.46	0.05143	1.8	231.5	8.4	228.6	4.2	260.4	41.5	1.2	230.0	5.5
	351		1138	547	0.25040	1.9	0.03584	1.0	0.51	0.05067	1.6	226.9	7.6	227.0	4.3	225.9	37.4	0.0	227.9	5.8
	352		1209	661	0.26116	1.8	0.03589	0.9	0.49	0.05277	1.6	235.6	7.7	227.3	4.0	319.0	36.8	3.5	228.2	5.5
	353		1102	564	0.25674	1.8	0.03638	1.0	0.53	0.05118	1.6	232.0	7.6	230.4	4.4	249.0	36.1	0.7	231.3	5.9
	354		286	286	0.24608	2.7	0.03603	1.1	0.42	0.04953	2.5	223.4	10.9	228.2	5.0	173.0	57.5	-2.2	229.9	6.2
VRG7546	355	Zircon	435	494	0.26319	2.3	0.03680	1.0	0.43	0.05187	2.1	237.2	9.7	233.0	4.5	279.6	47.5	1.8	234.4	6.0
	356		134	46	0.26488	3.8	0.03556	1.1	0.30	0.05402	3.6	238.6	16.0	225.3	5.0	371.8	80.7	5.6	227.5	6.2
	358		252	255	0.25008	2.5	0.03630	1.0	0.40	0.04997	2.3	226.6	10.3	229.9	4.6	193.5	54.2	-1.4	231.6	5.9
	359		168	74	0.24981	3.2	0.03608	1.1	0.33	0.05022	3.0	226.4	13.0	228.5	4.7	205.1	70.2	-0.9	230.6	6.2
	364		150	69	0.16750	4.8	0.03571	1.2	0.24	0.03402	4.6	157.3	14.0	226.2	5.2	0.1	0.0	-43.8	228.3	6.5
	365		412	304	0.24596	2.6	0.03548	1.1	0.41	0.05029	2.4	223.3	10.5	224.7	4.8	208.3	55.2	-0.6	226.2	6.1
	367		120	66	0.21858	4.1	0.03522	1.2	0.30	0.04501	3.9	200.7	14.9	223.1	5.4	0.1	0.2	-11.2	225.4	6.5
	368		447	299	0.24771	2.7	0.03657	1.2	0.43	0.04913	2.5	224.7	11.0	231.5	5.3	154.0	57.8	-3.0	233.0	6.7
	369		300	215	0.25628	2.9	0.03739	1.1	0.38	0.04971	2.7	231.7	12.2	236.6	5.2	181.7	63.3	-2.1	238.4	6.4
	370		419	377	0.25357	2.1	0.03715	1.0	0.47	0.04951	1.9	229.5	8.8	235.1	4.6	172.1	44.3	-2.5	236.6	6.0
	371		755	596	0.25527	2.2	0.03588	1.0	0.46	0.05160	1.9	230.8	9.0	227.2	4.5	267.8	44.6	1.6	228.4	5.8
	372		1302	1870	0.26212	1.8	0.03642	0.9	0.49	0.05221	1.6	236.4	7.7	230.6	4.1	294.5	36.5	2.5	231.3	5.5
	373		321	221	0.26007	2.7	0.03058	1.1	0.41	0.06167	2.5	234.7	11.5	194.2	4.3	662.8	53.5	17.3	195.7	5.3
	374		508	322	0.25522	2.2	0.03647	1.0	0.48	0.05075	1.9	230.8	9.0	230.9	4.8	229.7	44.1	0.0	232.3	5.9
	375		447	260	0.25287	2.4	0.03598	1.0	0.41	0.05097	2.2	228.9	9.8	227.9	4.4	239.5	50.2	0.4	229.4	5.8
	376		845	506	0.25212	2.0	0.03588	0.9	0.46	0.05096	1.7	228.3	8.0	227.3	4.0	239.0	40.1	0.5	228.3	5.5
	377		226	131	0.27130	4.0	0.03662	1.2	0.31	0.05373	3.8	243.7	17.3	231.9	5.5	359.9	85.4	4.9	233.8	6.7
	378		747	454	0.25565	2.0	0.03654	0.9	0.46	0.05074	1.9	231.2	8.4	231.4	4.2	229.0	41.9	-0.1	232.5	5.6
	379		390	247	0.24105	2.6	0.03581	1.0	0.38	0.04882	2.4	219.4	10.5	226.8	4.5	139.1	57.6	-3.4	228.4	5.8
	383		368	134	0.25856	2.2	0.03557	1.0	0.46	0.05272	2.0	233.5	9.2	225.3	4.4	316.6	44.7	3.5	226.9	5.8
	384		353	154	0.24551	2.6	0.03595	1.0	0.37	0.04954	2.5	222.9	10.6	227.7	4.3	173.4	57.3	-2.1	229.3	5.8

Supplementary Table II.2. Continued

Rock Nr.	Spot Nr.	Studied fraction	U (ppm)	Pb (ppm)	Isotopic data ²⁰⁷Pb/²³⁵U	±1σ (%)	²⁰⁶Pb/²³⁸U	±1σ (%)	rho	²⁰⁷Pb/²⁰⁶Pb	±1σ (%)	Ages ²⁰⁷Pb/²³⁵U	±2σ (Ma)	²⁰⁶Pb/²³⁸U	±2σ (Ma)	²⁰⁷Pb/²⁰⁶Pb	±2σ (Ma)	Disc. (%)	RDC age ²⁰⁶Pb/²³⁸U	±2σ (Ma)
VRG7546	385		210	109	0.24320	3.3	0.03443	1.2	0.35	0.05124	3.1	221.0	13.3	218.2	5.0	251.5	71.8	1.3	220.1	6.3
	386		181	41	0.26851	3.4	0.03588	1.1	0.31	0.05427	3.2	241.5	14.6	227.3	4.7	382.4	72.5	5.9	229.3	6.2
	387		219	154	0.24940	3.4	0.03547	1.3	0.38	0.05100	3.1	226.1	13.9	224.7	5.8	240.9	72.6	0.6	226.6	6.9
	388		56	19	0.19895	7.6	0.03552	1.6	0.22	0.04063	7.4	184.2	25.7	225.0	7.2	0.1	0.1	-22.1	227.8	8.1
	389		355	452	0.27273	2.5	0.03676	1.0	0.41	0.05380	2.2	244.9	10.8	232.7	4.6	362.8	50.9	5.0	234.4	6.0
	390	Zircon	65	27	0.27183	4.7	0.03519	1.7	0.37	0.05602	4.3	244.2	20.3	223.0	7.6	453.2	96.1	8.7	225.6	8.4
	391		61	23	0.25265	6.6	0.03455	1.5	0.23	0.05303	6.5	228.7	27.4	219.0	6.6	330.3	146.5	4.3	221.6	7.5
	392		66	22	0.22581	5.2	0.03558	1.4	0.28	0.04603	5.0	206.7	19.5	225.4	6.4	0.1	9.6	-9	228.1	7.3
	393		179	199	0.26902	3.6	0.03580	1.1	0.30	0.05451	3.4	241.9	15.4	226.7	4.8	392.1	76.3	6.3	228.7	6.2
	394		253	307	0.24991	3.1	0.03537	1.1	0.36	0.05125	2.9	226.5	12.8	224.0	5.0	252.2	67.6	1.1	225.8	6.1
	395		145	69	0.24820	3.4	0.03574	1.2	0.36	0.05037	3.2	225.1	13.8	226.4	5.4	212.2	73.8	-0.6	228.5	6.5

Supplementary Table IV.1. Mafic clot types and analyzed minerals of the studied rocks from the Ditrău Alkaline Massif (Romania). Modal compositions are given in vol%

	Sample	LBH2	LB8	LB16f (felsic part)	LB16m (mafic part)	LI18f (fine-grained)	LI18c (coarse-grained)	LHH23/1	LTa29	LTo35	LN50/1	LO52/1	LBH55/1
	Rock type	MDo	D	Do	PlPxH	Mo	M	M	M	MG	MG	L	MDo
Mafic clot type and modal proportion in the host (vol%)	*Amp-A*	x (13)				x (2)	x (8)		x (3)	x (1)			
	Bt-Xen												x (20)
	Bt-Dom							x (18)					
	Bt-Ran									x (2)			x (3)
	AmpBt	x (4)				x (1)	x (1)		x (2)	x (6)			
	AmpCpx-TtnOpqBt								x (2)				
Analysed phases	**Act**								x				
	Amp	x		x	x	x	x		x	x		x	
	Cpx			x	x				x			x	
	Pl	x	x	x		x	x	x	x	x	x	x	x

Abbreviations: D – diorite, Do – diorite with oriented texture, L – lamprophyre, M – monzonite, Mo – monzonite with oriented texture, MDo – monzodiorite with oriented texture, MG – monzogranite, PlPxH – plagioclase-bearing pyroxene hornblendite;

Act – actinolite, Amp – amphibole, Bt – biotite, Cpx – clinopyroxene, Opq – opaque minerals, Ttn – titanite;

Amp-A – amphibole-rich aggregate, *AmpBt* – amphibole + biotite cluster, *AmpCpxTtnOpqBt* – amphibole + clinopyroxene + titanite + opaque minerals ± biotite aggregate, *Bt-Dom* – biotite-rich clot in certain domains of the rocks where feldspars are absent, *Bt-Ran* – randomly distributed biotite-rich aggregate, *Bt-Xen* – xenolith-related biotite-rich cluster

Supplementary Table IV.2. Characteristic textural features of the studied clinopyroxene crystals from the Ditrău Alkaline Massif (Romania)

Sample	Rock type	Groundmass clinopyroxene					Clot-forming clinopyroxene					Proportion in the clots (vol%)
		Optical properties	Habit	Size (mm)	Texture	Abundance (vol%)	Optical properties	Habit	Size (mm)	Texture	Clot type	
LB16m mafic part	PlPxH	Pale green, pale brown	H	0.1–2	-	4	Pale green, pale brown	H–X	0.1–1	Granoblastic	Orbicular inclusion (Cpx + Bt)	40
LTa29	M	-	-	-	-	-	Pale green, pale brown	H–X	0.5–1	± Act mantle	*AmpCpxTtnOpqBt*	10
LO52/1	L	Colorless, pale brown	H–X	0.5–2	Bt mantle	2	Colorless, pale brown	H–X	0.5–2	Chloritized, Bt mantle	Orbicular inclusion (Bt ± Cpx ± Amp)	0–20

Abbreviations: L – lamprophyre, M – monzonite, PlPxH – plagioclase-bearing pyroxene hornblendite;

Act – actinolite, Amp – amphibole, Bt – biotite, Cpx – clinopyroxene;

AmpCpxTtnOpqBt – amphibole + clinopyroxene + titanite + opaque minerals ± biotite aggregate;

H – hypidiomorphic, X – xenomorphic

Supplementary Table IV.3. Major (wt%) and trace element (ppm) compositions of the analyzed clinopyroxene populations from the Ditrău Alkaline Massif (Romania). Clot-forming clinopyroxene data are marked in bold

Sample	LB16m (mafic part)				LTa29		LO52/1		
Rock type	Plagioclase-bearing pyroxene hornblendite				Monzonite		Lamprophyre		
Location	G	G	G	OI	C	C	G	G	OI
Spot	LB16 22_01	LB16 32_01	LB16 32_02	**LB16 33_01**	**LTa29 04_01**	**LTa29 04_02**	LO52_1 12_01	LO52_1 12_02	**LO52_1 38_01**
Area	Core	Core	Rim	**Core**	**Rim**	**Core**	Core	Rim	**Rim**
Mineral	Al-Di	Di	Al-Fe-Na-Di	**Di**	**Al-Fe-Di**	**Al-Di**	Al-Na-Di	Subsilicic Agt	**Al-Fe-Na-Di**
Major elements (wt%)									
SiO₂	52.28	52.61	51.58	**53.50**	**50.22**	**51.21**	49.18	42.85	**49.86**
TiO₂	0.78	0.67	0.97	**0.32**	**0.74**	**0.78**	2.00	1.22	**1.88**
Al₂O₃	2.75	2.06	3.15	**1.13**	**3.10**	**2.54**	6.54	11.84	**6.25**
Fe₂O₃	2.32	2.80	4.22	**2.58**	**5.17**	**3.14**	3.40	16.81	**3.70**
FeO	6.68	6.26	6.85	**4.35**	**6.64**	**7.01**	3.42	0.43	**2.48**
MnO	0.12	0.25	0.36	**0.35**	**0.52**	**0.45**	0.08	0.33	**0.10**
MgO	12.53	12.71	11.48	**14.27**	**10.89**	**11.79**	12.50	10.30	**13.26**
CaO	22.17	22.56	21.54	**23.38**	**21.83**	**21.88**	21.50	12.75	**21.41**
Na₂O	1.21	1.17	1.54	**0.90**	**1.33**	**1.17**	1.54	2.88	**1.62**
K₂O	0.02	0.00	0.04	**0.00**	**0.00**	**0.00**	0.05	1.16	**0.05**
Total	100.86	101.10	101.72	**100.78**	**100.45**	**99.97**	100.20	100.57	**100.60**
mg#	0.77	0.78	0.75	**0.85**	**0.74**	**0.75**	0.86	0.82	**0.90**
En	37.45	37.39	34.63	**40.76**	**32.79**	**35.42**	39.50		**41.47**
Fe	14.92	14.91	18.64	**11.25**	**19.97**	**17.34**	11.65		**10.38**
Wo	47.64	47.70	46.72	**48.00**	**47.23**	**47.24**	48.85		**48.15**
Jd								5.65	
Aeg								21.90	
Ca-Mg-Fe								72.45	
Trace elements (ppm)									
Sc	49.56	71.24	72.53	**44.05**	**31.19**	**25.97**	46.44	60.37	**61.53**
V	207.66	245.23	252.68	**135.39**	**133.99**	**129.43**	201.55	301.06	**263.53**
Cr	139.32	192.40	195.81	**68.46**	**3.31**	**1.93**	1292.85	3623.38	**1569.87**
Ni	70.92	81.81	66.67	**63.74**	**5.25**	**9.13**	94.73	216.38	**207.87**
Rb	<0.44	2.31	<0.27	**<0.23**	**<0.111**	**0.71**	3.23	3.33	**<0.37**
Sr	64.18	54.86	58.36	**91.65**	**51.91**	**73.54**	157.98	119.84	**124.53**
Y	21.00	18.33	13.60	**20.87**	**17.70**	**19.80**	21.87	15.39	**18.88**
Zr	465.84	611.41	588.04	**253.57**	**497.89**	**317.52**	114.29	123.52	**82.12**
Nb	1.42	1.51	1.07	**0.48**	**1.80**	**1.27**	1.56	1.58	**1.26**
Cs	<0.209	<0.140	<0.120	**<0.109**	**<0.063**	**<0.065**	<0.237	<0.26	**<0.221**
Ba	0.71	9.25	1.34	**0.16**	**0.20**	**3.12**	5.34	11.52	**1.59**
La	22.00	21.23	15.22	**17.65**	**30.37**	**24.59**	10.91	9.25	**6.75**
Ce	51.60	46.20	31.17	**44.20**	**66.09**	**60.28**	34.93	30.51	**22.21**
Pr	6.37	5.49	3.56	**6.17**	**7.31**	**7.54**	5.62	5.32	**3.86**
Nd	25.61	21.32	13.95	**25.57**	**24.16**	**27.39**	26.27	24.91	**18.47**
Sm	5.46	4.58	3.29	**6.44**	**4.15**	**5.27**	6.60	6.94	**5.42**
Eu	1.61	1.31	0.99	**1.89**	**1.15**	**1.49**	2.44	2.23	**1.93**
Gd	4.82	4.34	2.91	**6.27**	**3.49**	**4.30**	6.28	6.59	**5.51**
Tb	0.68	0.61	0.40	**0.78**	**0.54**	**0.69**	0.93	0.92	**0.78**
Dy	4.23	3.78	2.42	**4.69**	**2.98**	**3.60**	5.11	4.35	**4.23**
Ho	0.72	0.64	0.51	**0.84**	**0.63**	**0.75**	0.94	0.70	**0.81**
Er	2.23	1.86	1.55	**2.08**	**1.88**	**2.14**	2.25	1.30	**1.87**
Tm	0.35	0.28	0.23	**0.28**	**0.34**	**0.33**	0.29	0.11	**0.23**
Yb	2.55	2.25	1.97	**1.84**	**2.60**	**2.41**	1.48	0.62	**1.28**
Lu	0.47	0.49	0.38	**0.31**	**0.59**	**0.48**	0.21	0.13	**0.17**
Hf	13.44	17.52	14.40	**7.31**	**13.28**	**8.64**	4.10	5.30	**3.60**
Ta	0.19	0.15	0.04	**0.06**	**0.15**	**0.16**	0.31	0.33	**0.22**
Pb	0.25	0.79	0.36	**0.28**	**0.35**	**1.70**	0.55	1.19	**0.39**
Th	0.10	0.61	0.27	**0.06**	**0.11**	**0.14**	0.16	0.13	**0.19**
U	0.01	0.02	0.01	**0.01**	**0.01**	**0.03**	0.06	0.04	**0.10**
(La/Sm)ₙ	0.70	2.89	1.71	**5.56**	**2.91**	**7.31**	0.83	0.78	**0.20**
(Gd/Yb)ₙ	0.77	1.20	2.76	**0.46**	**1.44**	**2.00**	8.56	3.47	**0.54**

Abbreviations: C – clot, G – groundmass, OI – orbicular inclusion;

Agt – aegirine-augite, Di – diopside

Supplementary Table IV.4. Distinct textural characteristics of the analyzed actinolite crystals from the Ditrău Alkaline Massif (Romania)

Sample	Rock type	Groundmass actinolite					Clot-forming actinolite					
		Optical properties	Habit	Size (mm)	Texture	Abundance (vol%)	Optical properties	Habit	Size (mm)	Texture	Clot type	Proportion in the clots (vol%)
LTa29	M	Blueish green	H–X	0.1–1	Sieved, fibrous	1	Blueish green	H–X	0.1–1	Sieved, fibrous; mantles Cpx; inclusion in Amp	*AmpCpxTtnOpqBt*	40

Abbreviations: M – monzonite;

Amp – amphibole, Cpx – clinopyroxene;

AmpCpxTtnOpqBt – amphibole + clinopyroxene + titanite + opaque minerals ± biotite aggregate;

H – hypidiomorphic, X – xenomorphic

Supplementary Table IV.5. Major (wt%) and trace element (ppm) compositions of the analyzed actinolite crystals from the Ditrău Alkaline Massif (Romania). Clot-forming actinolite data are marked in bold

Sample	LTa29				
Rock type	Monzonite				
Location	C	G	C	C	G
Spot	LTa29 04_03	LTa29 12_02	LTa29 20_01	LTa29 32_01	LTa29 51_03
Area	Core	Rim	Rim	Core	Rim
Mineral		Act	Mg-Hbl	Act	Act

Major elements (wt%)

SiO$_2$	**66.80**	52.95	**49.95**	**52.54**	54.21
TiO$_2$	**0.00**	0.16	**0.05**	**0.19**	0.12
Al$_2$O$_3$	**21.01**	3.18	**4.85**	**3.12**	1.22
Fe$_2$O$_3$	**0.00**	5.48	**5.05**	**4.87**	1.07
FeO	**0.36**	8.74	**13.15**	**10.55**	13.44
MnO	**0.04**	0.93	**0.96**	**0.90**	1.07
MgO	**0.13**	15.19	**11.76**	**14.25**	14.10
CaO	**0.79**	12.06	**11.93**	**11.99**	12.48
Na$_2$O	**10.15**	0.49	**0.65**	**0.60**	0.19
K$_2$O	**1.03**	0.19	**0.28**	**0.15**	0.06
Total	**100.29**	99.37	**98.63**	**99.14**	97.96

mg#	**0.40**	0.76	**0.61**	**0.71**	0.65

T Si	**9.43**	7.51	**7.31**	**7.52**	7.86
T Al ^{IV}	**0.00**	0.49	**0.69**	**0.48**	0.14
C Al ^{VI}	**3.50**	0.04	**0.15**	**0.05**	0.06
C Ti $^{4+}$	**0.00**	0.02	**0.01**	**0.02**	0.01
C Fe $^{2+}$	**0.04**	1.04	**1.61**	**1.26**	1.63
C Fe $^{3+}$	**0.00**	0.58	**0.56**	**0.52**	0.12
C Mg^{2+}	**0.03**	3.21	**2.56**	**3.04**	3.05
C Mn^{2+}	**0.01**	0.11	**0.12**	**0.11**	0.13
B Ca^{2+}	**0.12**	1.83	**1.87**	**1.84**	1.94
B Na$^+$	**1.88**	0.17	**0.13**	**0.16**	0.06
A Na$^+$	**0.90**		**0.06**	**0.00**	
A K$^+$	**0.18**	0.03	**0.05**	**0.03**	0.01

Trace elements (ppm)

Sc	**41.69**	39.05	**31.33**	**41.45**	38.15
V	**206.21**	146.31	**188.74**	**176.97**	177.20
Cr	**2.82**	5.90	**56.24**	**2.86**	5.53
Ni	**7.22**	11.32	**16.72**	**11.73**	6.11
Rb	**4.26**	5.49	**19.58**	**0.52**	1.05
Sr	**51.49**	32.27	**17.15**	**76.24**	34.22
Y	**11.36**	5.87	**10.62**	**12.84**	7.44
Zr	**600.39**	349.01	**128.50**	**597.02**	402.10
Nb	**1.93**	3.66	**2.38**	**6.52**	0.12
Cs	**<0.082**	<0.104	**0.20**	**<0.059**	<0.095
Ba	**416.10**	15.74	**23.70**	**5.52**	9.26
La	**5.60**	10.91	**1.99**	**3.29**	3.29
Ce	**22.48**	19.02	**10.54**	**12.34**	7.65
Pr	**3.55**	2.02	**2.35**	**2.13**	1.19
Nd	**13.69**	6.28	**11.93**	**9.50**	4.83
Sm	**2.91**	1.27	**3.07**	**2.32**	1.05
Eu	**0.51**	0.52	**0.26**	**0.79**	0.27
Gd	**2.50**	1.10	**3.07**	**2.33**	0.99
Tb	**0.41**	0.15	**0.46**	**0.40**	0.20
Dy	**2.27**	1.01	**2.48**	**2.18**	1.14
Ho	**0.43**	0.22	**0.47**	**0.49**	0.26
Er	**1.15**	0.63	**1.02**	**1.48**	0.89
Tm	**0.18**	0.11	**0.14**	**0.24**	0.15
Yb	**1.23**	0.91	**0.79**	**2.01**	1.49
Lu	**0.29**	0.21	**0.10**	**0.53**	0.42
Hf	**16.14**	14.41	**6.65**	**17.00**	12.17
Ta	**0.17**	0.07	**0.23**	**0.16**	0.02
Pb	**5.53**	0.56	**0.39**	**0.38**	2.22
Th	**0.11**	0.42	**0.04**	**0.43**	0.24
U	**0.03**	0.07	**0.00**	**1.03**	0.03
ΣREE	**110.24**	89.27	**80.62**	**94.33**	69.41
(La/Sm)$_N$	**1.20**	5.36	**0.40**	**0.89**	1.96
(Gd/Yb)$_N$	**1.65**	0.97	**3.14**	**0.94**	0.54

Abbreviations:

C – clot,

G – groundmass;

Act – actinolite,

Hbl – hornblende

Supplementary Table IV.6. Characteristic textural features of the studied amphibole crystals from the Ditrău Alkaline Massif (Romania)

Sample	Rock type	Groundmass amphibole					Clot-forming amphibole					
		Optical properties	Habit	Size (mm)	Texture	Abundance (vol%)	Optical properties	Habit	Size (mm)	Texture	Clot type	Proportion in the clots (vol%)
LBH2	MDo	Green–dark brownish green; ± zoned	I–X	0.1–4	Oriented; Ap, Opq, Ttn, Zrn inclusions	3	Green–dark brownish green; ± zoned	I–X	0.1–3	Ap, Opq, Ttn, Zrn inclusions	*Amp-A, AmpBt*	~100, 40
LB16m (mafic part)	PlPxH	Yellow–dark brownish green; ± zoned	I–H	0.5–2	Ap, Ttn inclusions	5	Yellow–dark brownish green; ± zoned	I–H	0.5–2	Ap, Ttn inclusions	*Amp-A, AmpBt*	~100, 50
LI18f (fine-grained)	Mo	Green–dark brownish green	I–H	0.2–1	Ttn inclusions	1	Green–dark brownish green	I–H	0.3–2	Ttn inclusions	*Amp-A, AmpBt*	~100, 50
LI18c (coarse-grained)	M	Green–dark brownish green	H	0.2–5	Ap, Ttn inclusions	6	Green–dark brownish green	H	2–4	Ap, Ttn inclusions	*Amp-A, AmpBt*	~100, 70
LTa29	M	Green–dark brownish green	H	0.2–2	Ap, Ttn inclusions	2	Green–dark brownish green	H	0.1–2	Ap, Ttn inclusions	*Amp-A, AmpBt, AmpCpxTtnOpqBt*	~100, 50, 40
LTo35	MG	Green–dark brownish green	I–H	0.1–2	Ap, Ttn, Zrn inclusions	3	Green–dark brownish green	I–H	0.3–2	Ap, Ttn, Zrn inclusions	*Amp-A, AmpBt*	~100, 60
LO52/1	L	Yellow–dark brownish green	I–H	0.1–1	-	20	Yellow–dark brownish green	I–H	0.1–0.5	-	*Amp-A,* Orbicular inclusion (Bt ± Cpx ± Amp)	~100, 0–30

Abbreviations: L – lamprophyre dyke, M – monzonite, Mo – monzonite with oriented texture, MDo – monzodiorite with oriented texture, MG – monzogranite, PlPxH – plagioclase-bearing pyroxene hornblendite;

Amp – amphibole, Ap – apatite, Bt – biotite, Cpx – clinopyroxene, Opq – opaque minerals, Ttn – titanite, Zrn – zircon;

Amp-A – amphibole-rich aggregate, *AmpBt* – amphibole + biotite aggregate, *AmpCpxTtnOpqBt* – amphibole + clinopyroxene + titanite + opaque minerals ± biotite aggregate;

I – idiomorphic, H – hypidiomorphic, X – xenomorphic

Supplementary Table IV.7. Major (wt%) and trace element (ppm) compositions of the analyzed amphibole populations from the Ditrău Alkaline Massif (Romania). Clot-forming amphibole data are marked in bold

Sample	LBH2												
Rock type	Monzodiorite with oriented texture												
Location	G	G	G	G	G	C	C	C	C	C	C	C	C
Spot	LBH2 29_01	LBH2 29_02	LBH2 31_01	LBH2 31_02	LBH2 31_03	**LBH2 53_01**	**LBH2 53_02**	**LBH2 56_01**	**LBH2 56_02**	**LBH2 56_03**	**LBH2 60_01**	**LBH2 60_02**	**LBH2 60_03**
Area	Core	Rim	Core	Transition	Rim	**Core**	**Rim**	**Core**	**Transition**	**Rim**	**Core**	**Transition (inner)**	**Transition (outer)**
Mineral	Hst	Hst	Hst	Hst	Hst	**Hst**	**Hst**	**Hst**	**Hst**	**Hst**	**Hst**	**Hst**	**Hst**

Major elements (wt%)

SiO$_2$	37.57	37.75	38.94	38.53	38.17	**38.09**	**37.93**	**37.99**	**37.98**	**38.65**	**39.45**	**38.87**	**38.84**
TiO$_2$	3.47	2.16	3.44	1.11	1.84	**2.08**	**1.72**	**2.03**	**2.73**	**2.45**	**3.39**	**2.87**	**2.80**
Al$_2$O$_3$	11.87	12.37	11.05	12.08	12.52	**12.40**	**12.16**	**12.27**	**11.54**	**12.06**	**11.60**	**11.46**	**11.35**
Fe$_2$O$_3$	4.33	7.38	3.04	8.54	6.82	**7.42**	**7.20**	**6.47**	**3.68**	**5.46**	**3.54**	**3.00**	**5.03**
FeO	18.31	16.60	16.43	14.88	16.80	**16.99**	**17.32**	**17.96**	**19.54**	**18.70**	**16.87**	**17.83**	**17.44**
MnO	0.73	1.13	0.71	0.91	0.98	**1.02**	**0.89**	**0.88**	**0.71**	**1.12**	**0.69**	**0.90**	**0.85**
MgO	6.43	6.17	8.65	7.42	6.43	**6.19**	**6.05**	**5.79**	**6.15**	**6.15**	**8.29**	**7.24**	**7.18**
CaO	10.43	10.10	10.78	10.46	10.21	**10.24**	**10.22**	**10.23**	**10.51**	**10.72**	**10.71**	**10.38**	**10.62**
Na$_2$O	2.80	2.84	2.79	2.77	2.88	**2.76**	**2.79**	**2.72**	**2.93**	**2.80**	**2.95**	**2.90**	**2.83**
K$_2$O	1.73	1.97	1.94	2.00	2.06	**2.08**	**2.00**	**1.98**	**1.81**	**1.89**	**1.85**	**1.88**	**1.66**
Total	97.66	98.48	97.77	98.72	98.72	**99.27**	**98.29**	**98.32**	**97.58**	**100.00**	**99.35**	**97.32**	**98.59**

mg#	0.38	0.40	0.48	0.47	0.41	**0.39**	**0.38**	**0.37**	**0.36**	**0.37**	**0.47**	**0.42**	**0.42**

T Si	5.89	5.87	6.02	5.94	5.91	**5.88**	**5.92**	**5.93**	**5.98**	**5.94**	**6.01**	**6.07**	**6.00**
T Al ^{IV}	2.11	2.13	1.98	2.06	2.09	**2.12**	**2.08**	**2.07**	**2.02**	**2.06**	**1.99**	**1.93**	**2.00**
C Al ^{VI}	0.08	0.14	0.03	0.14	0.20	**0.14**	**0.16**	**0.19**	**0.13**	**0.13**	**0.09**	**0.18**	**0.07**
C Ti $^{4+}$	0.41	0.25	0.40	0.13	0.21	**0.24**	**0.20**	**0.24**	**0.32**	**0.28**	**0.39**	**0.34**	**0.32**
C Fe $^{2+}$	2.40	2.16	2.13	1.92	2.18	**2.19**	**2.26**	**2.35**	**2.58**	**2.40**	**2.15**	**2.33**	**2.25**
C Fe $^{3+}$	0.51	0.86	0.35	0.99	0.80	**0.86**	**0.85**	**0.76**	**0.44**	**0.63**	**0.41**	**0.35**	**0.59**
C Mg^{2+}	1.50	1.43	1.99	1.71	1.48	**1.43**	**1.41**	**1.35**	**1.44**	**1.41**	**1.88**	**1.68**	**1.65**
C Mn^{2+}	0.10	0.15	0.09	0.12	0.13	**0.13**	**0.12**	**0.12**	**0.09**	**0.15**	**0.09**	**0.12**	**0.11**
B Ca^{2+}	1.75	1.68	1.79	1.73	1.70	**1.69**	**1.71**	**1.71**	**1.77**	**1.77**	**1.75**	**1.74**	**1.76**
B Na$^+$	0.25	0.32	0.21	0.27	0.30	**0.31**	**0.29**	**0.29**	**0.23**	**0.23**	**0.25**	**0.26**	**0.24**
A Na$^+$	0.60	0.54	0.62	0.55	0.56	**0.52**	**0.56**	**0.53**	**0.67**	**0.60**	**0.62**	**0.61**	**0.61**
A K$^+$	0.35	0.39	0.38	0.39	0.41	**0.41**	**0.40**	**0.40**	**0.36**	**0.37**	**0.36**	**0.37**	**0.33**

Trace elements (ppm)

Sc	11.01	9.82	12.71	12.79	10.98	**20.47**	**22.37**	**20.35**	**10.43**	**8.76**	**11.75**	**12.14**	**13.63**
V	184.24	276.41	202.21	188.17	278.96	**282.14**	**283.19**	**266.22**	**215.29**	**261.24**	**229.47**	**213.90**	**193.27**
Cr	3.45	3.10	0.98	<0.39	3.55	**3.96**	**4.31**	**7.00**	**1.50**	**3.25**	**<0.37**	**<0.37**	**0.54**
Ni	4.61	4.85	5.31	3.52	4.89	**3.61**	**3.41**	**4.24**	**4.73**	**4.72**	**4.65**	**4.60**	**5.56**
Rb	12.06	20.05	14.60	10.14	20.09	**22.59**	**24.55**	**20.84**	**15.10**	**21.66**	**16.35**	**15.82**	**11.13**
Sr	492.04	129.90	138.60	53.04	117.72	**88.29**	**88.51**	**81.71**	**158.64**	**151.50**	**79.76**	**93.12**	**202.26**
Y	31.49	15.74	25.70	8.87	16.36	**19.84**	**18.35**	**22.46**	**19.70**	**16.28**	**24.88**	**18.71**	**24.74**
Zr	558.58	833.52	761.42	454.09	912.02	**1419.75**	**1425.10**	**972.65**	**698.53**	**989.15**	**877.47**	**767.62**	**482.56**
Nb	145.20	113.50	179.45	53.26	127.52	**142.48**	**137.55**	**192.15**	**139.06**	**98.03**	**175.80**	**145.59**	**156.30**
Cs	<0.068	<0.067	<0.068	<0.075	<0.077	**<0.069**	**0.15**	**<0.078**	**<0.072**	**<0.080**	**<0.067**	**0.19**	**<0.060**
Ba	716.79	106.32	177.95	29.17	87.12	**52.73**	**52.27**	**52.29**	**95.63**	**116.31**	**21.74**	**18.30**	**371.89**
La	58.17	53.36	67.11	29.73	68.70	**71.09**	**69.02**	**80.58**	**56.12**	**55.08**	**84.74**	**63.65**	**58.07**
Ce	129.72	92.86	130.99	53.07	117.13	**116.71**	**111.93**	**136.10**	**104.60**	**94.52**	**154.60**	**114.46**	**119.59**
Pr	16.25	8.58	13.59	5.42	10.49	**10.35**	**10.01**	**12.18**	**10.34**	**8.74**	**15.24**	**11.56**	**13.46**
Nd	60.65	24.39	42.08	16.79	29.80	**28.46**	**27.49**	**35.37**	**32.13**	**25.30**	**45.94**	**35.10**	**45.16**
Sm	11.45	3.56	7.01	2.61	4.29	**4.51**	**4.03**	**5.39**	**4.89**	**3.61**	**6.35**	**5.55**	**7.68**
Eu	3.06	1.30	1.98	0.68	1.24	**1.31**	**1.27**	**1.49**	**1.54**	**1.32**	**1.68**	**1.48**	**2.10**
Gd	9.18	3.02	5.43	2.01	3.46	**3.61**	**3.45**	**4.28**	**3.91**	**3.02**	**5.07**	**4.15**	**5.95**
Tb	1.26	0.50	0.85	0.29	0.48	**0.55**	**0.48**	**0.66**	**0.59**	**0.46**	**0.80**	**0.60**	**0.94**
Dy	6.70	2.54	4.42	1.36	2.69	**3.13**	**2.76**	**3.48**	**3.30**	**2.62**	**4.64**	**3.30**	**4.69**
Ho	1.23	0.63	0.98	0.34	0.63	**0.69**	**0.64**	**0.78**	**0.73**	**0.57**	**0.86**	**0.71**	**0.94**
Er	3.23	1.68	2.67	0.87	1.74	**2.02**	**1.88**	**2.17**	**2.04**	**1.73**	**2.59**	**1.95**	**2.33**
Tm	0.39	0.27	0.40	0.14	0.27	**0.33**	**0.26**	**0.36**	**0.30**	**0.28**	**0.39**	**0.30**	**0.33**
Yb	2.80	2.28	2.80	1.19	2.16	**2.42**	**2.01**	**2.78**	**2.30**	**2.32**	**2.97**	**2.39**	**2.39**
Lu	0.51	0.52	0.56	0.29	0.52	**0.58**	**0.49**	**0.62**	**0.52**	**0.50**	**0.61**	**0.47**	**0.47**
Hf	14.73	17.61	18.48	10.80	21.11	**43.09**	**44.97**	**28.99**	**16.11**	**18.81**	**24.93**	**18.55**	**11.81**
Ta	5.98	1.19	2.93	0.83	1.11	**0.84**	**0.90**	**1.01**	**1.69**	**1.13**	**3.13**	**2.38**	**3.35**
Pb	1.80	1.61	3.28	1.05	1.53	**1.60**	**1.67**	**1.65**	**1.41**	**1.29**	**1.21**	**1.97**	**1.34**
Th	0.35	0.35	2.22	0.07	0.25	**1.01**	**0.95**	**0.94**	**0.25**	**0.31**	**0.35**	**0.19**	**0.19**
U	0.06	0.04	0.05	0.01	0.07	**0.21**	**0.11**	**0.22**	**0.07**	**0.17**	**0.10**	**0.05**	**0.06**
ΣREE	347.11	221.04	319.27	136.45	270.93	**286.06**	**276.44**	**329.04**	**253.44**	**225.12**	**363.11**	**276.52**	**302.46**
(La/Sm)$_N$	3.17	9.36	5.98	7.11	10.00	**9.84**	**10.70**	**9.34**	**7.17**	**9.53**	**8.33**	**7.16**	**4.72**
(Gd/Yb)$_N$	2.65	1.07	1.57	1.37	1.30	**1.21**	**1.39**	**1.25**	**1.38**	**1.05**	**1.38**	**1.40**	**2.01**
Eu/Eu*	0.91	1.20	0.98	0.90	0.98	**0.99**	**1.04**	**0.94**	**1.07**	**1.22**	**0.90**	**0.94**	**0.95**

159

Supplementary Table IV.7. Continued

Sample	LBH2											
Rock type	Monzodiorite with oriented texture											
Location	C	C	C	C	C	G	G	G	G	C	C	C
Spot	LBH2 60_04	LBH2 61_01	LBH2 61_02	LB16 35_01	LB16 35_02	LB16 36_01	LB16 36_02	LB16 36_03	LB16 36_04	LB16 37_01	LB16 37_02	LB16 37_03
Area	Rim	Core	Rim	Core	Rim	Core	Transition (inner)	Transition (outer)	Rim	Transition	Core	Rim
Mineral	Hst	Hst	Hst	Hst	Hst	Hst	Hst	Hst	Hst	Hst	Hst	Hst

Major elements (wt%)

SiO$_2$	37.98	38.51	38.68	39.55	40.47	40.37	41.00	41.18	40.17	39.68	40.67	40.30
TiO$_2$	2.43	2.54	2.17	5.25	3.10	5.38	3.94	3.30	3.09	3.44	4.92	1.79
Al$_2$O$_3$	12.25	11.59	11.80	12.35	12.12	12.69	11.85	11.48	12.03	12.17	12.30	12.27
Fe$_2$O$_3$	5.37	6.57	6.00	0.00	2.82	0.00	0.00	2.98	2.69	2.09	0.00	4.32
FeO	17.93	16.67	17.17	14.11	13.89	12.43	14.56	12.79	14.23	15.71	13.65	14.49
MnO	1.07	0.85	0.90	0.37	0.42	0.29	0.29	0.49	0.50	0.36	0.28	0.43
MgO	6.18	7.08	6.41	10.50	10.31	11.63	10.86	10.86	9.96	9.41	10.95	9.53
CaO	10.41	10.48	10.21	10.89	10.97	11.11	11.10	10.81	11.02	11.10	11.27	10.90
Na$_2$O	2.86	2.86	2.66	3.04	2.85	3.24	3.08	2.89	2.84	2.72	3.12	2.92
K$_2$O	1.85	1.70	1.76	1.37	1.65	1.09	1.37	1.23	1.41	1.78	1.25	1.84
Total	98.34	98.85	97.76	97.43	98.59	98.23	98.05	98.01	97.95	98.47	98.40	98.79

mg#	0.38	0.43	0.40	0.57	0.57	0.63	0.57	0.60	0.55	0.52	0.59	0.54

T Si	5.92	5.94	6.03	5.99	6.08	6.01	6.16	6.17	6.08	6.02	6.09	6.09
T Al ^{IV}	2.08	2.06	1.97	2.01	1.92	1.99	1.84	1.83	1.92	1.98	1.91	1.91
C Al ^{VI}	0.17	0.05	0.20	0.20	0.22	0.24	0.26	0.20	0.23	0.20	0.26	0.27
C Ti $^{4+}$	0.29	0.29	0.25	0.60	0.35	0.60	0.45	0.37	0.35	0.39	0.55	0.20
C Fe $^{2+}$	2.34	2.15	2.24	1.79	1.74	1.55	1.83	1.60	1.80	1.99	1.71	1.83
C Fe $^{3+}$	0.63	0.76	0.70	0.00	0.32	0.00	0.00	0.34	0.31	0.24	0.00	0.49
C Mg^{2+}	1.44	1.63	1.49	2.37	2.31	2.58	2.43	2.43	2.25	2.13	2.44	2.15
C Mn^{2+}	0.14	0.11	0.12	0.05	0.05	0.04	0.04	0.06	0.06	0.05	0.04	0.05
B Ca^{2+}	1.74	1.73	1.70	1.77	1.77	1.77	1.79	1.74	1.79	1.80	1.81	1.76
B Na$^+$	0.26	0.27	0.30	0.23	0.23	0.23	0.21	0.26	0.21	0.20	0.19	0.24
A Na$^+$	0.60	0.59	0.51	0.66	0.60	0.71	0.69	0.58	0.62	0.61	0.71	0.62
A K$^+$	0.37	0.34	0.35	0.27	0.32	0.21	0.26	0.24	0.27	0.34	0.24	0.35

Trace elements (ppm)

Sc	9.38	16.89	10.27	29.58	23.27	22.40	22.05	22.73	22.78	21.92	25.55	26.42
V	255.68	246.42	262.89	304.40	257.94	280.08	234.46	243.18	294.73	242.41	277.48	271.71
Cr	2.71	19.74	2.52	248.78	180.74	262.17	206.23	191.64	255.82	119.97	131.96	203.95
Ni	4.28	11.35	4.24	152.09	139.24	182.01	158.99	159.90	138.32	135.87	174.09	114.03
Rb	21.96	13.34	18.19	6.62	7.74	6.61	6.51	7.73	7.95	7.12	6.99	6.68
Sr	149.28	120.92	131.68	619.63	218.46	719.47	461.51	255.96	300.73	434.86	541.86	318.63
Y	16.85	17.32	17.32	24.82	11.87	27.16	31.07	29.23	10.90	26.48	26.98	18.75
Zr	1026.46	811.34	834.97	126.61	219.88	147.99	258.68	307.80	251.64	243.47	185.12	317.50
Nb	110.33	144.69	131.32	58.96	67.59	84.97	146.28	117.86	61.19	112.72	100.09	116.85
Cs	<0.058	<0.060	<0.058	<0.24	<0.24	<0.26	<0.26	<0.25	<0.25	<0.231	<0.230	<0.233
Ba	85.05	158.26	81.15	382.76	289.71	369.62	363.12	259.08	316.57	373.00	367.39	317.47
La	59.32	64.84	58.77	14.17	13.34	17.80	29.73	36.08	17.51	29.89	22.41	29.28
Ce	102.16	113.63	102.61	40.65	29.18	52.10	78.31	83.14	38.15	72.64	61.29	67.36
Pr	9.45	10.95	10.17	6.33	4.22	8.01	11.17	10.90	5.30	9.54	8.84	8.82
Nd	27.91	32.03	30.50	30.90	18.96	38.55	47.66	46.22	22.38	43.76	40.86	36.88
Sm	3.99	4.87	4.71	7.89	4.92	9.07	9.93	9.37	4.73	9.22	9.42	7.43
Eu	1.37	1.37	1.47	2.52	1.17	2.92	2.99	2.86	1.22	2.54	2.88	2.01
Gd	3.24	3.78	3.80	7.27	4.39	9.25	8.87	8.52	4.43	8.05	8.42	6.59
Tb	0.47	0.53	0.56	1.00	0.56	1.20	1.24	1.18	0.57	1.09	1.04	0.82
Dy	2.89	3.06	3.16	5.47	3.11	5.87	6.49	6.07	2.88	6.17	6.10	4.50
Ho	0.62	0.62	0.60	0.98	0.47	1.09	1.20	1.15	0.44	1.07	1.06	0.77
Er	1.76	2.02	1.85	2.51	1.12	2.42	3.01	2.79	1.00	2.62	2.83	1.81
Tm	0.28	0.26	0.30	0.27	0.12	0.35	0.36	0.31	0.14	0.32	0.28	0.18
Yb	2.51	2.07	2.27	1.61	0.87	1.84	2.43	2.11	0.90	1.98	1.85	1.07
Lu	0.49	0.52	0.55	0.18	0.17	0.24	0.31	0.32	0.18	0.29	0.26	0.23
Hf	20.63	21.44	18.95	3.71	6.20	4.51	7.18	7.46	6.20	6.66	5.31	7.80
Ta	1.41	2.55	2.05	2.77	4.00	3.98	6.74	4.85	3.61	5.29	4.97	6.01
Pb	1.29	1.42	1.77	1.20	1.09	1.40	1.07	2.78	0.98	1.37	1.68	1.00
Th	0.35	0.78	0.38	0.10	0.02	0.14	0.15	0.12	0.08	0.18	0.15	0.08
U	0.17	0.33	0.03	0.01	<0.00	0.02	0.00	0.01	0.00	0.01	0.04	0.00
ΣREE	242.68	274.76	248.89	176.15	117.76	200.27	256.83	262.98	133.52	237.59	220.07	212.92
(La/Sm)$_N$	9.28	8.31	7.79	1.12	1.69	1.23	1.87	2.40	2.31	2.02	1.49	2.46
(Gd/Yb)$_N$	1.04	1.48	1.35	3.65	4.07	4.07	2.95	3.27	3.97	3.29	3.68	4.99
Eu/Eu*	1.16	0.97	1.06	1.01	0.77	0.97	0.97	0.98	0.81	0.90	0.99	0.88

Supplementary Table IV.7. Continued

Sample	LI18f (fine-grained)					LI18c (coarse-grained)								
Rock type	Monzonite with oriented texture					Monzonite								
Location	G	G	C	C	C	C	C	C	C	C	C	C	G	G
Spot	LI18 05_01	LI18 05_02	LI18 07_01	LI18 07_02	LI18 07_03	LI18 28_03	LI18 28_04	LI18 32_01	LI18 32_02	LI18 32_03	LI18 33_01	LI18 33_02	LI18 42_01	LI18 42_02
Area	Core	Rim	Core	Transition	Rim	Core	Rim	Core	Transition	Rim	Core	Rim	Core	Transition
Mineral	Hst		Hst	Hst	Hst	Hst	Hst	Hst	Hst	Hst	Hst	Hst	Hst	Hst

Major elements (wt%)

SiO_2	25.80	6.07	38.43	37.95	37.23	38.07	37.30	38.91	38.27	36.97	37.51	38.36	37.19	38.64
TiO_2	1.22	0.07	3.41	2.35	1.71	2.36	1.52	3.17	0.51	1.80	2.06	1.84	0.98	1.76
Al_2O_3	7.86	2.13	12.42	12.39	12.43	11.77	12.66	11.31	11.94	12.82	12.61	11.92	12.53	11.94
Fe_2O_3	4.31	0.00	4.40	6.94	7.56	6.23	10.11	4.49	9.34	8.01	5.57	4.95	7.61	7.46
FeO	15.62	1.60	16.22	16.98	18.60	17.99	17.94	16.88	16.17	17.69	17.23	19.97	17.63	15.67
MnO	0.92	0.11	0.95	1.06	1.17	1.06	1.03	1.08	1.01	1.01	0.99	1.20	1.11	1.04
MgO	2.21	0.64	7.41	5.64	4.61	5.77	4.24	7.34	5.74	4.88	6.13	4.96	5.34	6.63
CaO	7.71	1.17	10.31	10.05	9.86	10.24	9.43	10.45	9.57	9.74	10.26	10.22	9.99	9.87
Na_2O	1.14	0.34	2.98	2.70	2.80	2.62	2.97	2.76	2.66	2.75	2.70	2.85	2.77	2.58
K_2O	1.60	0.26	1.55	1.36	2.07	1.83	2.06	1.68	2.46	2.16	1.98	1.92	2.44	2.14
Total	68.40	12.38	98.06	97.41	98.03	97.94	99.28	98.06	97.67	97.83	97.05	98.18	97.58	97.73

mg#	0.20	0.42	0.45	0.37	0.31	0.36	0.30	0.44	0.39	0.33	0.39	0.31	0.35	0.43

T Si	5.95	7.17	5.92	5.94	5.88	5.97	5.83	6.02	6.02	5.83	5.91	6.04	5.89	6.01
T Al ^{IV}	2.05	0.83	2.08	2.06	2.12	2.03	2.17	1.98	1.98	2.17	2.09	1.96	2.11	1.99
C Al ^{VI}	0.09	2.13	0.18	0.23	0.20	0.14	0.16	0.09	0.23	0.22	0.25	0.25	0.23	0.21
C Ti $^{4+}$	0.21	0.06	0.39	0.28	0.20	0.28	0.18	0.37	0.06	0.21	0.24	0.22	0.12	0.21
C Fe $^{2+}$	3.01	1.58	2.09	2.22	2.46	2.36	2.34	2.19	2.13	2.33	2.27	2.63	2.34	2.04
C Fe $^{3+}$	0.75	0.00	0.51	0.82	0.90	0.74	1.19	0.52	1.10	0.95	0.66	0.59	0.91	0.87
C Mg^{2+}	0.76	1.13	1.70	1.32	1.09	1.35	0.99	1.69	1.35	1.15	1.44	1.16	1.26	1.54
C Mn^{2+}	0.18	0.11	0.12	0.14	0.16	0.14	0.14	0.14	0.13	0.14	0.13	0.16	0.15	0.14
B Ca^{2+}	1.90	1.48	1.70	1.69	1.67	1.72	1.58	1.73	1.61	1.65	1.73	1.72	1.70	1.65
B Na$^+$	0.10	0.52	0.30	0.31	0.33	0.28	0.42	0.27	0.39	0.35	0.27	0.28	0.30	0.35
A Na$^+$	0.42	0.26	0.59	0.50	0.53	0.52	0.48	0.56	0.42	0.49	0.56	0.59	0.55	0.42
A K$^+$	0.47	0.38	0.30	0.27	0.42	0.37	0.41	0.33	0.49	0.44	0.40	0.39	0.49	0.42

Trace elements (ppm)

Sc	3.86	1.38	11.68	7.79	8.50	16.67	15.92	20.98	17.19	7.97	27.65	3.49	15.29	13.93
V	105.47	28.86	103.74	99.39	191.21	198.10	232.26	187.71	198.90	207.87	241.06	204.15	196.46	182.92
Cr	<0.53	0.50	14.10	2.71	1.15	1.91	1.84	1.89	10.63	7.65	1.45	0.50	2.50	3.18
Ni	1.47	0.44	22.46	11.38	1.97	3.05	3.04	2.52	1.87	1.10	2.60	1.51	2.16	2.74
Rb	11.57	4.04	9.68	10.93	21.96	14.61	24.58	12.79	15.08	23.05	23.76	17.79	18.63	21.64
Sr	81.45	19.90	992.06	1120.77	119.73	137.85	67.82	135.61	45.19	105.69	57.60	108.93	52.75	70.88
Y	13.58	3.84	32.73	30.61	25.57	20.45	16.97	22.14	4.09	24.33	30.48	14.37	6.13	13.28
Zr	480.42	122.30	589.40	734.83	775.95	572.69	743.88	516.21	354.88	778.90	1197.03	457.39	433.91	541.10
Nb	116.11	21.25	155.62	156.81	135.56	129.61	93.66	141.85	7.53	124.70	132.42	93.80	26.24	58.95
Cs	<0.167	<0.037	<0.22	<0.21	<0.21	<0.136	<0.144	<0.133	<0.135	<0.140	<0.136	<0.137	<0.144	<0.147
Ba	47.48	14.54	851.74	1087.19	83.58	139.18	54.87	185.26	17.40	71.76	55.28	70.03	29.21	46.48
La	32.93	9.49	52.05	72.53	54.05	54.64	45.24	60.63	6.88	55.16	67.60	36.05	19.38	34.07
Ce	72.31	17.87	134.52	172.89	110.75	104.50	80.80	114.54	12.97	110.93	120.51	70.71	32.26	56.11
Pr	7.89	1.86	18.59	22.80	11.50	10.25	7.89	11.58	1.33	11.50	11.33	7.02	3.03	4.93
Nd	25.03	6.28	75.97	86.43	39.50	32.73	26.06	38.76	4.63	37.27	36.44	22.14	9.84	15.22
Sm	3.53	0.92	13.48	15.70	5.53	4.76	3.84	5.46	0.66	5.47	5.46	3.19	1.34	2.43
Eu	1.06	0.27	3.60	3.82	1.72	1.43	1.23	1.58	0.37	1.63	1.48	1.04	0.52	0.80
Gd	3.11	0.83	10.74	10.92	4.42	3.99	3.71	4.47	0.62	4.55	5.01	2.82	1.17	1.75
Tb	0.37	0.10	1.42	1.37	0.70	0.57	0.52	0.64	0.08	0.70	0.73	0.37	0.18	0.31
Dy	2.36	0.66	7.80	7.10	4.33	3.38	2.94	3.84	0.55	4.07	4.70	2.27	1.09	1.66
Ho	0.51	0.14	1.31	1.15	0.94	0.68	0.57	0.79	0.13	0.78	1.07	0.47	0.21	0.41
Er	1.36	0.42	3.30	2.99	2.68	2.15	1.81	2.16	0.41	2.50	3.27	1.37	0.63	1.56
Tm	0.23	0.06	0.41	0.46	0.50	0.33	0.26	0.32	0.10	0.42	0.56	0.25	0.10	0.28
Yb	2.48	0.62	2.82	3.33	4.98	3.03	2.81	2.42	1.20	3.83	4.75	2.26	1.15	2.75
Lu	0.50	0.13	0.67	0.73	0.87	0.62	0.79	0.43	0.31	0.87	1.01	0.50	0.42	0.57
Hf	13.51	3.42	16.86	27.70	22.48	14.28	22.51	12.45	8.78	22.45	39.96	10.56	13.02	13.18
Ta	0.82	0.20	4.34	5.06	1.05	1.37	0.90	1.55	0.01	1.00	0.98	0.57	0.07	0.15
Pb	0.85	0.35	1.82	2.12	1.56	1.30	1.80	1.34	1.22	1.52	1.46	1.25	1.19	1.22
Th	0.20	0.93	0.27	1.61	0.37	0.29	0.35	0.08	0.01	0.39	0.67	0.14	0.07	0.58
U	0.02	0.02	0.06	0.15	0.03	0.03	0.02	0.01	0.01	0.03	0.08	0.03	0.00	0.05
ΣREE	171.10	44.88	371.09	440.63	276.54	260.18	211.36	290.75	51.51	271.97	322.05	168.32	92.74	150.06
(La/Sm)$_N$	5.83	6.45	2.41	2.88	6.10	7.17	7.36	6.93	6.52	6.30	7.73	7.06	9.03	8.76
(Gd/Yb)$_N$	1.01	1.08	3.08	2.65	0.72	1.07	1.07	1.49	0.41	0.96	0.85	1.01	0.83	0.51
Eu/Eu*	0.97	0.95	0.91	0.89	1.06	1.00	0.99	0.98	1.75	1.00	0.86	1.05	1.26	1.18

Supplementary Table IV.7. Continued

Sample	LI18c (coarse-grained)					LTa29							
Rock type	Monzonite					Monzonite							
Location	G	G	G	G	G	G	G	C	C	C	C	C	C
Spot	LI18 42_03	LI18 43_01	LI18 43_02	LI18 43_03	LI18 43_04	LTa29 01_01	LTa29 01_02	LTa29 04_04	LTa29 04_05	LTa29 31_03	LTa29 31_04	LTa29 35_03	LTa29 35_04
Area	Rim	Core	Transition (inner)	Transition (outer)	Rim	Core	Rim	Core	Rim	Core	Rim	Core	Rim
Mineral	Hst	Hst	Hst	Hst	Hst	Mg-Hst	Mg-Hst	Mg-Hst	Mg-Hst	Mg-Hst	Mg-Hst	Mg-Hst	Mg-Hst
Major elements (wt%)													
SiO_2	37.58	38.91	39.02	38.80	37.35	39.92	39.79	40.43	39.92	39.84	39.57	40.18	40.40
TiO_2	2.28	2.52	2.90	0.88	1.80	3.16	2.77	3.20	3.14	3.59	2.82	2.95	2.57
Al_2O_3	12.61	11.59	11.53	12.42	12.70	11.51	11.36	11.33	11.61	11.54	11.31	11.12	11.32
Fe_2O_3	7.53	5.47	4.40	9.11	8.16	4.14	3.86	3.85	2.08	1.22	2.64	4.38	3.91
FeO	17.71	17.90	17.83	15.00	19.17	15.13	15.12	15.12	15.91	16.66	15.71	14.68	14.93
MnO	1.28	1.12	1.00	0.71	1.05	0.81	0.84	0.81	0.85	0.67	0.62	0.64	0.78
MgO	5.18	6.18	7.04	6.75	4.28	8.61	8.77	9.02	8.95	9.03	8.94	9.19	9.08
CaO	9.91	9.91	10.44	9.76	9.82	10.94	11.37	11.09	11.29	11.27	11.17	11.40	11.36
Na_2O	2.82	2.97	2.99	2.82	2.92	2.01	1.80	2.15	2.24	2.46	2.21	1.82	1.81
K_2O	2.00	1.88	1.81	2.09	2.07	1.87	1.76	1.76	1.79	1.79	1.81	1.64	1.90
Total	98.89	98.44	98.95	98.35	99.32	98.10	97.42	98.77	97.77	98.05	96.79	98.00	98.07
mg#	0.34	0.38	0.41	0.44	0.28	0.50	0.51	0.52	0.50	0.49	0.50	0.53	0.52
T Si	5.86	6.04	6.01	5.99	5.84	6.10	6.12	6.12	6.11	6.09	6.12	6.12	6.16
T Al ^{IV}	2.14	1.96	1.99	2.01	2.16	1.90	1.88	1.88	1.89	1.91	1.88	1.88	1.84
C Al ^{VI}	0.17	0.16	0.11	0.26	0.18	0.17	0.17	0.14	0.21	0.17	0.19	0.12	0.19
C Ti $^{4+}$	0.27	0.29	0.34	0.10	0.21	0.36	0.32	0.36	0.36	0.41	0.33	0.34	0.29
C Fe $^{2+}$	2.31	2.33	2.30	1.94	2.51	1.93	1.94	1.91	2.04	2.13	2.03	1.87	1.90
C Fe $^{3+}$	0.88	0.64	0.51	1.06	0.96	0.48	0.45	0.44	0.24	0.14	0.31	0.50	0.45
C Mg^{2+}	1.20	1.43	1.62	1.55	1.00	1.96	2.01	2.04	2.04	2.06	2.06	2.09	2.06
C Mn^{2+}	0.17	0.15	0.13	0.09	0.14	0.10	0.11	0.10	0.11	0.09	0.08	0.08	0.10
B Ca^{2+}	1.65	1.65	1.72	1.62	1.65	1.79	1.87	1.80	1.85	1.85	1.85	1.86	1.86
B Na$^+$	0.35	0.35	0.28	0.38	0.35	0.21	0.13	0.20	0.15	0.15	0.15	0.14	0.14
A Na$^+$	0.50	0.54	0.62	0.46	0.53	0.38	0.41	0.43	0.52	0.57	0.52	0.40	0.39
A K$^+$	0.40	0.37	0.35	0.41	0.41	0.36	0.34	0.34	0.35	0.35	0.36	0.32	0.37
Trace elements (ppm)													
Sc	25.06	16.85	12.99	12.46	12.47	16.38	18.46	16.39	16.80	14.26	15.75	16.21	16.95
V	222.88	184.25	185.28	172.26	217.71	233.49	249.11	219.15	238.59	222.09	220.88	236.91	220.62
Cr	1.44	1.33	2.93	2.97	1.89	9.05	8.11	9.44	12.05	4.13	5.50	4.34	10.34
Ni	1.83	2.20	2.29	3.05	1.95	12.14	13.62	13.98	13.00	11.48	11.56	12.29	11.43
Rb	21.14	11.29	16.84	15.27	18.71	12.99	12.46	11.29	12.69	12.26	12.45	13.00	13.31
Sr	76.21	122.40	88.19	83.38	74.36	175.25	162.50	193.10	196.48	197.24	199.43	182.85	183.53
Y	27.96	21.17	21.82	10.42	19.51	17.35	10.21	18.79	16.30	17.99	18.55	15.28	14.41
Zr	970.94	565.17	628.08	422.46	558.61	537.83	451.77	482.13	554.93	440.72	487.01	486.47	555.23
Nb	124.95	130.78	136.02	51.21	99.37	155.60	47.42	137.57	113.55	124.24	134.29	106.79	89.11
Cs	<0.150	<0.137	<0.143	<0.137	<0.133	<0.077	<0.079	<0.086	<0.071	<0.077	<0.081	<0.084	<0.086
Ba	71.03	163.69	53.40	70.72	59.83	168.00	144.94	150.75	158.41	154.55	150.30	148.08	147.84
La	60.40	56.86	63.08	30.03	41.71	44.46	41.18	54.55	54.07	52.77	54.01	50.92	49.97
Ce	112.61	107.71	115.74	53.87	75.69	79.65	64.99	103.33	96.29	100.03	103.97	92.92	84.83
Pr	10.94	10.95	11.03	5.11	7.34	7.94	5.98	10.28	9.27	9.71	10.25	9.07	8.00
Nd	36.19	35.41	34.48	16.28	23.80	25.38	17.48	30.91	27.41	29.23	30.70	27.51	23.73
Sm	5.70	5.68	5.06	2.58	3.20	4.07	2.59	4.58	4.04	4.22	4.77	4.26	3.58
Eu	1.46	1.48	1.56	0.83	1.02	1.29	0.89	1.55	1.46	1.50	1.67	1.40	1.35
Gd	4.95	4.74	4.14	2.15	3.08	3.47	1.86	3.78	3.22	3.49	3.61	3.34	2.80
Tb	0.70	0.60	0.59	0.29	0.47	0.53	0.31	0.61	0.48	0.53	0.54	0.51	0.42
Dy	4.42	3.84	3.71	1.60	3.12	2.82	1.55	3.13	2.67	2.88	3.13	2.65	2.29
Ho	0.97	0.74	0.74	0.37	0.72	0.65	0.34	0.66	0.55	0.66	0.66	0.55	0.47
Er	3.04	2.22	2.17	1.06	2.14	1.72	0.91	1.87	1.72	1.77	1.77	1.51	1.42
Tm	0.53	0.36	0.36	0.19	0.32	0.25	0.16	0.28	0.28	0.30	0.27	0.23	0.24
Yb	4.79	3.12	2.77	1.83	3.64	1.77	0.96	1.93	1.74	2.05	1.93	1.59	1.63
Lu	0.98	0.68	0.56	0.46	0.78	0.33	0.22	0.39	0.37	0.39	0.39	0.32	0.33
Hf	27.91	13.59	16.15	9.30	13.64	12.91	11.43	12.34	12.37	10.35	10.68	10.89	11.88
Ta	1.14	1.51	1.26	0.52	0.56	2.74	0.72	2.05	1.50	1.95	1.85	1.90	1.26
Pb	1.44	1.23	1.25	1.31	1.44	3.44	1.87	1.05	1.04	1.00	1.57	1.38	1.07
Th	0.45	0.16	0.20	0.11	0.31	1.22	0.07	0.19	0.18	0.21	0.26	0.15	0.11
U	0.02	0.01	0.01	0.01	0.02	0.37	0.01	0.01	0.01	0.05	0.05	0.01	0.01
ΣREE	300.71	272.40	280.80	139.53	199.00	208.05	168.09	253.02	236.66	241.78	251.96	228.26	212.40
(La/Sm)$_N$	6.62	6.25	7.78	7.27	8.14	6.82	9.93	7.44	8.36	7.81	7.07	7.46	8.72
(Gd/Yb)$_N$	0.84	1.23	1.21	0.95	0.68	1.59	1.57	1.59	1.50	1.37	1.52	1.70	1.39
Eu/Eu*	0.84	0.87	1.04	1.07	0.99	1.04	1.24	1.14	1.23	1.19	1.23	1.13	1.30

Supplementary Table IV.7. Continued

Sample	LTo35						LO52/1		
Rock type	Monzogranite						Lamprophyre		
Location	G	G	C	C	C	C	G	G	G
Spot	LTo35 36_01	LTo35 36_02	**LTo35 47_01**	**LTo35 47_02**	**LTo35 60_01**	**LTo35 60_02**	LO52_1 47_01	LO52_1 47_02	LO52_1 50_01
Area	Core	Rim	**Core**	**Rim**	**Core**	**Rim**	Core	Rim	Core
Mineral	Fe-Hbl	Fe-Hbl	**Fe-Hbl**	**Fe-Hbl**	**Fe-Hbl**	**Fe-Hbl**	Mg-Hst	Fe-Prg	Fe-Krs

Major elements (wt%)

SiO_2	43.86	43.41	**43.11**	**43.66**	**43.26**	**43.97**	39.92	39.82	32.81
TiO_2	1.81	1.62	**1.88**	**1.54**	**1.57**	**1.60**	0.89	2.27	29.17
Al_2O_3	7.47	8.13	**7.85**	**8.06**	**7.87**	**7.36**	13.26	12.84	4.18
Fe_2O_3	7.48	6.37	**7.09**	**6.78**	**7.72**	**6.49**	6.21	2.00	0.00
FeO	18.01	18.88	**18.76**	**18.91**	**18.08**	**18.50**	13.91	16.76	4.09
MnO	0.96	1.15	**1.04**	**0.96**	**1.10**	**0.88**	0.31	0.38	0.00
MgO	6.55	6.11	**6.16**	**6.46**	**6.58**	**6.74**	9.07	8.78	2.24
CaO	10.23	10.25	**10.12**	**10.55**	**10.63**	**10.27**	10.92	11.34	23.60
Na_2O	1.66	1.93	**1.98**	**1.88**	**1.76**	**1.77**	2.80	2.86	0.62
K_2O	0.96	0.96	**1.09**	**1.03**	**0.95**	**1.10**	1.94	1.67	0.33
Total	98.98	98.81	**99.06**	**99.83**	**99.53**	**98.69**	99.22	98.71	97.04

mg#	0.39	0.37	**0.37**	**0.38**	**0.39**	**0.39**	0.54	0.48	0.49

T Si	6.68	6.65	**6.60**	**6.62**	**6.59**	**6.73**	6.01	6.05	6.42
T Al ^{IV}	1.32	1.35	**1.40**	**1.38**	**1.41**	**1.27**	1.99	1.95	1.58
C Al ^{VI}	0.03	0.12	**0.02**	**0.07**	**0.00**	**0.05**	0.37	0.35	0.00
C Ti $^{4+}$	0.21	0.19	**0.22**	**0.18**	**0.18**	**0.18**	0.10	0.26	4.29
C Fe $^{2+}$	2.30	2.42	**2.40**	**2.40**	**2.30**	**2.37**	1.75	2.13	0.67
C Fe $^{3+}$	0.86	0.73	**0.82**	**0.77**	**0.89**	**0.75**	0.70	0.23	0.00
C Mg $^{2+}$	1.49	1.39	**1.41**	**1.46**	**1.49**	**1.54**	2.04	1.99	0.65
C Mn $^{2+}$	0.12	0.15	**0.14**	**0.12**	**0.14**	**0.11**	0.04	0.05	0.00
B Ca $^{2+}$	1.67	1.68	**1.66**	**1.71**	**1.73**	**1.68**	1.76	1.85	4.95
B Na $^{+}$	0.33	0.32	**0.34**	**0.29**	**0.26**	**0.32**	0.24	0.15	-3.56
A Na $^{+}$	0.16	0.26	**0.25**	**0.27**	**0.26**	**0.21**	0.58	0.69	3.80
A K $^{+}$	0.19	0.19	**0.21**	**0.20**	**0.18**	**0.21**	0.37	0.32	0.08

Trace elements (ppm)

Sc	44.90	35.40	**32.66**	**36.88**	**58.07**	**36.77**	14.67	23.43	22.64
V	240.91	244.60	**248.60**	**253.22**	**244.26**	**232.23**	325.68	338.13	303.86
Cr	19.05	17.17	**18.55**	**16.12**	**19.11**	**27.10**	0.76	20.76	30.41
Ni	11.16	10.31	**11.13**	**11.26**	**10.44**	**10.83**	43.66	49.59	50.76
Rb	6.21	8.66	**11.82**	**9.04**	**7.47**	**7.65**	23.15	17.55	5.29
Sr	29.91	46.00	**46.28**	**39.68**	**40.58**	**32.79**	262.21	284.93	428.39
Y	155.87	219.85	**232.53**	**193.37**	**222.81**	**165.06**	25.46	34.66	25.02
Zr	54.17	66.83	**67.78**	**50.29**	**68.36**	**50.64**	517.38	371.35	339.36
Nb	278.67	311.25	**318.27**	**287.75**	**352.98**	**270.21**	118.42	119.00	81.20
Cs	<0.065	<0.061	**0.13**	**<0.058**	**<0.052**	**<0.052**	<0.23	0.30	<0.200
Ba	11.67	23.82	**26.86**	**19.50**	**14.02**	**12.48**	484.50	481.14	440.54
La	34.06	58.15	**59.32**	**35.37**	**52.43**	**32.36**	74.68	76.47	68.31
Ce	141.29	209.38	**214.63**	**135.59**	**212.14**	**129.56**	130.40	136.17	117.82
Pr	25.50	35.65	**36.15**	**24.55**	**40.04**	**23.35**	13.85	15.04	13.04
Nd	117.74	157.58	**160.70**	**115.67**	**191.12**	**107.00**	47.05	52.59	46.07
Sm	34.50	44.90	**46.33**	**37.43**	**56.08**	**32.70**	7.71	9.94	8.39
Eu	3.29	4.03	**3.98**	**4.08**	**4.27**	**3.48**	2.69	3.77	3.22
Gd	32.05	41.53	**43.75**	**35.90**	**51.32**	**30.69**	6.34	8.46	7.11
Tb	5.42	7.08	**7.37**	**6.26**	**8.39**	**5.39**	0.92	1.22	0.93
Dy	30.99	41.33	**41.81**	**35.97**	**46.68**	**30.98**	4.78	6.27	5.14
Ho	6.12	8.11	**8.65**	**7.19**	**8.96**	**6.31**	0.87	1.26	0.93
Er	15.70	22.23	**23.38**	**19.56**	**22.69**	**16.92**	2.36	3.40	2.28
Tm	2.29	3.23	**3.44**	**2.85**	**3.16**	**2.49**	0.32	0.48	0.29
Yb	13.83	19.23	**20.70**	**17.59**	**18.69**	**15.24**	2.33	2.94	2.06
Lu	2.08	2.86	**3.03**	**2.64**	**2.76**	**2.32**	0.43	0.51	0.37
Hf	3.91	4.47	**4.45**	**3.23**	**5.94**	**4.49**	12.29	6.73	6.58
Ta	9.54	15.32	**17.52**	**12.19**	**12.91**	**12.14**	3.44	4.13	3.70
Pb	3.99	2.94	**3.13**	**2.72**	**2.93**	**2.67**	2.10	2.18	2.16
Th	2.16	0.72	**0.75**	**0.42**	**0.36**	**0.33**	5.27	8.05	7.38
U	1.00	0.46	**0.51**	**0.38**	**0.28**	**0.40**	2.14	3.52	3.14
ΣREE	665.62	910.54	**938.43**	**710.90**	**999.61**	**640.63**	334.87	376.62	323.62
$(La/Sm)_N$	0.62	0.81	**0.80**	**0.59**	**0.58**	**0.62**	6.05	4.80	5.08
$(Gd/Yb)_N$	1.87	1.75	**1.71**	**1.65**	**2.22**	**1.63**	2.20	2.33	2.79
Eu/Eu*	0.30	0.28	**0.27**	**0.34**	**0.24**	**0.33**	1.17	1.25	1.27

Abbreviations:
C – clot,
G – groundmass;
Hbl – hornblende,
Hst – hastingsite,
Krs – kaersutite,
Prg – pargasite

Supplementary Table IV.8. The most important textural features of the studied plagioclase crystals from the Ditrău Alkaline Massif (Romania)

Sample	Rock type	Groundmass plagioclase				Plagioclase in synneusis		
		Habit	Size (mm)	Texture	Abundance (vol%)	Habit	Size (mm)	Texture
LBH2	MDo	I–X	0.2–3	Oriented; ± sericitized core; Ap, Ttn, Zrn inclusions	60	-	-	-
LI18f (fine-grained)	Mo	H–X	0.3–2	Oriented; ± sericitized core; Ap, Ttn, Zrn inclusions	40	-	-	-
LTa29	M	I–X	0.2–2; <5 (megacryst)	± sericitized core; Ap, Ttn, Zrn inclusions	40	-	-	-
LTo35	MG	I–H	0.3–2; <5 (megacryst)	± sericitized core; Ap, Ttn, Zrn inclusions	40	I–H	0.4–2	± sericitized core; Ap, Bt, Opq, Ttn, Zrn inclusions

Abbreviations: M – monzonite, Mo – monzonite with oriented texture, MDo – monzodiorite with oriented texture, MG – monzogranite;

Ap – apatite, Bt – biotite, Opq – opaque minerals, Ttn – titanite, Zrn – zircon;

I – idiomorphic, H – hypidiomorphic, X – xenomorphic

Supplementary Table IV.9. Major (wt%) and trace element (ppm) compositions of the analyzed plagioclase populations from the Ditrău Alkaline Massif (Romania). Clot-forming plagioclase data are marked in bold, data of plagioclase in synneusis orientation are marked in italics

Sample	LBH2					LB8					
Rock type	Monzodiorite with oriented texture					Diorite					
Location	G	G	G	G	G	G (impinged)	G (impinged)	G (impinged)	G (aggregated)	G (aggregated)	G (aggregated)
Spot	LBH2 06_01	LBH2 06_02	LBH2 24_01	LBH2 24_02	LBH2 24_03	LB8 14_01	LB8 14_02	LB8 14_03	LB8 20_01	LB8 20_02	LB8 20_03
Area	Core (clear)	Rim (clear)	Core (sericitized)	Transition (clear)	Rim (clear)	Core (sericitized)	Core (clear)	Rim (clear)	Core (sericitized)	Core (clear)	Rim (clear)
Zonation	Unzoned		Complex			Complex			Normal		

Major elements (wt%)

SiO_2	64.78	64.17	67.02	64.47	68.16	67.35	65.24	67.47	66.60	67.95	69.38
TiO_2	0.01	0.00	0.00	0.00	0.07	0.03	0.00	0.07	0.00	0.00	0.02
Al_2O_3	21.53	21.53	20.27	21.59	19.49	20.32	22.15	20.41	20.49	20.52	19.71
FeO	0.23	0.11	0.00	0.04	0.00	0.00	0.00	0.00	0.06	0.05	0.05
MnO	0.06	0.00	0.01	0.01	0.00	0.00	0.05	0.05	0.00	0.08	0.06
MgO	0.00	0.01	0.05	0.00	0.00	0.04	0.00	0.00	0.00	0.00	0.00
CaO	3.10	3.53	1.05	3.20	0.36	1.41	3.14	1.36	1.35	1.16	0.37
Na_2O	9.74	9.63	10.69	9.63	11.36	10.83	9.70	10.90	10.75	11.25	11.15
K_2O	0.18	0.10	0.04	0.06	0.06	0.05	0.10	0.10	0.10	0.05	0.01
Total	99.64	99.08	99.14	99.01	99.50	100.03	100.37	100.36	99.35	101.06	100.75

An	14.81	16.76	5.12	15.47	1.71	6.71	15.07	6.42	6.45	5.36	1.80
Ab	84.15	82.70	94.62	84.17	97.92	93.02	84.34	93.01	92.96	94.36	98.13
Or	1.03	0.54	0.26	0.36	0.37	0.27	0.59	0.57	0.60	0.28	0.08

Trace elements (ppm)

Rb	0.93	0.35	12.40	3.65	29.12	1.20	2.60	0.61	14.58	18.40	2.37
Sr	1880.40	1787.30	1477.55	1857.62	1190.99	1655.89	1589.35	837.66	1684.74	1757.42	1686.72
Y	0.02	0.02	0.03	0.04	0.66	0.04	<0.0071	0.01	0.02	0.03	0.09
Ba	391.02	345.01	598.58	324.73	1125.07	512.50	498.73	316.41	739.34	575.92	437.49
La	12.24	10.81	1.81	7.72	11.18	0.97	4.53	0.47	3.73	11.43	0.60
Ce	5.48	4.78	0.91	3.01	7.28	0.40	1.89	0.12	1.73	4.97	0.39
Pr	0.20	0.16	0.07	0.12	0.60	0.04	0.06	0.00	0.06	0.16	0.04
Nd	0.32	0.21	0.09	0.13	1.68	0.03	0.09	<0.00	0.09	0.21	0.08
Sm	0.01	0.00	0.01	0.01	0.24	<0.00	<0.00	<0.00	0.01	0.01	0.02
Eu	0.26	0.18	0.07	0.18	0.28	0.04	0.17	0.03	0.15	0.26	0.16
Gd	0.02	0.01	<0.00	<0.00	0.21	0.01	<0.0183	<0.0167	<0.0266	<0.026	0.01
Tb	0.00	0.00	0.00	<0.00	0.02	<0.00249	<0.00	<0.00	<0.00	0.00	0.00
Dy	<0.00	0.01	0.01	0.01	0.12	<0.00	<0.00	<0.00	<0.00	<0.00	0.01
Ho	0.00	0.00	<0.0035	0.00	0.03	<0.0026	<0.00	0.00	<0.00	<0.0041	0.01
Er	<0.00	0.01	<0.00	0.00	0.03	<0.00	<0.00	<0.00	<0.00	<0.00	0.01
Tm	<0.00	0.00	0.00	<0.00	0.01	<0.00248	0.00	<0.00	<0.00	<0.00	<0.00
Yb	0.00	<0.00	<0.00	0.00	0.03	0.00	<0.00	<0.00	<0.00	<0.00	0.01
Lu	0.00	0.00	0.00	0.00	0.01	0.00	<0.00	<0.00	0.00	0.00	<0.00
Hf	0.00	0.01	0.00	0.06	0.12	0.00	<0.00	<0.00	<0.00	<0.00	0.02
Pb	6.52	5.86	1.59	4.96	5.70	2.53	5.95	1.77	4.86	10.36	6.70
ΣREE	18.54	16.20	2.99	11.23	22.37	1.54	6.75	0.63	5.79	17.07	1.42
Eu/Eu*	65.64	94.07			3.76						29.90

Supplementary Table IV.9. Continued

Sample	LB8						LB16f (felsic part)		LI18f (fine-grained)		
Rock type	Diorite						Diorite with oriented texture		Monzonite with oriented texture		
Location	G	G	G	G	G	G	G	G	G	G	G
Spot	LB8 31_01	LB8 31_02	LB8 31_03	LB8 52_01	LB8 52_02	LB8 53_01	LB16 12_01	LB16 12_02	LI18 01_01	LI18 01_02	LI18 01_03
Area	Core (sericitized)	Core (clear)	Rim (clear)	Core (sericitized)	Transition (clear)	Rim (clear)	Core (clear)	Rim (clear)	Core (sericitized)	Transition (inner, clear)	Transition (outer, clear)
Zonation	Normal			Normal			Normal		Complex		

Major elements (wt%)

SiO_2	67.38	68.03	68.19	64.60	64.63	68.78	65.05	67.43	67.16	65.08	65.42
TiO_2	0.00	0.00	0.00	0.05	0.08	0.00	0.00	0.00	0.00	0.00	0.10
Al_2O_3	20.39	19.88	19.79	22.25	21.87	19.56	22.03	20.59	20.20	21.63	21.33
FeO	0.08	0.00	0.01	0.09	0.07	0.00	0.15	0.00	0.00	0.00	0.08
MnO	0.03	0.00	0.00	0.08	0.00	0.00	0.00	0.06	0.08	0.00	0.00
MgO	0.01	0.00	0.00	0.00	0.01	0.01	0.00	0.00	0.00	0.00	0.00
CaO	1.25	0.93	0.73	3.53	3.09	0.49	3.05	1.50	1.43	3.02	2.64
Na_2O	10.48	11.13	11.06	9.47	9.44	11.42	9.68	10.86	10.60	9.40	9.80
K_2O	0.00	0.15	0.06	0.11	0.05	0.05	0.06	0.01	0.06	0.11	0.10
Total	99.62	100.12	99.84	100.16	99.25	100.30	100.02	100.45	99.53	99.23	99.47

An	6.18	4.36	3.50	16.96	15.26	2.32	14.80	7.07	6.92	14.96	12.90
Ab	93.81	94.80	96.16	82.43	84.42	97.42	84.88	92.86	92.76	84.42	86.54
Or	0.01	0.84	0.34	0.61	0.32	0.26	0.32	0.07	0.32	0.62	0.56

Trace elements (ppm)

Rb	10.08	14.02	<0.30	1.49	27.36	1.31	0.29	11.07	8.96	<0.29	<0.29
Sr	1479.12	1779.50	568.46	1651.71	1131.81	1415.04	1743.44	776.73	3814.52	2817.56	2380.04
Y	0.13	0.02	<0.0046	0.01	0.02	0.00	0.01	0.01	0.15	0.02	0.01
Ba	1307.30	829.54	83.30	883.37	1541.85	520.87	318.34	1040.82	202.72	225.84	228.81
La	67.25	5.92	0.66	9.90	0.53	0.71	5.24	0.74	21.41	8.30	3.25
Ce	30.44	2.73	0.22	5.68	0.29	0.43	2.28	0.19	14.93	3.41	2.10
Pr	1.24	0.12	0.01	0.23	0.01	0.01	0.08	0.00	0.78	0.35	0.08
Nd	1.97	0.11	<0.00	0.39	0.04	0.02	0.16	0.01	1.22	0.75	0.06
Sm	0.12	<0.029	0.01	0.02	<0.00	<0.0169	0.01	0.00	0.06	0.07	<0.0264
Eu	1.30	0.26	0.02	0.39	0.07	0.03	0.17	0.05	0.34	0.17	0.22
Gd	0.07	<0.00	0.02	0.03	<0.031	<0.0230	0.01	<0.0065	0.08	<0.037	0.01
Tb	0.01	<0.00	<0.00	0.00	0.00	<0.00	0.00	<0.00097	0.01	<0.00	<0.00
Dy	0.02	0.01	<0.00	<0.00	0.01	<0.00	0.00	0.00	<0.00	0.01	<0.00
Ho	0.00	<0.00	<0.00	0.00	<0.00	<0.00	0.00	<0.00	0.01	0.01	<0.00
Er	0.02	<0.00	<0.00	<0.00	<0.00	<0.00	<0.00	<0.00	0.02	<0.00	<0.00
Tm	0.00	<0.00	<0.00	<0.00	<0.00268	0.00	<0.00	<0.00	0.01	<0.00	<0.00
Yb	0.02	<0.00	<0.00	<0.00	<0.00	<0.00	<0.00	0.00	0.01	<0.00	0.01
Lu	0.00	<0.00	<0.00	<0.00	<0.00	<0.00	<0.00112	<0.00	<0.00	<0.00	<0.00
Hf	0.03	<0.00	<0.00	<0.00	0.00	<0.00	<0.00	<0.00	0.14	<0.00	<0.00
Pb	7.28	5.33	1.69	4.25	1.49	1.83	8.12	13.74	8.90	7.00	6.11
ΣREE	102.60	9.17	0.94	16.66	0.98	1.21	7.95	1.01	39.02	13.08	5.73
Eu/Eu*	42.00		6.72	47.73			62.81		14.55		

Supplementary Table IV.9. Continued

Sample	LI18f (fine-grained)					LI18c (coarse-grained)					
Rock type	Monzonite with oriented texture					Monzonite					
Location	G	G	G	G	G	G	G	G	G	G	G
Spot	LI18 01_04	LI18 02_01	LI18 02_02	LI18 02_03	LI18 02_04	LI18 38_01	LI18 38_02	LI18 38_03	LI18 38_04	LI18 40_01	LI18 40_02
Area	Rim (clear)	Core (clear)	Transition (inner, sericitized)	Transition (outer, clear)	Rim (clear)	Core (clear)	Transition (inner, sericitized)	Transition (outer, clear)	Rim (clear)	Core (clear)	Rim (clear)
Zonation	Complex	Complex				Complex				Unzoned	

Major elements (wt%)

SiO_2	68.93	64.48	67.87	65.26	68.86	65.33	67.88	64.19	65.10	65.02	65.40
TiO_2	0.00	0.00	0.00	0.00	0.00	0.00	0.03	0.00	0.02	0.03	0.00
Al_2O_3	19.77	21.40	19.97	22.09	19.95	21.15	20.01	22.12	21.62	20.93	21.61
FeO	0.04	0.03	0.06	0.13	0.00	0.03	0.06	0.09	0.00	0.15	0.17
MnO	0.00	0.00	0.00	0.00	0.00	0.00	0.04	0.01	0.00	0.00	0.01
MgO	0.00	0.00	0.00	0.00	0.00	0.00	0.02	0.02	0.00	0.00	0.00
CaO	0.59	3.10	0.85	2.99	0.64	2.67	0.70	3.46	3.00	2.68	3.02
Na_2O	11.03	9.56	10.94	9.67	11.20	9.90	10.99	9.71	9.55	9.84	9.69
K_2O	0.00	0.21	0.04	0.12	0.09	0.07	0.10	0.10	0.06	0.11	0.05
Total	100.36	98.78	99.73	100.26	100.74	99.14	99.84	99.70	99.34	98.77	99.94

An	2.85	15.01	4.10	14.48	3.04	12.91	3.38	16.34	14.73	13.01	14.65
Ab	97.15	83.77	95.64	84.83	96.43	86.71	96.07	83.07	84.94	86.33	85.09
Or	0.00	1.21	0.25	0.69	0.53	0.38	0.56	0.58	0.32	0.65	0.27

Trace elements (ppm)

Rb	<0.29	<0.28	25.57	<0.27	<0.28	1.36	11.37	0.44	10.12	<0.209	<0.205
Sr	2011.58	2656.49	2972.37	2569.77	899.59	1921.55	1720.75	1547.02	1902.91	2047.03	2098.25
Y	<0.0051	0.01	1.15	0.01	0.00	0.01	0.05	0.01	0.01	0.01	0.01
Ba	99.29	273.24	673.63	329.15	51.99	262.26	331.14	266.31	365.89	252.29	221.13
La	0.73	6.20	86.13	7.17	0.16	6.33	9.92	12.20	9.42	6.53	7.04
Ce	0.58	2.88	41.96	3.88	0.10	3.63	5.36	5.88	4.68	3.37	3.13
Pr	0.02	0.11	5.96	0.15	<0.00	0.14	0.24	0.22	0.16	0.12	0.12
Nd	0.04	0.17	14.32	0.25	0.01	0.19	0.37	0.44	0.26	0.22	0.16
Sm	0.01	0.02	1.01	0.04	<0.00	0.01	0.01	0.00	0.01	0.01	0.00
Eu	0.07	0.23	0.28	0.22	0.01	0.29	0.32	0.28	0.27	0.23	0.18
Gd	<0.0262	0.01	0.48	<0.00	0.01	0.01	<0.024	0.01	<0.031	0.00	<0.037
Tb	<0.00	<0.00	0.05	<0.0039	<0.0039	<0.00	0.00	0.00	0.00	<0.00	0.00
Dy	<0.00	<0.00	0.25	<0.00	<0.00	<0.00	0.01	<0.0117	<0.00	<0.00	0.00
Ho	<0.00	<0.00	0.04	0.00	<0.00	<0.00	0.00	<0.00	<0.00	0.00	<0.00
Er	<0.00	<0.00	0.10	0.00	<0.00	<0.00	0.01	<0.00	0.00	<0.00	<0.00
Tm	<0.00	<0.00	0.01	<0.00	<0.00	<0.00	0.00	<0.00	<0.00	<0.00276	<0.0039
Yb	<0.00	<0.00	0.05	<0.00	<0.00	<0.00	<0.0120	<0.00	<0.00	<0.00	<0.00
Lu	<0.00	<0.00	0.00	<0.00	<0.00	<0.00	<0.00	<0.00	<0.00	<0.00	<0.00
Hf	<0.00	<0.00	0.03	<0.00	<0.00	0.00	0.03	<0.00	0.04	<0.0105	0.00
Pb	5.02	6.24	4.42	6.33	1.25	7.30	5.64	7.46	7.23	6.94	7.24
ΣREE	1.46	9.63	151.79	11.71	0.29	10.61	16.29	19.04	14.82	10.49	10.64
Eu/Eu*		58.16	1.22			103.27		141.00		123.48	

Supplementary Table IV.9. Continued

Sample	LHH23/1								LTa29	
Rock type	Monzonite								Monzonite	
Location	G	G	G	C	C	G	G	G	C	C
Spot	LHH_23_1 05_01	LHH_23_1 05_02	LHH_23_1 05_03	LHH_23_1 13_01	LHH_23_1 13_02	LHH_23_1 15_01	LHH_23_1 15_02	LHH_23_1 15_03	LTa29 10_01	LTa29 10_02
Area	Core (sericitized)	Transition (clear)	Rim (clear)	Core (clear)	Rim (clear)	Core (clear)	Transition (clear)	Rim (clear)	Core (sericitized)	Transition (clear)
Zonation	Complex			Normal		Complex			Normal	

Major elements (wt%)

SiO_2	67.80	66.00	68.86	65.92	68.96	65.55	67.36	66.15	63.43	63.41
TiO_2	0.00	0.00	0.00	0.00	0.09	0.00	0.01	0.03	0.02	0.00
Al_2O_3	20.56	21.42	19.39	21.46	19.60	21.31	19.90	20.89	23.48	22.93
FeO	0.00	0.00	0.12	0.17	0.24	0.05	0.05	0.03	0.12	0.09
MnO	0.01	0.00	0.06	0.03	0.02	0.01	0.00	0.05	0.00	0.05
MgO	0.01	0.00	0.00	0.01	0.00	0.00	0.02	0.00	0.00	0.03
CaO	1.43	2.38	0.46	2.66	0.38	2.58	1.14	2.28	4.73	4.11
Na_2O	10.45	10.25	11.44	9.98	11.37	9.76	10.65	10.05	8.61	9.06
K_2O	0.03	0.03	0.10	0.09	0.06	0.02	0.02	0.08	0.16	0.20
Total	100.30	100.07	100.43	100.31	100.71	99.28	99.15	99.56	100.56	99.87

An	7.01	11.35	2.18	12.76	1.79	12.73	5.56	11.10	23.08	19.81
Ab	92.82	88.46	97.28	86.72	97.86	87.13	94.31	88.43	76.00	79.06
Or	0.17	0.19	0.55	0.52	0.36	0.13	0.12	0.47	0.92	1.13

Trace elements (ppm)

Rb	9.84	0.23	29.13	<0.198	0.52	8.56	0.72	3.37	19.60	<0.35
Sr	522.62	718.83	32.99	553.94	102.98	507.71	576.22	463.13	2575.57	2456.77
Y	0.02	0.01	1.18	<0.0035	<0.00	0.04	0.02	0.01	0.06	0.03
Ba	125.96	116.78	220.92	230.18	13.06	450.28	133.60	82.63	1119.43	627.24
La	14.60	7.01	1.61	34.22	0.97	14.90	18.81	9.91	13.17	12.24
Ce	4.38	1.71	2.70	9.08	0.24	3.36	4.35	2.45	7.58	5.92
Pr	0.18	0.05	0.29	0.20	0.01	0.09	0.09	0.05	0.31	0.23
Nd	0.28	0.10	1.07	0.19	0.02	0.16	0.09	0.09	0.54	0.28
Sm	0.01	<0.00	0.23	0.01	0.01	0.02	<0.0168	<0.00	0.03	0.01
Eu	0.17	0.11	0.17	0.65	0.07	0.36	0.60	0.30	0.48	0.31
Gd	<0.0173	<0.0180	0.16	<0.00	0.01	0.01	<0.0162	0.03	0.02	0.01
Tb	<0.00	<0.00	0.04	<0.00	<0.00	0.00	<0.00	<0.00	0.00	0.00
Dy	<0.00	<0.00	0.21	<0.0115	<0.00	0.00	<0.00	<0.00	0.02	0.00
Ho	<0.00	<0.00281	0.04	<0.00	<0.00	0.00	<0.00	<0.00	0.00	<0.00
Er	<0.00	<0.00	0.11	<0.00	<0.00	<0.00	<0.00	<0.00	<0.00	<0.00
Tm	0.01	<0.00	0.02	<0.00	<0.00	<0.00	0.01	<0.00	0.00	<0.00
Yb	0.01	<0.00	0.16	<0.00	0.00	0.00	<0.00	<0.00	<0.00	<0.00
Lu	0.00	<0.0029	0.02	<0.00	0.00	<0.00	<0.00	<0.00	0.00	<0.0024
Hf	<0.00	<0.00	1.66	<0.00	<0.00	<0.00	<0.00	<0.00	<0.00	0.00
Pb	3.63	4.39	6.29	5.20	0.77	6.19	5.46	3.25	3.88	4.10
ΣREE	19.65	8.99	8.02	44.34	1.33	18.96	23.97	12.83	22.22	19.04
Eu/Eu*			2.62		30.72	69.16			54.32	110.32

Sample	LTa29									
Rock type	Monzonite									
Location	C	C	C	C	G	G	M	M	M	M
Spot	LTa29 10_03	LTa29 27_01	LTa29 27_02	LTa29 27_03	LTa29 29_01	LTa29 29_02	LTa29 40_01	LTa29 40_02	LTa29 40_03	LTa29 44_01
Area	Rim (clear)	Core (sericitized)	Transition (clear)	Rim (clear)	Core (sericitized)	Rim (clear)	Core (clear)	Transition (innermost, sericitized)	Transition (intermediate, clear)	Core (clear)
Zonation	Normal	Reverse			Reverse		Normal			
Major elements (wt%)										
SiO₂	64.16	67.94	63.97	64.21	65.38	64.51	61.11	59.52	63.31	61.41
TiO₂	0.00	0.00	0.00	0.00	0.05	0.08	0.04	0.00	0.00	0.00
Al₂O₃	22.55	20.04	22.89	22.60	21.56	22.38	24.55	24.30	23.20	24.25
FeO	0.26	0.17	0.12	0.07	0.00	0.19	0.14	0.09	0.00	0.02
MnO	0.10	0.15	0.01	0.00	0.00	0.00	0.03	0.09	0.00	0.05
MgO	0.00	0.00	0.00	0.00	0.00	0.02	0.01	0.01	0.03	0.00
CaO	3.97	0.69	4.05	3.97	2.78	3.97	6.11	5.38	4.82	6.03
Na₂O	9.25	10.51	9.26	9.03	9.81	9.24	7.88	5.75	8.20	7.77
K₂O	0.09	0.97	0.03	0.12	0.15	0.05	0.09	2.28	0.10	0.10
Total	100.39	100.46	100.33	100.01	99.73	100.45	99.96	97.43	99.66	99.61
An	19.07	3.29	19.44	19.40	13.43	19.16	29.81	29.08	24.39	29.84
Ab	80.38	91.17	80.40	79.88	85.70	80.55	69.66	56.26	75.02	69.59
Or	0.54	5.53	0.17	0.72	0.87	0.29	0.54	14.66	0.58	0.56
Trace elements (ppm)										
Rb	<0.37	23.23	7.96	2.04	34.33	<0.35	35.19	42.94	2.58	<0.35
Sr	2367.73	898.10	2385.17	2408.50	1949.33	2470.5	3518.83	5051.42	3600.01	3905.78
Y	0.04	0.20	0.02	0.01	0.06	0.01	0.05	0.94	0.02	0.02
Ba	538.68	313.51	796.80	423.80	1047.80	298.82	1429.38	443.80	726.28	813.81
La	9.91	2.28	6.45	7.20	4.28	8.30	19.68	39.66	12.57	15.74
Ce	4.50	0.80	2.57	2.84	2.17	3.35	12.65	28.41	6.99	9.09
Pr	0.15	0.10	0.09	0.08	0.07	0.11	0.55	2.00	0.25	0.36
Nd	0.27	0.29	0.15	0.15	0.14	0.16	0.89	3.92	0.41	0.55
Sm	0.01	0.06	0.01	<0.0149	0.01	0.02	0.05	0.43	0.02	0.01
Eu	0.21	0.04	0.21	0.22	0.09	0.24	0.52	0.82	0.45	0.42
Gd	<0.00	0.03	<0.0142	<0.0144	<0.015	<0.0148	0.02	0.23	<0.0252	0.00
Tb	<0.00	0.01	<0.00	<0.00	<0.00249	<0.00	0.00	0.04	0.01	0.00
Dy	<0.0094	0.04	<0.00	0.00	0.01	<0.00	0.01	0.19	<0.00	0.00
Ho	0.00	0.01	<0.00	<0.00	<0.00	0.00	0.00	0.05	0.00	<0.00
Er	<0.00	0.02	<0.00	<0.00	<0.00	<0.00	0.00	0.12	0.00	0.00
Tm	0.00	0.00	<0.00	<0.00	<0.00	<0.00237	0.00	0.02	0.00	<0.00
Yb	<0.00	0.01	<0.00	<0.0101	<0.00	<0.00	<0.00	0.13	0.00	0.00
Lu	0.00	0.00	<0.00	<0.00	<0.00	<0.00	0.00	0.01	<0.00	<0.00
Hf	<0.00	0.05	<0.00	<0.00	0.01	0.00	0.00	0.02	0.00	<0.00
Pb	3.78	1.46	3.68	3.61	2.27	3.36	3.71	6.43	3.75	3.72
ΣREE	15.08	3.91	9.49	10.50	6.82	12.19	34.42	76.97	20.72	26.20
Eu/Eu*		3.14					58.27	7.85		277.37

Supplementary Table IV.9. Continued

Sample	LTa29		LTo35								
Rock type	Monzonite		Monzogranite								
Location	M	M	G	G	G	G	G	G	G	G	*S*
Spot	LTa29 44_02	LTa29 44_03	LTo35 03_01	LTo35 03_02	LTo35 03_03	LTo35 12_01	LTo35 12_02	LTo35 12_03	LTo35 12_04	LTo35 12_05	*LTo35 14_01*
Area	Transition (outermost, clear)	Rim (clear)	Core (sericitized)	Transition (clear)	Rim (clear)	Core (sericitized)	Transition (innermost, clear)	Transition (intermediate, sericitized)	Transition (outermost, clear)	Rim (clear)	*Core (sericitized)*
Zonation	Normal		Normal			Complex					*Complex*
Major elements (wt%)											
SiO$_2$	63.91	69.44	65.03	64.93	69.26	67.21	64.96	65.82	64.70	65.13	*62.46*
TiO$_2$	0.06	0.00	0.00	0.02	0.00	0.00	0.00	0.00	0.02	0.01	*0.00*
Al$_2$O$_3$	22.67	19.37	21.21	21.10	19.13	20.29	21.47	21.21	21.48	21.61	*22.87*
FeO	0.05	0.03	0.00	0.09	0.07	0.00	0.17	0.04	0.07	0.07	*0.23*
MnO	0.02	0.00	0.00	0.01	0.00	0.07	0.00	0.00	0.07	0.00	*0.00*
MgO	0.01	0.00	0.00	0.04	0.00	0.06	0.03	0.00	0.00	0.00	*0.00*
CaO	4.17	0.05	2.72	2.79	0.19	1.36	3.25	2.58	2.88	3.18	*4.93*
Na$_2$O	8.87	11.50	10.11	9.82	11.64	10.68	9.73	9.99	9.76	9.51	*8.49*
K$_2$O	0.09	0.05	0.15	0.20	0.14	0.14	0.18	0.04	0.07	0.06	*0.09*
Total	99.84	100.44	99.22	98.99	100.44	99.81	99.79	99.68	99.05	99.58	*99.08*
An	20.51	0.24	12.82	13.43	0.91	6.50	15.40	12.45	13.96	15.56	*24.18*
Ab	78.95	99.48	86.33	85.46	98.31	92.68	83.57	87.34	85.65	84.09	*75.28*
Or	0.54	0.27	0.85	1.12	0.78	0.82	1.02	0.20	0.39	0.34	*0.55*
Trace elements (ppm)											
Rb	1.25	7.05	14.03	<0.31	<0.29	1.80	0.67	<0.28	31.59	<0.44	*<0.29*
Sr	2988.40	1780.27	876.56	788.96	254.57	1165.31	1527.10	826.67	1019.01	799.69	*758.21*
Y	0.02	0.09	0.07	0.03	<0.0051	0.07	0.08	0.03	0.30	0.03	*0.03*
Ba	713.35	495.97	61.31	149.06	9.24	95.48	547.44	87.47	280.57	90.44	*63.72*
La	12.99	1.53	1.15	4.67	0.07	3.27	17.79	5.82	5.92	3.91	*1.70*
Ce	6.28	1.76	1.41	4.45	0.07	3.72	17.97	4.48	6.60	3.69	*1.94*
Pr	0.23	0.07	0.13	0.29	0.00	0.28	1.21	0.28	0.58	0.25	*0.16*
Nd	0.35	0.14	0.32	0.57	0.01	0.68	2.75	0.69	1.40	0.48	*0.36*
Sm	0.00	0.02	0.02	0.05	<0.00	0.05	0.22	0.04	0.26	0.03	*0.04*
Eu	0.38	0.04	0.03	2.01	0.39	1.56	4.48	1.90	1.85	1.82	*1.65*
Gd	<0.0156	<0.0170	0.05	0.04	<0.0142	<0.0154	0.07	0.02	0.06	0.01	*0.01*
Tb	0.00	<0.0027	0.00	0.00	<0.00	0.00	0.00	0.00	0.01	0.00	*0.00*
Dy	0.00	0.00	0.02	0.01	<0.00	0.00	0.02	0.01	0.04	<0.00	*0.01*
Ho	<0.00	0.00	<0.00	<0.00	0.00	0.00	0.01	0.00	0.02	0.00	*0.00*
Er	0.00	0.01	0.01	0.00	<0.00	0.00	0.00	0.01	0.02	<0.00	*0.00*
Tm	0.00	<0.0027	<0.00	<0.00	<0.00	<0.00	<0.00	<0.00	0.00	<0.00	*<0.00*
Yb	0.01	0.01	0.01	<0.00	<0.0100	<0.0108	0.00	<0.00	0.03	<0.00	*<0.00*
Lu	<0.00268	0.00	0.00	<0.00	<0.00	<0.0026	0.00	<0.00	0.01	0.00	*<0.00*
Hf	<0.00	0.00	<0.00	<0.00	<0.00	<0.00	<0.00	<0.00	0.03	<0.00	*<0.00*
Pb	4.40	2.54	1.02	10.20	2.17	12.67	12.13	10.82	12.86	10.03	*10.48*
ΣREE	20.27	3.67	3.22	12.12	0.54	9.65	44.60	13.30	17.09	10.23	*5.89*
Eu/Eu*			2.94	140.37			114.11	181.65	45.09	294.43	*229.08*

170

Sample	LTo35											
Rock type	Monzogranite											
Location	S	S	S	S	S	S	S	G	G	G	G	G
Spot	LTo35 14_02	LTo35 14_03	LTo35 14_04	LTo35 14_05	LTo35 14_06	LTo35 19_01	LTo35 19_02	LTo35 43_01	LTo35 43_02	LTo35 43_03	LTo35 43_04	LTo35 63_01
Area	Transition (clear)	Rim (clear)	Core (sericitized)	Transition (clear)	Rim (clear)	Core (clear)	Rim (clear)	Core (clear)	Transition (inner, sericitized)	Transition (outer, clear)	Rim (clear)	Transition (innermost, sericitized)
Zonation	Complex		Normal			Unzoned		Complex				Complex
Major elements (wt%)												
SiO_2	61.34	59.79	61.12	65.94	65.25	64.54	64.17	65.34	63.46	65.37	69.08	64.21
TiO_2	0.05	0.00	0.05	0.00	0.00	0.00	0.04	0.00	0.01	0.00	0.07	0.04
Al_2O_3	23.60	20.48	24.39	21.59	21.93	22.18	21.75	21.69	21.06	21.65	19.15	22.50
FeO	0.07	0.08	0.05	0.00	0.06	0.15	0.19	0.02	0.80	0.05	0.00	0.09
MnO	0.10	0.00	0.00	0.00	0.13	0.00	0.04	0.03	0.02	0.00	0.04	0.01
MgO	0.01	0.04	0.01	0.01	0.00	0.00	0.00	0.01	0.23	0.00	0.00	0.00
CaO	5.49	3.54	5.98	3.18	3.31	3.27	3.54	3.21	2.50	2.98	0.15	3.41
Na_2O	8.07	8.20	8.14	9.70	9.61	9.30	9.38	9.75	9.58	9.87	11.38	9.51
K_2O	0.28	0.05	0.03	0.19	0.07	0.24	0.13	0.09	0.17	0.04	0.09	0.09
Total	99.02	92.18	99.77	100.62	100.37	99.69	99.25	100.14	97.83	99.95	99.95	99.86
An	26.88	19.22	28.83	15.16	15.91	16.03	17.13	15.33	12.48	14.25	0.72	16.43
Ab	71.48	80.44	71.01	83.75	83.68	82.57	82.14	84.18	86.49	85.53	98.76	83.05
Or	1.64	0.34	0.16	1.09	0.41	1.40	0.73	0.49	1.03	0.21	0.52	0.52
Trace elements (ppm)												
Rb	<0.30	1.17	0.84	25.50	<0.37	0.31	21.35	0.63	0.47	<0.27	<0.28	26.29
Sr	765.05	781.45	949.00	945.11	884.57	146.85	947.23	789.43	792.88	757.33	192.94	1004.12
Y	0.02	0.02	0.08	0.28	0.04	0.06	2.17	1.06	0.03	0.01	<0.0052	0.10
Ba	71.61	75.87	114.07	87.10	73.71	11.02	54.95	76.01	61.46	44.33	5.75	95.48
La	2.64	2.69	4.22	11.61	2.26	1.04	23.08	5.69	2.52	1.35	0.04	1.17
Ce	2.62	2.98	4.35	12.28	2.37	1.25	31.62	7.26	2.40	1.37	0.08	1.18
Pr	0.18	0.23	0.32	0.81	0.17	0.09	2.54	0.72	0.16	0.11	0.01	0.09
Nd	0.44	0.48	0.89	1.72	0.45	0.21	6.79	2.42	0.36	0.25	<0.00	0.14
Sm	<0.0151	0.06	0.10	0.18	0.04	0.02	0.92	0.31	0.03	0.03	<0.00	0.03
Eu	1.66	1.51	2.13	1.11	1.73	0.17	0.32	1.85	1.55	1.40	0.14	0.15
Gd	0.03	0.05	0.07	0.08	<0.019	0.03	0.62	0.38	0.01	<0.0146	<0.0146	<0.0146
Tb	<0.00234	0.00	0.00	0.01	0.00	0.00	0.09	0.03	0.00	0.00	0.00	0.00
Dy	0.00	0.01	<0.00	0.03	0.01	0.02	0.44	0.21	0.01	0.01	<0.00	0.02
Ho	0.00	0.00	<0.00	0.01	0.00	0.00	0.09	0.04	0.00	<0.00	<0.00	0.00
Er	<0.00	<0.0107	0.03	0.01	<0.00	0.00	0.15	0.07	<0.00	0.00	<0.00	0.01
Tm	0.00	<0.00	<0.00	0.00	<0.00	0.00	0.02	0.01	<0.00	0.00	<0.00	0.00
Yb	<0.00	0.01	0.02	0.03	0.01	0.00	0.09	0.07	<0.00	<0.00	0.00	0.01
Lu	<0.00	0.00	<0.00	0.00	<0.00	<0.00	0.02	0.01	<0.00	<0.00	<0.00	0.00
Hf	<0.00	<0.00	0.01	0.02	<0.00	0.02	0.29	<0.00	<0.00	<0.00	0.00	0.01
Pb	10.43	10.84	11.96	8.34	10.58	2.14	6.97	10.30	9.35	8.38	1.76	1.27
ΣREE	7.60	8.04	12.22	28.16	7.08	2.90	68.96	20.12	7.07	4.55	0.27	2.89
Eu/Eu*		86.28	79.78	28.22		19.72	1.30	16.47	256.86			

Sample	LTo35				LN50/1		LBH55/1				
Rock type	Monzogranite				Monzogranite		Monzodiorite with oriented texture				
Location	G	G	G	G	G	G	G	G	G	G	G
Spot	LTo35 63_02	LTo35 63_03	LTo35 63_04	LTo35 63_05	LN50_1 28_01	LN50_1 28_02	LBH55_1 04_01	LBH55_1 04_02	LBH55_1 20_01	LBH55_1 20_02	LBH55_1 20_03
Area	Transition (intermediate, clear)	Core (clear)	Transition (outermost, clear)	Rim (clear)	Core (clear)	Rim (clear)	Core (sericitized)	Rim (clear)	Core (sericitized)	Rim (clear)	Transition (clear)
Zonation	Complex				Normal		Reverse		Complex		

Major elements (wt%)

SiO$_2$	64.38	65.19	65.88	68.69	67.78	69.18	67.53	64.10	66.97	68.87	64.84
TiO$_2$	0.10	0.06	0.00	0.05	0.03	0.00	0.00	0.06	0.00	0.00	0.08
Al$_2$O$_3$	22.48	21.68	21.88	19.75	21.03	19.83	20.69	21.76	21.13	20.44	21.93
FeO	0.12	0.11	0.00	0.12	0.10	0.02	0.00	0.32	0.07	0.07	0.14
MnO	0.04	0.00	0.00	0.05	0.00	0.00	0.00	0.04	0.06	0.01	0.00
MgO	0.01	0.00	0.00	0.02	0.00	0.00	0.00	0.02	0.04	0.00	0.00
CaO	3.81	3.27	3.18	0.39	1.67	0.84	1.58	3.57	1.92	1.18	3.46
Na$_2$O	9.28	9.62	9.74	11.28	10.72	11.40	10.48	9.12	10.57	10.92	9.44
K$_2$O	0.10	0.07	0.01	0.08	0.28	0.11	0.13	0.11	0.18	0.04	0.06
Total	100.32	100.00	100.68	100.43	101.61	101.39	100.41	99.10	100.94	101.52	99.95

An	18.39	15.76	15.27	1.85	7.79	3.89	7.64	17.67	9.04	5.64	16.78
Ab	81.02	83.85	84.67	97.70	90.64	95.51	91.62	81.71	89.95	94.12	82.85
Or	0.59	0.40	0.06	0.44	1.58	0.60	0.74	0.62	1.01	0.24	0.37

Trace elements (ppm)

Rb	0.37	31.83	0.60	<0.27	4.13	6.50	53.26	2.43	42.79	<0.24	0.67
Sr	787.91	780.68	762.98	771.61	99.87	173.82	1371.54	1138.54	1223.05	830.69	1315.26
Y	0.03	0.31	0.04	0.03	1.60	2.58	0.19	0.02	0.30	0.02	0.01
Ba	89.56	71.99	70.67	55.17	85.66	147.03	1660.98	412.30	685.33	76.82	388.86
La	2.71	8.07	3.73	1.53	1.82	2.97	61.82	20.66	15.04	1.87	14.10
Ce	3.01	8.70	3.07	1.75	2.66	4.65	34.61	9.71	9.47	0.81	5.97
Pr	0.25	0.62	0.21	0.14	0.38	0.56	1.44	0.33	0.69	0.03	0.18
Nd	0.49	1.40	0.44	0.33	1.15	1.89	2.14	0.46	1.87	0.04	0.33
Sm	0.05	0.14	0.05	0.04	0.22	0.36	0.08	<0.0180	0.32	<0.00	0.01
Eu	1.73	1.19	1.61	1.34	0.06	0.10	2.41	0.77	0.69	0.10	0.54
Gd	0.03	0.05	0.02	0.01	0.23	0.31	0.04	0.02	0.12	<0.00	<0.00
Tb	0.00	0.01	0.00	0.00	0.02	0.05	0.01	<0.00280	0.01	<0.0032	0.00
Dy	0.01	0.06	0.01	0.00	0.22	0.31	0.04	<0.0108	0.04	<0.00	<0.00
Ho	0.00	0.01	0.00	0.00	0.04	0.08	0.00	<0.00	0.02	<0.00	<0.00
Er	0.00	0.04	0.00	0.01	0.09	0.21	0.01	0.00	0.02	0.01	<0.00
Tm	0.00	0.01	<0.00230	0.00	0.01	0.04	0.00	0.00	0.01	<0.00311	<0.00
Yb	<0.00	0.02	<0.00	0.00	0.08	0.21	0.02	<0.00	0.02	0.00	<0.00
Lu	<0.00	0.00	<0.00	<0.00	0.02	0.03	0.00	<0.00	0.00	<0.00	<0.00
Hf	<0.00	0.03	0.01	<0.00	0.97	1.46	0.09	<0.00	0.16	0.02	<0.00
Pb	10.24	8.07	8.82	9.06	2.99	4.66	3.76	5.08	3.76	1.31	5.06
ΣREE	8.31	20.64	9.17	5.19	8.60	14.36	102.82	31.96	28.61	2.88	21.14
Eu/Eu*	151.65	41.89	181.10	193.51	0.78	0.91	121.36		10.73		

Supplementary Table IV.9. Continued

Sample	LBH55/1	
Rock type	Monzodiorite with oriented texture	
Location	G	G
Spot	LBH55_1 28_01	LBH55_1 28_02
Area	Core (clear)	Rim (clear)
Zonation	Unzoned	

Major elements (wt%)

SiO_2	64.70	64.63
TiO_2	0.06	0.00
Al_2O_3	22.55	22.73
FeO	0.01	0.19
MnO	0.02	0.03
MgO	0.00	0.03
CaO	3.88	3.99
Na_2O	9.40	8.99
K_2O	0.16	0.19
Total	100.79	100.78

An	18.39	19.48
Ab	80.72	79.44
Or	0.89	1.08

Trace elements (ppm)

Rb	3.83	1.94
Sr	1138.49	1225.30
Y	0.02	0.02
Ba	569.68	557.65
La	25.42	40.91
Ce	11.91	27.43
Pr	0.42	1.29
Nd	0.56	2.52
Sm	0.00	0.08
Eu	0.73	0.64
Gd	<0.0168	0.04
Tb	0.00	<0.0027
Dy	<0.00	<0.00
Ho	<0.00	<0.00
Er	<0.00	0.00
Tm	<0.00	<0.00
Yb	<0.00	<0.00
Lu	<0.00	<0.00
Hf	<0.00	0.00
Pb	4.59	4.65
ΣREE	39.06	72.92
Eu/Eu*		35.97

Abbreviations: C – clot, G – groundmass, M – megacryst, S – synneusis

DECLARATION OF THE SUPERVISOR

I, *Elemér Pál-Molnár*, hereby confirm that the content of the dissertation is based on the independent work of **Luca Kiri**, the doctoral candidate, and that she has contributed decisively to the results through her independent creative activity. I consider the entire dissertation to be eligible for support from a professional and academic point of view and recommend its acceptance.

Szeged (Hungary), 15 November 2023

....

Elemér Pál-Molnár, DSc

PhD supervisor

Where it all began: the author and her Dad at a drilling site in Altheim (Austria), 1998

IXIXI